UNIVERSITY OF OKLAHOMA

GRADUATE COLLEGE

ELECTROMAGNETICALLY INDUCED TRANSPARENCY WITH LAGUERRE-GAUSSIAN LASER MODES IN ULTRACOLD RUBIDIUM

A DISSERTATION

SUBMITTED TO THE GRADUATE FACULTY

in partial fulfillment of the requirements for the

Degree of

DOCTOR OF PHILOSOPHY

By

THOMAS GLENON AKIN
Norman, Oklahoma
2015

ELECTROMAGNETICALLY INDUCED TRANSPARENCY WITH LAGUERRE-GAUSSIAN LASER MODES IN ULTRACOLD RUBIDIUM

A DISSERTATION APPROVED FOR THE
HOMER L. DODGE DEPARTMENT OF PHYSICS AND ASTRONOMY

BY

Dr. Eric R. I. Abraham, Chair

Dr. Karl H. Sievers

Dr. Alberto M. Marino

Dr. Michael A. Morrison

Dr. Ian R. Sellers

Acknowledgements

From the intrinsic self-promoting nature of a work like this, it may appear that I claim sole responsibility for the contents of this dissertation. I would like to rectify this injustice and recognize the talented and supporting individuals involved in the creation of this work. First, I acknowledge my dissertation advisor, Eric Abraham. This work is a result of Eric's judicious superposition of freedom for enquiry and careful guidance. I am appreciative of the latitude that Eric provides, allowing me to formulate my own questions. Of equal importance is Eric's uncanny ability to recognize when to intervene with advise or expertise.

I also acknowledge Alberto Marino, whose expertise in quantum optics aided and motivated many areas of study in this project. Next, I thank Michael Morrison. Although he entered retirement during my tenure at the University of Oklahoma, Michael maintained an active presence in our research group. Michael's theoretical background was indispensable to me when I was developing the models for this work.

When I first joined Eric Abraham's laboratory, he was in the process of re-launching his atomic rubidium experiment. I was very fortunate to have a fellow graduate student, Sean Krzyzewski, join the group shortly after me. Together, we built the entire apparatus from the optics table - up. Sean's skill and dili-

gent attitude challenged me to work toward my full potential. I am grateful for our resident theorist, James Dizikes, for asking probing questions throughout my graduate career. James is a wonderful fountain of theoretical knowledge, which I often tapped when building the models for this work.

I acknowledge my family: mother Connie, father Terry, brother Tim, brother Theo, grandfather Glenn, and grandmother June. I literally could not have done this without first being conceived by my parents (but that was the easy part). More importantly, I am grateful for the encouraging environment in which my parents raised me. They have always valued education, and their principles formed the foundation of my character. I would like to thank my grandparents for their perpetual support, and for serving as role models on how to live an enriched life.

Finally, I acknowledge Sara Barber (spouse) and Ginger Elanore Pooh (*Canis lupis familiaris*). Sara and I defended our dissertations within twenty-six hours of each other. Sara's intimate understanding of the process involved in a work of this scale tailored her support with a precision that was essential for shortening the time constant characterizing my distress. I have unabating gratitude that I had the opportunity to complete this experience with Sara. Though Ginger does not have any cognitive understanding of this work, her unconditional comfort is a contributing factor to my positive attitude throughout this process.

Contents

List of Tables

List of Figures

Abstract

We demonstrate electromagnetically induced transparency using lasers in the Laguerre-Gaussian mode. The probe transmission is studied in an ultracold gas for the D2 line in both ^{85}Rb and ^{87}Rb. We consider the Lambda EIT configuration when the control laser is in the Laguerre-Gaussian mode. We compare these results to a similar configuration, but with the control laser in the fundamental laser mode. We model the transmission of a probe laser under both configurations, and we find good agreement with the experiment. We conclude that the use of Laguerre-Gaussian modes in electromagnetically induced transparency results in narrower resonance linewidths as compared to uniform control laser intensity. The narrowing of the linewidth is caused by the spatial distribution of the Laguerre-Gaussian intensity profile. This narrowing is dependent on the relative beam sizes between the control laser and the probe laser. We examine the EIT spectrum characteristics changing parameters of the Laguerre-Gaussian control laser, such as beam waist and Rabi frequency. We found that the EIT resonance is optimized when the Laguerre-Gaussian control and the Gaussian probe have the same waist size. Additionally, the spatial structure of the probe transmission is manipulated using the Laguerre-Gaussian control laser. A control laser in the Laguerre-Gaussian mode is characterized with annular intensity profiles. This results in the increased transmission of the probe in regions of high control intensity, and high absorption

in the central, dark region of the Laguerre-Gaussian mode. We transferred the image of the control laser to the probe laser.

Chapter 1

Introduction

This dissertation is primarily concerned with the role that a control laser propagating in the Laguerre-Gaussian laser mode has on electromagnetically induced transparency. We touch, very briefly, on the inclusion of higher orders of laser modes in electromagnetically induced transparency. We also use the ultracold atoms confined to a red-detuned Laguerre-Gaussian mode to measure the mode purity of the laser. This chapter will give a brief overview of electromagnetically induced transparency, and the roles that Laguerre-Gaussian modes contribute to the optical technique. Finally, an outline of the thesis will be provided.

1.1 Overview of the dissertation

Electromagnetically induced transparency (EIT) is an optical technique used to manipulate quantum states of atoms and photons [1]. A control laser modifies the absorption profile of a probe laser. The control laser couples atomic states, causing coherent destructive interference of excitation pathways of the atom. The result is an increased transmission of the probe laser tuned to an atomic resonance where absorption is otherwise expected. Figure 1.1 shows a typical EIT transmission spectrum (blue curve) in addition to a two level transmission spectrum (red curve). When $\Delta_p = 0$ (probe on resonance with atomic transition), the destructive interference results in the shown transmission window. Applications of EIT range from coherent storage of light in the atomic medium for quantum information storage [2, 3], nonlinear optics [4], and lasing without population inversion [5].

Initial spectroscopic studies of EIT were performed in an atomic gas at room temperature [6]. Large laser powers can overcome the Doppler broadening, but cause homogeneous line broadening. However, specific Doppler-free techniques produce EIT signals in a room temperature gas with moderate laser powers [7–10]. Alternatively, experiments that produce ultracold samples of atomic gases result in Doppler-broadening smaller than the natural linewidth of the atomic transition. The reduced transverse motion of cold atoms also suppresses the decoherence due to diffusion. Ultracold gases also offer high densities, typically in the range from $10^9 - 10^{12}$ cm^{-3}. For these reasons, EIT has been extensively studied in this environment [11–15].

One consequence of EIT is the slowing of light in an atomic sample. The destructive interference of excitation pathways in EIT leads to a sub-natural linewidth transmission feature. There is no theoretical minimum to the linewidth, which is only limited by experimental decoherences, such as background magnetic fields, laser linewidth, atomic collisions, and other homogeneous broadening [1]. Slow light results from enhancement of the slope of the dispersion in the frequency

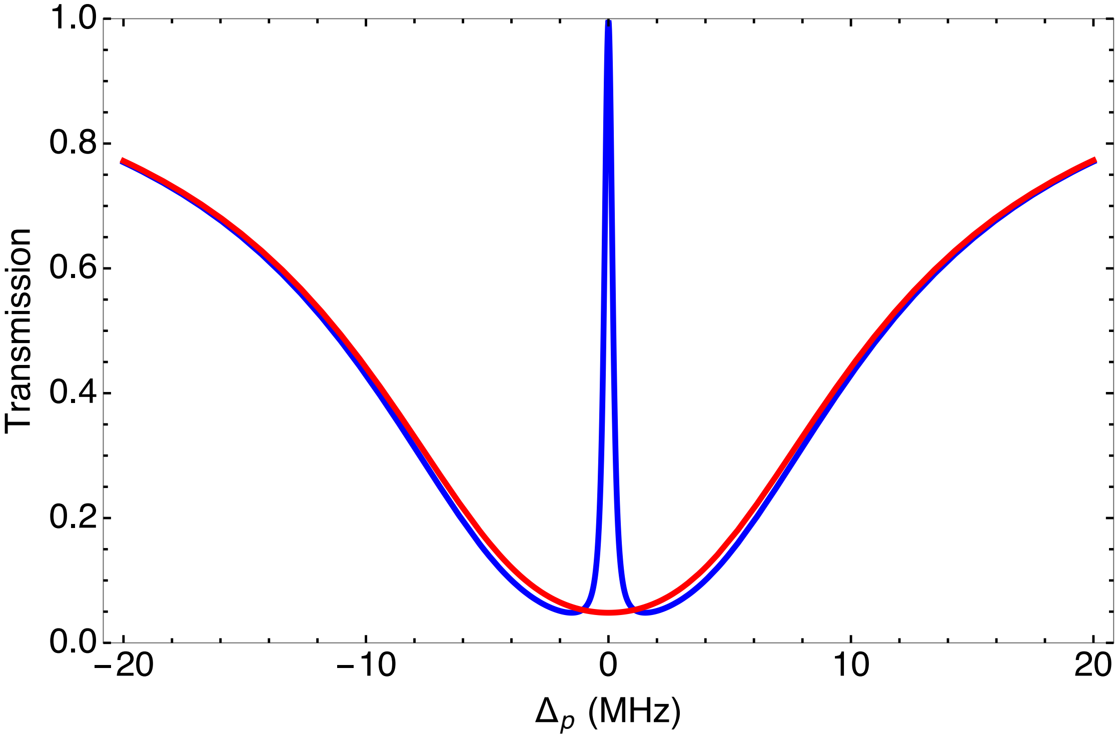

Figure 1.1: The transmission spectrum for a two level atom (red curve), and an EIT level scheme (blue curve). The control laser couples the atomic states, causing coherent destructive interference between two excitation pathways. The narrow transmission feature is characteristic to EIT.

range near the EIT resonance. Lowering of the intensity of the control field leads to narrowing of the EIT linewidth and results in the decreasing of probe group velocity. Speeds many orders of magnitude less than c have been achieved in an ultracold gas [16] and in room temperature gases [17, 18]. A slowed probe pulse propagating through the medium can be coherently stored in and retrieved from the atoms by adiabatically switching the control laser off and on [2, 3].

Incorporation of a laser propagating in a Laguerre-Gaussian (LG_p^ℓ) mode to EIT is of considerable interest. The azimuthal winding phase ($e^{i\ell\phi}$) leads to quantized orbital angular momentum (OAM) of $\ell\hbar$ per photon. The OAM forces the intensity to go to zero at the center, and the additional p radial nodes give rise to "doughnut" shaped beams, or even concentric ring intensity patterns and a spatially varying Rabi frequency. A control laser with a large Rabi frequency (as compared to the decoherence rates) increases the signal contrast of the EIT feature, while a small Rabi frequency results in a narrower EIT resonance. Placing a control laser in an LG_p^ℓ mode, and aligning the probe laser to the central node causes most of the probed atoms to experience a low control field, resulting in a narrowing of the EIT resonance. Then, the control laser power can be increased, improving the signal. Previously, sub-natural linewidths were observed in the EIT transmission spectra using an LG_0^1 control beam in room temperature gases [19, 20]. Remarkably, the LG_0^1 control laser reduced the EIT linewidth by a factor of 2 as compared to a similar experiment with the control in a Gaussian mode. It was proposed in ref. [20]

that the OAM of the control beam could decrease the decoherences due to transit effects of the room temperature gas. However, they show that increasing OAM does not increase the narrowing and argue that the reduction in EIT linewidth is due entirely to the spatial dependence of the control Rabi frequency.

We measure EIT transmission spectra using an LG_0^1 laser mode in ultracold atoms prepared in a magneto-optical trap (MOT). We find narrowing of the EIT resonance, and in the ultracold system transit decoherences are negligible. We measure EIT linewidths with the control beam in the LG_0^1 mode and the probe in the fundamental Gaussian mode for four different EIT configurations of the D2 line for both $^{85}\mathrm{Rb}$ and $^{87}\mathrm{Rb}$. We compare this data with EIT spectra where both the probe and the control lasers are in the fundamental Gaussian mode. A theoretical model is used to analyze each configuration. We use a density matrix formalism for a six level system composing the two ground-state hyperfine levels and the four excited-state hyperfine levels of the D2 transition in $^{85}\mathrm{Rb}$ and $^{87}\mathrm{Rb}$. We model the fields as plane-waves when the control is in the fundamental mode, and include the spatially varying Rabi frequency when the control is in the LG_0^1 mode [19, 21]. A transmission spectrum is generated from the steady-state solutions of the density matrix equations. We find good agreement between the model and the experiment. For both theory and experiment, we observe narrower EIT resonance features with the control laser in the LG_0^1 mode than with the control laser in the Gaussian mode.

Improvements on the coherence of our system allowed us to study, in more detail, the effect that the LG_0^1 has on EIT. In principle, the experimentalist can generate an LG_0^1 mode of any size (within the diffractive limit). We examined (both theoretically and experimentally) the characteristics of the EIT resonances with the control laser in the LG_0^1 mode. In particular, we varied the size of the LG_0^1 control mode with respect to the Gaussian probe mode. Using the contrast (height) and width of the EIT resonance as our benchmark, we conclude that the conditions for EIT are optimized when the waists of the two modes are the same.

Use of the well defined OAM states of the LG_0^1 laser mode for quantum information is gaining in popularity. A probe laser carrying OAM generates a manifold of information degrees of freedom, allowing multi-dimensional quantum computing and encryption [22]. Storage of LG_p^ℓ probe pulses in gases has been demonstrated in both room temperature gases [23–26], and in ultracold gases [27–30]. Transferring OAM states from the control laser in an LG_0^1 mode to the Gaussian probe laser was recently demonstrated using EIT assisted storage of a probe pulse in a solid state medium [31]. The experiment stored the probe pulse using a Gaussian control, then read the pulse using an LG_0^1 mode. Conservation of OAM resulted in the transfer of the OAM from the control laser to the probe laser. Also, conservation of OAM in four-wave mixing processes was extensively studied [32].

This work explores the transferring of information from the control laser to the probe laser via EIT. While we do not transfer OAM from the control to the probe, we do observe the mapping of the control spatial intensity structure to the probe. The intensity distribution of the LG_0^1 mode spatially manipulates the linear susceptibility of the atomic medium. The image of an LG_0^1 laser mode was transferred to a probe laser in a room temperature gas [33]. Surprisingly, the free space propagation of the transmitted probe maintained a donut shape over long distances $\approx$ 2m. We performed a study in an ultracold gas where the probe is in the Gaussian mode, and the control is in the LG_0^1 mode. A Λ-configuration is created on the hyperfine levels of the D2 transition in ^{85}Rb. With the assistance of EIT, we observed the transfer of the donut intensity pattern onto the probe laser, maintaining its shape for a propagation distance of $\approx$ 2 m.

1.2 Outline of the dissertation

Chapter 2 will provide a theoretical basis for the experimental results of this dissertation. A simple, two level atom will lend itself to understanding the mechanisms responsible for absorption, laser cooling, and laser trapping. We will then add a third level to our model to describe electromagnetically induced transparency. As our experiment evolved, more levels will need to be added to describe our various systems. Chapter 3 will describe the experimental apparatus used to make the measurements described in this dissertation. This description will cover the lasers, vacuum system, trapping system, detection system, instruments, and computer control used by our group. Chapter 4 will present EIT spectra with an analysis for configurations with the control laser in the LG_0^1 mode and in the Gaussian mode. In chapter 5, we will focus on EIT with the control laser in the LG_0^1 mode. In particular, we will show results for optimization of the EIT spectra for various transverse mode overlapping between the LG_0^1 control laser and the Gaussian mode probe laser. This is verified by our theoretical model. Chapter 6 will present measurements of probe transmission manipulation. This is caused by spatial variation of the transverse profile of the LG_0^1 laser mode.

Appendix A displays spectra for the control laser in higher order LG_p^ℓ modes. In particular, we employ the LG_0^5 mode and the LG_1^2 mode. Appendix B presents analysis of 2D confinement of ultracold ^{87}Rb atoms using a red and blue detuned LG_0^1 laser mode. The distribution of atoms confined by the dipole potential of the LG_0^1 laser beam is a good measurement of laser mode purity.

Chapter 2

Theoretical formalism

2.1 Introduction

This dissertation is an experimental endeavor. However, the theoretical tools necessary to describe the atomic systems are accessible to us mere mortal experimentalists. As such, a great effort is made to provide a firm theoretical description of the results presented hereafter. This chapter will develop the relevant theory for this work. In most cases, we will use a semi-classical model of the atom and electromagnetic field. Derivations for Electromagnetically Induced Transparency (EIT) using various laser transverse modes will be a large portion of this chapter. For this analysis, the control laser will possibly have the Gaussian or Laguerre-Gaussian transverse mode, and the probe laser will be in the Gaussian mode.

Since Laguerre-Gaussian modes are central to this dissertation, section 2.2 will introduce the characteristics of lasers. Section 2.3 will briefly describe the atomic angular momentum coupling responsible for the rich atomic structures of ^{85}Rb and ^{87}Rb. Section 2.4 introduces transitions in a two-level atom. With this simple model, we are able to understand laser cooling and trapping in section 2.5. In section 2.7, we add a third level to describe EIT. The experimental results presented in chapters 4 - 6 are described with level structures that are more complex than a three level atom. To model these systems, we develop an EIT model that uses four-levels (section 2.8) and six-levels (section 2.9). Finally, we focus on the transfer of the transverse intensity profile of the Laguerre-Gaussian control laser to the probe laser in section 2.10.

2.2 Lasers

The word "Laser" is an acronym whose components are **L**ight **A**mplification through **S**timulated **E**mission **R**adiation. The laser can be summarized into four main components. The first piece is the **Gain Medium**. Photons must be generated from somewhere. There exists some medium that is excited to some meta-stable state (the medium can be composed of atoms, molecules, crystals, semiconductors, etc...). In most cases, electrons are excited into the meta-stable state. The process of "lasing" begins with the spontaneous decay of the electron to the ground state, resulting in the emission of a photon. The photon will propagate through the medium, stimulating other meta-stable, excited electrons to de-excite to the ground state. Each relaxation causes the emission of a photon with the same frequency, phase, and propagation direction as the photon that stimulated the decay. Surrounding the medium with a second component, called the **Resonator/Cavity**, is key to photon amplification. The cavity is typically composed of two mirrors whose separation distance determines the longitudinal modes (selected frequencies) and the lindewidth of the laser. With the set up described thus far, photons are stimulated to emit radiation along a preferential direction selected by the cavity. Each photon reflects back and forth between the mirrors of the cavity, and after some time all the atoms decay to the ground state. No more photons can be added to the field. This brings us to the third laser element. A **Pumping Mechanism** is introduced to continuously promote the stimulated electrons back into the meta-stable state, where more stimulated emission can occur. The pumping mechanism may be a flash lamp (as in the ruby laser), a high voltage source (as in the Helium-Neon laser), an injection current (as in the semi-conductor laser), and many other sources of replenishing energy. Finally, we need some way to **Extract the Energy**. This is simply done by partially silvering only one of the resonator mirrors (i.e., making the reflectivity of one mirror 90% and the other 100%) [34].

The four elements that were just summarized gives rise to some unique properties. Namely, lasers are monochromatic, coherent, and collimated. The degree at which a light source is monochromatic can be defined by a quality factor, Q (see figure 2.1) [34].

$$Q = \frac{\nu}{\Delta\nu}, \tag{2.1}$$

where ν is the peak frequency and $\Delta\nu$ is the full width at half maximum of the intensity. If one decreases the line width, one would expect an increase in the quality of monochromatic emission. For comparison, table 2.1 shows the quality

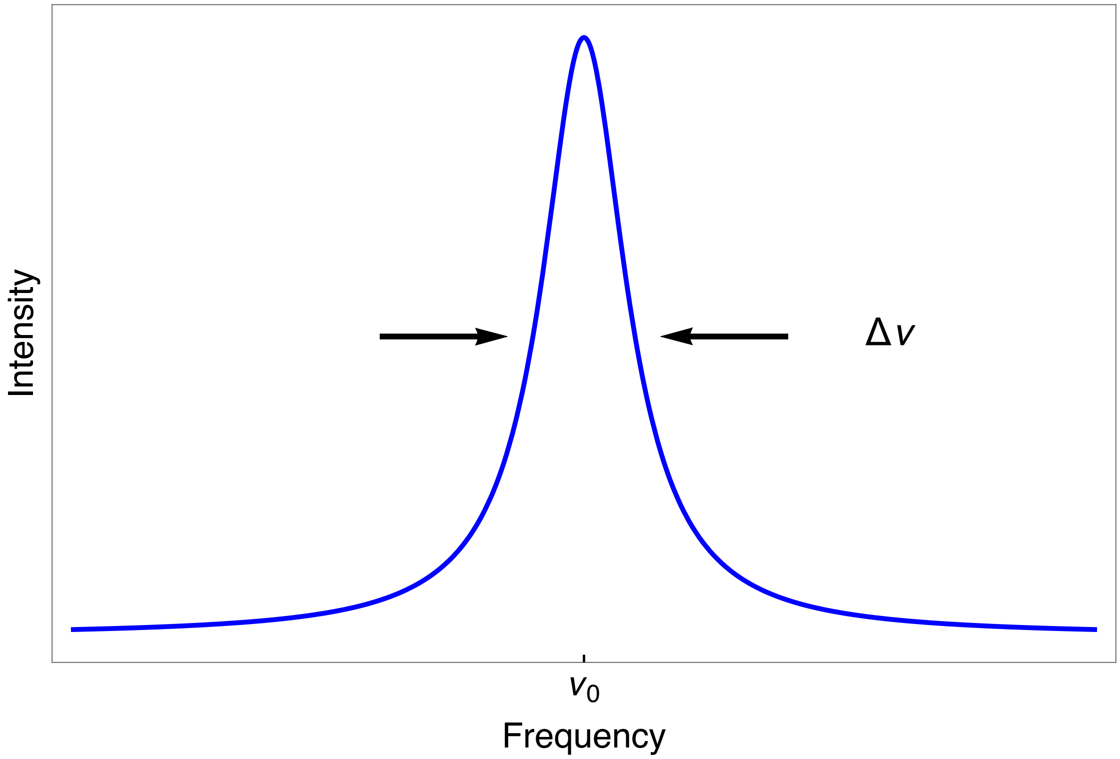

Figure 2.1: An emission line for a typical laser. The definition of $\Delta\nu$ is the full width at half the maximum intensity, and the definition of the peak frequency is the frequency at which the distribution reaches a maximum.

Table 2.1: Q-factors for a typical diode laser and the sun.

	$\Delta\nu$	ν	$\boldsymbol{Q}$
Laser	100 Hz	3.84×10^{14} Hz	3.84×10^{12}
Sun	10^{14} Hz	6×10^{14} Hz	6

factors of the laser and the sun.

The remaining properties of a laser to be discussed involve the coherence and collimation. We can describe the coherence both spatially and temporally. The spatial coherence is a characteristic length in which all the photons are in phase with each other. Similarly, the temporal coherence is a characteristic time in which all the photons are in phase with each other. They are related by the photon velocity, or $l = c\tau$. The collimation of radiation implies that all the photons remain close to the propagation axis. This property gives rise to a boundary condition that we will apply later to Maxwell's equations later [34].

With an understanding of the elements of a laser, we can now describe the transverse structure of laser beams. Laser beams in the Laguerre-Gaussian transverse mode are popular in atomic and molecular experiments due to their intrinsic orbital angular momentum. Electric and magnetic fields carry momentum and energy [35]. It will be shown that the LG modes carry orbital angular momentum described by the azimuthal phase. Further, the quantity ℓ is an integer associated with the eigenvalue of the quantum orbital angular momentum operator L_z [36]. To proceed with this conversation, we will need to employ Maxwell's equations.

2.2.1 Laser field solutions

Let's begin with Maxwell's equations. Although the cavity contains the gain medium, we can approximate a medium as non-dispersive. Consider Maxwell's equations for electric and magnetic fields in a vacuum (no sources nor currents) [35].

$$\nabla \cdot \mathbf{E} = 0 \tag{2.2a}$$

$$\nabla \times \mathbf{E} + \frac{1}{c}\frac{\partial \mathbf{B}}{\partial t} = 0 \tag{2.2b}$$

$$\nabla \cdot \mathbf{B} = 0 \tag{2.2c}$$

$$\nabla \times \mathbf{B} - \frac{1}{c}\frac{\partial \mathbf{E}}{\partial t} = 0 \tag{2.2d}$$

Here, **E** is the electric field vector, **B** is the magnetic field vector, and c is the vacuum speed of light. If we know the electric field, then (through the equations above) we can easily find the magnetic field of a traveling wave through the Poynting vector. Taking the curl of equation (2.2c), we get

$$\nabla \times (\nabla \times \mathbf{E}) = -\frac{1}{c}\frac{\partial^2(\nabla \times \mathbf{B})}{\partial t^2}. \tag{2.3}$$

Making a substitution of equation (2.2d), along with a derivative identity, we get the wave equation,

$$\nabla^2 \mathbf{E} = \frac{1}{c^2}\frac{\partial^2 \mathbf{E}}{\partial t^2}. \tag{2.4}$$

The general solution to equation (2.4) is of the form

$$\mathbf{E}(\mathbf{r}, t) = \mathcal{E}(\mathbf{r})\hat{\epsilon}e^{-i\omega t}, \tag{2.5}$$

where $\mathcal{E}(\mathbf{r})$ is the spatial component of the electric field, $\mathbf{r}$ is the position vector, $\hat{\epsilon}$, and ω is the angular frequency of the field. Substituting equation (2.5) into equation (2.4), we get the following differential equation for defining the spatial piece of the electric field.

$$\nabla^2 \mathcal{E} + k^2 \mathcal{E} = 0, \tag{2.6}$$

where we introduced the wave number $k = \omega/c$. We may make symmetry arguments to attempt to simplify the problem. The shape of the cavity implies a cylindrical symmetry. But for reasons that will become apparent later, I will remain in Cartesian coordinates, where the fields propagate in the z-direction.

I now introduce a condition that stems from one of the well known properties of a laser beam. We require that a laser be well collimated. Then the fields remain close to the z-axis. This is known as the paraxial approximation. In Cartesian coordinates, the Laplacian in equation 2.6 is defined in terms of x, y, and z. Under the paraxial approximation, the curvature of the field in the z-direction is very small compared to the x- and y-directions. Therefore, we can approximate that $\frac{\partial^2 \mathcal{E}}{\partial z^2} \to 0$.

$$\nabla_\perp^2 \mathcal{E}(x,y) + 2ik\frac{\partial}{\partial z}\mathcal{E}(z) = 0, \tag{2.7}$$

where the Laplacian in Cartesian coordinates $\nabla_\perp^2 = \frac{\partial^2}{\partial x^2} + \frac{\partial^2}{\partial y^2}$, describes the transverse structure of the field.

Fundamental transverse mode

The simplest solution (also called the *Gaussian mode*) to equation (2.7) is:

$$\mathcal{E}(x,y,z) = \mathcal{E}_0 e^{-\frac{x^2+y^2}{w(z)}} e^{\mathrm{i}\frac{k(x^2+y^2)}{2R(z)}} e^{-\mathrm{i}\psi(z)}, \tag{2.8}$$

where $w(z)$ is the radius of the laser at the position z, $R(z)$ is the radius of the wavefront at the position z, and $\psi(z)$ is the so-called Gouy phase. The position $z = 0$ corresponds to the waist (focus) of the laser. These parameters define the transverse mode of the Gaussian laser. More specifically, we define the beam radius, wavefront radius, and Gouy phase as [34]:

$$\begin{aligned} w^2(z) &= w_0^2\left(\frac{(z_r^2+z^2)}{z_r^2}\right) \\ R(z) &= \frac{z_r^2+z^2}{z} \\ \psi(z) &= \arctan\left(\frac{z}{z_r}\right), \end{aligned} \tag{2.9}$$

where $z_r = kw_0^2/2$.

Hermite-Gaussian modes

Higher order solutions to equation (2.7) that have rectangular symmetry are the *Hermite-Gaussian* laser modes.

$$\mathcal{E}_{m,n} \propto \left(\frac{2}{\pi n! m!}\right)^{1/2} H_m\left(\frac{\sqrt{2}x}{w(z)}\right) H_n\left(\frac{\sqrt{2}y}{w(z)}\right) e^{-\frac{x^2+y^2}{w(z)}} e^{\mathrm{i}\frac{k(x^2+y^2)}{2R(z)}} e^{-\mathrm{i}(n+m+1)\psi(z)}, \tag{2.10}$$

where $H_n(x)$ are the Hermite polynomials and n is an index describing the order of the mode. This work does not concern itself with these modes; we only note this mode in passing. Figure 2.2 shows several Hermite Gaussian modes. It is interesting, however, to note that these modes can be converted into modes associated with this work: the Laguerre-Gaussian modes.

Laguerre-Gaussian modes

The solution of interest for this work has azimuthal symmetry. Recasting equation (2.7) into cylindrical coordinates requires us to write the transverse Laplacian as:

$$\nabla_\perp^2 = \frac{1}{r}\frac{\partial}{\partial r}\left(r\frac{\partial}{\partial r}\right) + \frac{1}{r^2}\frac{\partial^2}{\partial \phi^2}, \tag{2.11}$$

where ϕ is the azimuthal winding phase, and r is the radial coordinate in the transverse plane. Solutions to equation (2.7) (using the Laplacian of the form

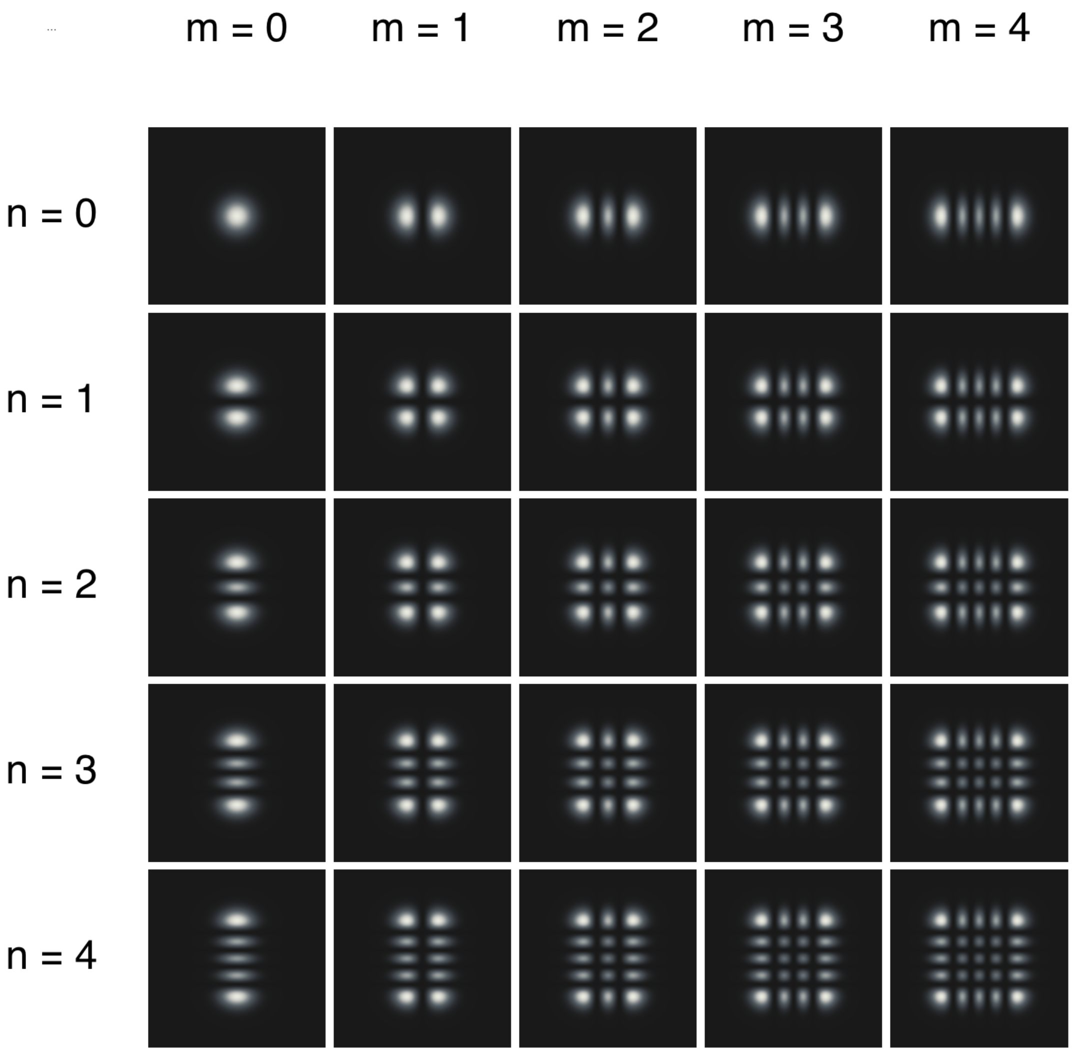

Figure 2.2: Several Hermite-Gaussian laser modes. The mode corresponding to $m = n = 0$ is the fundamental (Gaussian) mode described by equation (2.8).

in equation (2.11)) are the so-called *Laguerre-Gaussian modes* (LG_p^ℓ). Figure 2.3 shows intensity profiles ($I \propto |\mathcal{E}|$) of several LG_p^ℓ modes.

$$\mathcal{E}_p^\ell(r,\phi,z) \propto \left(\frac{\sqrt{2}r}{w(z)}\right)^{|\ell|} L_p^{|\ell|}\left(\frac{2r^2}{w(z)^2}\right) e^{-r^2/w(z)^2} e^{\mathrm{i}kr^2/2R(z)} e^{-\mathrm{i}\ell\phi} e^{-\mathrm{i}(2p+\ell+1)\psi(z)}. \tag{2.12}$$

The azimuthal phase $e^{-i\ell\phi}$ gives rise to $\ell\hbar$ of orbital angular momentum per photon. The azimuthal winding phase also forces the electric field to have $p+1$ anti-nodes. These characteristics are illustrated in figures 2.3 and 2.4. Figure 2.3 shows the transverse intensity patterns for several values of p and ℓ. Figure 2.4 shows the interference pattern of an LG_p^ℓ laser mode with a plane wave. The number of spirals is equal to the winding number, ℓ. As a note, setting $\ell = p = 0$ results in the fundamental mode described in equation (2.8). In equation (2.12), $w(z)$ is the waist (transverse $1/e$ radius of the electric field), $R(z)$ is the wavefront curvature, and $\psi(z)$ is the Gouy phase.

The associated Laguerre polynomial, $L_p^{|\ell|}$, is related to the Laguerre polynomial through the following relation [37]:

$$(-1)^\ell \frac{\mathrm{d}^{|\ell|}}{\mathrm{d}r^{|\ell|}} L_{p+|\ell|}(r). \tag{2.13}$$

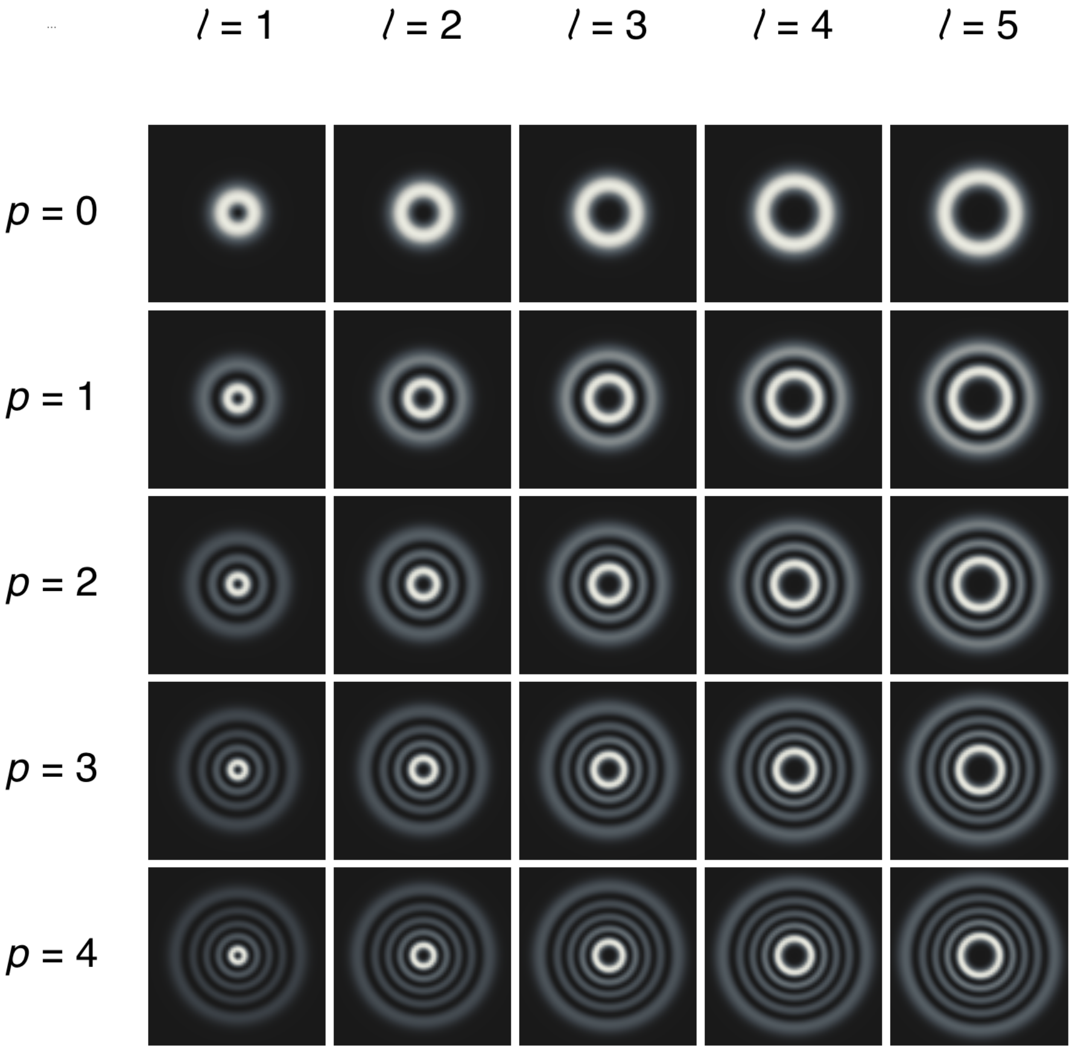

Figure 2.3: Intensity profiles for LG_0^1 through LG_3^5. The $p+1$ intensity anti-nodes describe the number of rings, while the winding number ℓ describes the orbital angular momentum of the LG_p^ℓ.

It is important to note that the associated Laguerre polynomials can be expanded as a linear combination of Hermite polynomials [38, 39].

$$\sum_{k=0} n + m (2\mathrm{i})^k P_k^{n-k,m-k}(0) H_{n+m-k}(x) H_k(y) =$$
$$2^{n+m} \times \begin{cases} (-1)^m m!(x + \mathrm{i}y)^{n-m} L_m^{n-m}(x^2 + y^2) & \text{for } n \geq m \\ (-1)^n n!(x + \mathrm{i}y)^{m-n} L_n^{m-n}(x^2 + y^2) & \text{for } m > n \end{cases} \tag{2.14}$$

This relationship provides one path for the experimental generation of LG_p^ℓ laser modes. In some cases, it is easier to generate Hermite-Gaussian laser modes. The experimentalist can convert the Hermite-Gaussian modes through astigmatic optical components in such a way that the appropriate superposition of Hermite-Gaussian modes results in an LG_p^ℓ [38, 39].

2.2.2 Orbital angular momentum

It is well understood that light has spin angular momentum, which is analogous to that of a particle. The spin is represented by the symbol, σ_z, and takes on values of +1 for right-hand circular polarization, −1 for right-hand circular polarization, and 0 for linear polarization. Additionally, light can also carry orbital angular momentum (OAM). In general, OAM is dependent upon the choice of coordinates. However, the LG_p^ℓ laser modes carry $\ell\hbar$ OAM for all choices of coordinates. This class of laser modes has intrinsic OAM [40].

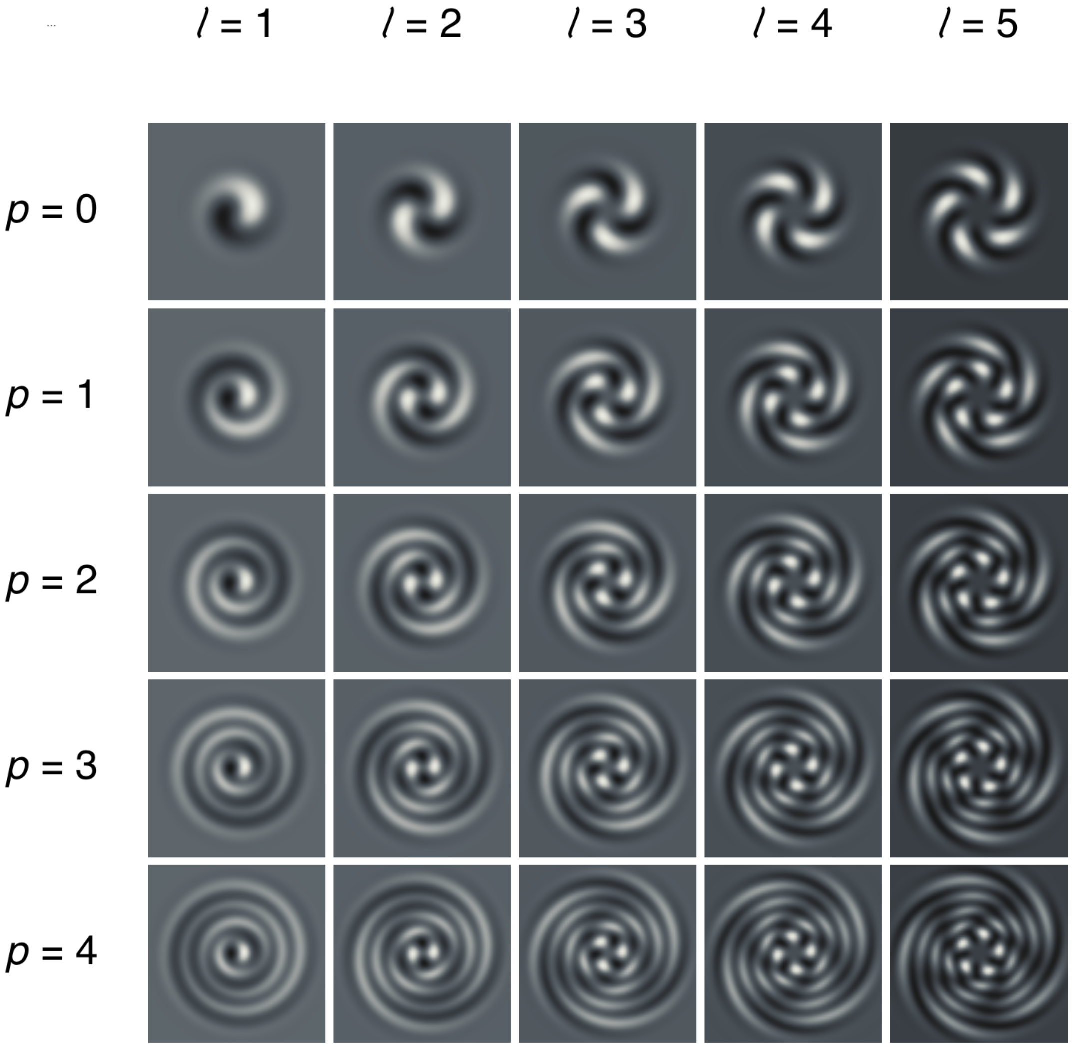

Figure 2.4: Interference patterns of a Gaussian mode ($p = \ell = 0$) with each of the profiles shown in figure 2.3 profiles for LG_0^1 through LG_3^5. The winding number ℓ describes the orbital angular momentum of the LG_p^ℓ mode. This is visualized with the interference pattern. The number of spirals is equal to the winding number, ℓ.

The OAM arises from the $e^{i\ell\phi}$ winding phase (see equation (2.12)). The node at the center of the LG_p^ℓ mode is a natural consequence of the OAM (see figure 2.3). One physical interpretation of the OAM property of light is that the winding phase leads to a helical wavefront, rotating about the node as the laser propagates. The winding phase is visualized by interfering a plane wave with an LG_p^ℓ mode, as shown in figure 2.4. The number of spirals corresponds to the winding number, ℓ. A wonderful review of photon OAM can be found in reference [37].

2.3 Atomic structure

This section summarizes the useful documents on ^{85}Rb [41] and ^{87}Rb [42]. We will report only the information necessary to describe the atomic structure of ^{85}Rb and ^{87}Rb, and we direct the reader to the reference for more information. We will start with the various angular momentum coupling that results in the structure of the rubidium atom. Then, we will briefly discuss the so-called Zeeman effect because it is key to understanding laser cooling and trapping.

Fine structure

The fine structure of an atom is the result of coupling between the orbital angular momentum ($\mathbf{L}$) of the valence electron with the spin angular momentum ($\mathbf{S}$) of that electron. The total electronic angular momentum is given by,

$$\mathbf{J} = \mathbf{S} + \mathbf{L}. \tag{2.15}$$

The operator, $\mathbf{J}$, has quantum numbers that lie within the range $|L - S| \leq J \leq L + S$. Spectroscopic notation describes the fine-structure states of the atom. In general, the notation takes the form:

$$n^{2S+1}L_J, \tag{2.16}$$

where n is the principle quantum number. However, we conventionally label L with letters that represent each of the orbital angular momentum values. Table 2.2 lists several of these symbols. The ground state of rubidium corresponds to $S = 1/2$, $L = 0$, $J = 1/2$, and $n = 5$. Therefore, the notation for the ground state of rubidium is $5^2\mathrm{S}_{1/2}$. The first excited state of rubidium has quantum numbers $S = 1/2$, $L = 1$, and $n = 5$. The possible eigenvalues of J are thus 1/2 and 3/2. This corresponds to the two fine-structure states, $5^2\mathrm{P}_{1/2}$ and $5^2\mathrm{P}_{3/2}$. We call the transition from the $5^2\mathrm{S}_{1/2}$ state to the $5^2\mathrm{P}_{1/2}$ state the D1 transition, and the transition from the $5^2\mathrm{S}_{1/2}$ state to the $5^2\mathrm{P}_{3/2}$ state the D2 transition. This work is performed entirely on the D2 transition.

Table 2.2: A list of spectroscopic symbols used to represent the valence electron orbital angular momentum.

L	**Letter**
0	S
1	P
2	D
3	F
4	G
5	H
6	I
7	K
8	L
9	M
10	N

Hyperfine structure

The hyperfine structure results from the coupling between the total electronic angular momentum, $\mathbf{J}$, and the total nuclear spin angular momentum, $\mathbf{I}$. The nuclear spin for ^{85}Rb is $I = 5/2$, and the nuclear spin for ^{87}Rb is $I = 3/2$. The "good" quantum number is the total angular momentum of the atom,

$$\mathbf{F} = \mathbf{J} + \mathbf{I} = \mathbf{S} + \mathbf{L} + \mathbf{I}. \tag{2.17}$$

Similar to the total electronic angular momentum, the quantum numbers of $\mathbf{F}$ must lie between:

$$|J - I| \leq F \leq J + I. \tag{2.18}$$

Consider, first, ^{85}Rb. As mentioned above, the ground state has quantum numbers $S = 1/2$, $L = 0$, $J = 1/2$, and $n = 5$. With these values, we can include the nuclear spin $I = 5/2$. From equation (2.18), we know that $\mathbf{F}$ can take on values of $F = 2, 3$. The atomic energy levels of the ground state are shifted depending on the value of F. There are two hyperfine states in the ground state. The D1 excited state has quantum numbers $S = 1/2$, $L = 1$, $J = 1/2$, $I = 5/2$, and $n = 5$. From equation (2.18), we know that $\mathbf{F}$ can take on values of $F = 2, 3$, leading to two hyperfine states in the D1 excited state. The D2 excited state has quantum numbers $S = 1/2$, $L = 1$, $J = 3/2$, $I = 5/2$, and $n = 5$. The total angular momentum for the excited D2 electronic state can take on values of $F = 1, 2, 3, 4$, leading to four hyperfine states in the D2 excited state.

Consider, next, ^{87}Rb. As mentioned above, the ground state has quantum numbers $S = 1/2$, $L = 0$, $J = 1/2$, and $n = 5$. To these values, we can include the nuclear spin $I = 3/2$. From equation (2.18), we know that $\mathbf{F}$ can take on values of $F = 1, 2$. The atomic energy levels of the ground state are shifted depending on the value of F. There are two hyperfine states in the ground state. The D1 excited state has quantum numbers $S = 1/2$, $L = 1$, $J = 1/2$, $I = 3/2$, and $n = 5$. From equation (2.18), we know that $\mathbf{F}$ can take on values of $F = 1, 2$, leading to two hyperfine states in the D1 excited state. The D2 excited state has quantum numbers $S = 1/2$, $L = 1$, $J = 3/2$, $I = 3/2$, and $n = 5$. The total angular momentum can take on values of $F = 0, 1, 2, 3$, leading to four hyperfine states in

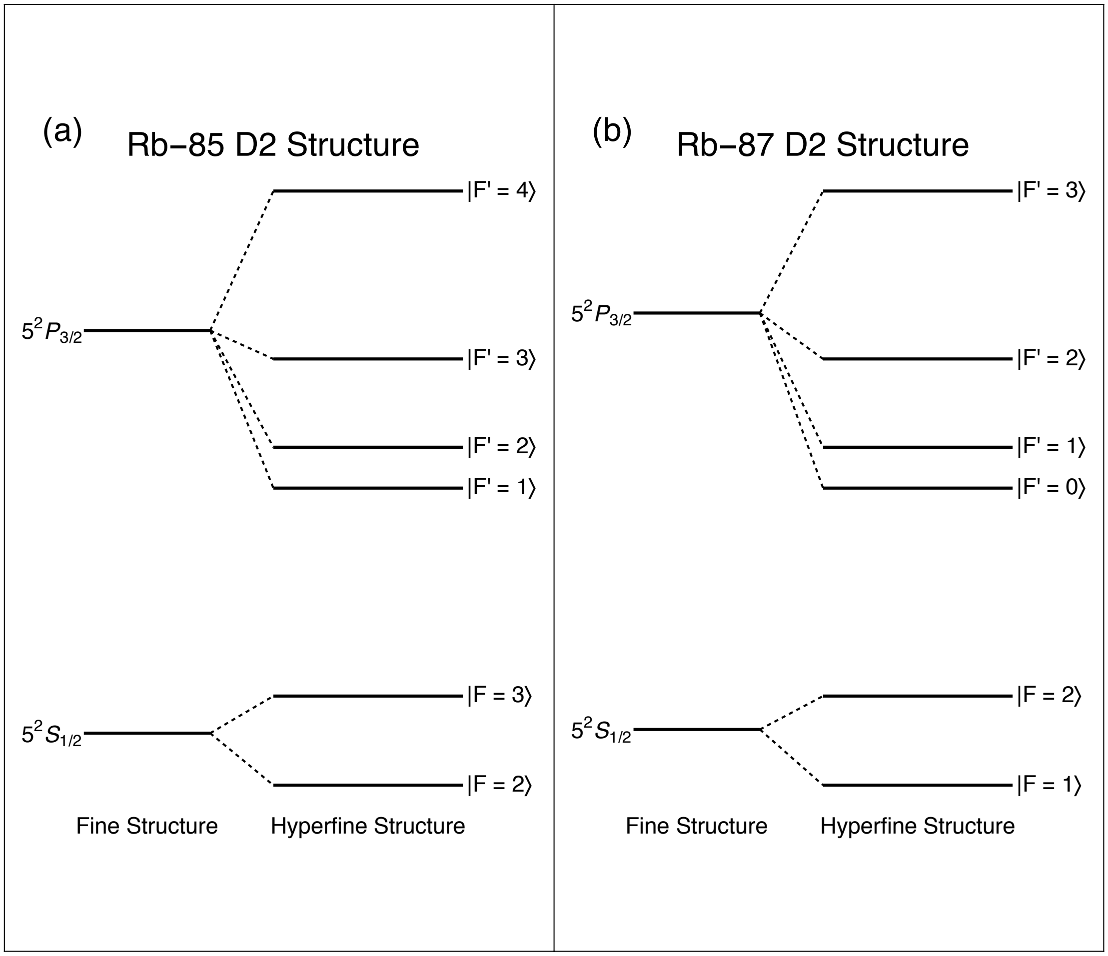

Figure 2.5: The fine and hyperfine structure of (a) ^{85}Rb and (b) ^{87}Rb. The ground state is resolved into two hyperfine levels, while the excited state is resolved into four hyperfine levels.

the D2 excited state.

Figure 2.5 summarizes this description.

Zeeman effect

The Zeeman effect is an interaction of the atom with a small, static magnetic field.

The hyperfine levels have $2F + 1$ magnetic sublevels. The sublevels describe the angular component of the electronic wavefunction. In the absence of a magnetic field ($B = 0$), all magnetic sublevels are degenerate. Applying a magnetic field lifts this degeneracy. If we define the direction of the static magnetic field to be in the $\hat{z}$ direction ($\mathbf{B} = B_z\hat{z}$), then the Hamiltonian that describes the interaction of the atom with the magnetic field is described as,

$$H_B = \frac{\mu_B}{\hbar}(g_S S_z + g_L L_z + g_I I_z)B_z, \tag{2.19}$$

where μ_B is the Bohr magneton. The parameters g_S, g_L, and g_I are the g-factors for the electron spin, electron orbital angular momentum, and the nuclear spin. These describe corrections to the magnetic dipole moments of the electron spin, electron orbital angular momentum, and the nuclear spin respectively.

If the field is small compared to the hyperfine splitting, then F is a good quantum number. The interaction Hamiltonian can then be written as,

$$H_B = \frac{\mu_B}{\hbar} g_F F_z B_z, \tag{2.20}$$

where g_F is the g-factor for the total angular momentum of the atom. To first order (for weak magnetic fields), we the magnetic sublevels of F, notated as m_F, split linearly.

$$\Delta E = \mu_B g_F m_F B_z, \tag{2.21}$$

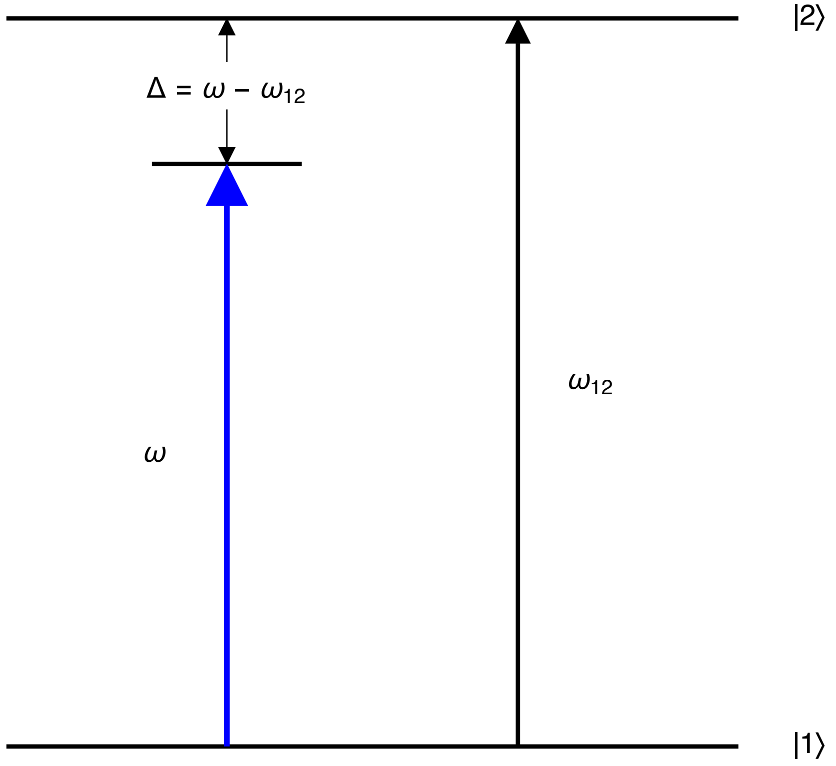

Figure 2.6: A simple, two level atom. The ground level is labeled $|1\rangle$, and the excited level is labeled $|2\rangle$. The resonant frequency is labeled ω_{12}. A monochromatic electric field is incident on the two level atom with frequency, ω, detuned from the resonance $\Delta = \omega - \omega_{12}$.

where we have used the eigenvalues of F_z defined as $m_F\hbar$.

2.4 Light interacting with two level atoms

Our atom will be treated as having two levels only: a ground level and an excited level (see figure 2.6). We will label the lower level, $|1\rangle$, and the upper level, $|2\rangle$. In reality, atoms are complex and have many (infinite) levels. However, if we assume that the frequency of the monochromatic light-field is near resonance to the $|1\rangle$ to $|2\rangle$ transition, then we can ignore the small probability of exciting the atom to other transitions.

There are many sources that describe two level transitions well [40,43,44]. It will serve our purposes to summarize assuming a steady-state[1] $(t \to \infty)$.

For this treatment, we assume the monochromatic light field has a frequency detuned from the resonance by $\Delta = \omega - \omega_{12}$. Here, ω is the frequency of the laser, $\omega_{12} = (E_2 - E_1)/\hbar$, and E_1 and E_2 are the energies of the states $|1\rangle$ and $|2\rangle$ respectively. The rate at which photons are scattered (absorbed, then re-emitted) is related to the fraction of the population in the excited state, as well as the decay rate of the atom, Γ. For a two level atom, the scattering rate is [43]

$$R_{\text{sc}} = \Gamma \rho_{22} = \Gamma \frac{\Omega^2/4}{\Delta^2 + \Gamma^2/4 + \Omega^2/2}, \tag{2.22}$$

where we have introduced a new term, ρ_{22}, known as the *density matrix element.* Density matrices will be employed more widely in the sections to come. It simply represents the fraction of atoms in the excited state.

Additionally, we have introduced a new quantity, Ω, known as the Rabi frequency. For a two level atom located at the position, $\mathbf{r}_0$, and driven by a light field with electric field amplitude, $\mathcal{E}(\mathbf{r}_0)$, and time averaged intensity [40],

$$I(\mathbf{r}_0) = \frac{1}{2} c \epsilon_0 \mathcal{E}^2(\mathbf{r}_0), \tag{2.23}$$

---

[1] We reserve a more detailed theoretical treatment of light interactions with matter for three levels and higher. In fact, under the limit that the control field goes to zero $(\Omega_c \to 0)$, we recover the results of this section.

the Rabi frequency is defined as:

$$\Omega^2 = \frac{2d^2}{\hbar} I. \tag{2.24}$$

Here, $d^2 = |\langle 1|\widehat{\mathbf{d}} \cdot \hat{\boldsymbol{\epsilon}}|2\rangle|^2$ is the square of the dipole matrix element[2], $\widehat{\mathbf{d}}$ is the dipole operator, and the polarization of the electric field is defined by $\hat{\boldsymbol{\epsilon}}$. The Rabi frequency describes the strength of the interaction of the light field with the atom.

Under the weak laser approximation ($\Omega^2 \ll \Gamma^2$), the scattering rate takes the form:

$$R_{\text{sc,weak}} = \Gamma \frac{\Omega^2/4}{\Delta^2 + \Gamma^2/4}. \tag{2.25}$$

This is a Lorentzian profile with a full-width at half max (FWHM) of Γ. At high pump (field) powers ($\Omega^2 \gg \Gamma^2$), the scattering rate takes the form:

$$R_{\text{sc,strong}} = \Gamma \frac{\Omega^2/4}{\Delta^2 + \Omega^2/2}. \tag{2.26}$$

The line shape is still Lorentzian, but the FWHM is $\sqrt{2}\Omega$ is broadened. This is known as power broadening. Figure 2.7 shows scattering line shapes for a two level atom for various pumping strengths. As the power increases, the fraction of atoms found in the excited state *saturates* at 1/2.

---

[2] We examine the dipole matrix elements with more detail in the remaining sections. The dipole matrix elements are dependent upon light-field polarizations, $\hat{\boldsymbol{\epsilon}}$. In our experiments, the dipole matrix elements are determined phenomenologically. We commonly use the values reported by [41, 42].

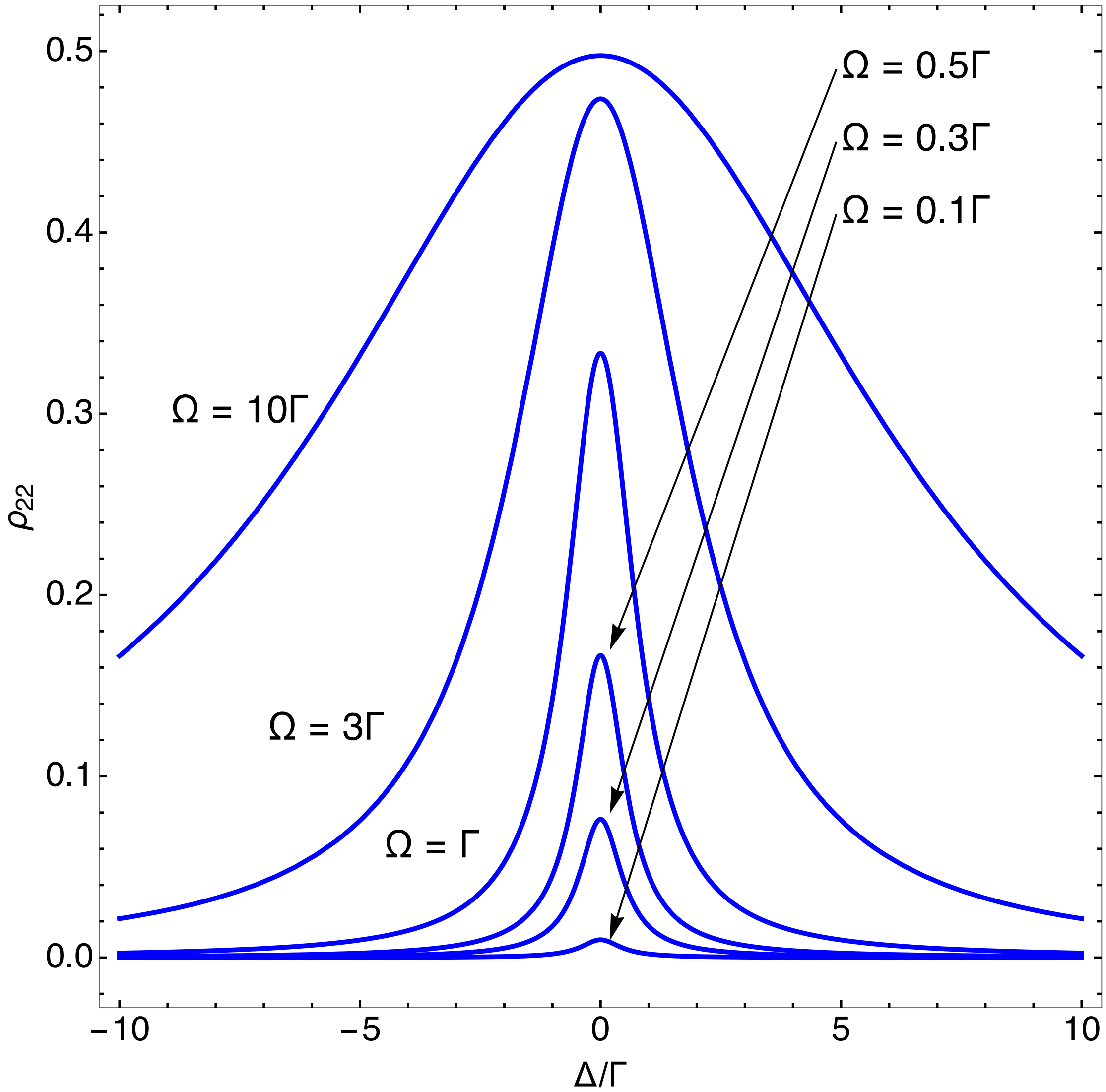

Figure 2.7: A plot of the fraction of population in the excited state (ρ_{22}). As the Rabi frequency (Ω) increases, we find that more of the ensemble of two level atoms are promoted to the excited state, reaching saturation at $\rho_{22} = 0.5$. Additionally, the scattering line-shape broadens.

2.5 Mechanical effects on atoms by light

Lasers are the workhorse for ultracold atomic physics. In general, we start with a gas of rubidium atoms at room temperature. Through the repeated process of absorption and emission of laser light, we can transfer momentum from the light field to the atoms, thus slowing them to ultracold temperatures. We will start with a description of radiation pressure. Then, expanding this concept to three dimensions we describe how to laser cool a gas of atoms. Finally, we will explain how adding a quadrupole magnetic field allows us to cool *and* trap atoms.

2.5.1 Radiation pressure

Light carries a quanta of momentum of $\hbar\mathbf{k}$ per photon. Therefore, the total rate of momentum transfer (the radiation force), is given by [43]

$$\mathbf{F}_{\text{rad}} = \hbar\mathbf{k}R_{\text{sc}}, \tag{2.27}$$

where R_{sc} is the scattering rate described in equation (2.22). Under the weak laser approximation, $\Omega \ll \Gamma$, the radiation force takes the form:

$$\mathbf{F}_{\text{rad}} = \hbar\mathbf{k}\Gamma\frac{\Omega^2/4}{\Delta^2 + \frac{\Gamma^2}{4}}. \tag{2.28}$$

A single laser directed in the opposite direction of the motion of an atom will exert a force described by equation 2.28, slowing it. In general, temperature is a measurement of the average motion of the atoms (usually as a spread of the velocities). Decreasing the average velocity of an ensemble of atoms results in a decrease of the temperature of the ensemble.

2.5.2 Laser cooling

Consider an atom moving in one dimension as describe by figure 2.8 (a). A laser field (laser 1) propagates in the same direction as the atom, and a second laser field (laser 2) propagates in the opposite direction as the atom. Both lasers are detuned *below* the rest frame atomic transition by an amount Δ. Since the atom is moving away (toward) laser 1 (2), then the light will be Doppler-shifted away (toward) the atomic transition by an amount $-kv$ $(+kv)$. Therefore, the detuning that the atom sees for each laser is given by:

$$\begin{aligned} \Delta_1 &= \Delta - kv \\ \Delta_2 &= \Delta + kv. \end{aligned} \tag{2.29}$$

The result is that the atom scatters more photons from laser 2 than from laser 1. The atom will absorb a photon preferentially from laser 2, receiving a momentum "kick" in the direction of laser 2. However, the atom will re-emit the photon, but in a random direction. This process occurs millions of times per second. The momentum *gained* by the atom from the re-emission of a photon averages-out to zero. Therefore, there is a net force opposing the motion of the atom. We can quantify this by considering the net force as the sum of the radiation force exerted by both lasers.

$$F_{\text{net}} = \hbar k \Gamma \left(\frac{1}{(\Delta - kv)^2 + \Gamma^2/4} - \frac{1}{(\Delta + kv)^2 + \Gamma^2/4} \right) \frac{\Omega^2}{4} \tag{2.30}$$

Interestingly, if the atom changes the direction of its motion toward laser 1, then the signs of the Doppler shift reverse. In this case, the atom now feels a larger radiation force from laser 1, which opposes the motion of the atom. The atom will always feel a force that opposes its motion along this one-dimensional axis.

For small atom speeds ($v \ll \Gamma/k$), we can expand the net force in equation (2.30) and take only the first order in v, represents the radiation force as a viscous damping force [43].

$$F_{\text{vis}} = \frac{1}{8} \hbar k^2 \Gamma \Omega^2 \frac{\Delta}{\Delta^2 + \Gamma^2/4} v \tag{2.31}$$

The viscous force is a damping force when the lasers are tuned below the atomic transition ($\Delta < 0$).

Laser cooling in all dimensions can be accomplished by aligning three sets of the laser pairs described thus far: one pair along each of the three orthogonal axes.

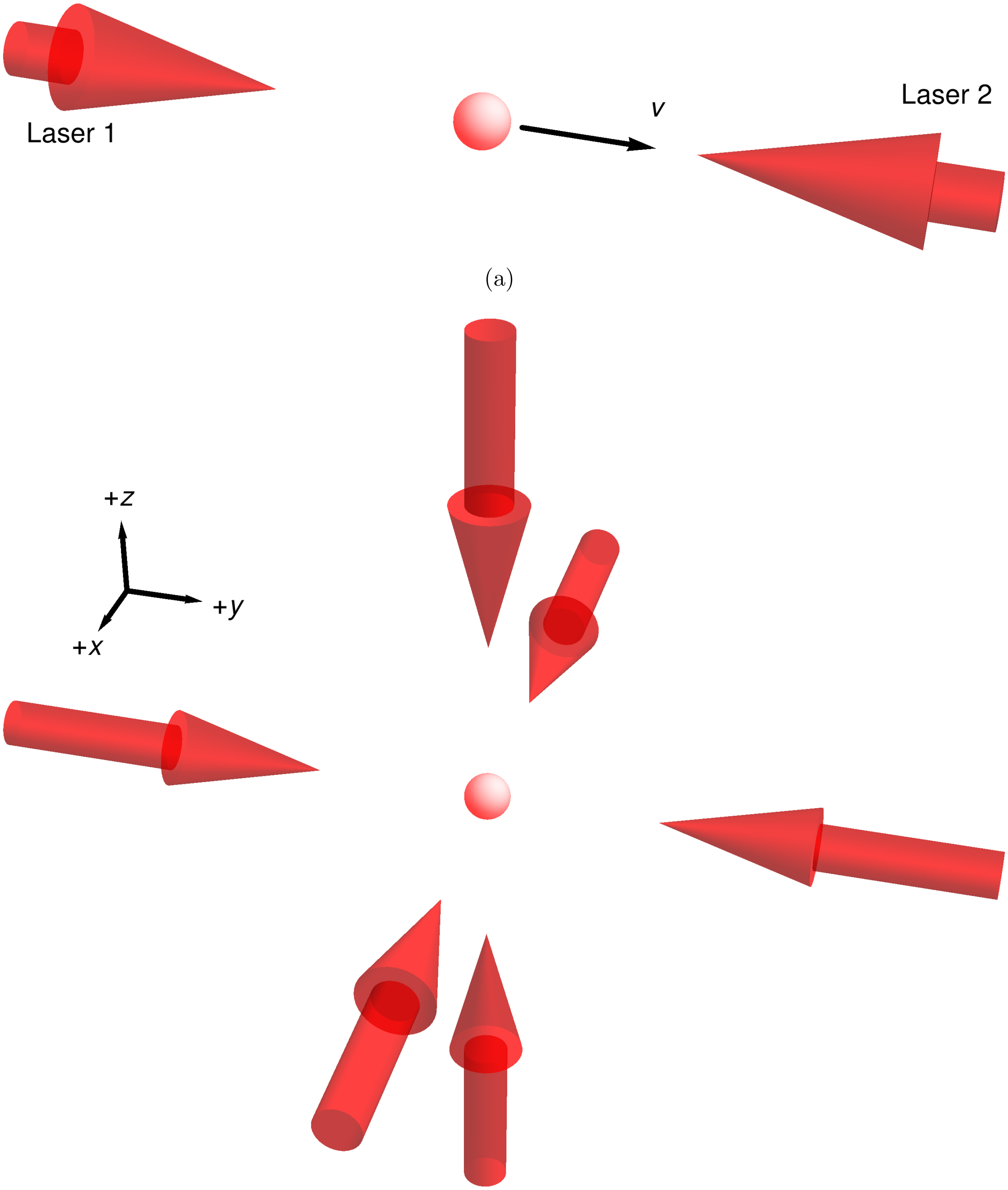

(a)

(b)

Figure 2.8: (a) A configuration for laser cooling of an atom moving in one-dimension. (b) A configuration for laser cooling of an atom moving in three-dimension.

Figure 2.8 (b) visualizes this configuration. Then, the viscous force becomes the vector:

$$\mathbf{F}_{\text{vis}} = \frac{1}{8}\hbar k^2 \Gamma \Omega^2 \frac{\Delta}{\Delta^2 + \Gamma^2/4}\mathbf{v}. \tag{2.32}$$

Cooling a gas in this manner creates an *optical molasses.* As its name suggests, the molasses is a “sticky”, viscous region in space where the atoms are slowed and cooled.

The process of re-emission is a random process. Therefore, there is a limit to how cold laser cooling can achieve (spoiler: we cannot get to absolute zero with this process). In fact, there are two limits. The first is the so-called *Doppler limit.* An atom nearly at rest will absorb a photon, at random, from one of the six lasers. It will then re-emit the photon in another random direction. This leads to a random walk of the atom, and heats the atoms to a temperature described by the relationship [43],

$$T_D = \frac{\hbar\Gamma}{2k_B}, \tag{2.33}$$

where k_B is the Boltzmann constant. For ^{87}Rb the Doppler limit is 146 μK. However, with a careful balancing of laser intensity and polarization, the laser cooling may reach even lower temperatures. This is the so-called “sub-Doppler” cooling introduced theoretically by reference [45], and experimentally verified in a MOT by reference [46]. Sub-Doppler cooling results from polarization gradients set by a standing wave produced by the trapping laser beams. As an atom moves

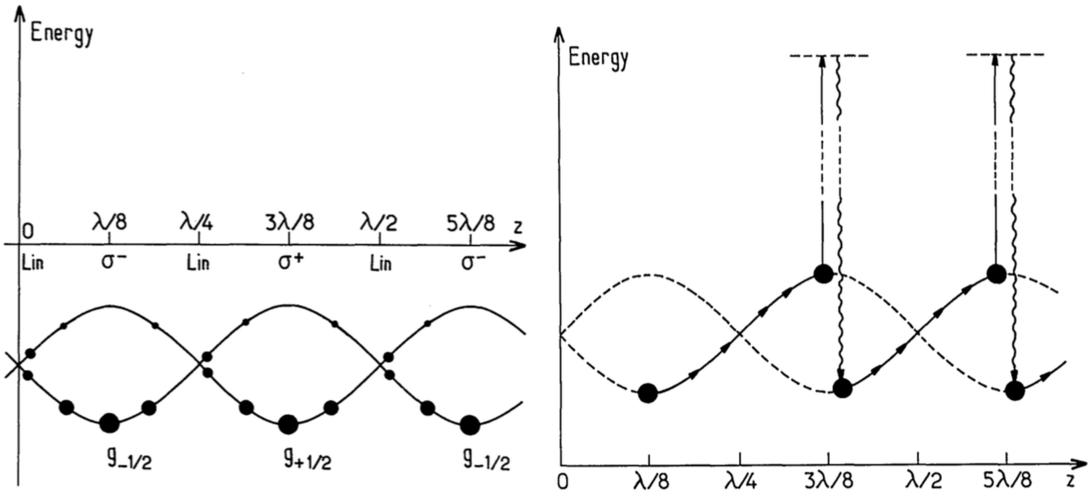

(a) (b)

Figure 2.9: Taken from reference [45]. (a) The light-shifted ground state sublevels for an atom with angular momentum $J_g = 1/2$. The filled circles shows the relative steady-state populations of the two levels. The atom is most populated in the states with the lowest energy. (b) A conceptual representation of Sisyphus cooling. Due to the time delay for optical pumping, the atom spends (on average) more time "climbing" the potential, thus decreasing its motion.

through space, it experiences changes in polarization (say σ^+ to linear to σ^-, as shown in figure 2.9). A key requirement for sub-Doppler cooling is a variation in magnetic sublevel population as an atom moves through space. The atom sees changes in polarization, and thus the potential for each magnetic sublevel changes. Figure 2.9 (a) illustrates the variation of the magnetic sublevel population. The atom is most populated in states with the lowest energy. The laser field optically pumps between the manifold of ground state magnetic sublevels. Due to the delay for optically pumping, the atom spends (on average) more time "climbing" the potential energy curve. This results in a decrease of the kinetic energy of the atom, thus cooling beyond the Doppler limit. A more rigorous presentation of this effect is found in reference [45]. The lower limit of sub-Doppler cooling is then set by the temperature associated with the change in momentum of one photon. This limit is the so-called *recoil-limit.*

$$T_r = \frac{(\hbar k)^2}{m k_B}, \tag{2.34}$$

where m is the mass of the atom. For ^{87}Rb, the recoil temperature is 198 nK.

2.5.3 Magneto-optical trap

The optical molasses will viscously cool the atoms, but the atoms will not be confined to a particular region in space. However, if we introduce a quadrupole field (produced with a pair of anti-Helmholtz coils), then we can cool and trap the atoms. Anti-Helmholtz coils are circular, current carrying coils of wire that are aligned axially, and separated by the radius of each of the coils. This configuration produces a linear magnetic filed that is zero at the center of the coils. Configuring the three pairs of counter-propagating lasers such that they cross at the center of the anti-Helmholtz coils (the location where the magnetic field goes to zero) specifies a location where the atoms will be confined. This configuration is called the *magneto-optical trap* (MOT), and was first demonstrated by [47]. Figure 2.10 visualizes the described configuration.

Consider an atom with a ground state having total angular momentum $F = 0$, and an excited state having total angular momentum $F' = 1$. The ground state has only one Zeeman level, $m_F = 0$. The excited state has three Zeeman levels, $m'_F = -1, 0, +1$. At the center of the anti-Helmholtz coils, all three of excited state sublevels are degenerate because the magnetic field is zero. As an atom moves away from the center of the coils, the magnetic field is non-zero and the degeneracy is lifted. Figure 2.11 and 2.12 show the magnetic field as a function of position in the x, y, and z directions. Additionally, these figures show how the degeneracy is lifted as a function of position in the x, y, and z directions. The z-axis is defined along the symmetric axis. The x- and y-axes are orthogonal to the symmetric axis. The origin (and center of the trap) is located at the center of the two anti-Helmholtz coils. For simplicity, the following narrative will be for the

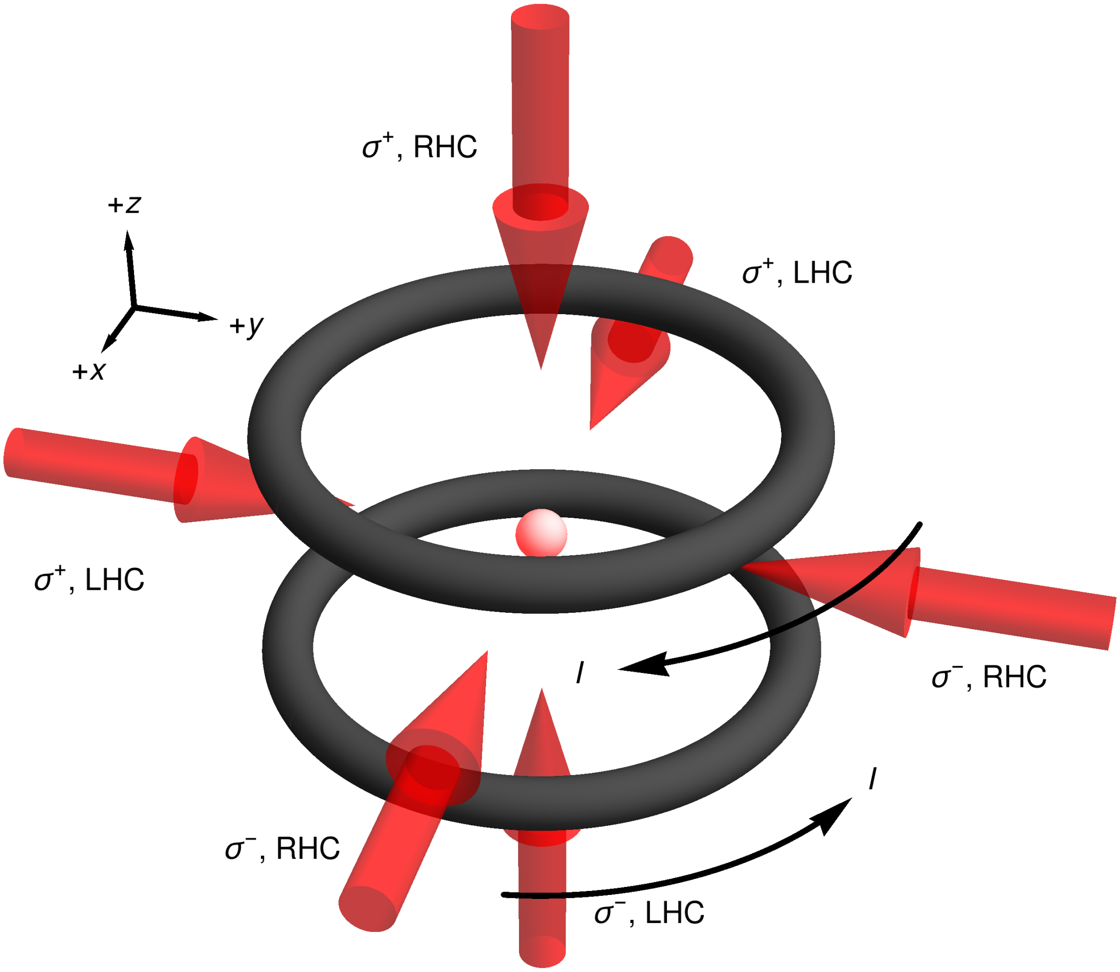

Figure 2.10: A representation of the magneto-optical trap. A pair of anti-Helmholtz coils create a linear magnetic field that is zero at the center of the trap. Three pairs of counter-propagating laser beams cool and trap the atoms at the center of the trap. The polarizations are chosen to match the correct selection rules for the shown direction of current flow, I.

x (and y) direction only. The same process occurs in the z dimension as well, but the slope of the magnetic field is negative.

Along the x-axis, the magnetic field has a positive slope and is linear. For small magnetic fields, the Zeeman effect is linear in magnetic field. The laser field is detuned below the field-free resonance of the $F = 0 \rightarrow F' = 1$ transition (just like in laser cooling). As the atom moves along the $+x$-axis, the $m_{F'} = -1$ level is shifted closer in energy to the energy of the laser, while the $m_{F'} = +1$ level is shifted further away from the energy of the laser. A laser with circular polarization described as σ^- can excite transition from $m_F = 0 \rightarrow m_F' = -1$, in agreement with the selection rule $\Delta m_F = -1$. So, an atom moving in the $+\hat{x}$ direction will come into resonance with a laser with σ^- polarization. Steering the σ^- laser to propagate in the $-\hat{x}$ direction will impart a force back toward the center of the trap.

Likewise, as an atom that moves in the $-\hat{x}$-direction, the $m_{F'} = +1$ level is shifted closer in energy to the energy of the laser, while the $m_{F'} = -1$ level is shifted further away from the energy of the laser. A laser with circular polarization described as σ^+ can excite transitions from $m_F = 0 \rightarrow m_F' = +1$, in agreement with the selection rule $\Delta m_F = +1$. So, an atom moving in the $-\hat{x}$ direction will come into resonance with a laser with σ^+ polarization. Steering the σ^+ laser to propagate in the $+\hat{x}$ direction will impart a force back toward the center of the trap.

The radiation force equation 2.28 can be modified by incorporating additional "detuning" caused by the magnetic field. Namely, for an atom moving along the $+x$-axis, detuning from each of the two lasers that the atom sees are:

$$\begin{aligned} \Delta_1 &= \Delta - kv - \mu\beta x/\hbar \\ \Delta_2 &= \Delta + kv + \mu\beta x/\hbar, \end{aligned} \tag{2.35}$$

where $B = \beta x$ is a linear model function for the magnetic field, $\beta = \mathrm{d}B/\,\mathrm{d}z$ is the gradient of the magnetic field, and μ is the magnetic moment. Substituting this into equation (2.30) leads to,

$$F_{\text{net}} = \hbar k\Gamma \left(\frac{1}{(\Delta - kv - \mu B/\hbar)^2 + \Gamma^2/4} - \frac{1}{(\Delta + kv + \mu B/\hbar)^2 + \Gamma^2/4} \right) \frac{\Omega^2}{4}. \tag{2.36}$$

For small speeds ($v \ll \Gamma/k$) and for small deviations from the center of the trap ($r \ll \hbar\Gamma/\mu\beta$), we can expand equation (2.36) in x and v, keeping only the first order terms.

$$F_{\text{net}} \approx \frac{1}{8}\hbar k^2 \Gamma \Omega^2 \frac{\Delta}{\Delta^2 + \Gamma^2/4} v + \frac{1}{8}\mu\beta k \Gamma \Omega^2 \frac{\Delta}{\Delta^2 + \Gamma^2/4} x \tag{2.37}$$

Employing the configuration described above creates an atom trap that has a restoring force (position dependent), and a viscous (velocity dependent) force. The MOT cools and traps atoms, and has been the workhorse for ultracold atomic

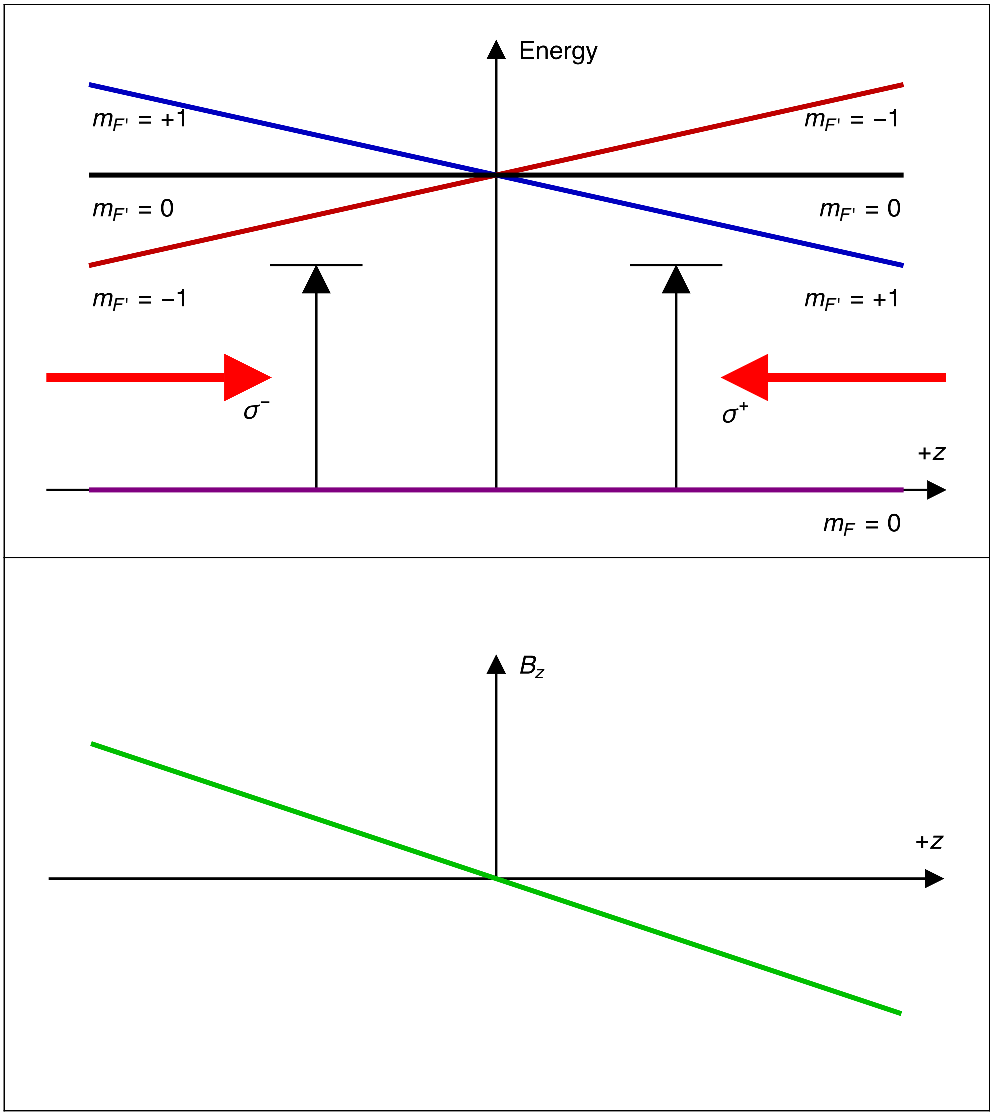

Figure 2.11: The principle of confinement in the z-dimension in a magneto-optical trap. The bottom panel shows the linear position dependence of the magnetic field. This field lifts the degeneracy of the magnetic sublevels in the excited state. As an atom moves to the right, the $m_{F'} = 1$ sublevel is shifted toward resonance with the σ^+ laser for an atom. The same process happens when the atom moves to the right, with the exception that the $m_{F'} = -1$ sublevel is shifted toward resonance with the σ^- laser for an atom. Therefore, the atom always feels a restoring force back to the position $z = 0$. The MOT is cools and traps atoms.

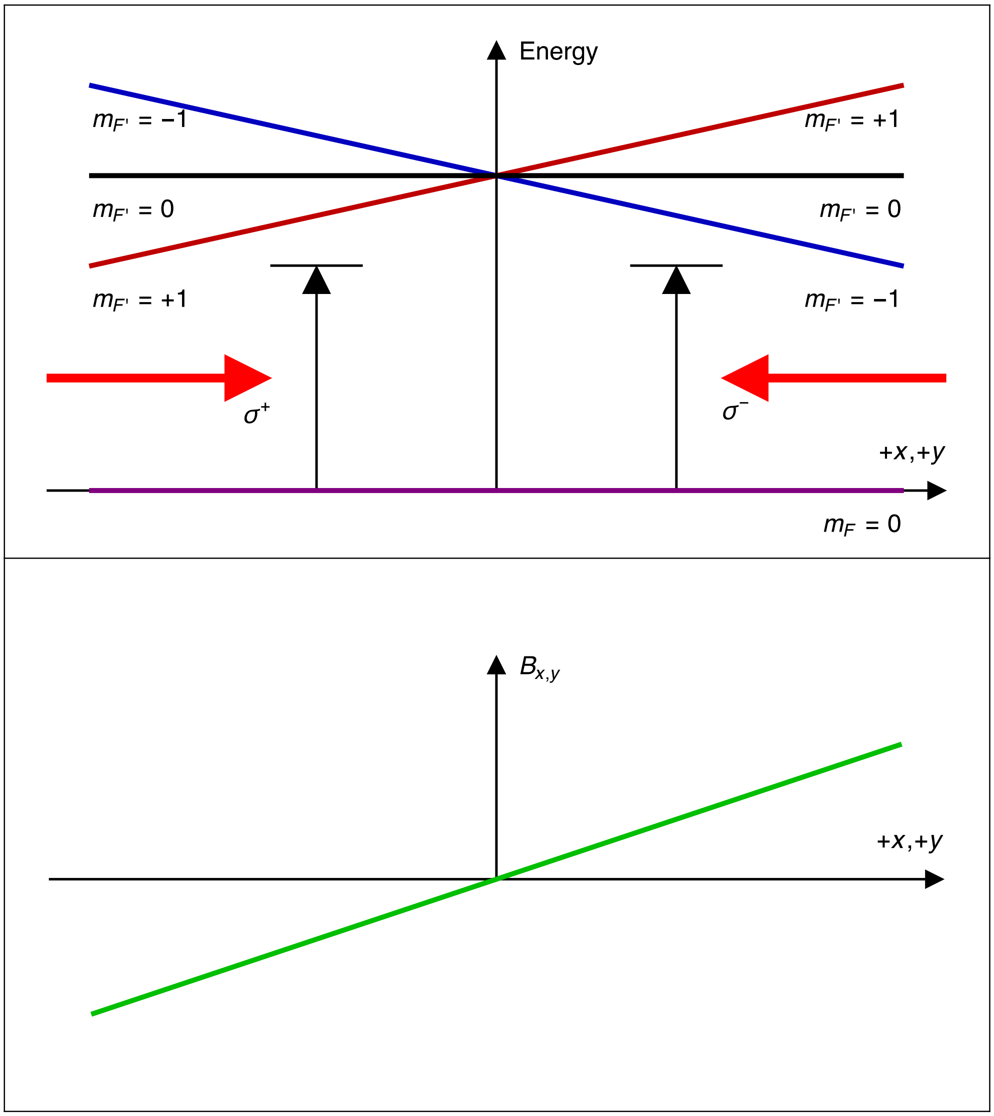

Figure 2.12: The principle of confinement in the x- and y-dimension in a magneto-optical trap. The bottom panel shows the linear position dependence of the magnetic field. This field lifts the degeneracy of the magnetic sublevels in the excited state. As an atom moves to the right, the $m_{F'} = 1$ sublevel is shifted toward resonance with the σ^+ laser for an atom. The same process happens when the atom moves to the right, with the exception that the $m_{F'} = -1$ sublevel is shifted toward resonance with the σ^- laser for an atom. Therefore, the atom always feels a restoring force back to the position $x = y = 0$. The MOT is cools and traps atoms.

physics for decades.

2.6 Unitary transformations

It is common, in quantum mechanics, to transform to a different picture. In our case the coupled terms in the interaction Hamiltonian (presented below) is oscillating at optical frequencies. It is often advantageous to rotate our system with the optical frequencies so that fast oscillations can be ignored (Rotating-Wave Approximation). Let $\widehat{U}$ be any unitary operator. Then, the state in the interaction picture is defined with the following rotation [43].

$$|\psi\rangle_T = \widehat{U}|\psi\rangle \tag{2.38}$$

I will denote all states and operators in the new picture with a subscript T, and all states and operators in the Shrödinger picture will have no mark. In a similar fashion, we can write the density operator in the interaction picture.

$$\begin{aligned} \widehat{\rho}_T &= |\psi\rangle_T \langle\psi|_T = \widehat{U}|\psi\rangle\langle\psi|\widehat{U}^\dagger \\ &= \widehat{U}\widehat{\rho}\widehat{U}^\dagger \end{aligned} \tag{2.39}$$

Likewise, to get back to the Shrödinger picture from the transformed picture,

$$\widehat{\rho} = \widehat{U}^\dagger \widehat{\rho}_T \widehat{U} \tag{2.40}$$

The equation of motion should apply to both pictures [43].

$$\mathrm{i}\hbar\frac{\partial}{\partial t}\widehat{\rho} = \left[\widehat{H}, \widehat{\rho}\right], \qquad \mathrm{i}\hbar\frac{\partial}{\partial t}\widehat{\rho}_T = \left[\widehat{H}_T, \widehat{\rho}_T\right] \tag{2.41}$$

Our goal is to determine $\widehat{H}_T$. Let's substitute equation (2.40) into the Shrödinger representation of (2.41).

$$\mathrm{i}\hbar\frac{\partial}{\partial t}\left(\widehat{U}^\dagger\widehat{\rho}_T\widehat{U}\right) = \left[\widehat{H}, \widehat{U}^\dagger\widehat{\rho}_T\widehat{U}\right] \tag{2.42}$$

Differentiate through with the time derivative.

$$\mathrm{i}\hbar\left(\frac{\partial\widehat{U}^\dagger}{\partial t}\widehat{\rho}_T\widehat{U} + \widehat{U}^\dagger\frac{\partial\widehat{\rho}_T}{\partial t}\widehat{U} + \widehat{U}^\dagger\widehat{\rho}_T\frac{\partial\widehat{U}}{\partial t}\right) = \left[\widehat{H}, \widehat{U}^\dagger\widehat{\rho}_T\widehat{U}\right] \tag{2.43}$$

Next, operate $\widehat{U}$ from the left, and operate $\widehat{U}^\dagger$ from the right.

$$\mathrm{i}\hbar\left(\widehat{U}\frac{\partial\widehat{U}^\dagger}{\partial t}\widehat{\rho}_T + \frac{\partial\widehat{\rho}_T}{\partial t} + \widehat{\rho}_T\frac{\partial\widehat{U}}{\partial t}\widehat{U}^\dagger\right) = \widehat{U}\left[\widehat{H}, \widehat{U}^\dagger\widehat{\rho}_T\widehat{U}\right]\widehat{U}^\dagger \tag{2.44}$$

Expand the commutator.

$$\begin{aligned}\mathrm{i}\hbar\left(\widehat{U}\frac{\partial\widehat{U}^\dagger}{\partial t}\widehat{\rho}_T + \frac{\partial\widehat{\rho}_T}{\partial t} + \widehat{\rho}_T\frac{\partial\widehat{U}}{\partial t}\widehat{U}^\dagger\right) &= \widehat{U}\widehat{H}\widehat{U}^\dagger\widehat{\rho}_T\widehat{U}\widehat{U}^\dagger - \widehat{U}\widehat{U}^\dagger\widehat{\rho}_T\widehat{U}\widehat{H}\widehat{U}^\dagger \\ &= \widehat{U}\widehat{H}\widehat{U}^\dagger\widehat{\rho}_T - \widehat{\rho}_T\widehat{U}\widehat{H}\widehat{U}^\dagger \\ &= \left[\widehat{U}\widehat{H}\widehat{U}^\dagger, \widehat{\rho}_T\right]\end{aligned} \tag{2.45}$$

Recalling,

$$\frac{\partial \widehat{U}\widehat{U}^{\dagger}}{\partial t} = \frac{\partial \widehat{U}}{\partial t}\widehat{U}^{\dagger} + \widehat{U}\frac{\partial \widehat{U}^{\dagger}}{\partial t} = 0 \tag{2.46}$$

We can simplify the LHS of equation (2.45).

$$\begin{aligned} \mathrm{i}\hbar\left(\frac{\partial \widehat{\rho}_T}{\partial t} + \widehat{\rho}_T\frac{\partial \widehat{U}}{\partial t}\widehat{U}^{\dagger} + \widehat{U}\frac{\partial \widehat{U}^{\dagger}}{\partial t}\widehat{\rho}_T\right) &= \\ \mathrm{i}\hbar\left(\frac{\partial \widehat{\rho}_T}{\partial t} + \widehat{\rho}_T\frac{\partial \widehat{U}}{\partial t}\widehat{U}^{\dagger} - \frac{\partial \widehat{U}}{\partial t}\widehat{U}^{\dagger}\widehat{\rho}_T\right) &= \\ \mathrm{i}\hbar\left(\frac{\partial \widehat{\rho}_T}{\partial t} - \left[\frac{\partial \widehat{U}}{\partial t}\widehat{U}^{\dagger}, \widehat{\rho}_T\right]\right) &= \\ &= \left[\widehat{U}\widehat{H}\widehat{U}^{\dagger}, \widehat{\rho}_T\right] \end{aligned} \tag{2.47}$$

Then,

$$\begin{aligned} \mathrm{i}\hbar\left(\frac{\partial \widehat{\rho}_T}{\partial t} - \left[\frac{\partial \widehat{U}}{\partial t}\widehat{U}^{\dagger}, \widehat{\rho}_T\right]\right) &= \left[\widehat{U}\widehat{H}\widehat{U}^{\dagger}, \widehat{\rho}_T\right] \\ \mathrm{i}\hbar\frac{\partial \widehat{\rho}_T}{\partial t} &= \left[\widehat{U}\widehat{H}\widehat{U}^{\dagger}, \widehat{\rho}_T\right] + \mathrm{i}\hbar\left[\frac{\partial \widehat{U}}{\partial t}\widehat{U}^{\dagger}, \widehat{\rho}_T\right] \end{aligned} \tag{2.48}$$

Therefore,

$$\mathrm{i}\hbar\frac{\partial \widehat{\rho}_T}{\partial t} = \left[\left(\widehat{U}\widehat{H}\widehat{U}^{\dagger} + \mathrm{i}\hbar\frac{\partial \widehat{U}}{\partial t}\widehat{U}^{\dagger}\right), \widehat{\rho}_T\right] \tag{2.49}$$

Comparing the second representation of equation (2.41) to the derived result in equation (2.49), we can write down the Hamiltonian in the transformed picture.

$$\widehat{H}_T = \widehat{U}\widehat{H}\widehat{U}^{\dagger} + \mathrm{i}\hbar\frac{\partial \widehat{U}}{\partial t}\widehat{U}^{\dagger} \tag{2.50}$$

We will use equation (2.50) to transform to the interaction picture. However, this operation can be used for any unitary transformation.

2.7 Light interacting with three level atoms: electromagnetically induced transparency

The following section is well known. We include this section as illustration, and we use it as a framework for the later sections. We will begin by considering the three level atom shown in figure 2.13. The closed three level system can be described by the following wavefunction:

$$|\psi\rangle = \sum_{i=1}^{3} c_i |i\rangle, \tag{2.51}$$

where $|c_i|^2$ is the probability of finding the atom in the state $|i\rangle$. It is useful to introduce a new operator that can describe a kind of average state of the atomic ensemble. The density matrix element is defined as:

$$\rho_{ij} = \langle i|\widehat{\rho}|j\rangle, \tag{2.52}$$

where we can then construct a matrix:

$$\rho = \begin{pmatrix} \rho_{11} & \rho_{12} & \rho_{13} \\ \rho_{21} & \rho_{22} & \rho_{33} \\ \rho_{31} & \rho_{32} & \rho_{33} \end{pmatrix}. \tag{2.53}$$

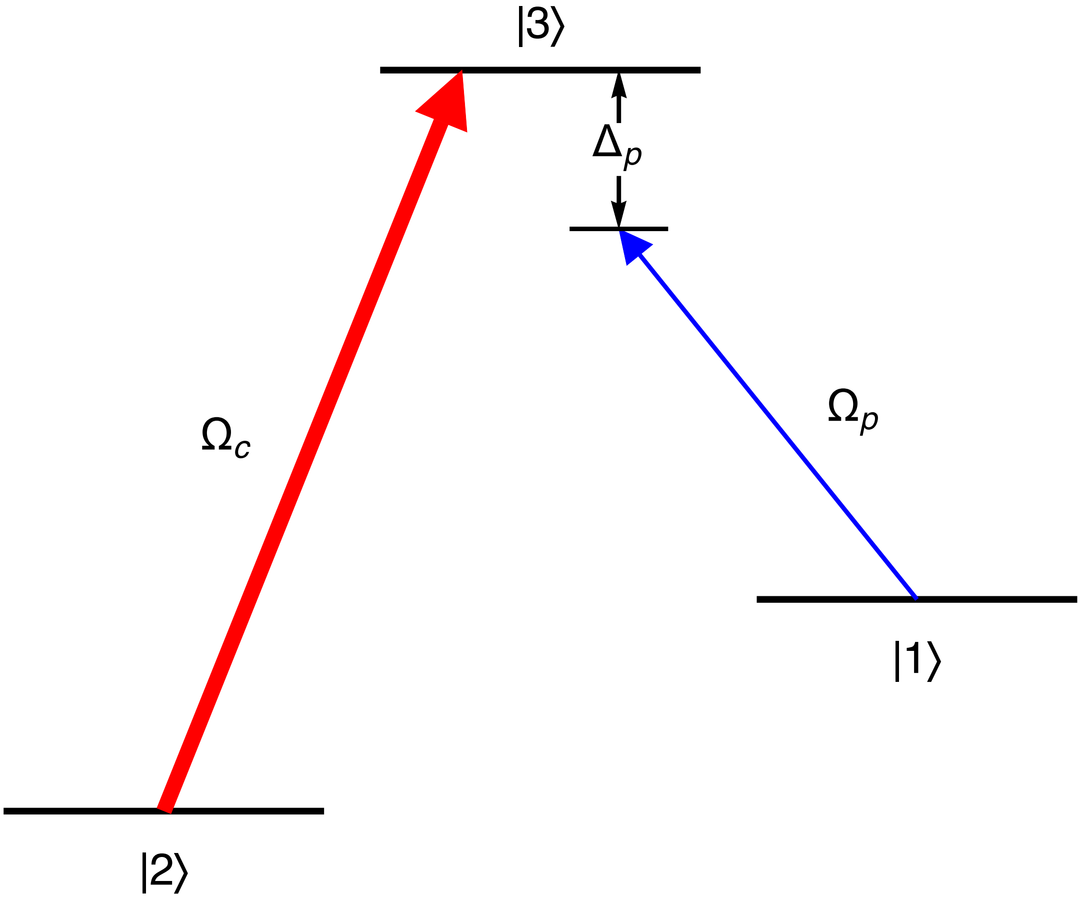

Figure 2.13: The three-level Λ-configuration. A strong control laser couples the states $|2\rangle$ and $|3\rangle$, while a weak probe laser scans about the $|1\rangle \rightarrow |3\rangle$ transition.

2.7.1 The Hamiltonian

The Hamiltonian is composed of the atomic Hamiltonian, $\widehat{H}_0$, and the interaction Hamiltonian, $\widehat{H}_I$, which describes the interaction of the atom with the fields. The total Hamiltonian is

$$\widehat{H} = \widehat{H}_0 + \widehat{H}_I, \tag{2.54}$$

where

$$\begin{aligned}\widehat{H}_0 &= E_1|1\rangle\langle 1| + E_2|2\rangle\langle 2| + E_3|3\rangle\langle 3| \\ \widehat{H}_I &= -d_{23}\mathcal{E}(t)\left(|2\rangle\langle 3| + |3\rangle\langle 2|\right) - d_{13}\mathcal{E}(t)\left(|1\rangle\langle 3| + |3\rangle\langle 1|\right).\end{aligned} \tag{2.55}$$

We find it useful in our formalism to represent many of these operators as matrices. The matrix representation of the total Hamiltonian is

$$\widehat{H} = \begin{pmatrix} \hbar\omega_1 & 0 & -d_{13}\mathcal{E}(t) \\ 0 & \hbar\omega_2 & -d_{23}\mathcal{E}(t) \\ -d_{13}\mathcal{E}(t) & -d_{23}\mathcal{E}(t) & \hbar\omega_3 \end{pmatrix}, \tag{2.56}$$

where d_{13} and d_{23} are the electric dipole matrix elements between states $1 \rightarrow 3$ and $2 \rightarrow 3$ respectively. The dipole matrix elements, $d_{mn} = \langle m|\widehat{\epsilon}\cdot\widehat{d}|n\rangle$ of dipole-allowed transitions are taken from refs. [41,42]. The rest are set to zero. $\mathcal{E}(t)$ is the electric field given by:

$$\mathcal{E}(t) = \mathcal{E}_c(r,\phi,z,t) + \mathcal{E}_p(r,\phi,z,t). \tag{2.57}$$

where we will assume that the fields are plane-waves. The experiment uses more complicated electric field modes. However, this section is intended to illustrate the general properties of EIT. For now, we will use a simple model for the fields: plane-waves. For this section, we will assume that the probe and the control laser are co-propagating along the same axis. The fields are then,

$$\begin{aligned}\mathcal{E}_c(r,\phi,z,t) &= \frac{1}{2}\mathcal{E}_c\left(e^{\mathrm{i}(\omega_c t - k_c z)} + e^{-\mathrm{i}(\omega_c t - k_c z)}\right) \\ \mathcal{E}_p(r,\phi,z,t) &= \frac{1}{2}\mathcal{E}_p\left(e^{\mathrm{i}(\omega_p t - k_p z)} + e^{-\mathrm{i}(\omega_p t - k_p z)}\right),\end{aligned} \tag{2.58}$$

where $\mathcal{E}_c$ and $\mathcal{E}_p$ are constants. To simplify matters, define the so-called Rabi-frequency.

$$\begin{aligned}\Omega_p &= -\frac{d_{13}\mathcal{E}_p}{\hbar} \\ \Omega_c &= -\frac{d_{23}\mathcal{E}_c}{\hbar}\end{aligned} \tag{2.59}$$

Additionally, we will make an approximation that control field only couples with the transition $|2\rangle \rightarrow |3\rangle$, and that the probe laser only couples the transition $|1\rangle \rightarrow |3\rangle$. This is valid (in general) for real atoms when proper polarizations are considered, or if the levels are sufficiently far apart. Then, the Hamiltonian can be recast as,

$$\begin{aligned}
\widehat{H}_0 &= \sum_{i=1}^{3} \hbar\omega_i |i\rangle\langle i| \\
\widehat{H}_I &= \hbar\Omega_c e^{\mathrm{i}(\omega_c t - k_c z + \ell_c \phi)} |2\rangle\langle 3| + \text{h.c.} + \Omega_p e^{\mathrm{i}(\omega_p t - k_p z + \ell_p \phi)} |1\rangle\langle 3| + \text{h.c.}
\end{aligned} \tag{2.60}$$

In order to eliminate the time-dependence of the Hamiltonian, we will need to make a Unitary transformation. We will use the prescription in section 2.6. Consider the following Unitary Operator.

$$\widehat{U}_1 = \begin{pmatrix} e^{-\mathrm{i}(\omega_p t + k_p z - \ell_p \phi)} & 0 & 0 \\ 0 & e^{-\mathrm{i}(\omega_c t - k_c z + \ell_c \phi)} & 0 \\ 0 & 0 & 1 \end{pmatrix} \tag{2.61}$$

From equation (2.50), we get that the transformed Hamiltonian is of the form,

$$\widehat{H}_T = \hbar \begin{pmatrix} \omega_p & 0 & \frac{1}{2}\Omega_p \left(1 + e^{-\mathrm{i}2(\omega_p t - k_p z)}\right) \\ 0 & \omega_c + \omega_{21} & \frac{1}{2}\Omega_c \left(1 + e^{-\mathrm{i}2(\omega_c t - k_c z + \ell_c \phi)}\right) \\ \frac{1}{2}\Omega_p \left(e^{\mathrm{i}2(\omega_p t - k_p z)} + 1\right) & \frac{1}{2}\Omega_c \left(e^{\mathrm{i}2(\omega_c t - k_c z + \ell_c \phi)} + 1\right) & \omega_{31} \end{pmatrix}, \tag{2.62}$$

where $\omega_{21} = \omega_2 - \omega_1$, and $\omega_{31} = \omega_3 - \omega_1$. Apply the rotating wave approximation, we assume that all the $e^{2i\omega t}$ terms are oscillating too fast, and that they will average out to zero. Then,

$$\widehat{H}_T = \hbar \begin{pmatrix} \omega_p & 0 & \frac{1}{2}\Omega_p \\ 0 & \omega_c + \omega_{21} & \frac{1}{2}\Omega_c \\ \frac{1}{2}\Omega_p & \frac{1}{2}\Omega_c & \omega_{31} \end{pmatrix} \tag{2.63}$$

Finally, we will make one more transformation using the following Unitary operator to shift the energy:

$$\widehat{U}_2 = \begin{pmatrix} e^{\mathrm{i}\omega_p t} & 0 & 0 \\ 0 & e^{\mathrm{i}\omega_p t} & 0 \\ 0 & 0 & e^{\mathrm{i}\omega_p t} \end{pmatrix}. \tag{2.64}$$

The final, transformed total Hamiltonian is:

$$\widehat{H}' = \frac{\hbar}{2} \begin{pmatrix} 0 & 0 & \Omega_p \\ 0 & 2(\Delta_c - \Delta_p) & \Omega_c \\ \Omega_p & \Omega_c & -2\Delta_p \end{pmatrix}, \tag{2.65}$$

where $\Delta_p = \omega_p - \omega_{31}$ and $\Delta_c = \omega_c - \omega_{32}$.

2.7.2 The master equation

We are working in the transformed picture. All transformed operators will be indicated with the prime. The equation of motion is given by [1]:

$$\mathrm{i}\hbar\dot{\widehat{\rho}'} = \left[\widehat{H}, \widehat{\rho}'\right] + \mathrm{i}\hbar\widehat{\mathcal{L}} + \mathrm{i}\hbar\widehat{\mathcal{L}}_d, \tag{2.66}$$

where the density matrix operator is transformed according to $\hat{\rho}' = \widehat{U}\rho\widehat{U}^{\dagger}$, $\widehat{\mathcal{L}}$ is an operator describing the losses and $\widehat{\mathcal{L}}_d$ is the so-called "Lindbald superoperator" [48, 49]. From [1], the loss operator is:

$$\widehat{\mathcal{L}} = \frac{\Gamma_{31}}{2}\left[2|1\rangle\langle 3|\widehat{\rho}'|3\rangle\langle 1| - |3\rangle\langle 3|\widehat{\rho}' - \widehat{\rho}'|3\rangle\langle 3|\right] + \frac{\Gamma_{32}}{2}\left[2|2\rangle\langle 3|\widehat{\rho}'|3\rangle\langle 2| - |3\rangle\langle 3|\widehat{\rho}\right] - \widehat{\rho}'|3\rangle\langle 3|\right], \tag{2.67}$$

I will then, define the $\mathcal{L}$ matrix in much the same as the density matrix.

$$\mathcal{L}_{ij} = \langle i|\widehat{\mathcal{L}}|j\rangle, \tag{2.68}$$

where we can construct the matrix,

$$\mathcal{L} = \begin{pmatrix} \Gamma_{31}\rho'_{33} & 0 & -\frac{1}{2}(\Gamma_{31}+\Gamma_{32})\rho'_{13} \\ 0 & \Gamma_{32}\rho'_{33} & -\frac{1}{2}(\Gamma_{31}+\Gamma_{32})\rho'_{23} \\ -\frac{1}{2}(\Gamma_{31}+\Gamma_{32})\rho'_{31} & -\frac{1}{2}(\Gamma_{31}+\Gamma_{32})\rho'_{32} & -(\Gamma_{31}+\Gamma_{32})\rho'_{33} \end{pmatrix} \tag{2.69}$$

There are other sources of loss and decoherences. The relaxation matrix describes the additional decoherence induced by the finite linewidth of the laser.

$$\widehat{\mathcal{L}}_d = -\sum_{i=1}^{3}\sum_{j=1}^{3}\gamma_{L,ij}\rho_{ij}|i\rangle\langle j| \tag{2.70}$$

where $\gamma_{\mathcal{L},ij}$ is a decoherence rate equal to the sum of the linewidths of the radiation connecting state $|i\rangle$ to $|j\rangle$. Therefore, in the simple three-level configuration, we have the following relations for the linewidths.

$$\gamma_{L,13} = \gamma_{L,31} = \gamma_p$$

$$\gamma_{L,23} = \gamma_{L,32} = \gamma_c$$

$$\gamma_{L,12} = \gamma_{L,21} = \gamma_p + \gamma_c$$

$$\gamma_{L,11} = \gamma_{L,22} = \gamma_{L,33} = 0$$

Then, we can construct a matrix of elements consisting of $\mathcal{L}_{d,ij} = \langle i|\widehat{\mathcal{L}}_d|j\rangle$.

$$\mathcal{L}_d = -\begin{pmatrix} 0 & (\gamma_p + \gamma_c)\rho'_{12} & \gamma_p\rho'_{13} \\ (\gamma_p + \gamma_c)\rho'_{21} & 0 & \gamma_c\rho'_{23} \\ \gamma_p\rho'_{31} & \gamma_c\rho'_{32} & 0 \end{pmatrix} \tag{2.71}$$

Again, representing equation (2.66) in matrix form is useful for our purposes.

$$
\begin{aligned}
\mathrm{i}\hbar \begin{pmatrix} \dot{\rho}'_{11} & \dot{\rho}'_{12} & \dot{\rho}'_{13} \\ \dot{\rho}'_{21} & \dot{\rho}'_{22} & \dot{\rho}'_{23} \\ \dot{\rho}'_{31} & \dot{\rho}'_{32} & \dot{\rho}'_{33} \end{pmatrix} = & \begin{pmatrix} 0 & 0 & \Omega_p \\ 0 & 2(\Delta_c - \Delta_p) & \Omega_c \\ \Omega_p & \Omega_c & -2\Delta_p \end{pmatrix} \cdot \begin{pmatrix} \rho'_{11} & \rho'_{12} & \rho'_{13} \\ \rho'_{21} & \rho'_{22} & \rho'_{23} \\ \rho'_{31} & \rho'_{32} & \rho'_{33} \end{pmatrix} \\
& - \begin{pmatrix} \rho'_{11} & \rho'_{12} & \rho'_{13} \\ \rho'_{21} & \rho'_{22} & \rho'_{23} \\ \rho'_{31} & \rho'_{32} & \rho'_{33} \end{pmatrix} \cdot \begin{pmatrix} 0 & 0 & \Omega_p \\ 0 & 2(\Delta_c - \Delta_p) & \Omega_c \\ \Omega_p & \Omega_c & -2\Delta_p \end{pmatrix} \\
& + \mathrm{i}\hbar \begin{pmatrix} \Gamma_{31}\rho'_{33} & 0 & -\frac{1}{2}(\Gamma_{31}+\Gamma_{32})\rho'_{13} \\ 0 & \Gamma_{32}\rho'_{33} & -\frac{1}{2}(\Gamma_{31}+\Gamma_{32})\rho'_{23} \\ -\frac{1}{2}(\Gamma_{31}+\Gamma_{32})\rho'_{31} & -\frac{1}{2}(\Gamma_{31}+\Gamma_{32})\rho'_{32} & -(\Gamma_{31}+\Gamma_{32})\rho'_{33} \end{pmatrix} \\
& - \mathrm{i}\hbar \begin{pmatrix} 0 & (\gamma_p+\gamma_c)\rho'_{12} & \gamma_p\rho'_{13} \\ (\gamma_p+\gamma_c)\rho'_{21} & 0 & \gamma_c\rho'_{23} \\ \gamma_p\rho'_{31} & \gamma_c\rho'_{32} & 0 \end{pmatrix}
\end{aligned}
\tag{2.72}
$$

Ultimately, we use *Mathematica* to solve this equation for the matrix elements of interest. Let us now concern ourselves with the solutions of equation (2.72).

2.7.3 Solutions

The off-diagonal density matrix elements contain the information about how the states couple. The solutions of equation (2.72) for each of the off diagonal density matrix elements are:

$$\begin{aligned}
\dot{\rho}'_{21} &= -\mathrm{i}\left(\Delta - \frac{\mathrm{i}}{2}\gamma_{21}\right)\rho'_{21} - \frac{\mathrm{i}}{2}\Omega_p\rho'_{23} + \frac{\mathrm{i}}{2}\Omega_c\rho'_{31} \\
\dot{\rho}'_{31} &= -\mathrm{i}\left(\Delta - \frac{\mathrm{i}}{2}\gamma_{31}\right)\rho'_{31} + \frac{\mathrm{i}}{2}\Omega_p(\rho'_{11} - \rho'_{33}) + \frac{\mathrm{i}}{2}\Omega_c\rho'_{21} \\
\dot{\rho}'_{32} &= -\frac{1}{2}\gamma_{32}\rho_{32} + \frac{\mathrm{i}}{2}\Omega_c(\rho'_{22} - \rho'_{33}) + \frac{\mathrm{i}}{2}\Omega_p\rho'_{12},
\end{aligned} \tag{2.73}$$

where we let $\Gamma_3 = \Gamma_{31} + \Gamma_{32}$ be the spontaneous decay rate from state $|3\rangle$. The coherence decay rates represent the strength of the coupling of our system to the environment. For our system, the primary sources of decoherence come from the spontaneous decay from the excited states to the ground states and from the linewidths and noise of the laser fields. We define the coherence decay rates as:

$$\begin{aligned}
\gamma_{21} &= 2(\gamma_p + \gamma_c) \\
\gamma_{31} &= \Gamma_3 + 2\gamma_p \\
\gamma_{32} &= \Gamma_3 + 2\gamma_c.
\end{aligned} \tag{2.74}$$

In reality, the environment couples with the system in other ways (e.g. stray magnetic fields). We account for these sources of decoherence by treating γ_p and γ_c as fitting parameters, matching it to our experimental data. This process is elaborated upon in later sections and chapters.

Suppose that the probe laser is significantly weaker than the control laser ($\Omega_p \ll \Omega_c$), then we can make assumptions about the relative fractions of the populations [50].

$$\begin{aligned} &\rho'_{11} \approx 1 \\ &\rho'_{22} \approx \rho'_{33} \approx \rho'_{23} \approx \rho'_{32} \approx 0. \end{aligned} \tag{2.75}$$

Now, the equations of motion become:

$$\begin{aligned} \dot{\rho}'_{21} &= -\mathrm{i}\left(\Delta - \frac{\mathrm{i}}{2}\gamma_{21}\right)\rho'_{21} + \frac{\mathrm{i}}{2}\Omega_c\rho'_{31} \\ \dot{\rho}'_{31} &= -\mathrm{i}\left(\Delta - \frac{\mathrm{i}}{2}\gamma_{31}\right)\rho'_{31} + \frac{\mathrm{i}}{2}\Omega_p + \frac{\mathrm{i}}{2}\Omega_c\rho'_{21}, \end{aligned} \tag{2.76}$$

where we have dropped the ρ'_{32} equation of motion because we are only concerned with the response of the probe. We will make an approximation that the system is in steady state ($\dot{\rho}'_{21} = \dot{\rho}'_{31} = 0$). Then, the equations of motion simplify to,

$$\begin{aligned} 0 &= -\mathrm{i}\left(\Delta - \frac{\mathrm{i}}{2}\gamma_{21}\right)\rho'_{21} + \frac{\mathrm{i}}{2}\Omega_c\rho'_{31} \\ 0 &= -\mathrm{i}\left(\Delta - \frac{\mathrm{i}}{2}\gamma_{31}\right)\rho'_{31} + \frac{\mathrm{i}}{2}\Omega_p + \frac{\mathrm{i}}{2}\Omega_c\rho'_{21}. \end{aligned} \tag{2.77}$$

Then,

$$\rho'_{21} = \frac{1}{2\left(\Delta - \frac{\mathrm{i}}{2}\gamma_{21}\right)}\Omega_c\rho'_{31}. \tag{2.78}$$

And,

$$\begin{aligned} 0 &= -\mathrm{i}\left(\Delta - \frac{\mathrm{i}}{2}\gamma_{31}\right)\rho'_{31} + \frac{\mathrm{i}}{2}\Omega_p + \frac{\mathrm{i}}{2}\Omega_c\rho'_{21} \\ &= -\mathrm{i}\left(\Delta - \frac{\mathrm{i}}{2}\gamma_{31}\right)\rho'_{31} + \frac{\mathrm{i}}{2}\Omega_p + \frac{\mathrm{i}}{4\left(\Delta - \frac{\mathrm{i}}{2}\gamma_{21}\right)}\left|\Omega_c\right|^2\rho'_{31}. \end{aligned} \tag{2.79}$$

Gathering ρ'_{31} terms,

$$\left(\Delta - \frac{\mathrm{i}}{2}\gamma_{31} - \frac{1}{4\left(\Delta - \frac{\mathrm{i}}{2}\gamma_{21}\right)}\left|\Omega_c\right|^2\right)\rho'_{31} = \frac{1}{2}\Omega_p. \tag{2.80}$$

Then, ρ'_{31} becomes,

$$\rho'_{31} = \frac{\frac{1}{2}\Omega_p\left(\Delta - \frac{\mathrm{i}}{2}\gamma_{21}\right)}{\left(\Delta - \frac{\mathrm{i}}{2}\gamma_{21}\right)\left(\Delta - \frac{\mathrm{i}}{2}\gamma_{31}\right) - \frac{1}{4}\Omega_c^2}. \tag{2.81}$$

This result is well known, and is found in many references. We direct the reader to references [1, 50].

We often want to represent ρ'_{31} as a complex quantity, such as the following.

$$\rho'_{31} = \rho'_{31,\mathrm{R}} + \mathrm{i}\rho'_{31,\mathrm{I}}, \tag{2.82}$$

where $\rho'_{31,\mathrm{R}}$ is the real part of ρ'_{31}, and $\rho'_{31,\mathrm{I}}$ is the imaginary part of ρ'_{31}. The real part of the density matrix element is related to the index of refraction of the atomic ensemble, while the imaginary part of the density matrix element is related to the absorption of the atomic medium. We can obtain the real and imaginary parts by multiplying the top and bottom by the complex conjugate of of the denominator.

$$\begin{aligned}\rho'_{31} &= \frac{\frac{1}{2}\Omega_p\Delta\left\{\Delta^2-\gamma_{21}\gamma_{31}-\frac{1}{4}\Omega_c^2+\frac{\mathrm{i}}{2}(\gamma_{21}+\gamma_{31})\Delta\right\}}{\left(\Delta^2-\frac{1}{4}\Omega_c^2-\gamma_{21}\gamma_{31}\right)^2+\frac{1}{4}(\gamma_{21}+\gamma_{31})^2\Delta^2}\\ &= \frac{\frac{1}{2}\Omega_p\Delta\left(\Delta^2-\gamma_{21}\gamma_{31}-\frac{1}{4}\Omega_c^2\right)+\mathrm{i}\frac{1}{4}\Omega_p\Delta^2(\gamma_{21}+\gamma_{31})}{\left(\Delta^2-\frac{1}{4}\Omega_c^2-\gamma_{21}\gamma_{31}\right)^2+\frac{1}{4}(\gamma_{21}+\gamma_{31})^2\Delta^2}\end{aligned} \tag{2.83}$$

Therefore,

$$\begin{aligned}\rho'_{31,\mathrm{R}} &= \frac{\frac{1}{2}\Omega_p\Delta\left(\Delta^2-\gamma_{21}\gamma_{31}-\frac{1}{4}\Omega_c^2\right)}{\left(\Delta^2-\frac{1}{4}\Omega_c^2-\gamma_{21}\gamma_{31}\right)^2+\frac{1}{4}(\gamma_{21}+\gamma_{31})^2\Delta^2}\\ \rho'_{31,\mathrm{I}} &= \frac{\frac{1}{4}\Omega_p\Delta^2(\gamma_{21}+\gamma_{31})}{\left(\Delta^2-\frac{1}{4}\Omega_c^2-\gamma_{21}\gamma_{31}\right)^2+\frac{1}{4}(\gamma_{21}+\gamma_{31})^2\Delta^2}.\end{aligned} \tag{2.84}$$

Figure 2.14 (a) shows a plot of the real part of the density matrix element ρ'_{31}, and is related to the index of refraction of an atomic ensemble prepared in this way. Figure 2.14 (b) shows a plot of the imaginary part of the density matrix element ρ'_{31}, and is related to the absorption of an atomic ensemble prepared in this way. For both these plots, we set the decoherence rate $\gamma_{21} = 0$ and we set the control Rabi frequency to $\Omega_c = \Gamma_3/2$. When the probe is tuned to the $|1\rangle \to |3\rangle$ transition ($\Delta = 0$), then the atom has no absorption. This results in complete transmission

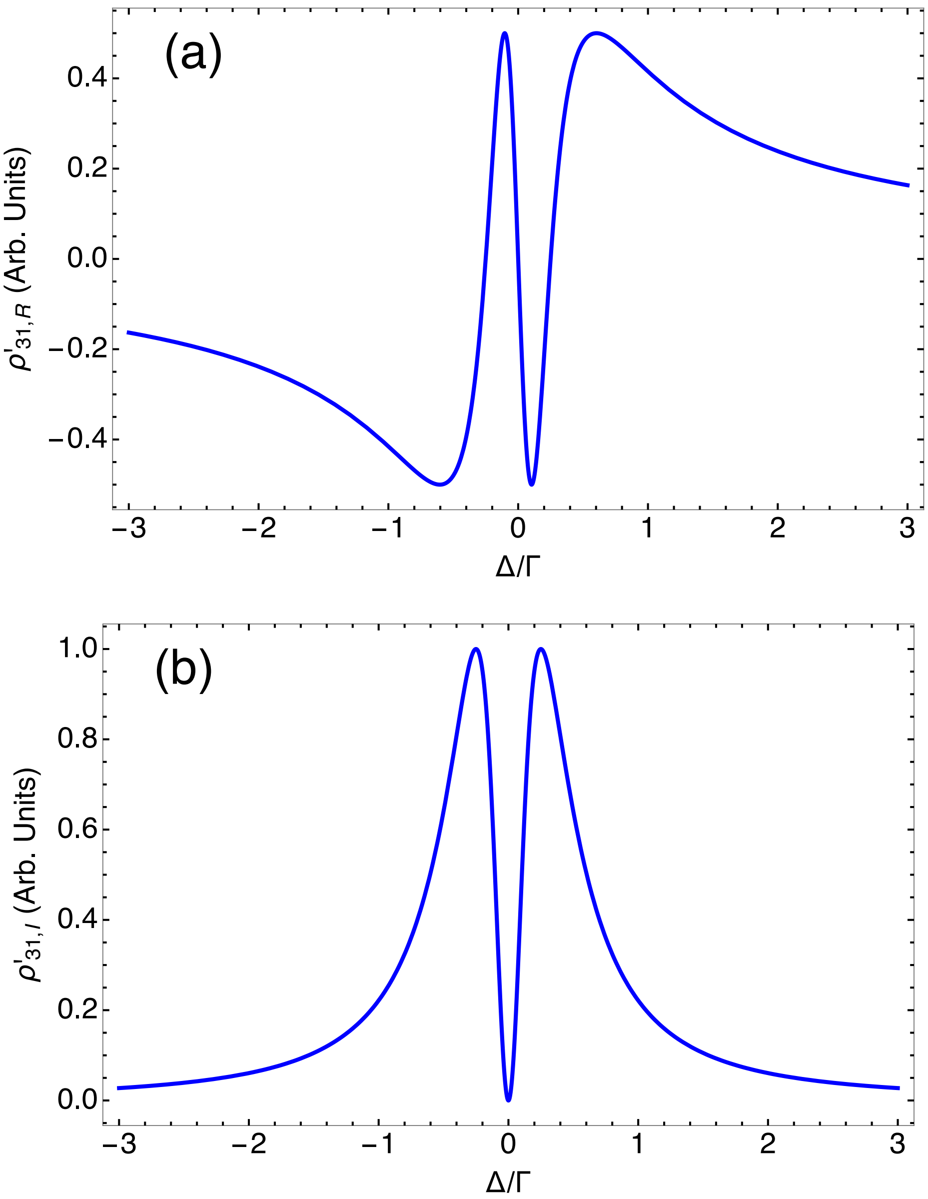

Figure 2.14: A plot of the (a) real part of the matrix element ρ'_{31}, and a plot of (b) the imaginary part of the matrix element ρ'_{31}. For these plots, $\gamma_{21} = 0$ and $\Omega_c = \Gamma_3/2$.

of the probe field, thus the name *electromagnetically induced transparency.*

Our experiment detects the transmission of a weak probe passing through a medium described by the four level model presented above. For a collection of atoms, we use a semi-classical model to describe the induced electric dipole moment of the ensemble of atoms. This is given by [43]:

$$p = N d_{13} \left(\rho'_{13}\right)^* = \epsilon_0 \chi \mathcal{E}_p, \tag{2.85}$$

where N is the number density of the atomic ensemble which we approximate to be constant, and χ is the susceptibility. From equation (2.85), the susceptibility is given by:

$$\chi = \frac{N}{\epsilon_0 \mathcal{E}} d_{13} \left(\rho'_{13}\right)^* = -\frac{N}{\epsilon_0 \hbar} \frac{d_{13}^2 \left(\rho'_{13}\right)^*}{\Omega_p}. \tag{2.86}$$

The imaginary part of the susceptibility describes the absorption of the laser passing through the medium. Applying Beer's Law to determine the transmitted fraction of the probe laser:

$$T = e^{-\mathrm{Im}[\chi] k_p z} \tag{2.87}$$

where z is the length of the atomic medium along the propagation direction. We let $z = 4$ mm, which is the $1/e^2$ diameter of the MOT.

Figure 2.15 shows several plots for EIT transmission spectra. Figure 2.15 (a) illustrates the affect of decoherences on the system. Transmission of 100% occurs

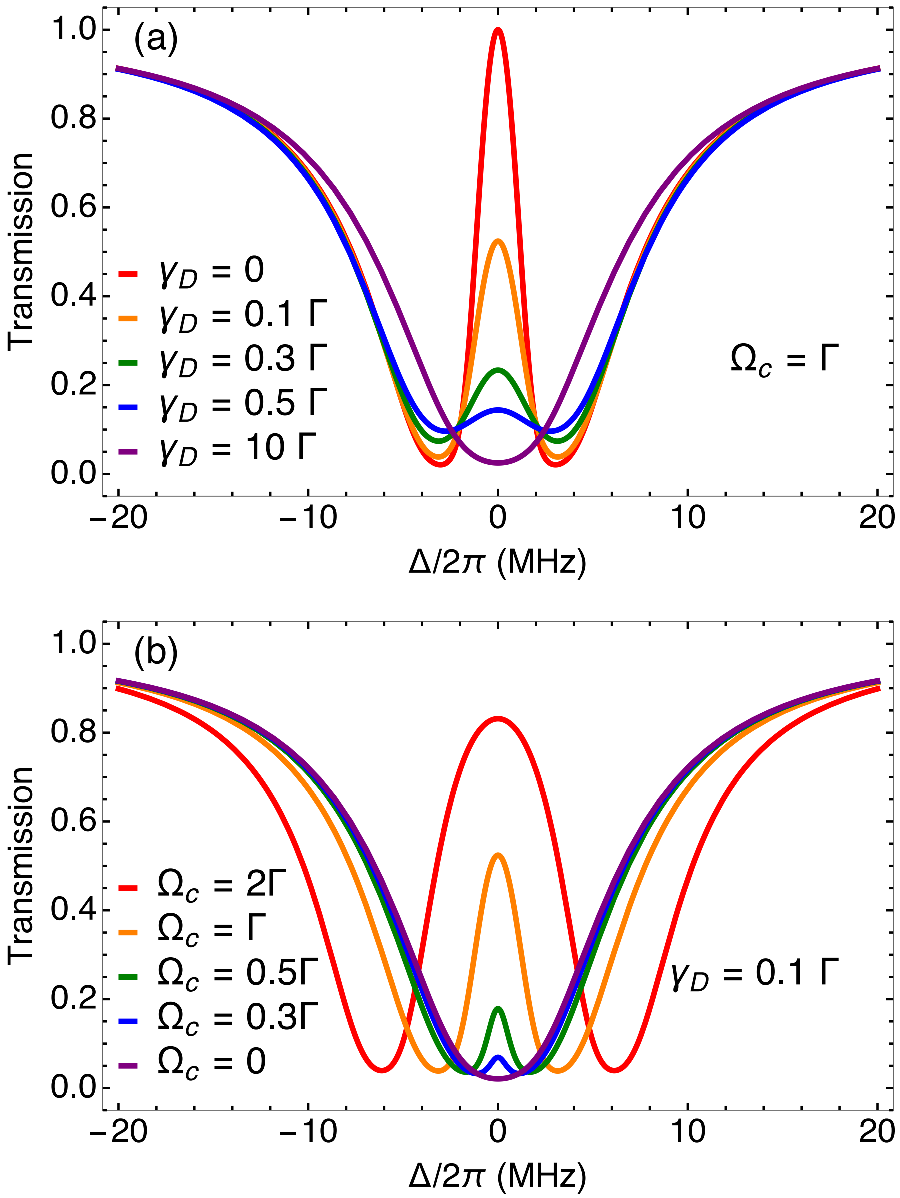

Figure 2.15: (a) Plot of several transmission spectra for ^{87}Rb. Increasing the decoherence rate decreases the transmission of the probe on resonance ($\Delta = 0$). (b) Plot of several transmission spectra for various control Rabi frequency values. Increasing the control Rabi frequency increases the transmission, but broadens the resonance feature.

at the probe resonance ($\Delta = 0$) when the decoherence rate is zero. Increasing the decoherence rate reduces the transmission at the probe resonance. This can be combated by increasing the control Rabi frequency. Driving harder with the control field increases the transmission of the probe on resonance. This is illustrated in figure 2.15 (b). However, increasing the control Rabi frequency broadens the EIT transmission feature. Applications of slow and stopped light require narrow EIT features with high transmission[3]. This is maximized for small decoherence rates and small control Rabi frequencies.

2.8 Electromagnetically induced transparency with four levels

This section examines EIT for a four level system containing one probe field, and one control field. The EIT transmission for this system is the same as the EIT transmission for the three level system. However, this configuration is necessary to describe the experiment in chapter 5 and appendix A. Additionally, the LG_0^1 spatial analysis found in this section has not been studied in the literature (to the best of our knowledge). More specifically, this section will analyze EIT resonances for several different LG_0^1 one sizes. We vary the waist of the control laser (w_c) with respect to the waist of the probe laser (w_p) to determine the effect of the spatial intensity overlap between the two modes.

---

[3] The group velocity for a probe pulse propagating through an EIT medium is inversely proportional to the slope of the EIT resonance feature. Narrowing the resonance feature results in steeper resonance slopes which results in slower group velocities.

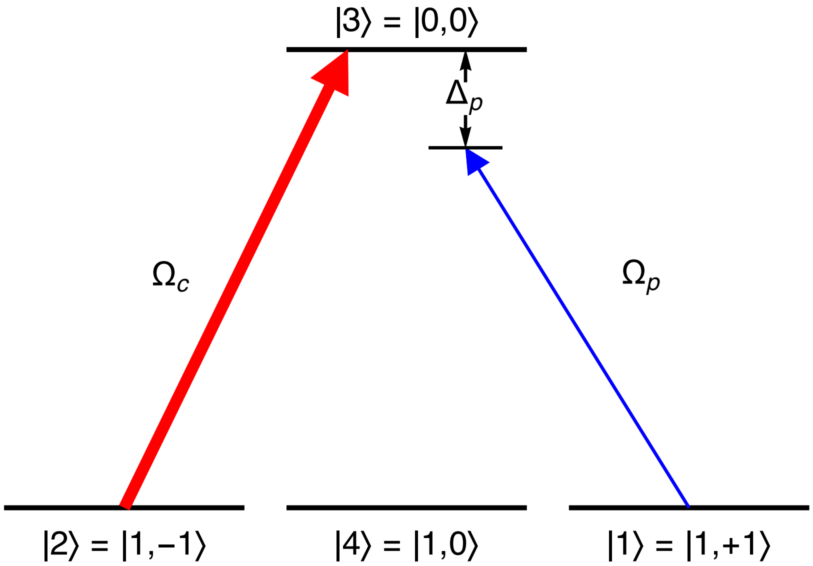

Figure 2.16: The figure shows the levels involved in EIT. The probe (thin blue arrow) couples the $|F = 1, m_F = +1\rangle \rightarrow |F' = 0, m_{F'} = 0\rangle$ magnetic sublevels using σ^- polarization. The control (thick red arrow) couples the $|F = 1, m_F = -1\rangle \rightarrow |F' = 0, m_{F'} = 0\rangle$ magnetic sublevels using σ^+ polarization. The state, $|4\rangle$, is included because the atom can decay to this state.

We use a density matrix formalism to describe a four level atom with three states belonging to the three magnetic sublevels of the $|F = 1, m_F = -1, 0, +1\rangle$ hyperfine level of the ${}^2S_{1/2}$ state in ^{87}Rb, and the final state belonging to the $|F' = 0, m_{F'} = 0\rangle$ magnetic state in the ${}^2P_{3/2}$ state in ^{87}Rb (see figure 2.16). We apply the density matrix formalism, as described by references [1, 19, 21, 51].

The total Hamiltonian for the atom interacting with an electric field is $\widehat{H} = \widehat{H}_0 + \widehat{H}_I$, where the Hamiltonian describing the atomic system is given by:

$$\widehat{H}_0 = \sum_{n=1}^{4} \hbar\omega_n |n\rangle\langle n|, \tag{2.88}$$

where $\hbar\omega_n$ is the energy of the nth level. For the configuration shown in figure 2.16, the Hamiltonian describing the interactions with the electric field can be written as:

$$\widehat{H}_I = \hbar\Omega_c(r)e^{\mathrm{i}(\omega_c t - k_c z + \ell_c\phi)}|2\rangle\langle 3| + \text{h.c.} + \hbar\Omega_p(r)e^{\mathrm{i}(\omega_p t + k_p z)}|1\rangle\langle 3| + \text{h.c.}, \tag{2.89}$$

where ω_p is the angular frequency and k_p is the wave number of the probe laser. Likewise, ω_c is the angular frequency, k_c is the wave number, and ℓ_c is the azimuthal charge of the control laser. The Rabi frequencies for this system are defined as:

$$\begin{aligned} \Omega_p(r) &= -\frac{d_{13}\mathcal{E}_p(r)}{\hbar}, \\ \Omega_c(r) &= -\frac{d_{23}\mathcal{E}_c(r)}{\hbar}. \end{aligned} \tag{2.90}$$

$\mathcal{E}_p(r)$ and $\mathcal{E}_c(r)$ are the possibly spatially dependent amplitudes of the probe and the control lasers. For this theoretical treatment, we model the probe and control Rabi frequencies after their corresponding spatial mode [38].

$$\begin{aligned} \mathcal{E}_p(r) &= \mathcal{E}_{0,p}e^{-r^2/w_{0,p}^2} \\ \mathcal{E}_c(r) &= \mathcal{E}_{0,c}\left(\frac{\sqrt{2}r}{w_{0,c}}\right)e^{-r^2/w_{0,c}^2} \end{aligned} \tag{2.91}$$

where $\mathcal{E}_{0,p}$ and $\mathcal{E}_{0,c}$ are constants, and $w_{0,p}$ and $w_{0,c}$ the waist of the probe and control laser. We define Rabi frequency constants, $\Omega_{0p,ij} = -\dfrac{d_{ij}\mathcal{E}_{0,p}}{\hbar}$ for the probe laser and $\Omega_{0c,kl} = -\dfrac{d_{kl}\mathcal{E}_{0,c}}{\hbar}$ for the control laser. These constants are used to compare different configurations of LG_0^1 as we change the size of the control laser with respect to the probe laser.

We use two unitary transformations on both the density matrix operator and the Hamiltonian. We transform into the rotating frame using the following unitary transformation:

$$\widehat{U}_1 = \exp\left[-\mathrm{i}(\omega_p t + k_p z)|1\rangle\langle 1| - \mathrm{i}(\omega_c t - k_c z + \ell_c \phi)|2\rangle\langle 2|\right]. \tag{2.92}$$

Also, we shift the zero point of the energy to the ground-state hyperfine level,$|F = 1\rangle$, using:

$$\widehat{U}_2 = \widehat{I}\exp\left[\mathrm{i}(\omega_p + \omega_1)t\right], \tag{2.93}$$

where $\widehat{I}$ is the identity operator. Applying the rotating wave approximation to the transformations made on the Hamiltonians in equations (2.89) and (2.88), we arrive at the following full Hamiltonian for our system:

$$\widehat{H}' = \hbar(\Delta_p - \Delta_c)|2\rangle\langle 2| - \hbar\Delta_p|3\rangle\langle 3| + \frac{1}{2}\hbar\Omega_p(|1\rangle\langle 3| + |3\rangle\langle 1|) + \frac{1}{2}\hbar\Omega_c(|2\rangle\langle 3| + |3\rangle\langle 2|), \tag{2.94}$$

where $\Delta_p = \omega_p - \omega_{13}$ and $\Delta_c = \omega_c - \omega_{23}$.

The time evolution of the density matrix is governed by the Liouville-von Neumann equation, given by equation (2.66). We build the loss operator in a similar fashion to equation (2.67):

$$\widehat{\mathcal{L}} = \frac{1}{2} \sum_{i=1,2,4} \Gamma_{3i} \left[2|i\rangle\langle 3|\hat{\rho}'|3\rangle\langle i| - |3\rangle\langle 3|\hat{\rho}' - \hat{\rho}'|3\rangle\langle 3| \right], \tag{2.95}$$

where $\Gamma_{3i} = \Gamma/3$ is the spontaneous decay rate from state 3 to i and the index $i = 1, 2, 4$ represents the three ground magnetic sublevels, and Γ is the natural line width of ^{87}Rb. The decoherence induced by the finite linewidth of the laser is given by [7, 49]:

$$\widehat{\mathcal{L}}_d = -\sum_{m=1}^{4} \sum_{n=1}^{4} \gamma_{mn} |m\rangle\langle m|\hat{\rho}'|n\rangle\langle n|, \tag{2.96}$$

where the dephasing rate, γ_{mn}, is the sum of the relevant laser linewidths connecting state $|m\rangle$ to $|n\rangle$. If we let γ_p and γ_c be the linewidths of the probe and control lasers, the dephasing rates are:

$$\begin{aligned} \gamma_{13} &= \gamma_{31} = \gamma_p, \\ \gamma_{23} &= \gamma_{32} = \gamma_c, \\ \gamma_{12} &= \gamma_{21} = \gamma_p + \gamma_c. \end{aligned} \tag{2.97}$$

All other dephasing rates are zero due to electric dipole selection rules.

We make two more assumptions in our model. The first is that the system is in steady state, which gives $\dfrac{\partial \hat{\rho}'}{\partial t} = 0$. The second is that the probe laser is significantly

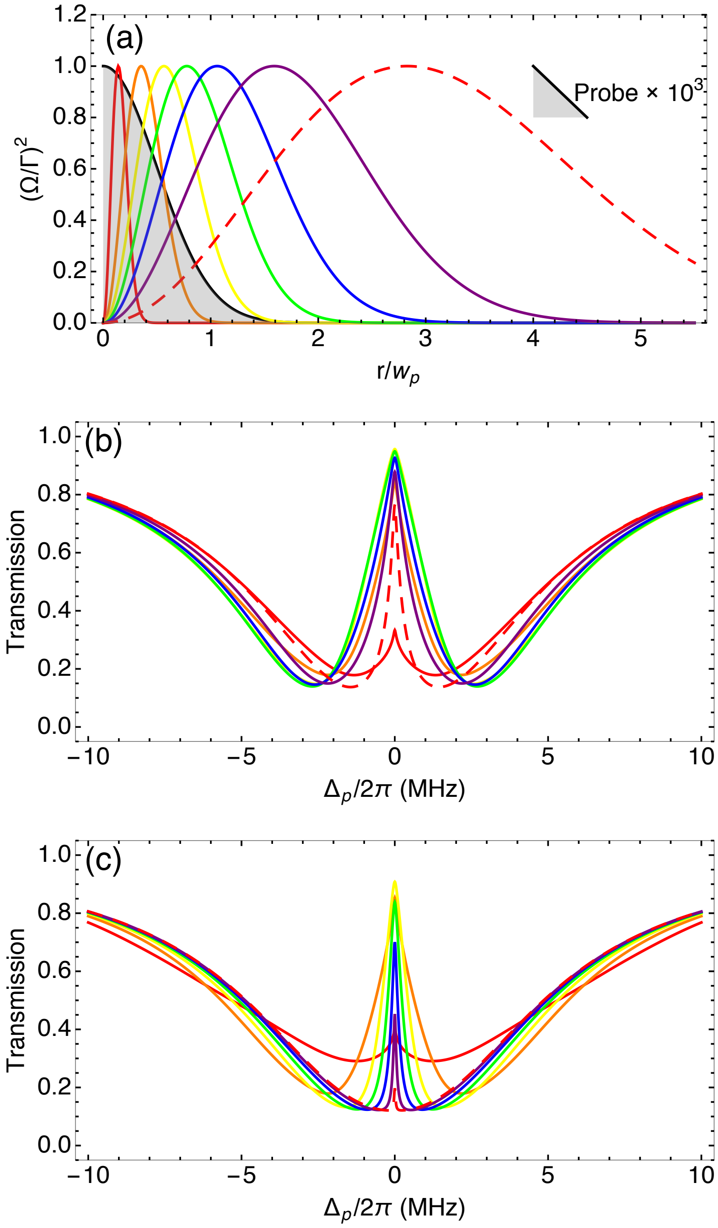

Figure 2.17: (a) A plot of the radial cross-section of the LG_0^1 control laser (colored curves), compared to the Gaussian probe (solid black curve, shaded to the axis). The corresponding EIT spectra are shown in (b) when the control Rabi frequency is held constant at $\Omega_{0c} = \Gamma$. The corresponding EIT spectra are shown in (c) when the control power is held constant at $P_c = 0.1$ mW. For (b) and (c), the decoherences in the system are set to $\gamma = 0.01$ MHz, the density of the atomic medium is 2×10^{11} cm^{-3}.

weaker than the control laser. In this approximation, the density matrix elements ($\rho'_{ij} = \langle i|\hat{\rho}'|j\rangle$) simplify: $\rho'_{11} \approx 1$, $\rho'_{nn} = 0$ for $n \neq 1$, and $\rho'_{14} = \rho'_{41} = \rho'_{42} = \rho'_{24} = 0$. Applying these assumptions and solving equation (2.66) for the off-diagonal density matrix elements associated with the three dipole-allowed transitions for the probe gives:

$$\rho'_{13}(r) = \frac{\frac{1}{2}\Omega_p(r)\left(\Delta_p - \Delta_c - \mathrm{i}(\gamma_p + \gamma_c)\right)}{\left(\Delta_p - \frac{\mathrm{i}}{2}(\Gamma + 2\gamma_p)\right)\left(\Delta_p - \Delta_c - \mathrm{i}(\gamma_p + \gamma_c)\right) - \frac{1}{4}\Omega_c^2(r)} \tag{2.98}$$

The presence of the strong control laser that couples state $|2\rangle$ to state $|3\rangle$ leads to an EIT feature in the density matrix element $\rho'_{13}(r)$. Mathematically, this comes from the Rabi frequency term, $\Omega_c(r)$, that appears in the expression for ρ'_{13} in equation (2.98). The r-dependence of the density matrix results from the spatial variation of the Rabi frequency. However, for our system, this dependence is only relevant in the cases involving a control in the LG_0^1 mode.

Again, we would like to predict the transmission of the probe passing through an ensemble of atoms. In this section, we included the transverse spatial dependence of the probe and control fields. Therefore, we can recast equations (2.85) through (2.87), but including the spatial dependence.

$$p(r) = Nd_{13}\left(\rho'_{13}(r)\right)^* = \epsilon_0\chi(r)\mathcal{E}_p(r), \tag{2.99}$$

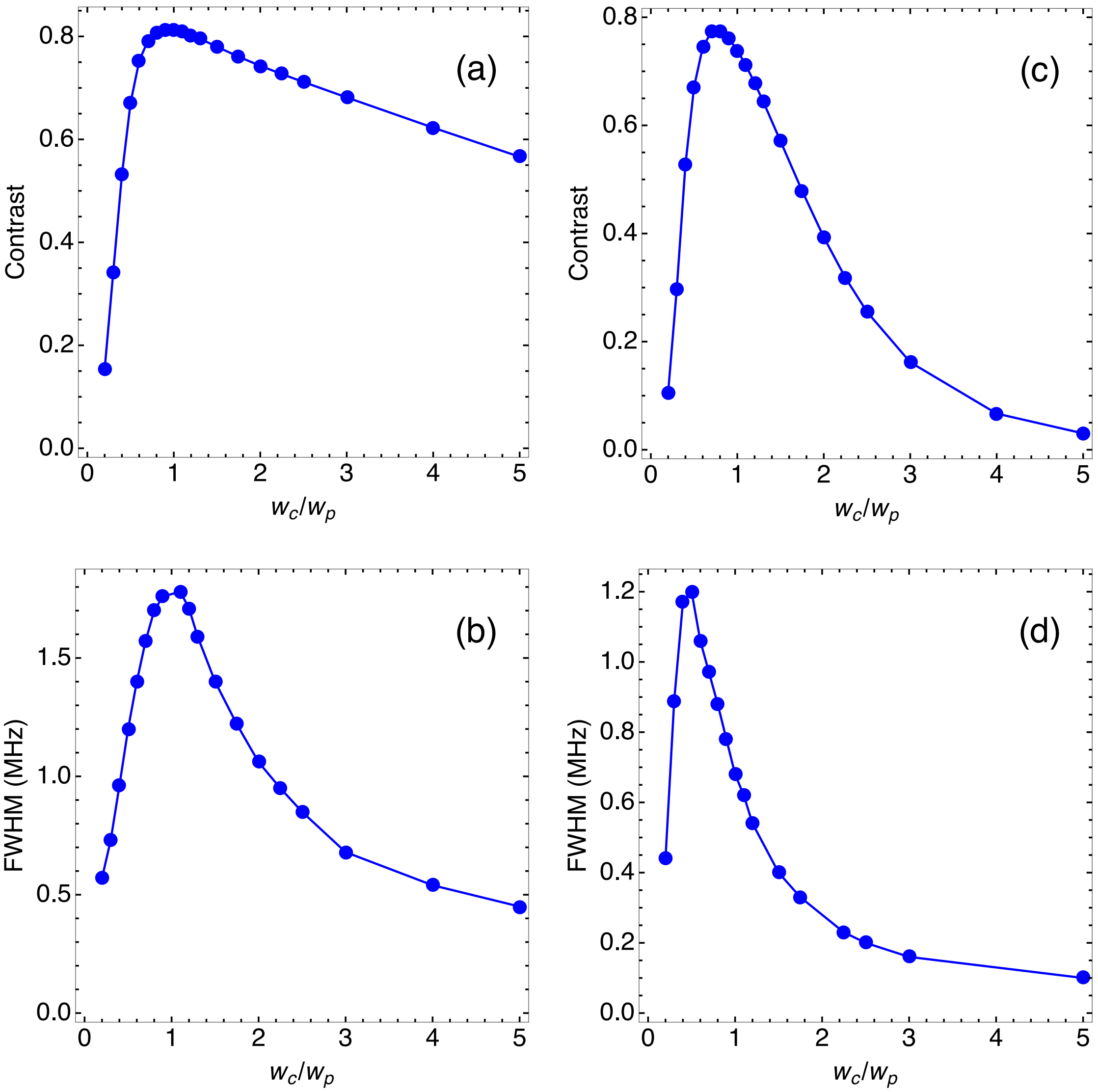

Figure 2.18: For each LG_0^1 mode in (a) and (b), the Rabi frequency is fixed ($\Omega_c = \Gamma$) and the decoherence rate is fixed ($\gamma = 0.01$ MHz). A plot of the (a) the EIT resonance contrast versus ratio of the LG_0^1 mode control waist to the Gaussian probe waist (w_c/w_p). Figure (b) is a plot of the EIT resonance full-width at half-max (FWHM) versus w_c/w_p. EIT conditions optimized for $w_c > w_p$ when Ω_c is fixed. For each LG_0^1 mode in (c) and (d), the control power is fixed ($P_c = 0.1$ mW) and the decoherence rate is fixed ($\gamma = 0.01$ MHz). A plot of the (c) the EIT resonance contrast versus ratio of the LG_0^1 mode control waist to the Gaussian probe waist (w_c/w_p). Figure (b) is a plot of the EIT resonance full-width at half-max (FWHM) versus w_c/w_p. EIT conditions optimized for $w_c \approx w_p$ when P_c is fixed.

From equation (2.99), the susceptibility is given by:

$$\chi(r) = \frac{N}{\epsilon_0 \mathcal{E}(r)} d_{13} \left(\rho'_{13}(r)\right)^* = -\frac{N}{\epsilon_0 \hbar} \frac{d_{13}^2 \left(\rho'_{13}(r)\right)^*}{\Omega_{p,13}(r)}. \tag{2.100}$$

Applying Beer's Law to determine the transmitted fraction of the probe laser:

$$T(\Delta_p) = \frac{\int_0^{w_{0,p}} I_{0,p} e^{-\mathrm{OD}(\Delta_p,r)} r\,dr}{\int_0^{w_{0,p}} I_{0,p} r\,dr} = \frac{2}{w_{0,p}^2} \int_0^{w_{0,p}} \exp\left(-\mathrm{Im}\left[\chi(\Delta_p, r)\right] k_p z\right) r\,dr \tag{2.101}$$

where $\mathrm{OD}(\Delta_p, r) = \mathrm{Im}\left[\chi(\Delta_p, r)\right] k_p z$ is the optical density, z is the length of the atomic medium along the propagation direction, Δ_p is included to emphasize the dependence on the probe detuning, and the probe laser intensity, $I_{0,p} \propto \Omega_p^2(r)$. We let $z = 4$ mm, which is the $1/e^2$ diameter of the MOT. We integrate over the region of the EIT interaction, which we take to be a circle with a radius equal to the waist of the probe laser. We do not integrate over all space for the sake of computation time. To the precision of the experiment, we find that integrating over the range $0 \leq r \leq w_{0,p}$ is adequate. We fit equation (2.101) to our data using Ω_{0c}, γ_p, γ_c, Δ_c, and N as fitting parameters.

Figure 2.17 (a) shows a plot of the radial intensity profile of several LG_0^1 mode control laser sizes. Plotted with the LG_0^1 laser modes for comparison, is the Gaussian probe. The resulting transmission spectrum, as determined by equation (2.101) are plotted in figure 2.17 (b). We use the EIT contrast (height with respect to minimum transmission value) and the resonance FWHM as metrics for the quality of the EIT spectrum.

The width of the EIT feature is determined from the model by measuring the full-width at half max (FWHM). Additionally, we determine the contrast of the EIT resonance to be height of the feature using the following relation,

$$h = \frac{T(0) - \min(T(\Delta_p))}{\min(T(\Delta_p))}. \tag{2.102}$$

Figures 2.18 (a) and (b) show the contrast and FWHM respectively for many LG_0^1 sizes (similar to figure 2.18 (a)) while keeping the control Rabi frequency fixed. For these plots, $\Omega_c = \Gamma$ and $\gamma_L = 0.01$ MHz. When keeping the control Rabi frequency fixed while adjusting the size of the control beam, the FWHM maximizes for control waist $w_c \approx w_p$. The FWHM decreases for control waists larger than the probe size ($w_c > w_p$). The physical interpretation of this result is that the FWHM increases with increasing control laser intensity. The region of high control intensity is overlapped with the probe when $w_c = w_p$. The result is broadening of the EIT feature (large FWHM).

The contrast maximizes for a waist corresponding to $w_c \approx w_p$. Our interpretation of this result requires an analysis of the manipulation of the dispersion caused by the spatial variation of the LG_0^1 mode control laser. To understand our results, we consider the inhomogeneous linear dispersion resulting from the spatial variation in intensity caused by the LG_0^1 mode. The index of refraction can be found by taking the real part of the dispersion [43].

$$n = \mathrm{Re}[\tilde{n}] \approx 1 + \frac{1}{2}\mathrm{Re}\left[\chi(\Delta_p, r)\right] \tag{2.103}$$

The LG_0^1 mode control laser manipulates the index of refraction such that the probe beam is optically guided by the control laser through the atomic medium [52]. When the waists of the two beams are approximately equal, then the probe is collimated well.

Figures 2.18 (c) and (d) show the contrast and FWHM respectively for many LG_0^1 sizes (similar to figure 2.18 (a)) while keeping the control power fixed. For these plots, $P_c = 0.1$ mW and $\gamma_L = 0.01$ MHz. When keeping the control power fixed while adjusting the size of the control beam, the FWHM maximizes for control waist $w_c \approx 0.5w_p$. The FWHM decreases for control waists larger than half the probe size ($w_c > 0.5w_p$). The physical interpretation of this result is that the FWHM increases with increasing control laser intensity. The region of high control intensity is overlapped with the probe when $w_c = 0.5w_p$. The result is broadening of the EIT feature (large FWHM). The results for the contrast are are similar to figures 2.18 (a).

We see different results for the FWHM between constant Rabi frequency and constant power. To understand this, we consider the effect of expanding the control laser size while keeping the power fixed. Increasing the size of the LG_0^1 mode control laser has two effects: (1) decreases the peak intensity of the laser and (2) increases the overlap of the darker central region of the LG_0^1 mode with the probe laser. Overall, this decreases the "average" control Rabi frequency experienced by the probe laser, leading to narrower EIT features. This does not occur when keeping the Rabi frequency fixed because this amounts to keeping the intensity fixed. These results are new, and not found in the literature.

2.9 Electromagnetically induced transparency with six levels

We model the experiment using the same density matrix formalism found in section 2.8 [1, 19, 21, 51]. We consider a six level atom with two levels belonging to the hyperfine levels in the ${}^2S_{1/2}$ state, and the remaining four levels belonging to the hyperfine levels in the ${}^2P_{3/2}$ state in rubidium. Figure 2.19 shows these states and identifies the four EIT configurations we model.

The total Hamiltonian for the atom interacting with an electric field is $\widehat{H} = \widehat{H}_0 + \widehat{H}_I$, where the Hamiltonian describing the atomic system is given by:

$$\widehat{H}_0 = \sum_{n=1}^{6} \hbar\omega_n |n\rangle\langle n|, \tag{2.104}$$

where $\hbar\omega_n$ is the energy of the nth level. For each configuration shown in figure 2.19, the Hamiltonian describing the interactions with the electric field can be

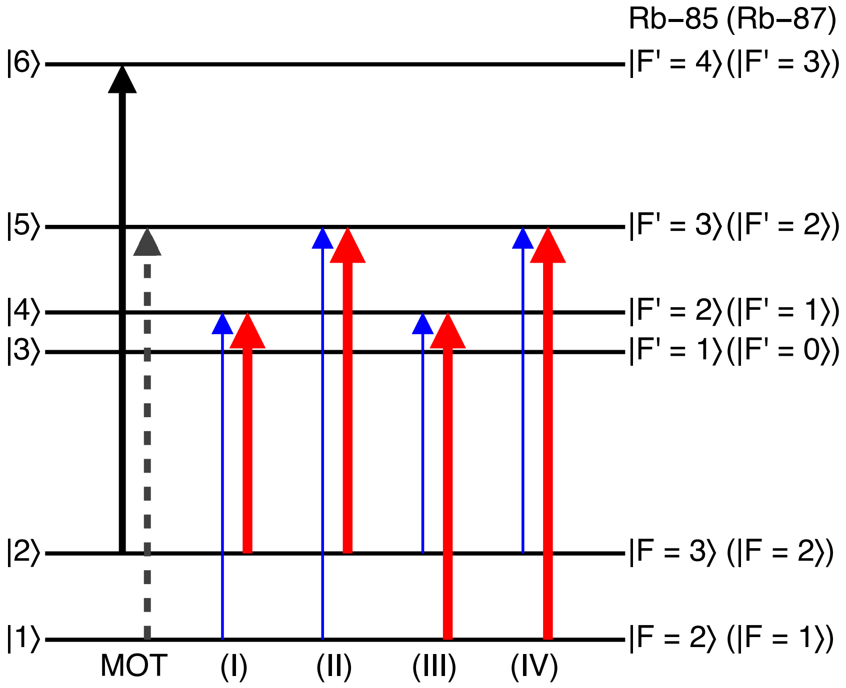

Figure 2.19: The six hyperfine states for the D2 transition in ^{85}Rb (^{87}Rb). The solid black arrow corresponds to the trapping laser, and the gray dashed arrow corresponds to the repumping laser in our magneto-optical trap (MOT). Four EIT configurations on the D2 transition are indicated with Roman numerals. The thin blue arrows represent the probe laser, while the thick red arrows represent the control laser.

	(I)	(II)	(III)	(IV)
i	1	1	2	2
k	2	2	1	1
l	4	5	4	5

Table 2.3: Appropriate indices for our level scheme.

written as:

$$\widehat{H}_I = \hbar\Omega_{c,kl}(r)e^{\mathrm{i}(\omega_c t - k_c z + \ell_c\phi)}|k\rangle\langle l| + \text{h.c.} + \sum_{j=i+2}^{i+4}\left[\hbar\Omega_{p,ij}(r)e^{\mathrm{i}(\omega_p t + k_p z)}|i\rangle\langle j| + \text{h.c.}\right], \tag{2.105}$$

where i and j are the level numbers of the states coupled by the probe laser, and k and l correspond to the level numbers of the states coupled by the control laser. Table 2.3 summarizes the level designations that are fixed for each configuration. The j index is summed over levels for allowed transitions. In equation (2.105), ω_p is the angular frequency and k_p is the wave number of the probe laser. Likewise, ω_c is the angular frequency, k_c is the wave number, and ℓ_c is the azimuthal charge of the control laser. The Rabi frequencies for the probe and control lasers are defined as:

$$\begin{aligned}\Omega_{p,ij}(r) &= -\frac{d_{ij}\mathcal{E}_p(r)}{\hbar},\\ \Omega_{c,kl}(r) &= -\frac{d_{kl}\mathcal{E}_c(r)}{\hbar}.\end{aligned} \tag{2.106}$$

$\mathcal{E}_p(r)$ and $\mathcal{E}_c(r)$ are the possibly spatially dependent amplitudes of the probe and the control lasers [38]:

$$\begin{aligned} &\mathcal{E}_p(r) = \mathcal{E}_{0,p} && \text{Probe in Gaussian mode} \\ &\mathcal{E}_c(r) = \begin{cases} \mathcal{E}_{0,c}\left(\dfrac{\sqrt{2}r}{w_{0,c}}\right) e^{-r^2/w_{0,c}^2} & \text{Control in LG}_0^1 \text{ mode} \\ \\ \mathcal{E}_{0,c} & \text{Control in Gaussian mode} \end{cases} \end{aligned} \tag{2.107}$$

where $\mathcal{E}_{0,p}$ and $\mathcal{E}_{0,c}$ are constants, and $w_{0,c}$ is the waist of the control laser. We define Rabi frequency constants, $\Omega_{0p,ij} = -\dfrac{d_{ij}\mathcal{E}_{0,p}}{\hbar}$ for the probe laser and $\Omega_{0c,kl} = -\dfrac{d_{kl}\mathcal{E}_{0,c}}{\hbar}$ for the control laser. These constants are used to compare different configurations of LG_0^1 and Gaussian control beams to be consistent with refs. [19, 20]. The previous model (section 2.8) incorporated the radial variation of the Gaussian and LG_0^1 modes. For this section, we approximate the Gaussian modes as plane waves for simplicity. To verify the plane-wave approximation for the Gaussian modes, we evaluated our model with the inclusion of the Gaussian spatial variation. To the precision of our experiment, we saw no effect on the calculations.

We use two unitary transformations on both the density matrix operator and the Hamiltonian. We transform into the rotating frame using the following unitary transformation:

$$\widehat{U}_1 = \exp\left[-\mathrm{i}(\omega_p t + k_p z)|i\rangle\langle i| - \mathrm{i}(\omega_c t - k_c z + \ell_c \phi)|k\rangle\langle k|\right]. \tag{2.108}$$

Also, we shift the zero point of the energy to the ground-state hyperfine level indicated by the index, i, using:

$$\widehat{U}_2 = \widehat{I}\exp\left[\mathrm{i}(\omega_p + \omega_i)t\right], \tag{2.109}$$

where $\widehat{I}$ is the identity operator. Applying the rotating wave approximation to the transformed, we arrive at the following full Hamiltonian for our system:

$$\begin{aligned}\widehat{H}' =&(-1)^k\hbar(\Delta_p - \Delta_c)|k\rangle\langle k| - \hbar\Delta_p|l\rangle\langle l| - \sum_{j=i+2,j\neq l}^{i+4}\hbar(\Delta_p + \omega_{li} - \omega_{ji}) \\ &+ \frac{1}{2}\sum_{j=i+2}^{i+4}\hbar\Omega_{p,ij}(|i\rangle\langle j| + |j\rangle\langle i|) + \frac{1}{2}\hbar\Omega_{c,kl}(|k\rangle\langle l| + |l\rangle\langle k|),\end{aligned} \tag{2.110}$$

where $\Delta_p = \omega_p - \omega_{li}$, $\Delta_c = \omega_c - \omega_{lk}$, and $\omega_{mn} = \omega_m - \omega_n$.

The time evolution of the density matrix is governed by the Liouville-von Neumann equation, described in previous sections. The loss operator and the decoherence operator are also described in previous sections. However, we will reproduce these operators here since we have complicated the level structure to six levels. We build the loss operator as follows:

$$\begin{aligned}\widehat{\mathcal{L}} =& \frac{1}{2}\sum_{j=i+2}^{i+3}\Gamma_{ji}\left[2|i\rangle\langle j|\hat{\rho}'|j\rangle\langle i| - |j\rangle\langle j|\hat{\rho}' - \hat{\rho}'|j\rangle\langle j|\right] \\ &+ \frac{1}{2}\sum_{m=4}^{5}\Gamma_{mk}\left[2|k\rangle\langle m|\hat{\rho}'|m\rangle\langle k| - |m\rangle\langle m|\hat{\rho}' - \hat{\rho}'|m\rangle\langle m|\right].\end{aligned} \tag{2.111}$$

The decoherence induced by the finite linewidth of the laser is given by:

$$\widehat{\mathcal{L}}_d = -\sum_{m=1}^{6}\sum_{n=1}^{6}\gamma_{mn}|m\rangle\langle m|\hat{\rho}'|n\rangle\langle n|. \tag{2.112}$$

For the six levels described here, the decoherence rates are defined as:

$$\begin{aligned}&\gamma_{i,i+2} = \gamma_{i+2,i} = \gamma_{i,i+3} = \gamma_{i+3,i} = \gamma_{i,i+4} = \gamma_{i+4,i} = \gamma_p, \\ &\gamma_{kl} = \gamma_{lk} = \gamma_c, \\ &\gamma_{12} = \gamma_{21} = \gamma_p + \gamma_c.\end{aligned} \tag{2.113}$$

All other dephasing rates are zero due to electric dipole selection rules.

We make the assumption that the system is in steady state, and that the probe laser is significantly weaker than the control laser. In this approximation, the density matrix elements ($\rho'_{nm} = \langle n|\hat{\rho}'|m\rangle$) simplify: $\rho'_{ii} \approx 1$, $\rho'_{nn} = 0$ for $n \neq i$, and $\rho'_{n,n+1} = \rho'_{n+1,n} = 0$ for $n = 1 \ldots 5$. Applying these assumptions and solving for the off-diagonal density matrix elements associated with the three dipole-allowed transitions for the probe gives:

$$\begin{aligned}
\rho'_{il}(r) &= \frac{\frac{1}{2}\Omega_{p,il}(r)\left(\Delta_p - \Delta_c - \mathrm{i}(\gamma_p+\gamma_c)\right)}{\left(\Delta_p - \frac{\mathrm{i}}{2}(\Gamma_{li}+\Gamma_{lk}+2\gamma_p)\right)\left(\Delta_p - \Delta_c - \mathrm{i}(\gamma_p+\gamma_c)\right) - \frac{1}{4}\Omega^2_{c,kl}(r)}, \text{ and} \\
\rho'_{ij}(r) &= \frac{\frac{1}{2}\Omega_{p,ij}(r)}{\Delta_p + \omega_{li} - \omega_{ji} - \frac{\mathrm{i}}{2}(\Gamma_{ji}+2\gamma_p)}, \text{ for } j = i+2\ldots i+4 \text{ and } j \neq l.
\end{aligned} \tag{2.114}$$

As a demonstration of the model, theoretical spectra for configuration (I) are shown for ^{85}Rb in figure 2.20 (a) and for ^{87}Rb in figure 2.20 (b). The dashed blue curve is a theoretical spectrum when the control laser is in the LG_0^1 mode, and the solid red curve is a theoretical spectrum when the control laser is in the Gaussian mode. For all curves, we assume the control Rabi frequency constant to be $\Omega_{0c,kl} = 20$ MHz, the control laser linewidth to be $\gamma_c = 1$ MHz, the probe laser linewidth to be $\gamma_p = 0.1$ MHz, the number density to be $N = 5 \times 10^{10}$ cm^{-3}, and the control laser detuning to be $\Delta_c = 0$. Our model agrees with previous results [20] that for control lasers with equal $\Omega_{0c,kl}$, EIT involving a control laser in the LG_0^1 mode results in a narrowing of the resonance feature. The density matrix elements, $\rho'_{ij}(r)$, corresponding to $j \neq l$ behave like two-level transitions. However, the presence of the strong control laser that couples state $|k\rangle$ to state $|l\rangle$ leads to an EIT feature in the density matrix element $\rho'_{il}(r)$. Mathematically, this comes from the Rabi frequency term, $\Omega_{c,kl}(r)$, that appears in the expression for ρ'_{il} in equation (2.114). Our physical interpretation is that the r-dependence of the

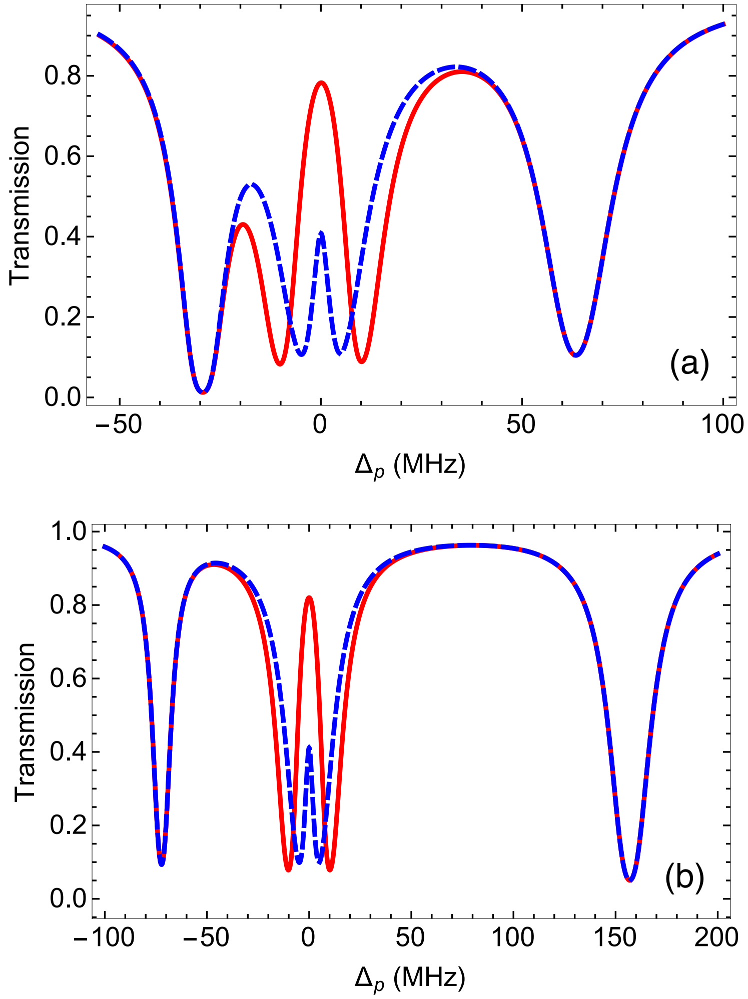

Figure 2.20: Theoretical curves of the transmission of the probe laser for configuration (I) EIT in (a) ^{85}Rb and (b) ^{87}Rb. The solid red curve indicates the control laser is in a Gaussian mode, and the dashed blue curve indicates the control laser in an LG_0^1 mode. In both scenarios, the control Rabi frequency is the same ($\Omega_{0c,kl} = 20$ MHz). The linewidth of the control laser is assumed to be $\gamma_c = 1$ MHz, the linewidth of the probe laser is set $\gamma_p = 0.1$ MHz, the number density is set to $N = 5 \times 10^{10}$ cm^{-3}, and the detuning of the control laser is set to $\Delta_c = 0$. The probe waist is $w_{0,p} = 430$ μm, and the control waist is $w_{0,c} = 270$ μm when in the LG_0^1 mode. The control field is a plane-wave otherwise. Due to the spatial dependence of a LG_0^1 mode laser, the model predicts that the EIT resonance with the same $\Omega_{0c,kl}$ is narrower for a control laser in the LG_0^1 mode than for a control laser in the Gaussian mode.

density matrix results from the spatial variation of the Rabi frequency. However, for our system, this dependence is only relevant in the cases involving a control in the LG_0^1 mode.

The induced electric dipole moment caused by a weak probe incident on an ensemble of atoms with six levels is given by:

$$p(r) = N \sum_{j=i+2}^{i+4} d_{ij} \left(\rho'_{ij}(r)\right)^* = \epsilon_0 \chi(r) \mathcal{E}_p(r), \tag{2.115}$$

From equation (2.115), the susceptibility is given by:

$$\chi(r) = \frac{N}{\epsilon_0 \mathcal{E}(r)} \sum_{j=i+2}^{i+4} d_{ij} \left(\rho'_{ij}(r)\right)^* = -\frac{N}{\epsilon_0 \hbar} \sum_{j=i+2}^{i+4} \frac{d_{ij}^2 \left(\rho'_{ij}(r)\right)^*}{\Omega_{p,ij}(r)}. \tag{2.116}$$

The imaginary part of the susceptibility describes the absorption of the laser passing through the medium. Applying Beer's Law to determine the transmitted fraction of the probe laser:

$$T = \frac{\int_0^{w_{0,p}} I_{0,p} e^{-\text{OD}(r)} r \, dr}{\int_0^{w_{0,p}} I_{0,p} r \, dr} = \frac{2}{w_{0,p}^2} \int_0^{w_{0,p}} \exp\left(-\text{Im}\left[\chi(r)\right] k_p z\right) r \, dr, \tag{2.117}$$

We fit equation (3.3) to our data using $\Omega_{0c,kl}$, γ_p, γ_c, Δ_c, and N as fitting parameters. The width of the EIT feature is determined from the model by measuring the full-width at half max (FWHM). This theoretical analysis resulted in a publication, found in reference [53].

2.10 Probe propagation under electromagnetically induced transparency conditions

Thus far, we have looked at the collective probe response to a probe passing through a sample of ultracold atoms under conditions of EIT. That is, the predicted results integrate over all the spatial features of the probe and control lasers. In this section, we will examine the spatial distribution of the probe transmission through the atomic medium under EIT conditions. It is not necessary to derive the associated density matrix elements for the probe transitions, as they have been formulated in the previous sections. For this section, we will assume that the atomic response is described by a three level, four level, or six level atom. Using a semi-classical model, the susceptibility is given by [43]:

$$\chi(r) = -\frac{N}{\epsilon_0 \hbar} \sum_{j=k}^{l} \frac{d_{ij}^2 \left(\rho'_{ij}(r)\right)^*}{\Omega_{p,ij}(r)}. \tag{2.118}$$

where the indices i, k, and l are adjusted to depending on the number of levels describing our atom.

$$
\begin{aligned}
i &= \begin{cases} 1, & \text{three levels} \\ 1, & \text{four levels} \\ i, & \text{six levels} \end{cases} \\
k &= \begin{cases} 3, & \text{three levels} \\ 3, & \text{four levels} \\ i+2, & \text{six levels} \end{cases} \qquad (2.119) \\
l &= \begin{cases} 3, & \text{three levels} \\ 3, & \text{four levels} \\ i+4, & \text{six levels} \end{cases}
\end{aligned}
$$

where table 2.3 describes the indices for the six level atom. The imaginary part of the susceptibility describes the absorption of the laser passing through the medium. Similar to the previous sections, we will apply Beer's Law to determine the transmitted fraction of the probe laser. In this section, we will *not* integrate over space. Rather, we will leave the position dependence.

$$I_{p,\text{out}}(r) = I_{p,\text{in}}(r)e^{-\text{OD}(r)}. \qquad (2.120)$$

Figure 2.21: A theoretical prediction for the output profile of the probe laser. The probe is initially in the Gaussian mode. An LG_0^1 mode control laser modifies the susceptibility of the atomic medium such that probe transmission occurs in regions of high control intensity, and probe absorption occurs in region of low control intensity. The result is a mapping of the LG_0^1 profile onto the probe laser.

As an exercise, we will apply Configuration (I) in the six level model to generate the figure 2.21. We let $z = 4$ mm, which is the $1/e^2$ diameter of the MOT. For the case of this study, we assume the probe laser has a Gaussian intensity profile, and the control laser is in the LG_p^ℓ laser mode. The probe waist is set to $w_p = 430$ μm and the control waist is set to $w_c = 270$ μm. The control Rabi frequency is defined as $\Omega_{0c,32} = 20$ MHz, the dephasing from the control laser is $\gamma_c = 1$ MHz, the dephasing from the probe laser is $\gamma_p = 0.1$ MHz, and the atomic density is $N = 5 \times 10^{10}$ cm^{-3}. Both laser fields are tuned to the resonance ($\Delta_p = \Delta_c = 0$).

Figure 2.21 shows a theoretical prediction for the transmission of the probe laser for the six level model of ^{85}Rb. We have chosen configuration (I) from figure 2.19. The probe transmission is highest in regions of high control intensity. Since the control laser is in the LG_0^1 mode, the probe transmission appears as a donut. These theoretical results are new, and do not appear in the literature (to the best of our knowledge).

Chapter 3

Experiment

3.1 Introduction

Electromagnetically induced transparency is performed in an ultracold gas of rubidium atoms. Many of the experimental techniques used to create ultracold atoms are standard, and are routinely used in atomic, molecular, and optical (AMO) laboratories. This chapter will detail the application of these techniques to our experiment.

In section 3.2, the construction and various components of the vacuum system will be explored. Section 3.3 will discuss the lasers we employ to cool, trap, manipulate, and probe an ensemble of atoms. Section 3.4 describes the optics we use to convert laser fundamental modes to the Laguerre-Gaussian (LG_p^ℓ) mode. In section 3.5 characterizes the magneto-optical trap (MOT). Section 3.6 will discuss the techniques uses to probe and characterize our trapped atoms. Finally, section 3.7 will describe each instrument used to measure EIT in an ultracold gas, and we will describe how we interface with all our instruments to control the experiment.

3.2 Vacuum system

Our vacuum chamber is designed for an ultracold rubidium experiment. Figure 3.1 shows a schematic of the chamber. There are two main chambers ("source chamber" and a "science chamber") connected by a slower tube and glass cell, which gives us optical access to the atoms. The source chamber contains an ampule of solid rubidium. Due to the low pressures inside the chamber, the room temperature rubidium atoms sublime off the surface. During normal operation, the source chamber is typically maintained at a pressure of 10^{-8} Torr using a 60 L/s sputter-ion pump. The atoms, through a random walk, find their way to the glass cell. Here, they are slowed and confined by a magneto-optical trap (MOT). Connected on the other end of the glass cell, the science chamber typically operates at a pressure of 10^{-10} Torr using a 30 L/s sputter-ion pump in conjunction with rubidium getter strips resting at the bottom of the science chamber. An ion gauge is connected to the top of the science chamber to monitor the pressure of the chamber.

In this section, we describe each of the vacuum components used to construct the chamber. We will detail the procedure used to clean and prepare the components to create ultrahigh vacuum (UHV). Finally, we will describe how to assemble the pieces, and pump the system to UHV.

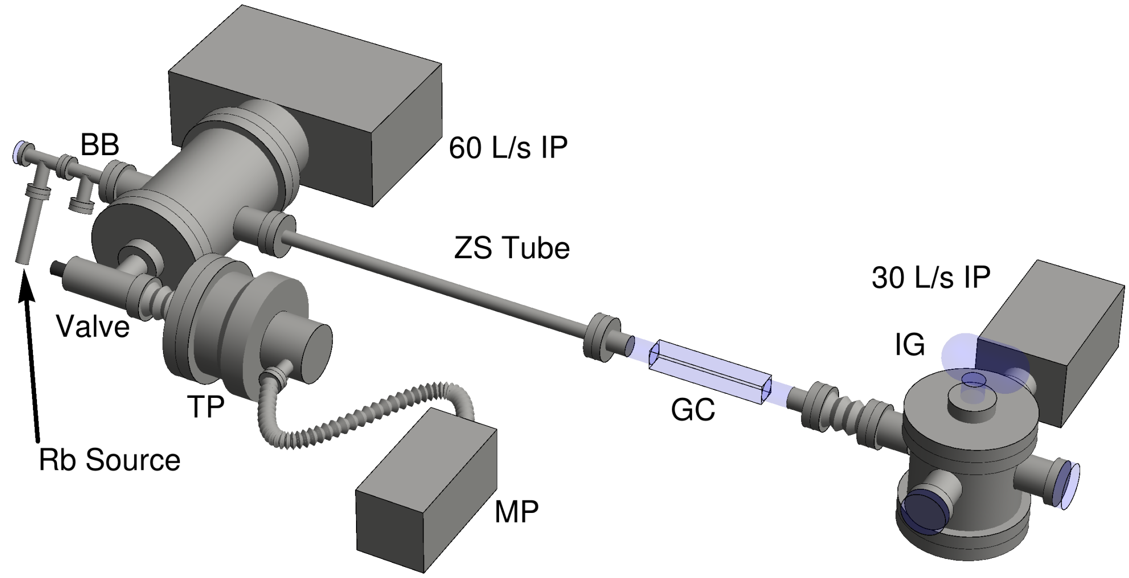

Figure 3.1: A representation of the vacuum chamber used to routinely produce ultracold ensemble of ^{85}Rb and ^{87}Rb. A rubidium ampule serves as our atomic source, and a steel ball can slide into the bath of the atomic beam to serve as a beam block (BB). The source chamber vacuum is maintained by a 60 L/s sputter-ion pump (IP). The rubidium atoms diffuse down the Zeeman slower (ZS) tube to the rectangular glass cell (GC), where the atoms are slowed and trapped by a magneto-optical trap. The "science chamber" pressure is maintained by a 30 L/s IP and rubidium getters. An ion gauge (IG) monitors the vacuum pressure. A valve can be opened during a "bake-out" of the chamber, where a mechanical pump (MP) backs a turbomolecular pump (TP), which pumps on the vacuum system. The valve is closed after "bake-out", and the TP an MP are removed from the system to reduce vibrations.

3.2.1 Vacuum chamber, flanges, and components

Our vacuum chambers, flanges, tubes, and gaskets are purchased from MDC MFC, Inc. and the Kurt J. Lesker Company. We use stainless steel conflat chambers that accommodate 1-1/3 inch, 2-3/4 inch, and 6 inch outer diameter flanges. When a flange or tube must be joined to each other or a chamber, we use copper gaskets. Copper gaskets can withstand higher temperatures (chamber baking) and can sustain a lower vacuum pressure [54].

The source chamber has four ports: two 2-3/4 inch ports and two 6 inch ports. Connected to one six inch port is a 6 inch to 2-3/4 inch converter flange, on which a valve is attached. The other 6 inch port is connected to a 60 L/s sputter-ion pump. One of the 2-3/4 inch ports is connected to a 2-3/4 to 1-1/3 inch converter flange, to which the rubidium source is attached. The rubidium source is an ampule manufactured by Alfa Aesar, a Johnson Matthey Company. It rests in a crushable steel tube, that can be compressed by a pair of pliers to break the ampule, exposing the rubidium to the chamber (see figure 3.2). Attached to the other 2-3/4 inch port is the Zeeman slower (ZS) tube, which leads to the science portion of the experiment.

The ZS tube has an outer diameter of 3/4 inch, and is connected to the glass cell with a 2-3/4 inch conflat flange. The glass cell is rectangular with dimensions of $1.4 \times 1.4 \times 11$ inch. The cell offers a great amount of optical access to the cham-

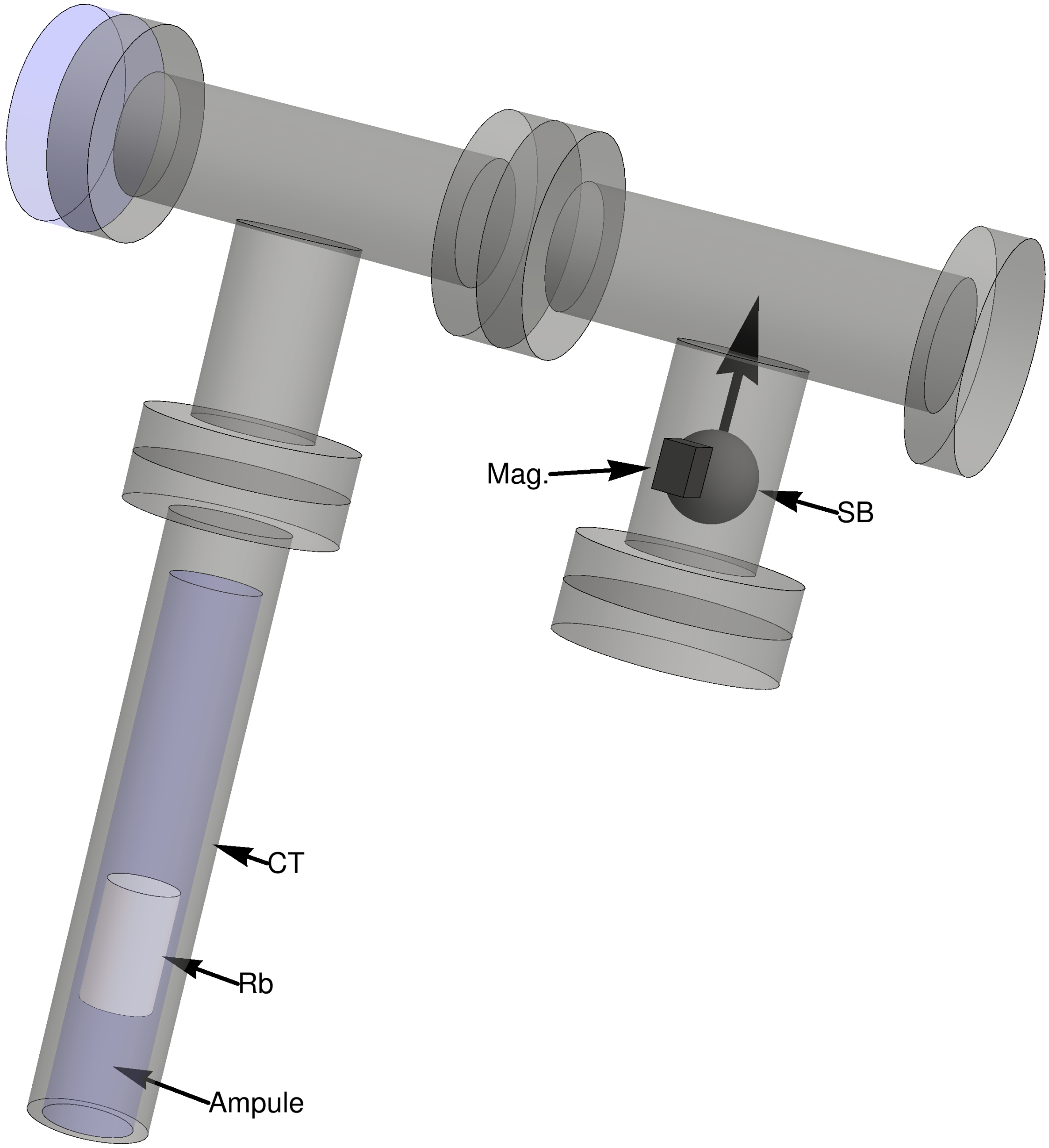

Figure 3.2: The rubidium source used in our experiment. A rubidium chunk (Rb) is sealed within a glass ampule. This ampule is placed inside a steel "crushable tube" (CT). The rubidium can be exposed to the vacuum by applying careful pressure to the CT with a pair of pliers. The resulting atomic beam can be blocked/unblocked by sliding a steel ball (SB) up/down the tube using a magnet (Mag.).

ber. However, it is not coated with an anti-reflection film. Therefore, we loose $\approx 4\%$ of the laser intensity off each surface due to reflections. The rectangular cell is connected to the "science chamber".

The science chamber is a 6 port chamber: four 2-3/4 inch ports cross in the horizontal plane, and two 6 inch ports are at the top and the bottom of chamber. The bottom port is connected to a blank 6 inch flange, in which a Rb getter is coiled at the bottom. The getter is only activated during the bake-out of the chamber. The top port is connected to a 6 inch to 2-3/4 inch converter flange, in which an ionization gauge is attached. The glass cell is attached to one of the 2-3/4 inch port. A 30 L/s sputter-ion pump is attached to another 2-3/4 port. Two windows are attached to the last two 2-3/4 inch ports: one opposite the rectangular cell to allow optical access for the ZS, and the other is positioned opposite the sputter-ion pump.

3.2.2 Cleaning procedure

While cleaning the conflat vacuum surfaces, it is important to avoid transferring the contaminants from the environment, and (most importantly) from one's hands to the vacuum pieces. Introducing pollutants (such as a single finger print) can be detrimental to a vacuum system. These oils will outgas over long time scales. Special gloves, aluminum foil, and rigorous cleaning steps are valuable tools used to combat the imposing environment. In particular, there are two sets of gloves to be worn in the process described below. These are the “Diamond Gloves” and the “Green Gloves”. However, while these gloves reduce the transfer of oil from skin to conflat surface, they still do not contain the necessary cleanliness required for UHV. Therefore, avoid touching all surfaces that will be exposed to the vacuum (even when hands are gloved).

While cleaning, one may find that certain regions in the conflat pieces are too confined to reach with one’s own extremities. Additional instruments such as tweezers, metal rods, *etc.* can be of some use. Therefore, all instruments used to clean and/or handle the conflat pieces should be as clean, if not cleaner than the conflat pieces themselves.

Prior to starting the cleaning process, it is necessary to establish a clean working space next to the area where the cleaning is taking place (*i.e.* next to the sink), as well as setting-up a clear space in the region of chamber construction. The former station ensures that the pieces stay clean while transitioning from step-to-step. Here, it is only necessary to clean a table top and cover it with clean tissue (such as Kim-wipes). The later working space guarantees a safe spot for the conflat pieces at the completion of the cleaning process, and it allows for easy access to the conflat pieces during construction of the chamber. Near the chamber, the “High-Vacuum Aluminum Foil” (purchased from All Foils, Inc.) is required to meet the clean criteria. Therefore, all surfaces that the conflat pieces are to rest on should be as clean, if not cleaner than the conflat pieces themselves.

Finally, let us bring special attention to the so called “knife edge” on each conflat piece. To understand the importance of preserving the knife edge, let us foreshadow a bit to how the vacuum is created. During the construction of the chamber, a copper gasket is sandwiched between two conflat pieces. The two pieces are procedurally brought together such that the knife edges cut into the gasket. This seals-off the atmosphere from the chamber. Naturally, any imperfections (dings, knicks, *etc.*) can lead to leaks in the system. Therefore, take special care to avoid impacting the knife edge, and avoid resting the conflat piece on the knife edge.

As a suggestive note before we begin with the list of steps, it is most efficient to apply one step to *every* conflat piece before moving on to the next step. Take special care to clean the knife edge while completing the steps below.

Rough cleaning and degreasing

When performing the first cleaning and degreasing of the vacuum components, wear green gloves. Lay-out clean paper towels on a clean table surface. Sprinkle soap into a tub, and fill with the tub with warm water. A clean cloth or sponge should be used throughout this step. Use Orange Glow as the degreasing agent. After using Orange Glow, wash with the soapy water. Rinse the component with tap water, then rinse with pure water (deionized water). Place conflat pieces on paper towels.

We remove the rest of the oils by submerging the components in a sonicator with a strong soap/detergent. The sonicator applies high-frequency mechanical oscillations to the bath. To prevent damage, it is important to prevent the components from resting against the sides and bottom of the bath. The parts are thus suspended in the bath. Not all parts can be sonicated. These components include those with lubricants (right angle valve), pumps, and gauges. We must degrease these components by hand.

Methanol and acetone pre-wash

The next cleaning stage uses organic solvents. Wear the Diamond Gloves (this pair of gloves is sufficient throughout the remainder of the procedure). Lay-out a new layer of paper towels. On top of the layer of paper towels, create a layer of Kim-wipes. Chemwipes should be used to wash the conflat pieces throughout this step, paying special attention to the knife edges. Apply Optima grade Methanol to Chemtronics wipes, and wash each piece. Apply Optima grade Acetone to Chemtronics wipes, and wash each piece. Place finished conflat pieces on a Kim-wipe layer.

Final methanol and acetone wash

The final cleaning stage involves a rinse of each of the components using the organic solvents. Lay-out a clean piece of High-Vacuum Aluminum Foil in the region of

Chamber Construction. Rinse each piece with Optima grade Methanol by spraying the Methanol directly onto the pieces. Rinse each piece with Optima grade Acetone by spraying the Acetone directly onto the pieces. Place finished conflat pieces on High-Vacuum Aluminum Foil. These pieces are now ready for assembly.

3.2.3 Chamber assembly

Now that we have clean conflat pieces that meet UHV quality, it is time to construct the chamber. Use copper gaskets and silver plated bolts to attach individual conflat pieces. The copper gasket only creates an adequate seal if the knife edge is unblemished, and if the two components cutting into gasket are brought together evenly. The chamber is constructed one joint at a time until the entire chamber is assembled. The following steps should aid in assembling the conflat pieces.

- Obtain the proper copper gasket and silver coated screws.
- Using the Chemtronics wipes, wipe the knife edge and surface exposed to the vacuum with Methanol. Pay special attention to the knife edge.
- Using the Chemtronics wipes, wipe the knife edge and surface exposed to the vacuum with Acetone. Pay special attention to the knife edge.
- Using the Chemtronics wipes, clean the entire copper gasket with Methanol.
- Using the Chemtronics wipes, clean the entire copper gasket with Acetone.

- Place the copper gasket on the knife edge of the most stable conflat component (there is a groove that this slips into).

- Bring the second conflat component such that it lies on the opposite side of the copper gasket.

- Insert the screws with washers through the holes in the conflat components, and finger tighten using the platenuts.

- Make sure all the screws are flush.

- Apply a constant torque to the screws using the appropriate sized wrench (this torque should be applied through an angle subtending about $\pi/4$ radians). Be aware of the resistance from an oxidized screw that may hinder one's judgment for constant torque application. To ensure that the components are brought together evenly, alternate screws such that the two pieces are brought together evenly.

- Repeat the previous step until the copper gasket is no longer visible when the observer peers down the joint between the two components.

- Warning: If one side of the joint is sealed completely, but another has some copper peaking through, then the system is most likely compromised. Such an observation implies that the two components were not joined evenly. The problem may be rectified if the remaining gap can be closed with torque from the wrench acting through $\pi/4$ rotation. However, if this does not seal the joint, then one must re-do the entire process with a new gasket for this particular joint.

- Repeat all above steps until the chamber is assembled.

3.2.4 Pumps

Vacuum pumps are crucial to maintaining an UHV. The order in which various pumps are applied to the system is crucial. This subsection will describe the types of pumps used on this system. We use three types of pumps: mechanical pump, turbomolecular pump, and sputter-ion pump. Figure 3.3 summarizes the pressure range of each pump.

A rotary vane mechanical pump is an oil-sealed pump (the oil provides an air-tight seal and provides lubrication as well). Gas enters the pump, is compressed by a rotor and vane, and is expelled to the atmosphere [54]. These pumps are dirty, and require precaution and routine maintenance. If the mechanical pump looses power (such as a "black-out"), then the fluid can be forced back into the chamber. Such an occurrence requires the disassembly of the system, followed by a repeat of the cleaning and assembly procedures. Overtime, dirt and debris from the rotary vane collects in the oil, and the ultimate pumping pressure increases. The oil must be replaced when it becomes too dirty. The mechanical pump used on our system is a Varian DS 102 dual stage rotary vane vacuum pump. The ultimate total pressure of mechanical pump is 10^{-3} Torr, and has a free air displacement of 1.7 L/s. Our mechanical pump serves as a roughing pump, and it also backs our turbomolecular pump.

The turbomolecular pump operates with a set of turbine fans that spin at 56,000 rotations per minute (RPM). The gas is compressed through momentum transfer from the rapidly rotating turbines to the gas molecules [54]. We use a Varian Turbo V-250 pump on our system, connected at the valve (see figure 3.1). The flow rate is 250 L/s, with an ultimate pressure of 10^{-11} Torr. If the inlet pressure or backing pressure is too high, then the turbomolecular pump will overheat. The pump should not be operated at a chamber pressure higher than 2×10^{-3} Torr if backed by a mechanical pump. Reaching the lower pressure limit is dependent upon the backing pressure on the outlet of the pump. To minimize vibrational noise in our experiment, this pump is only operated during bake-out. At the end of the bake-out of the chamber, the valve is closed and the turbomolecular pump is turned-off while the sputter-ion pumps operate to maintain UHV.

The sputter-ion pump is ideal for our experiment. It has no moving parts (no vibrations), the pump does not use fluids or organic contaminants, and it can pump to UHV regimes [54]. The sputter-ion pump generates high-energy electrons using a high-voltage across an anode and a cathode. The electrons are confined in a quadrupole electric field, and a homogeneous magnetic field forces the electrons into circular paths, maximizing the path length of high-energy electrons (the so-

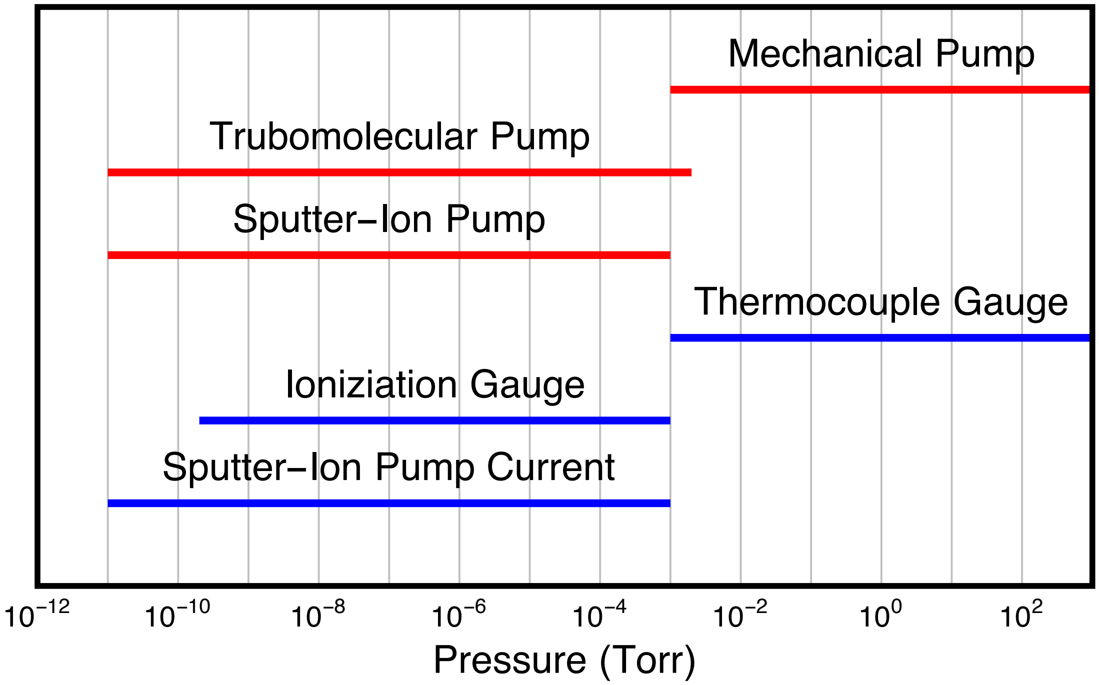

Figure 3.3: The operational ranges of our pumps (red lines), and our gauges (blue lines).

called Penning trap). This increases the probability that a gas molecule entering the pump will become ionized from collisions with the electrons. Ionized particles are more reactive than neutral particles to the surfaces of the pump (typically titanium). Therefore, any particle that enters the pump is removed from the vacuum system. We use two sputter-ion pumps manufactured by Varian, Inc.: a pump with a rate of 30 L/s is attached to the science chamber, and a pump with a rate of 60 L/s is attached to the source chamber. The operating range of our sputter-ion pumps is 10^{-11} Torr to 10^{-3} Torr.

3.2.5 Gauges

To measure the pressure, we use three methods: thermocouple gauge, ionization gauge, and the pump current measured from the sputter ion pump. Each of these gauges operate over limited ranges. In combination, we can measure the pressure over most of the range of our system.

The thermocouple gauge measures the pressure of gas by measuring the amount of heat transferred to a gas. As the gas pressure decreases inside the vacuum chamber, so too does the rate of heat transfer. The gauge heats a wire by passing current through the wire. The wire is exposed to the vacuum chamber, and is thus transferring heat from the wire to the gas. A thermistor is used to measure the temperature of the wire, and a controller monitors the heat transferred and, therefore, the pressure of the gas. While these gauges are robust and fast, they are not very accurate as they depend on the thermal properties of the gas in the chamber [54]. We use Varian Type 0531 thermocouples on our system. The range in which these thermocouples can operate is 1×10^{-3} Torr to 2 Torr. We typically use thermocouple gauges at early stages of pumping (when the pressure is relatively high).

As the pressure in our chamber decreases, we engage the ionization gauge. Ionization gauges operate in the high and UHV range. In this regime, the low particle density can be determined by ionizing the gas molecules surrounding the

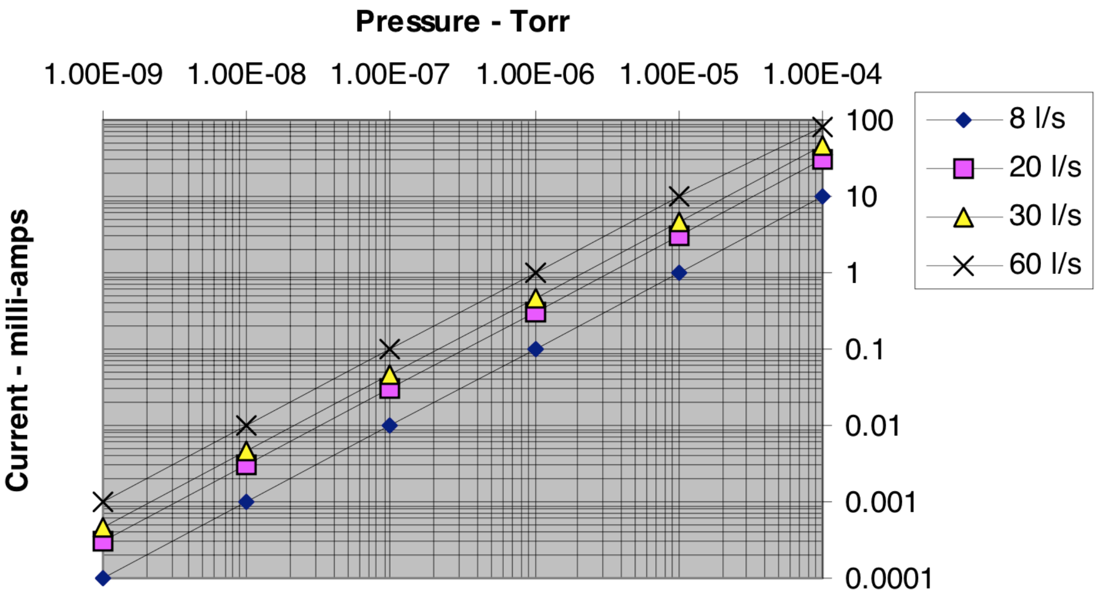

Figure 3.4: A plot provided by Varian, Inc. used to convert a measurement of the pump current to gas pressure inside the vacuum system. Four curves are given. Our system employs two pumps only. We use the data for the 30 L/s pump (yellow triangles) and the 60 L/s pump (black "x's").

gauge with high energy electrons. The positively ionized molecules collected on an "ion collector" (usually held at ground or biased with negative voltage). Measuring the number of ions collected is directly related to the number density of the gas. If the temperature is constant, then the measurement is one of pressure [54]. We have one ionization gauge mounted on the science chamber. It is manufactured by MDC Vacuum Products, LLC. The style of ionization gauge is a glass envelope ionization gauge tube. The range for which it can measure gas pressure is 1×10^{-3} Torr to 2×10^{-10} Torr. When the ionization gauge is allowed to come into contact with high pressure gasses, the filament wires often become contaminated. Before measuring the pressure, one must outgas the gauge for 15-20 minutes [54]. During normal operation of the experiment, we do not operate the ionization gauge (this is to preserve its lifetime). Instead, we monitor the pressure of the system using the pump current measured by the sputter-ion pumps on both the source and science chambers.

The controller for the sputter-ion pump (Varian MiniVac Controller) monitors the pump current. The current is reported as a voltage dropped across a component with the relationship, 1 V = 1 mA. One can measure the output voltage, and consulting figure 3.4, determine the pressure of the chamber. The pressure range for which the sputter-ion can record the pressure is the same as the operational range of the sputter-ion pump itself.

3.2.6 Vacuum baking

Despite our careful cleaning and construction procedure, particles are inevitably bonded to the surfaces of the chamber, where they will limit our pressure by continuously outgassing. To successfully get to the UHV regime, we bake the chamber to high temperatures to remove most of these particles from the chamber walls, while pumping the particles out of the system.

Once the vacuum pieces are assembled, we make a conflat connection between the turbomolecular pump to the valve. The mechanical pump is attached to the outlet of the turbomolecular pump using a KF-25 connection. We first begin the baking of the chamber by preparing the heating elements. We use heating tape (Omegalux STH-101-060) powered by variable transformers to heat the chamber. Fist, we wrap the entire chamber in aluminum foil, taking great care not to allow the foil to come into contact with glass surfaces (the aluminum foil can scratch the glass). Thermistors are placed in contact with the chamber at strategic points to monitor the temperature of the chamber. Next, we uniformly wrap the chamber with the heating tape, taking care not to overlap any of the wrappings (this can overheat points of the chamber). We then wrap a second layer of aluminum foil around the heating tape. Finally, the entire chamber is insulated with fiberglass wrapped in a third layer of aluminum foil. Layering in this fashion ensures even heating of the chamber. For most regions of the chamber, we slowly heat the

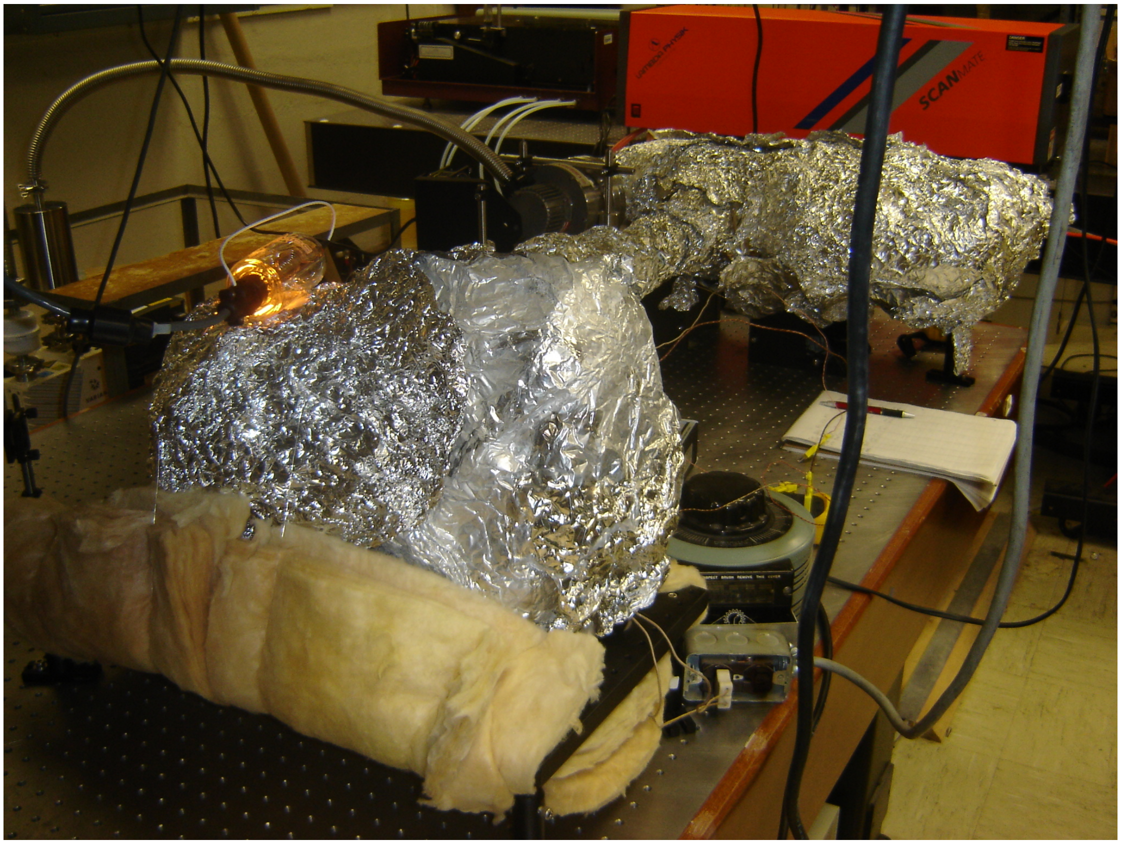

Figure 3.5: A photograph of the vacuum system during vacuum baking. The chamber is wrapped with (starting at the chamber exterior and working outward) aluminum foil, heating tape, aluminum foil, fiberglass insulation, and aluminum foil. The turbomolecular pump (backed by the mechanical pump) is pumping out the outgassed particles. The ion gauge (glowing device in the foreground) monitors the pressure.

chamber to a temperature of ≈ 250°C. While steel can be heated to 300°C, the sputter-ion pump magnets cannot be heated to that temperature. We must be careful to avoid heating the inlet to the turbomolecular pump; we keep the inlet below 120°C to protect the turbomolecular pump. Figure 3.5 is a picture of our vacuum chamber prepared for baking.

Prior to baking, we start the mechanical pump to rough-out the chamber (the turbomolecular pump is off). We attach a thermocouple gauge to the outlet of the turbomolecular pump to monitor the pressure. When the pressure falls below range of the thermocouple (10^{-3} Torr), we begin the spin-up cycle of the turbomolecular pump. We also turn-on the ionization gauge, to monitor the pressure. The variational transformers are turned-on, and the power is increased in small increments over time to prevent damage to the windows and chamber joints. Figure 3.6 (a) is a plot of the chamber temperature as measured for the first couple days for a typical bake-out. Figure 3.6 (b) is a plot of the chamber pressure as measured for the first couple days for a typical baking-out. The initial increase in temperature results in an increase in the outgassing molecules bonded to the chamber. This results in a spike the pressure. As the turbomolecular pump removes these particles from the chamber, the pressure decreases.

The turbomolecular pump (backed by the mechanical pump) operate on the chamber for several days to remove most of the outgassed molecules. Then, the sputter-ion pumps are turned-on, and all pumps operate on the chamber until the

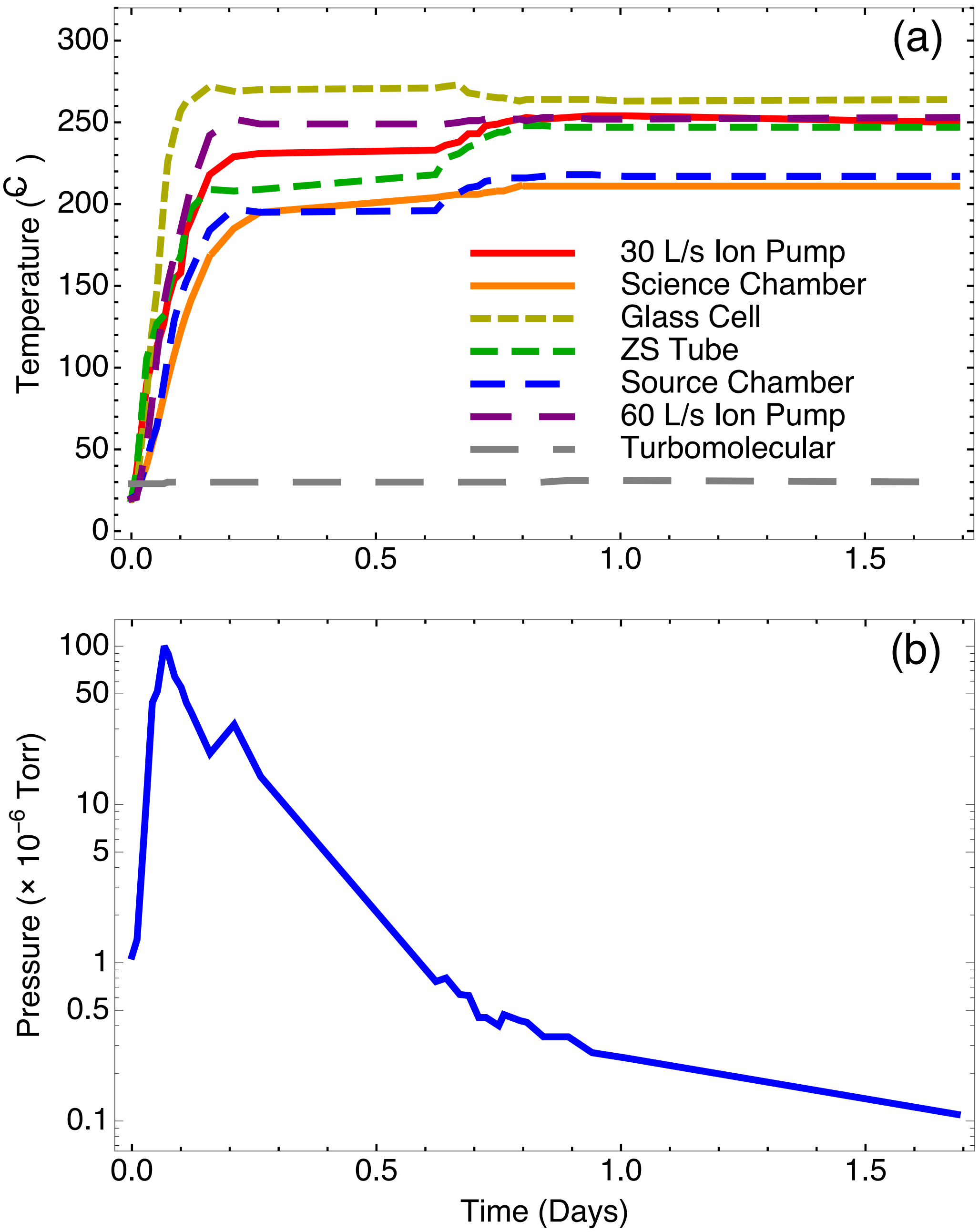

Figure 3.6: (a) Monitored chamber temperature vs. number of days for the first couple days of a typical bake-out. (b) The corresponding pressure of the chamber vs. number of days for the first couple days of a typical bake-out.

pressure reaches 10^{-9} Torr. At this point, the variational transformers are slowly turned-off over the course of hours. As the chamber cools, the pressure typically drops to a pressure of 10^{-11} Torr to 10^{-10} Torr. At this point, we seal the valve connected to the turbomolecular pump. When properly sealed, the turbomolecular pump (backed by the mechanical pump) is no longer pumping on the chamber. The turbomolecular pump is then powered down. When the turbines slow sufficiently ($<$ 1000 RPM), the mechanical pump can then be powered down.

3.3 Laser system

All transitions involved in our experiment (trapping, cooling, optical pumping, and EIT) are on the D2 line in both ^{85}Rb and ^{87}Rb isotopes. The D2 transition corresponds to a laser wavelength, $\lambda_L \approx 780$ nm. Our lab uses two types of lasers to produce 780 nm coherent light. Primarily, we use low power laser diodes (which are relatively inexpensive), but require some work to improve their spectral quality for atomic physics. Additionally, our lab operates a Titanium-Sapphire (Ti:S). However, the Ti:S laser is not used in the EIT experiment. We use diode lasers for all experiments in this dissertation. This section will describe the construction, stabilization, and amplification of diode lasers.

3.3.1 External cavity diode laser

External cavity diode lasers (ECDL) have been used in atomic physics experiments for decades [55]. An injection current is delivered to the active region located between n- and p-type cladding layers of a diode. Electrons are excited into the conduction band of the semi-conductor, creating a whole in the valence band. The emitted light from the re-combination of the electron-whole pair is dependent upon the band gap of semi-conductor material, but is typically much broader than atomic transitions. For rubidium, we use diodes constructed with GaAlAs layers. The spectrum of the laser diode is very broad ($\sim$ 10 nm). An external cavity can tighten the line width to $\leq$ 1 MHz)

We have two ECDL designs in operation. The "old-laser" design involves a combination of commercially- and home-built components (see figure 3.7 (a)). A Sharp GH0781JA2C laser diode is inserted into a Thorlabs LDM21 laser mount. The laser mount accepts an injection current from a Thorlabs LDC500 diode driver. Additionally, a Wavelength Electronics PTC 2500 controller stabilizes the temperature of the laser diode. We construct the external cavity using blazed 1200 lines/mm ruled diffraction grating mirrors (GR13-1205) specified for 500 nm. The grating is aligned to the Littrow angle: an alignment such that the incidence angle of the laser diode output and the first diffraction order angle are identical [55]. The diffracted order is retro-reflected back to the laser diode while the output of the

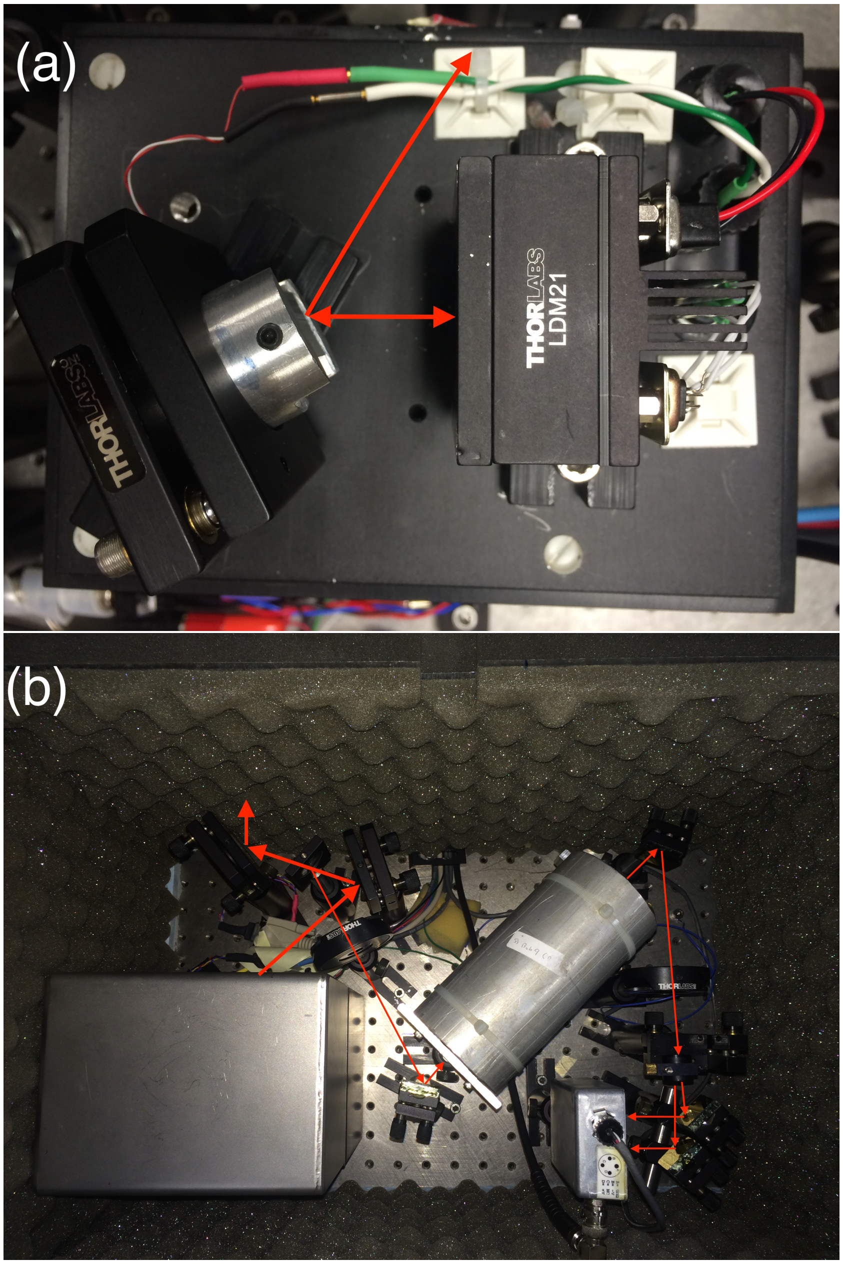

Figure 3.7: (a) A photograph of the external cavity diode laser for our old set-up. The laser mount is purchased from from Thorlabs. The laser mount and the baseplate are temperature stabilized. (b) A photograph of the DAVLL set-up for the old laser design. The ECDL is contained within the steel lid in the lower left corner. The entire set-up is contained within a box designed to eliminate temperature fluctuations and acoustic noise.

zero-order reflected by the grating (figure 3.7 (a)). The Littrow angle is defined as:

$$\sin\theta_L = \frac{\lambda}{2d}, \tag{3.1}$$

where θ_L is the Littrow angle, λ is the laser wavelength, and d is the line spacing. Making small adjustments to the grating angle allows for fine-tuning of the laser wavelength. We can tune the laser electronically by attaching piezoelectric transducers (PZT) stacks to the grating. Applying a voltage across the PZT increases the length of the PZT stack proportional to the voltage applied. Changing the voltage across the PZT stack attached to the grating changes the aligned angle of the grating. Therefore, the laser wavelength selected by the cavity is tuned with adjustments of the voltage applied to the PZT stack.

The second laser design is our so-called “new laser” design. Figure 3.8 (a) is a photograph of the new laser design. It follows the design introduced by reference [56], and our implementation of the design is expertly described in the dissertation of Sean P. Krzyzewski [57].

There are key construction differences between both laser designs. One of us (Krzyzewski) took the lead on implementing the new design. As such, Krzyzewski has a nice write-up about the characteristics of the two laser designs [57]. We find that this model is slightly more stable. This is most likely due to the much more solid construction. In principle, both ECDLs operate as described by [55].

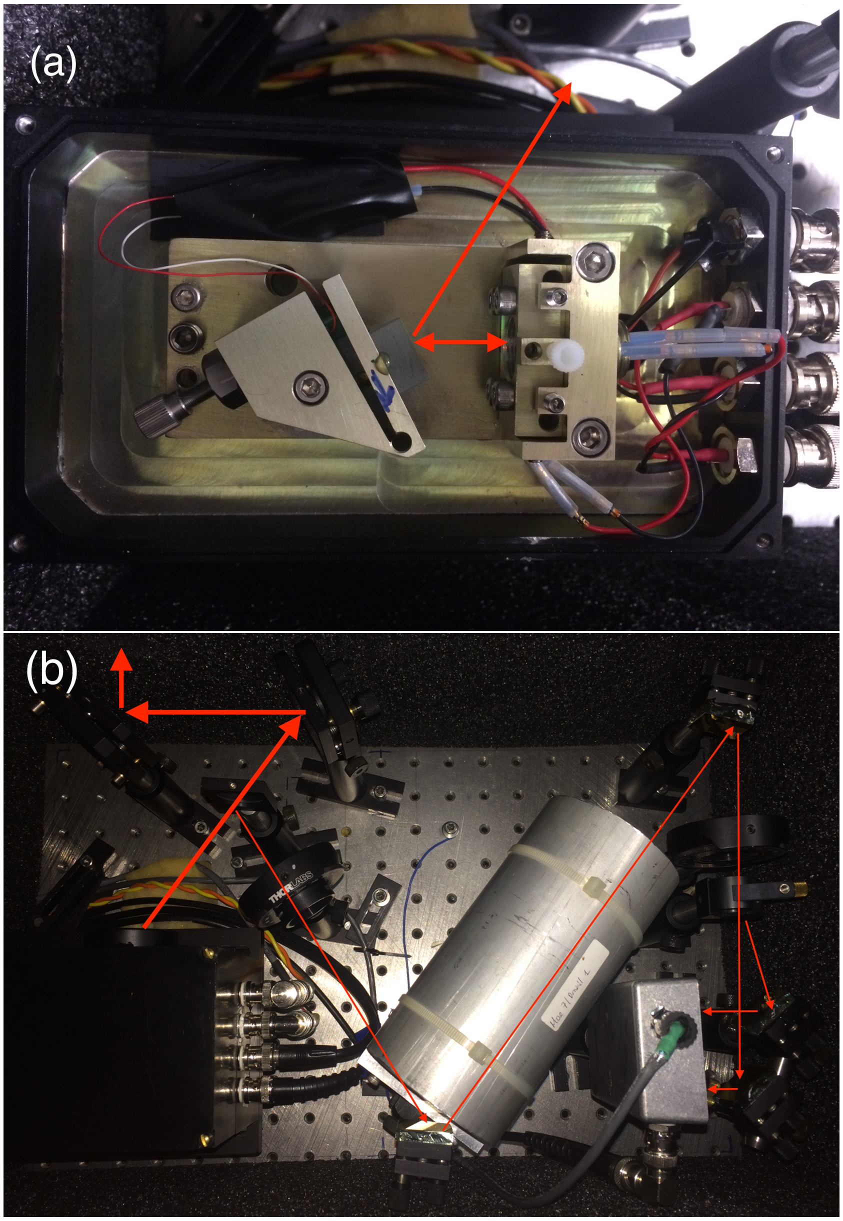

Figure 3.8: (a) A photograph of the external cavity diode laser for our new set-up. The entire system is manufactured in our machine shop. The baseplate is temperature stabilized. (b) A photograph of the DAVLL set-up for the old laser design. The ECDL is contained within the steel lid in the lower left corner. The entire set-up is contained within a box designed to eliminate temperature fluctuations and acoustic noise.

3.3.2 Frequency stabilization

All of our ECDL are locked to an atomic transition using a dichroic-atomic-vapor laser lock (DAVLL) signal [58, 59]. The set-up for both ECDL designs are shown in figures 3.7 (b) and 3.8 (b). Consider figure 3.9. A linearly polarized laser passing through the rubidium cell in the absence of the magnetic field will result in a Doppler broadened absorption profile, as shown in figure 3.10. Linear polarization is a linear combination of σ^+ and σ^- polarization. In the presence of a magnetic field, the transition caused by the σ^+ component of the polarization is Zeeman shifted-up in frequency (energy), while the transition caused by the σ^- component of the polarization is Zeeman shifted-down in frequency (energy). After passing through the cell (in the presence of a magnetic field), the two polarizations are separated and recorded on a photodiode. Subtracting the two signals gives an error signal similar to the red curve in figure 3.10. The frequency can be stabilized to an atomic transition by feeding the DAVLL error signal into a servo-side lock box (described in [57, 60]). A set-point monitor can be monitored on an oscilloscope, and the set-point can be adjusted using knobs on the lock box. The locking point on the DAVLL error signal is zero volts, and we adjust the set-point such that the zero-crossing corresponds to a atomic transition (as determined by a saturation-absorption signal). The lock box will send feedback to the PZT stack

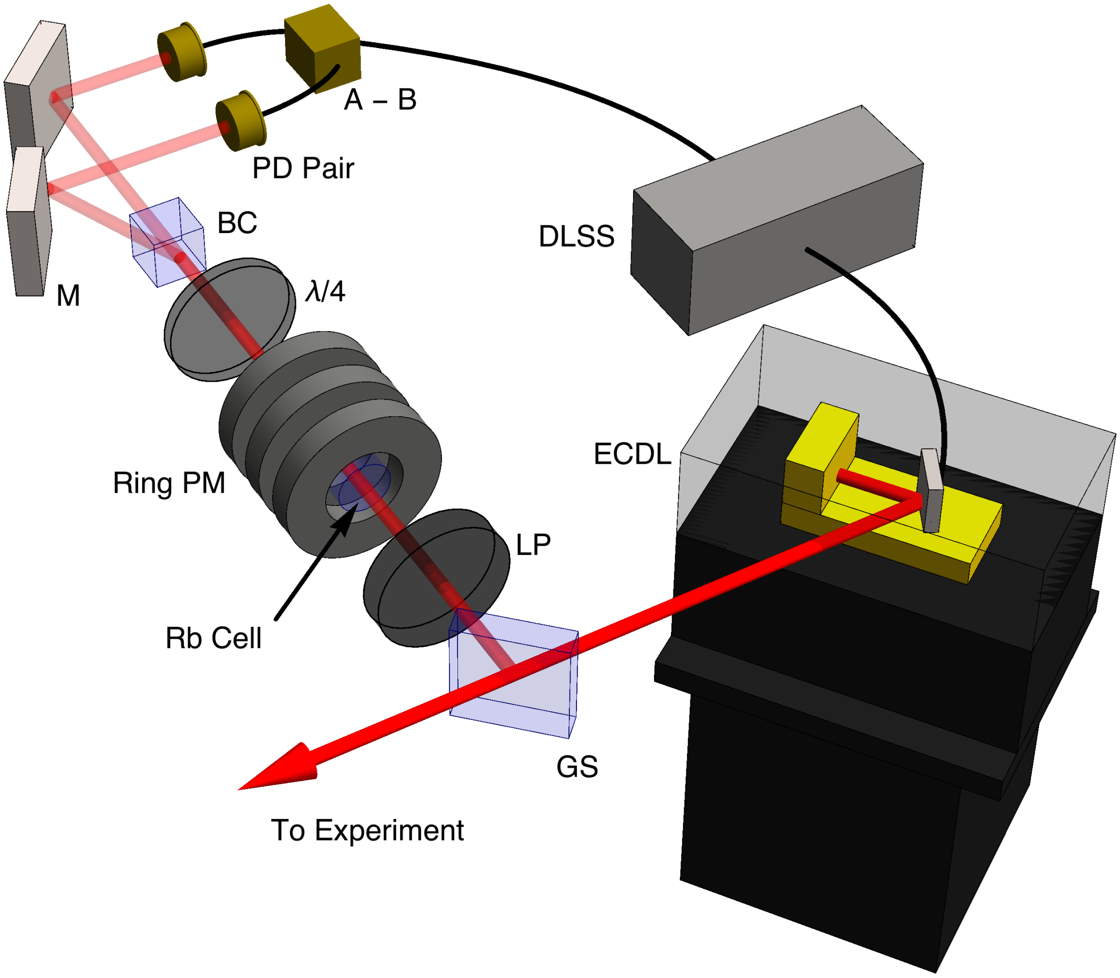

Figure 3.9: The general lay-out of all of our external cavity diode lasers (ECDL). A laser diode is mounted and temperature stabilized. A grating is aligned to the Littrow angle to establish an external cavity. The output of the external cavity is sent to the experiment. Using a glass slide (GS) we pick-off 4% of the laser to generate an error signal using a DAVLL set-up. The picked-off beam is sent through a linear polarizer (LP). It is then directed through a Rb cell surrounded by a series of ring permanent magnets (PM). The beam transmitted through the Rb cell is then passed through a $\lambda/4$ wave plate, where its linear and horizontal polarizations components are divided using a birefringent crystal (BC). Two photodiodes record the two polarizations, and their signal is subtracted. The subtracted signal is sent to a diode laser servo-sidelock box (DLSS), which stabilizes the frequency through feedback to the PZT on the grating.

on the diffraction grading of ECDL such that the set-point remains at zero.

Tuning the laser is done with three “knobs”, all of which are ways to adjust the lasing mode *prior* to locking the laser. Each process tunes different regimes, with different levels of finesse. The finest method for frequency tuning is by use of the diffraction grating. Adjustment of the injection current is a technique used to adjust the frequency by coarser amounts. The third (and coarsest method) of frequency adjustment is through the adjustment of the laser diode/ECDL temperature.

Step 1 of frequency stabilization involves the grating. We have two ways to make adjustments to the grating. The most precise method is through adjustment of the voltage across the PZT. This is usually reserved for the very last step, as the tuning range is typically only 2 GHZ. By using the adjustment screw, we can tune the entire spectrum of the laser diode (typically 1,000s of GHz). The first step to frequency stabilization is to adjust the screw by hand until the laser is within 20-50 GHz of the desired atomic transition. This step is typically done once every 2-4 weeks.

Step 2 of frequency stabilization involves the injection current. Adjustment of the injection current causes the ECDL mode to “hop” to another supportable cavity mode. For our system, empirical adjustment of the injection current hops in steps of 2-4 GHz across a range of about 50 GHz. We adjust the current until we get within 2 GHz of the desire atomic transition.

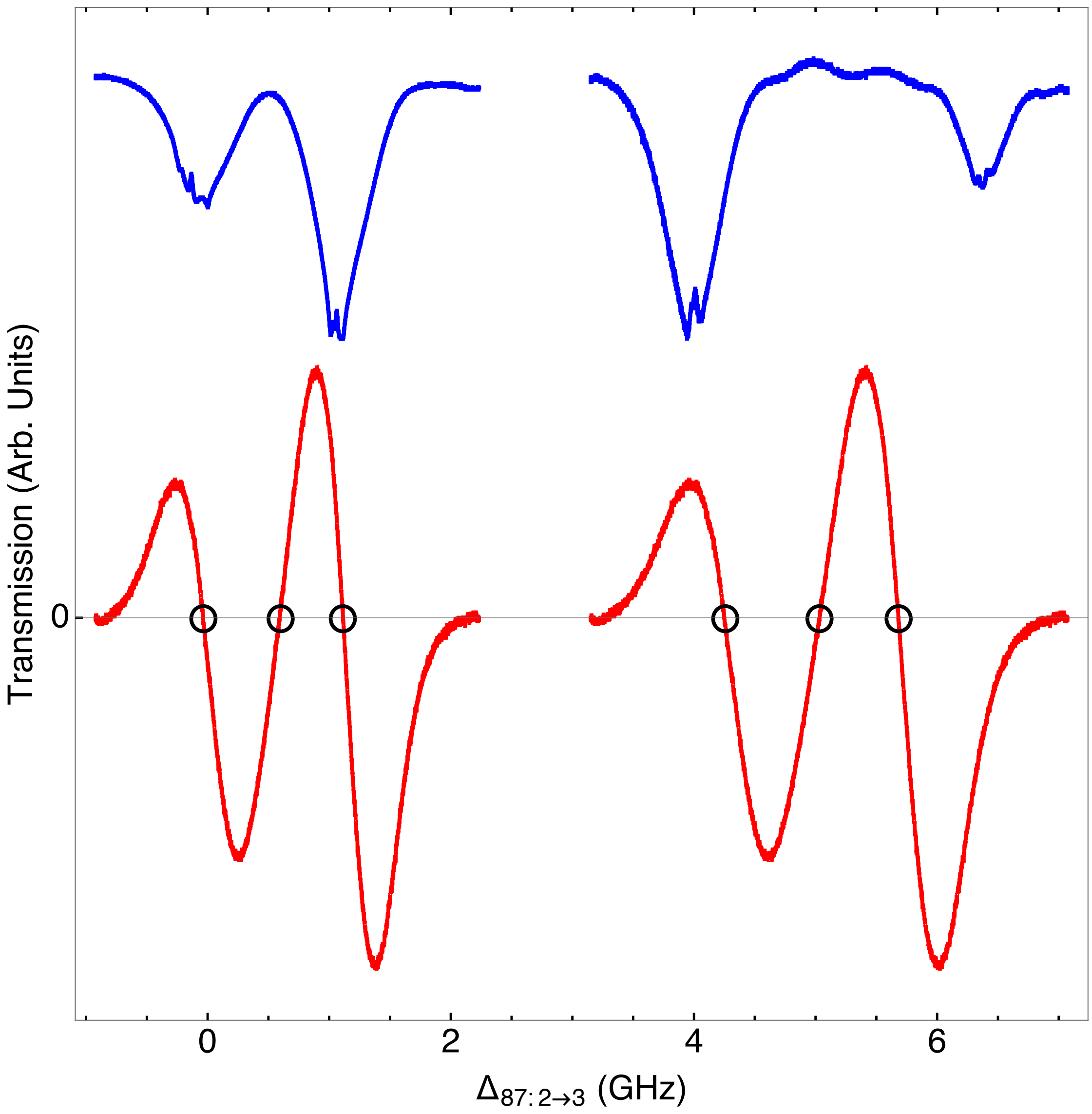

Figure 3.10: A measurement of the saturation-absorption spectrum (upper blue curve), and DAVLL signal (lower red curve). Both curves were made simultaneously. The black circles indicate possible locking points on the DAVLL signal. Adjusting the set-point shifts the DAVLL signal up/down, thus changing the zero-crossing. Locking to the DAVLL signal provides freedom to lock anywhere within the plotted range.

The coarsest tuning is temperature. In our experience, a decrease of 1°C will increase the laser frequency by about 100 GHz. In general, we stabilize the temperature of the laser diode to 1°C above room temperature with linear stability of 0.0014°C. This is typically adjusted once every month to year, and is generally left untouched. If we cannot get within 4 GHz of an atomic transition using step 2, then we make an adjustment to the laser diode/ECDL temperature. We then repeat steps 1 and 2.

Step 3 of frequency stabilization involves adjustment of the voltage across the PZT. This gives us very precise and continuous tuning of the frequency. During this step, we monitor the saturation-absorption spectrum to tune to the desired atomic transitions (see figure 3.10). The laser is tuned to the appropriate transition as identified by the saturation absorption signal. We adjust the adjust the lock set-point such that a DAVLL slope crosses zero volts at the identified atomic transition. The lock is then engaged by flipping a switch on the servo-side-lock box. Small adjustments of the set-point can be made to optimize an empirical signal (e.g. transmission measurement, MOT fluorescence, etc.).

3.3.3 Tapered amplifier

The diode lasers are low power (typically 30-60 mW). Cooling and trapping atoms requires higher power. To that end, we employ a tapered amplifier (TA) chip (manufactured by m2k Laser) in the master-oscillator power amplifier (MOPA) configuration. The TA is a large, semi-conductor gain medium (relative to the laser diode). A lower powered ECDL serves as a seeding laser that is coupled into the TA facet. The seeding laser stimulates coherent emission from TA that matches the phase and frequency of the seeding laser. The output of the TA can exceed 1 W of laser power.

The mount is built by the machine shop belonging to our department. Figure 3.11 is a representation of the set-up for the seeding laser and the TA. It is modeled off a similar design for our "new-laser" design, and is introduced by reference [56]. One of us (Krzyzewski) spent a considerable amount of effort describing the construction of our TA mount. I encourage the reader to read Krzyzewski's dissertation for more information [57].

The injection current for the TA is provided by a Wavelength Electronics Model LFI-4532 laser diode driver. The baseplate and TA mount are temperature stabilized using a TEC and a thermistor powered by a Wavelength Electronics PTC 5000. There are two aspherical lenses with a focal length $f = 3.1$ mm. One lens positioned at the input facet of the TA couples the seeding laser into the TA. The other lens is positioned at the output facet of the TA to collimate the amplified laser light. An unseeded TA will fluoresce when provided with an injection current. We find that the optimum coupling of our seed laser into the TA can be achieved by first collimating the fluorescence leaking from the input facet by adjusting the aspherical lens located at the input facet. The seeding laser is coarsely coupled

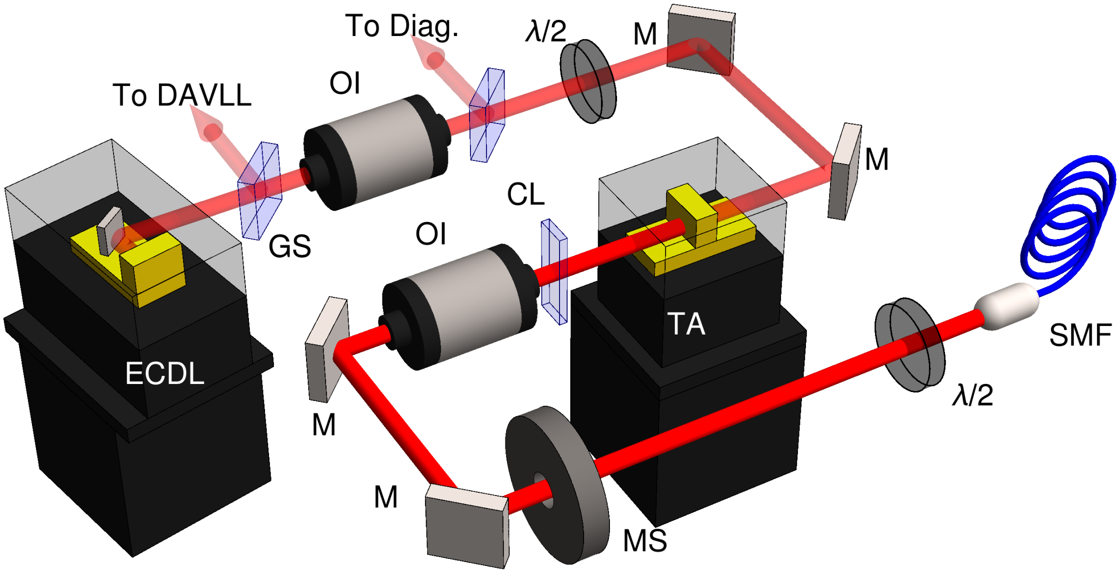

Figure 3.11: A representation of the external cavity diode laser (ECDL) and the tapered amplifier (TA) arranged in the MOPA configuration. This is the set-up used to generate the amplified light for our trapping laser. An optical isolator (OI) prevents unwanted feed-back to the ECDL from reflections of optical elements. Two steering mirrors align the seeding ECDL into the TA. The output of the TA is divergent in the horizontal axis. We use a cylindrical lens to collimate along the horizontal axis only. Two more steering mirrors couple the amplified light into a single mode (SM) fiber optic, which spatially filters the amplified light before sending the light to the magneto-optical trap as the trapping laser.

into the TA by aligning it to the collimated fluorescence. The coupling is optimized by making small adjustments to the steering mirrors (see figure 3.11) while maximizing the output power of the TA using a power meter.

The specifications of our TA require 20-30 mW of seeding power. Using two-mirrors, we can iteratively steer the seeding laser such that it overlaps with the collimated fluorescence leaking from the input facet. Fine-adjustments can be made by monitoring the power of the amplified light while adjusting the steering mirrors for the seeding laser. Finally, after coupling the seeding laser into the TA, we adjust the aspherical lens on the output facet of the TA such that the amplified light is collimated over large distances.

We operate the TA at an injection current (1-1.2 A) to extend its lifetime. At this injection current, we get 300 mW of laser power out of the TA. After cleaning the transverse profile of the output from the TA (by coupling into a single mode fiber), we get 175 mW to devote to laser cooling and trapping.

3.4 Diffractive optics and Laguerre-Gaussian modes

Most lasers are characterized by the fundamental transverse mode. For this experiment, we employed lasers with higher-order transverse modes. In particular, the so-called Laguerre-Gaussian (LG_p^ℓ) mode (see subsection 2.2.1). These laser modes are characterized by an $e^{\mathrm{i}\ell\phi}$ winding phase, resulting in an orbital angular momentum (OAM) of $\ell\hbar$ per photon. The OAM necessarily forces the electric field to vanish at the center of the beam, with $p+1$ concentric rings. This leads to the characteristic "donut" intensity pattern of a laser propagating in a LG_p^ℓ.

Diffractive optics can transform, external to the laser cavity, the Gaussian output of a laser into LG_p^ℓ modes. A diffractive optic is a transparent optic where lithography techniques are used to etch microscopic structures on the surface. These structures are designed such that the laser wavefront evolves into the desired form via Huygens' principle. Two optics are necessary to control both the intensity and phase. Diffractive optics can create high-order LG_p^ℓ modes [61], with

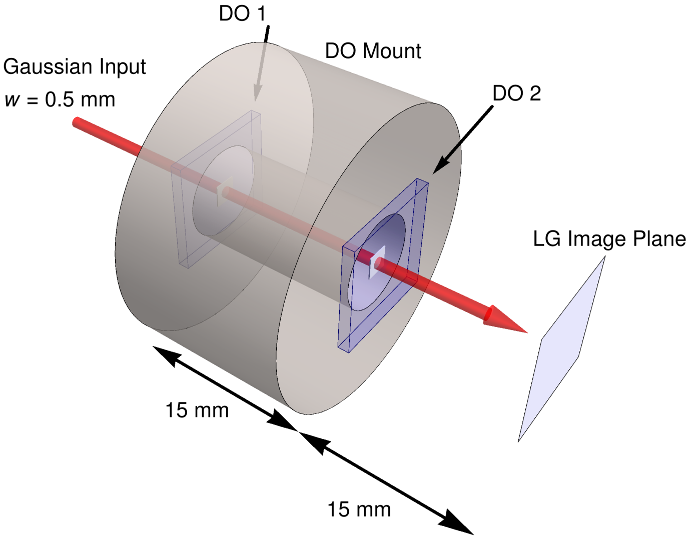

(a)

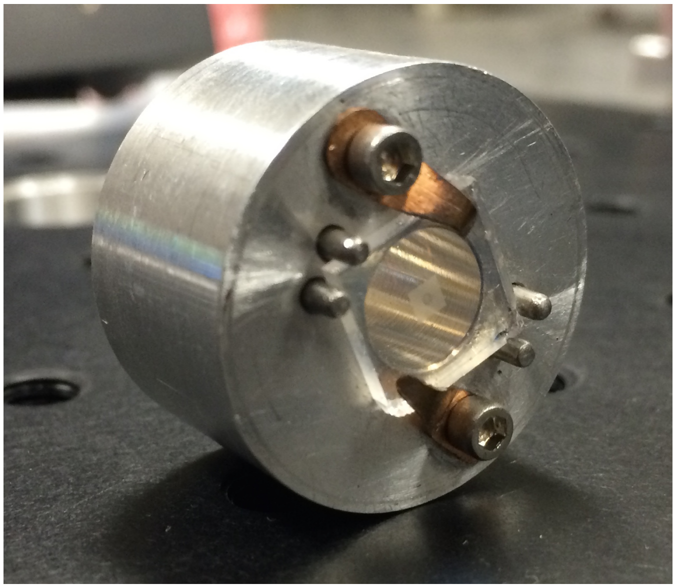

(b)

Figure 3.12: (a) A schematic of the diffractive optics (DO) used to generate the LG_p^ℓ modes in this experiment. Two DOs are required to make the transformation. (b) An image of the DOs mounted in a holder designed to position the DOs as specified by (a).

Table 3.1: Reproduced from reference [62]. Comparison of various LG_p^ℓ mode beam characteristics using different external cavity generation methods.

Creation method	ℓ	$p = 0$ purity	$p = 1$ purity	Conversion efficiency	Extinction Ratio $\times 10^{-2}$
Spiral phase plate	1	78.5% [67]			
	2	50% [67]			
Computer generated holograms	1	93% [68]	80% [69]	40%	
	3	77% [68]			
	6	62.8% [68]			
Diffractive optics (Ref. [62])	1	92.9%		40%	2.5 ± 0.8
	2		99.3%	60%	3.3 ± 0.8

demonstrated mode purities much higher than those formed with other methods [62]. The compact diffractive optics have proven advantageous in quantum information processing, where the large numerical aperture of these optics gather the largest fraction of the fluorescence emitted by an ion trapped on a chip [63–65]. Recently, diffractive optic elements have been used to create blue detuned bottle beam traps [66].

Our diffractive optics are created by the Diffractive Optic Corporation (DOC). Figure 3.12 (a) shows the appropriate alignment of the two diffractive optics, and figure 3.12 (b) shows the mount we use to maintain the tolerances set by the diffractive optics. Table 3.1 summarizes the mode purity and conversion efficiency for our diffractive optics. The etched surfaces of the diffractive optics face each other. The two optics must be aligned parallel to each other to within ±3 arc-minutes (along any axis). The separation from etch-surface of optic 1 to the etch-surface of optic 2 is (15 ± 0.2) mm. Deviations beyond the tolerances provided by the DOC

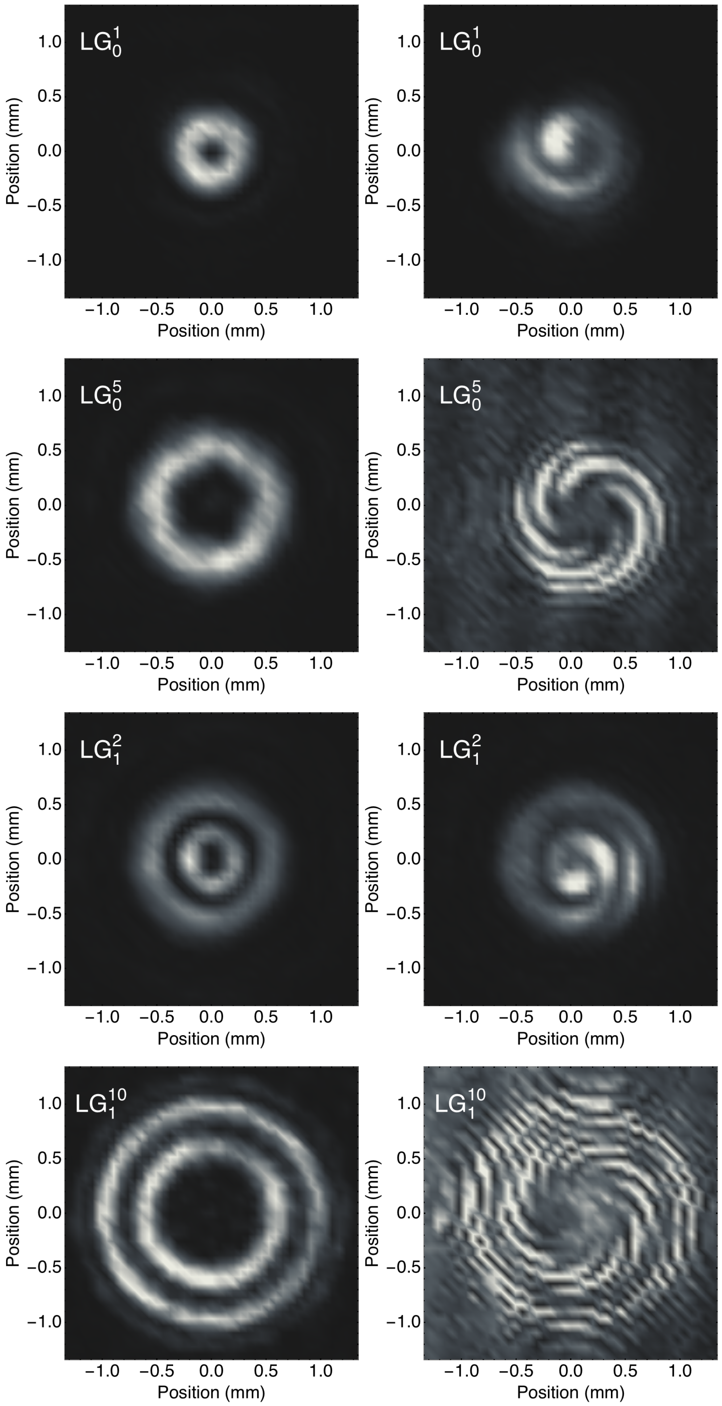

Figure 3.13: Four LG_p^ℓ modes generated from our diffractive optics (first column), and their corresponding interference patterns (second column). We show the LG_0^1, LG_0^5, LG_1^2, and LG_1^{10} laser modes.

results in inhomogeneous intensity distributions and degradation of the azimuthal phase.

The optics are designed such that a pure LG_p^ℓ is produced at an image plane 15 mm behind the second optic. However, we have observed that the LG_p^ℓ generally propagates in a good approximation to an LG_p^ℓ for distances on the order of meters [62]. We have the capability of producing LG_0^1, LG_0^5, LG_1^2, LG_1^{10}, and LG_2^3 modes using five pairs of diffractive optics. Figure 3.13 shows measurements of a few selections of these modes. This work employs the LG_0^1 mode for the this study of EIT, but we also explore the incorporation of LG_0^5 and LG_1^2 modes in appendix A. Figure 3.13 shows several LG_p^ℓ modes measured in this lab.

3.5 Magneto-optical trap

The theory of our magneto-optical trap (MOT) is explored in chapter 2. To experimentally implement the MOT, we employ two laser fields in conjunction with two current carrying wires in the anti-Helmholtz configuration. One laser field functions as the trapping laser (amplified by a TA in the MOPA configuration), and the other laser functions as a repumping laser. Additionally, we use three pairs of rectangular coils in an approximation of the Helmholtz configuration to eliminate magnetic fields along each of the orthogonal directions. Figure 3.14 shows a level diagram with indicated transitions for the trapping and repumping lasers. This section will describe these components in detail with three subsections de-

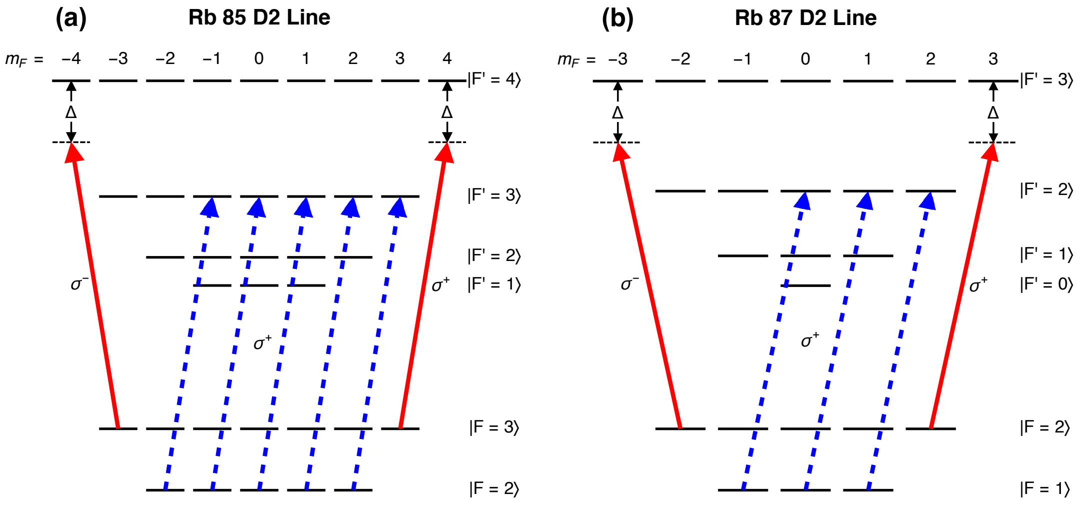

Figure 3.14: A level diagram indicating the appropriate transitions for (a) ^{85}Rb and (b)^{87}Rb. The trapping laser is indicated by the red arrows, and the repumping laser is indicated by the dashed blue arrows. The detuning various from experiment to experiment, but is typically $\Delta/2\pi \approx 10 - 20$ MHz.

voted to the four components, and a final subsection describing the properties and characteristics of the MOT.

3.5.1 Cooling and trapping laser

The trapping laser with TA is described in subsection 3.3.3 and is shown in figure 3.11. The output of the TA is spatially filtered using a polarization maintaining single mode fiber (SMF), ensuring uniform cooling and trapping. We typically get 175 mW out of the SMF cable. A UniBlitz shutter is placed before the SMF cable to shutter the trapping beam. For this experiment, the trapping laser does not need to be shuttered. The SMF are very sensitive to the alignment of the input linear polarization to the fast axis of fiber. Perturbations of the fiber (mechanical, temperature, etc.) can lead to rotations of the polarization of the laser as it propagates through the fiber. Therefore, the polarization of the laser can rotate over long periods of time, and drastically change the properties of the MOT. To ensure a fixed polarization, we place a polarizing beam splitter (PBS) cube directly after the output of the fiber. We exerted great effort in aligning the input polarization to the fast axis of the SMF. This was done by monitoring the power reflected from the PBS cube while empirically adjusting angle of a $\lambda/2$ waveplate before the input coupler of the SMF. As a result, the power fluctuations are negligible over the duration of an experiment.

We telescope the trapping laser to a $1/e^2$ diameter of 2.5 cm. This is the largest beam size that will pass through our optics. Larger trapping beams slow atoms over a larger volume, increasing the numbers confined in our MOT. After telescoping the trapping laser we split the trapping beam into six beams using five PBS cubes. A $\lambda/2$ wave plate allows us to tune the power of each of the six beams by rotating fast axis of the wave plate, thus balancing the MOT. The transmission/reflection of each beam through each PBS cube is then sent through a $\lambda/4$ wave plate. The fast axis of the $\lambda/4$ wave plate is then adjusted to produce σ^+ or σ^- light depending on which axis the trapping beam propagates. Table 3.2 describes the specific polarizations corresponding to the coordinates and quantization axis defined in figure 3.15.

Table 3.2: Cataloged polarizations states for each of the laser beams that make-up our magneto-optical trap (MOT). These polarizations are specific to the configuration as described in figure 3.15. $\sigma^{\pm}$ polarizations drive $\Delta m_F = \pm 1$ transitions as described by the quantization axis defined by the magnetic field. Right circularly handed (RHC) and Left circularly handed (LHC) are defined relative to the laser propagation axis.

Laser	**Propagation Axis**	**Polarization**	**Handedness**
Trapping	$+\hat{x}$	σ^+	LHC
	$-\hat{x}$	σ^-	RHC
	$+\hat{y}$	σ^+	LHC
	$-\hat{y}$	σ^-	RHC
	$+\hat{z}$	σ^-	LHC
	$-\hat{z}$	σ^+	RHC
Repumping	$+\hat{z}$	σ^+	RHC

Finally, we steer (using mirrors) three of the beams along three orthogonal axes, and the reaming three beams are steered counter-propagating to the first three beams. Alignment of the beams is challenging because of the glass cell. There are not any orthogonal ports or windows to help guide the trapping beams. To guide the four beams in the horizontal axis, we built an alignment tool (see figure 3.16). The tool is a cross, milled to rest centered on the anti-Helmholtz coils. Descending from each arm of the cross, we attach irises. Two of the beams are aligned such that each pass through two irises along the length of an arm. The tool is then removed, and the other two beams are aligned to their counter-propagating partner. The two beams along the vertical axis (the axis of the anti-Helmholtz coils) are aligned using the symmetry of the anti-Helmholtz coils. The center of the anti-Helmholtz coils can be easily located, and the beams can be aligned to the center using a hole made in tape and/or paper and a hole drilled through the center of the alignment tool in figure 3.16.

The MOT is first optimized through iterative adjustments of the fast axis of each $\lambda/2$ wave plate are made while monitoring the MOT with charge coupled devices (CCD) and photodiodes. Then, small steering adjustments of the trapping beams are made to optimize MOT numbers and symmetry. Finally, iterative adjustments of fast axis of each $\lambda/4$ wave plate are made to minimize the temperature of the MOT by optimizing sub-Doppler cooling.

3.5.2 Repumping laser

The cycling transition of the trapping laser is not a closed transition. The trapping laser is typically detuned 20 MHz below the cycling transition. There is an appreciable probability that trapping laser will drive a transition form $|F=3\rangle \rightarrow |F=2\rangle$ ($|F=2\rangle \rightarrow |F=1\rangle$) in ^{85}Rb (^{87}Rb). The atom will then decay to the lower hyperfine ground state: $|F=2\rangle$ ($|F=1\rangle$) in ^{85}Rb (^{87}Rb). If the MOT employs a trapping laser only, then the ensemble of atoms will be optically pump the lower hyperfine ground state, no longer mechanically effected by the trapping laser. Therefore, we use a second ECDL that is frequency stabilized using a DAVLL to the $|F=2\rangle \rightarrow |F'=3\rangle$ ($|F=1\rangle \rightarrow |F'=2\rangle$) in ^{85}Rb (^{87}Rb), as shown in figure 3.14. The repumping laser will optically pump the atoms back into the cycling transition of the trapping laser.

Figure 3.17 shows the basic set-up of the repumping laser. The output of

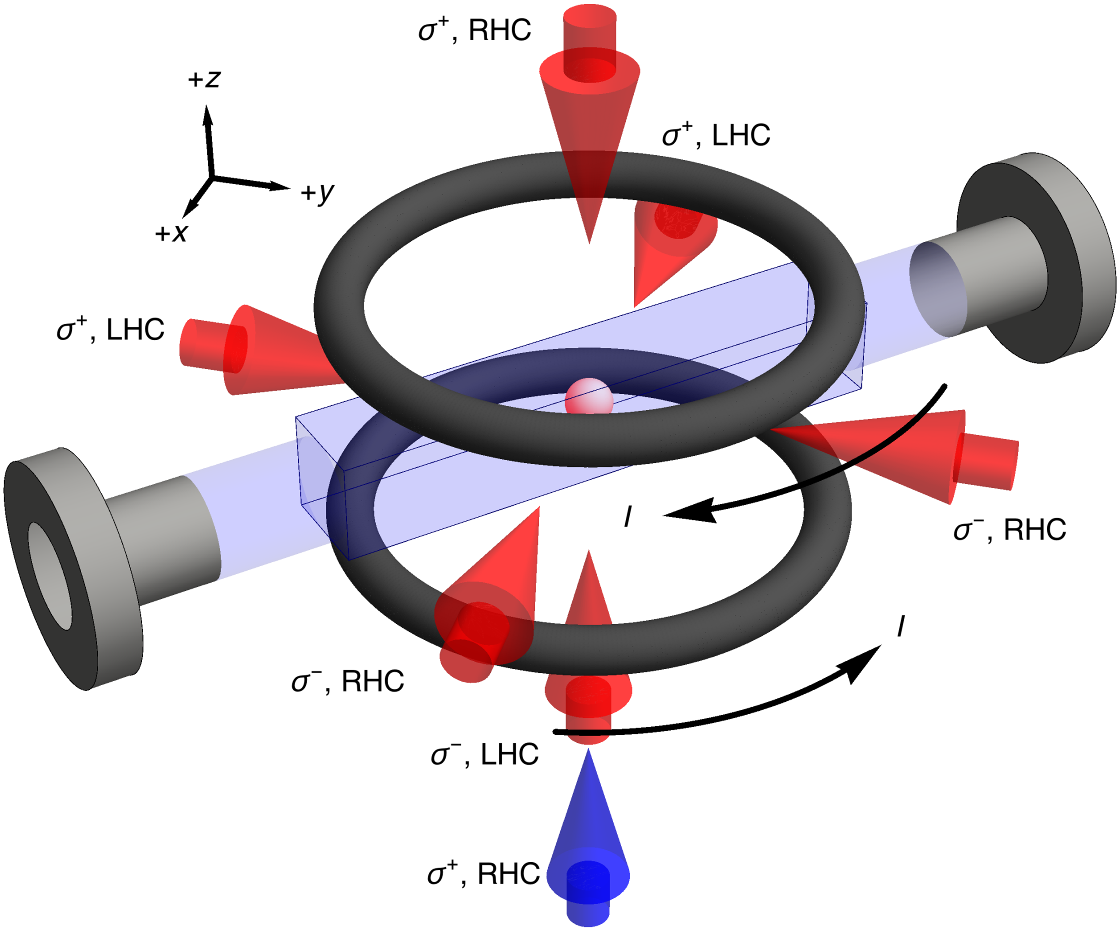

Figure 3.15: The configuration of our trapping beams, repumping beam, and anti-Helmholtz coils. The x-, y-, and z-axis is defined in the upper left-hand corner of the figure. The corresponding polarization (σ^+ or σ^-, and right hand circular (RHC) or left hand circular (LHC)) is indicated next to each beam. The direction of the current for each of the coils is also indicated. Figures 2.11 and 2.12 show the magnetic filed and restoring force experienced by the ensemble atoms along the x-, y-, and z-axis.

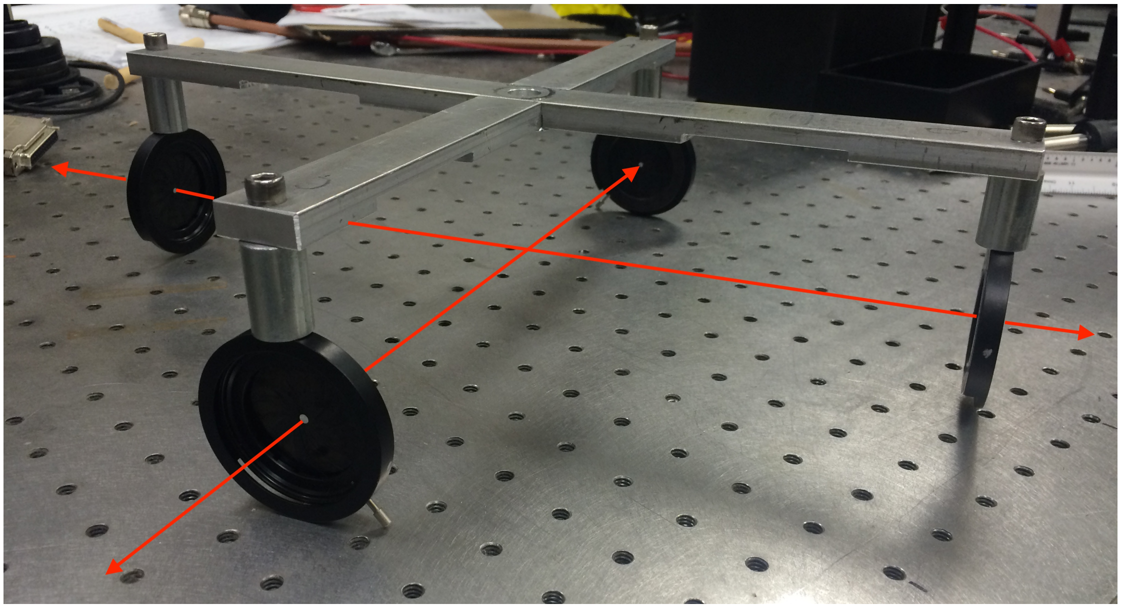

Figure 3.16: The tool we built to align the four trapping laser beams that span the horizontal plane.

the repumping laser passes through an optical isolator to prevent scattered light from reaching the ECDL. We telescope the repumping laser to mode match with an acoustic-optical beam deflector (AOBD). The AOBD operates with the same principle as the AOM. The AOBD acts as a shutter for the repumping laser in this experiment.

After passing through the AOBD, we enlarge the repumping laser using a telescope. The repumping laser is telescoped such that it is the same size as the trapping laser, ensuring that atoms will be laser cooled and trapped over the entire volume of the crossed-trapping beams. Finally, the repumping laser is overlapped with one of the trapping beams by steering the beam through the back of one of the PBS cubes that divides the trapping laser beams. The fast axis of a $\lambda/2$

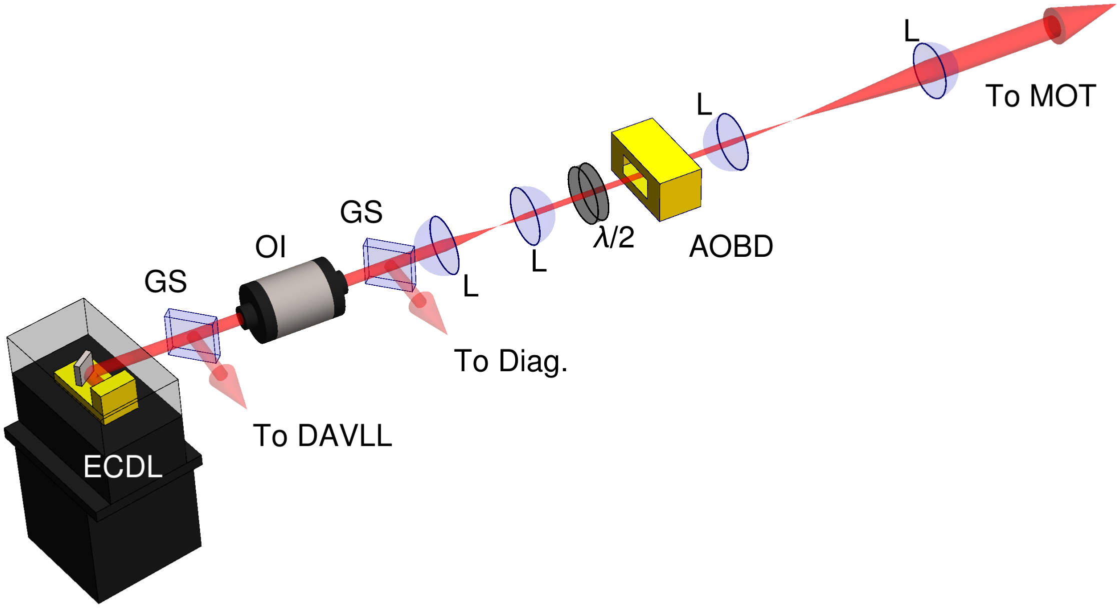

Figure 3.17: The set-up for the repumping laser. It is an external cavity diode laser (ECDL) that is frequency stabilized by a dichroic atomic vapor laser lock (DAVLL). The laser is telescoped to mode match the acousto-optic beam deflector (AOBD). After passing through the AOBD, the laser is telescoped to match the size of the trapping laser. It is then steered to co-propagate with the trapping laser.

wave plate is aligned so that the repumping beam co-propagates with one trapping beam only[1]. The final state of the repumping laser is σ^+ polarization (RHC), which optically pumps on the transitions described by figure 3.14 (a) and (b) for ^{85}Rb and ^{87}Rb.

3.5.3 Anti-Helmholtz coils

Two circular current carrying coils are positioned along the vertical axis such that they are centered on the glass cell. The current in the two wires travel in opposite directions (the so-called "anti-Helmholtz configuration"). This configuration produces non-uniform magnetic field that is linear along the vertical and radial axes. At the center of the two coils, the magnetic field is zero. The housing, mounting stand, and winding of the coils was done by the machine shop in the Homer L. Dodge Department of Physics and Astronomy.

The current for the coils is provided by a Sorensen HPD 15-20 power supply, and can deliver 0-20 A to the coils. In this experiment, fast switching of the current is necessary. We use a home-built circuit to quickly turn on/off the current going to the anti-Helmholtz coils. The circuit has a rise/fall time of 10 μs.

---

[1] A single repumping beam is desired to reduce the amount of light scattering off the glass cell.

3.5.4 Zeroing coils

Minimizing stray-DC magnetic fields is crucial for EIT experiments. Some common sources of DC magnetic fields include the Earth's magnetic field, the iron rich bricks in the walls, the permanent magnets on the two sputter-ion pumps, and the optical posts may become magnetized. Magnetic fields lift the degeneracy of the atomic hyperfine sublevels, which leads to broadening of the EIT resonance and increased decoherence in the system. To manage stray-magnetic fields, we use three pairs of rectangular coils that are arranged along the three orthogonal axes in an approximation to the Helmholtz configuration. Figure 3.18 shows the arrangement of these coils with respect to the MOT, as well as the cell.

A CircuitSpecialists.com CSIPPS33T programmable DC power supply provides current to the rectangular coils. Three channels output three independent currents, allowing for mA precision for each pair of coils. We minimize stray-magnetic fields using two procedures:

1. **Lakeshore Model 420 Gaussmeter:** This is the coarsest method, and is the first step you take toward minimizing the magnetic field. The precision our probe is 3 mG.

   (a) One axis at a time, adjust the current in such a way as to minimize the measured magnetic field as recorded by a Hall probe.

   (b) Naturally, we cannot place the Hall probe *inside* the chamber. Therefore,

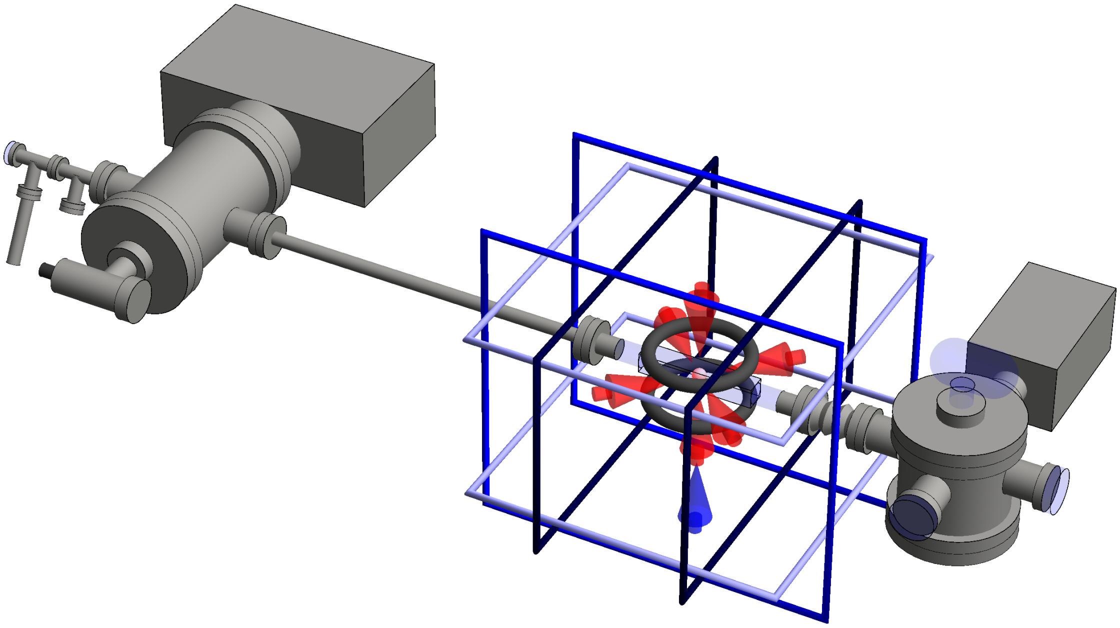

Figure 3.18: The trapping laser beams are indicated by red arrows. The repumping laser beam is the vertical blue arrow entering from the bottom of the cell. The gray circular coils are the anti-Helmholtz coils used for the MOT. The three pairs of rectangular Helmholtz coils reduce the background magnetic fields. The hue of blue indicates matching pairs of coils.

    it is best to minimize the magnetic field on both sides of the cell along the axis of interest.

    (c) After completing all three axes, it is best to repeat as necessary.

2. **EIT Signal:** This is the finest method, and follows the Hall probe procedure.

    (a) EIT is very sensitive to magnetic fields.

    (b) Magnetic fields lift the degeneracy of the hyperfine sublevels.

    (c) If the system is otherwise coherent, then the multiple EIT resonances can be resolved for each sublevel.

    (d) Figure 3.19 (a) shows a typical EIT resonance in the presence of a non-zero DC magnetic field.

    (e) We adjust the current flowing through each pair of coils one channel at a time with the goal of collapsing the multiple EIT features into a single EIT resonance.

    (f) After completing all three axes, it is best to repeat as necessary.

    (g) Figure 3.19 (b) shows a typical EIT resonance after minimizing the DC magnetic field.

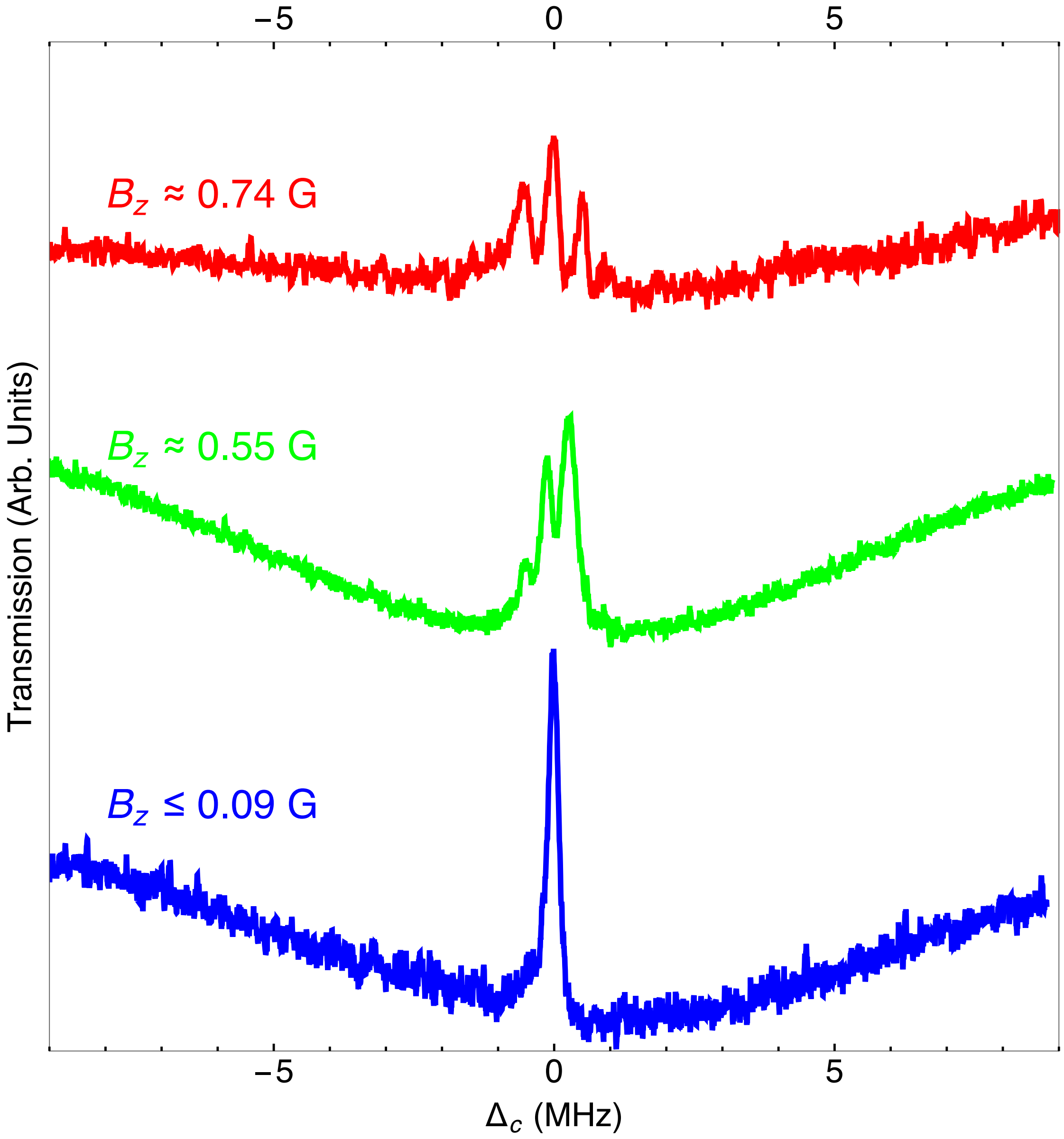

Figure 3.19: A spectrum of a typical EIT resonance in the presence of a non-zero DC magnetic field is shown by the red curve. The green curve shows a spectrum showing a typical EIT resonance after partially canceling the DC magnetic field. The blue curve shows an EIT spectrum when the DC magnetic field has been cancelled to the best precision obtained by our experiment. The spectrum gives an upper limit $B \leq 0.09$ mG.

3.5.5 MOT summary

Figure 3.18 shows the components of the MOT. For scale and relationship, the vacuum system is included with the MOT. The representation of the chamber is accurate for routine experiments. The valve is closed, the turbomolecular pump is removed from the chamber, and the mechanical pump is also removed. The sputter-ion pumps work on the chamber to maintain a vacuum. The MOT is loaded from the background vapor of rubidium. Figure 3.20 shows the entire optics table.

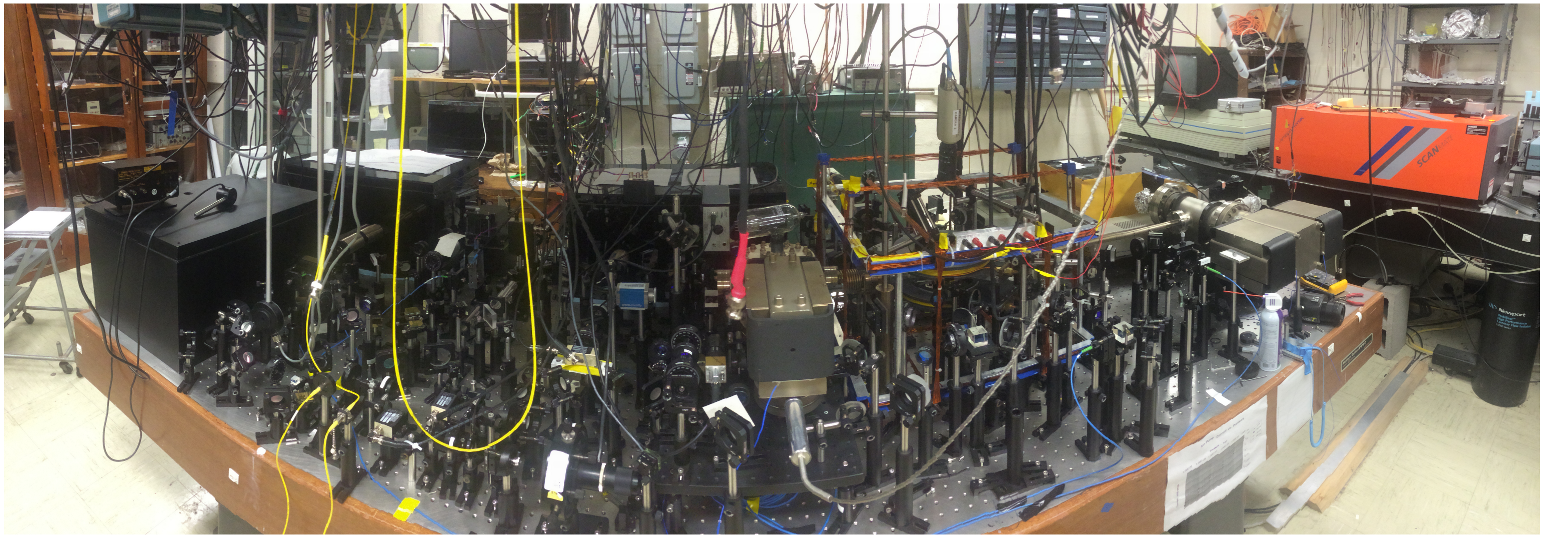

Figure 3.20: A photograph of the full apparatus used for the LG experiment.

3.6 Fluorescence and absorption detection

Section 3.5 described how we produce an ensemble of ultracold atoms. This section will discuss how we probe and detect the atomic ensemble. Fluorescence detection involves the collection of photons scattered by the near resonant trapping beams from the MOT. We image the fluorescence using a charge coupled device (CCD) camera, and we also focus the fluorescence onto a photodiode. Both fluorescence detection methods provide characteristics of the MOT, but are not as accurate as absorption techniques.

Absorption detection employs a weak probe that is resonant with an atomic transition. The ensemble of atoms absorb photons from the weak probe. The reduced transmission of the probe is detected with both a CCD camera and with a photodiode.

The section will begin by describing the fluorescence detection. We will then discuss absorption detection. In general, for each of these techniques, we will develop the formalism used to determine the characteristic of our ultracold ensemble of atoms. This description will conclude with our specific implementation of fluorescence and absorption detection.

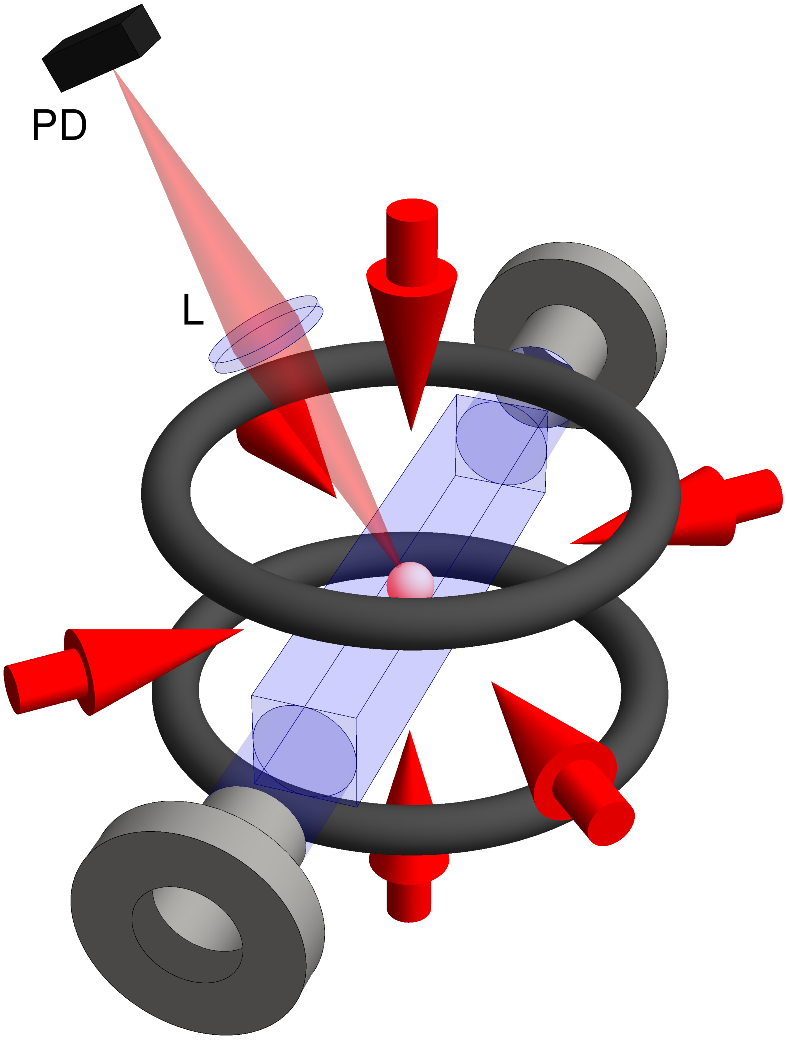

Figure 3.21: The set-up for our fluorescence detection. The lens is position twice its focal length from the confined atoms. The photodiode is placed behind the lens by an additional length of twice its focal length.

3.6.1 Fluorescence detection

We measure the total number of atoms in our MOT using the fluorescence of the confined atoms. The trapping laser is close to resonance (we are typically 20 MHz detuned below the resonance). As a result, the atoms are continuously scattering photons. We position a lens at a position twice the focal length from the trapped atoms. On the other side of the lens, we position a photodiode at a distance of twice the focal length behind the lens (see figure 3.21). For this configuration, the total number of atoms measured by the photodiode is given by the relation [70],

$$N = \frac{4\pi I_{pd}}{\Omega_L \mathcal{R}(0.96)^k \hbar\omega R_{\text{sc}}}, \tag{3.2}$$

where I_{pd} is the photocurrent from the photodiode, Ω_L is the solid angle subtended by the lens, $\mathcal{R}$ is the responsivity of the photodiode, k is the number of uncoated glass surfaces between the confined atoms and the lens, and R_{sc} is the photon scattering rate given by equation (2.22).

In addition to a measurement of the total number of atoms, we use fluorescence detection to measure the loading rate of the MOT. This helps us to monitor the background pressure of the chamber. In general, an increase in the loading rate by a second approximately indicates an increase in the background pressure by an order of magnitude. Figure 3.22 shows a typical fluorescence measurement of the MOT loading rate.

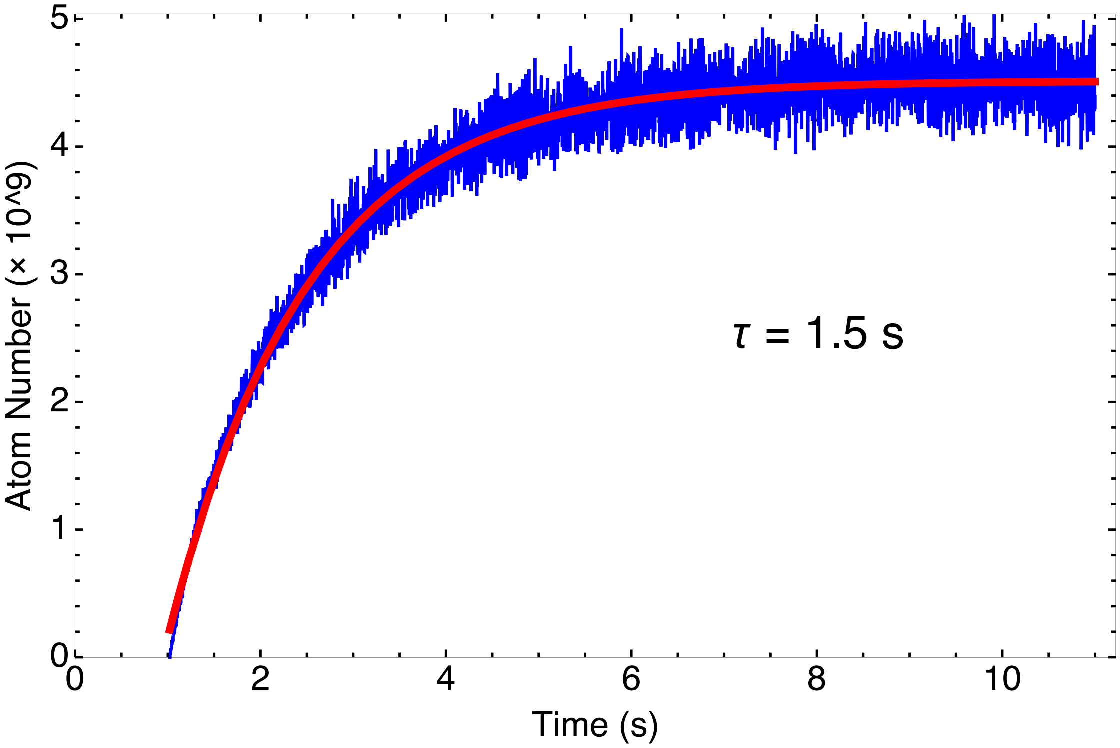

Figure 3.22: A typical fluorescence measurement of the loading rate of our magneto-optical trap.

3.6.2 Absorption imaging

The absorption imaging follows from Beer's Law. Consider an absorbing medium illuminated by a laser (figure 3.23). The intensity of the laser before entering the medium is I_0. The direction of the laser propagation is z, and the boundary of the absorbing medium will be chosen to be $z = 0$, and x and y make up a plane perpendicular to the probe laser beam. Then, we expect the intensity to decay exponentially with distance traveled through the medium.

$$\frac{\mathrm{d}I(x,y,z)}{\mathrm{d}z} = -\sigma_0 n(x,y,z) I(x,y,z), \tag{3.3}$$

where σ_0 is the resonant scattering cross-section (more on this later), $n(x,y,z)$ is the number density, and $I(x,y,z)$ is the intensity of the laser at a position (x,y,z) as it propagates through the medium. We can integrate both sides.

$$\int_{I_0(x,y)}^{I_{\text{out}}(x,y)} \frac{\mathrm{d}I}{I} = -\sigma_0 \int_{-\infty}^{+\infty} n(x,y,z)\,\mathrm{d}z \tag{3.4}$$

The left hand side is simple enough to carry through. However, in order to carry out the integration of the right-hand side, we will first model the density profile. To lowest order, the MOT can be expressed as a harmonic oscillator (see subsection 2.5.3). Using equation (B.4), we model the density as a Gaussian. The density

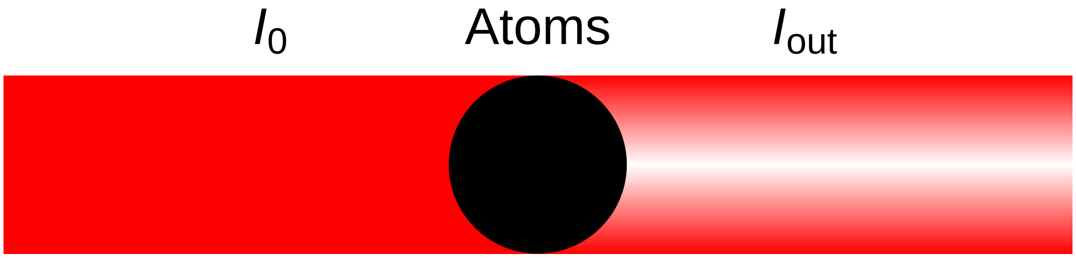

Figure 3.23: The general concept for absorption imaging uses Beer's Law. A laser with initial intensity I_0 resonantly illuminates a sample of atoms. The atoms absorb an amount of light that is related to the trap density. What emerges is a reduced intensity I_{out}. Measuring these two intensities gives us information about the trap characteristics.

is then expressed as:

$$n(x, y, z) = n_{\text{peak}} \exp\left(-\frac{(x - x_0)^2}{2\chi^2} - \frac{(y - y_0)^2 + (z - z_0)^2}{2\psi^2}\right), \tag{3.5}$$

where n_{peak} is the peak density, x_0 is the center of the trap in the x-dimension as defined by the CCD chip, y_0 is the center of the trap in the y-dimension as defined by the CCD chip, z_0 is the center of the trap in the z-dimension, χ is the width of the trap in the x-dimension, and ψ is the width of the trap in the y- and z-dimensions[2].

So, integrating the equation (3.5) yields

---

[2] We have assumed that the symmetries of the MOT apparatus reflect the symmetries of the MOT. The MOT coils are cylindrically symmetric. A rotation in a plane parallel to the MOT coils is invariant. Therefore, the trap size in the y and z directions will be assumed to be identical.

$$\begin{aligned}\int_{-\infty}^{+\infty} n(x,y,z)\,\mathrm{d}z &= n_{\text{peak}} \exp\left(-\frac{(x-x_0)^2}{2\chi^2} - \frac{(y-y_0)^2}{2\psi^2}\right) \int_{-\infty}^{+\infty} \exp\left(-\frac{(z-z_0)^2}{2\psi^2}\right) \mathrm{d}z \\ &= \sqrt{2\pi}\psi n_{\text{peak}} \exp\left(-\frac{(x-x_0)^2}{2\chi^2} - \frac{(y-y_0)^2}{2\psi^2}\right)\end{aligned} \tag{3.6}$$

Now, we can write this in a more compact form by introducing the column density.

$$\begin{aligned}\tilde{n}(x,y) &= \sqrt{2\pi}\psi n_{\text{peak}} \exp\left(-\frac{(x-x_0)^2}{2\chi^2} - \frac{(y-y_0)^2}{2\psi^2}\right) \\ &= \tilde{n}_{\text{peak}} \exp\left(-\frac{(x-x_0)^2}{2\chi^2} - \frac{(y-y_0)^2}{2\psi^2}\right),\end{aligned} \tag{3.7}$$

where $\tilde{n}(x,y)$ is the column density distribution in the plane transverse to the probe laser, n_{peak} is the peak number density, and $\tilde{n}_{\text{peak}} = \sqrt{2\pi}n_{\text{peak}}$ is the peak column density. Combining equations (3.7) and (3.6) with equation (3.4), we get

$$\ln\left(\frac{I_{\text{out}}(x,y)}{I_0(x,y)}\right) = -\sigma_0\tilde{n}(x,y).$$

Now, we will define the optical density (similar to that in chapter 2) as:

$$\text{OD}(x,y) \equiv \sigma_0\tilde{n}(x,y) = \ln\left(\frac{I_0(x,y)}{I_{\text{out}}(x,y)}\right), \tag{3.8}$$

In practice, we measure $I_0(x,y)$ and $I_{\text{out}}(x,y)$. Then use the relation in equation (3.8), as well as the relations therein to get various characteristics of the trap. For example, from equations (3.7) and (3.8), we can find the peak density of the

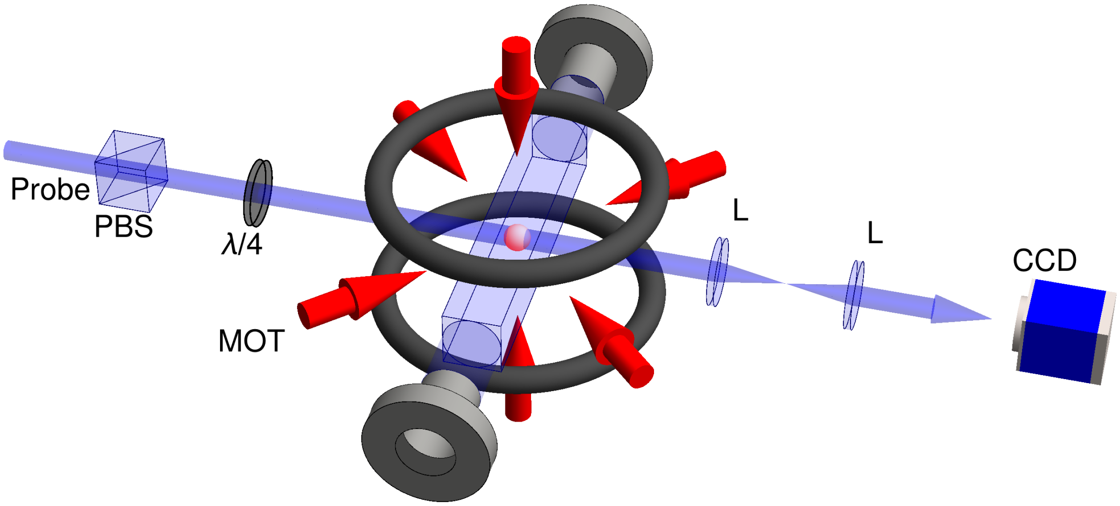

Figure 3.24: The experimental set-up for absorption imaging. We send a collimated probe laser, tuned to the cycling transition $|F = 3, m_F = +3\rangle \rightarrow |F' = 4, m_{F'} = +4\rangle$ ($|F = 3, m_F = +3\rangle \rightarrow |F' = 4, m_{F'} = +4\rangle$) in ^{85}Rb (^{87}Rb). The shadow caused by the absorption of atoms confined to the magneto-optical trap is imaged on the CCD camera via a pair of lenses.

cloud by measuring the peak optical density: $\tilde{n}_{\text{peak}} = \sqrt{2\pi} n_{\text{peak}} = \text{OD}_{\text{peak}}/\sigma_0$. The next subsection will describe how we measure $I_0(x, y)$ and $I_{\text{out}}(x, y)$.

3.6.3 Experimental procedure

To image the atoms, we illuminate the sample of trapped atoms with a weak, collimated probe laser resonant with the ^{85}Rb $|F = 3\rangle \rightarrow |F' = 4\rangle$ hyperfine transition. The transverse mode quality of the probe laser is cleaned up using a Thorlabs P3-780PM-FC polarization maintaining fiber optic. The probe beam is then expanded to have a waist $w_0 \approx 1$ cm so that the laser can be approximated as a plane wave. The probe beam has linear polarization. The probe beam is then directed into the chamber, and is overlapped with the trapped atoms. Atoms absorb the resonant light, reducing the intensity of the probe laser. After passing through the cloud of atoms, the probe laser is directed onto a CCD chip[3]. This is done one of two ways, described below.

The first set-up is shown by figure 3.23. The collimated probe to directly illuminate the CCD chip. In this set-up, the dimensions of the trap can be determined directly from the size of the pixels. The array of pixels (see figure 3.26) is a coordinate plane with the size of each pixel defining position grid for which we can measure distances. Therefore, each pixel count gives us a specific intensity at a specific point in space.

Figure 3.24 shows an absorption imaging set-up that uses a pair of plano convex lenses to image the shadow onto the CCD ship. We find that the shadow caused by the MOT diffracts over short distances away from the MOT. Imaging the MOT in this fashion minimizes the diffraction of the shadow. The first lens has a focal point of $f_1 = 150$ mm, and the second lens has a focal point $f_2 = 300$ mm. This corresponds to a magnification of the image by a factor of 2, which is advantageous for measuring the dipole trap (typically much smaller in size than the MOT). Figure 3.25 shows a typical absorption measurement using this set-up. The horizontal axes give the positions of the MOT in the plane transverse to the propagation of the probe laser. The vertical axis is the optical density of the MOT.

---

[3] We use one of two CCD cameras. We use a Spectrum One 3000, liquid nitrogen cooled CCD camera for sensitive detection, and a Pulnix room temperature CCD camera when high sensitivity is not required.

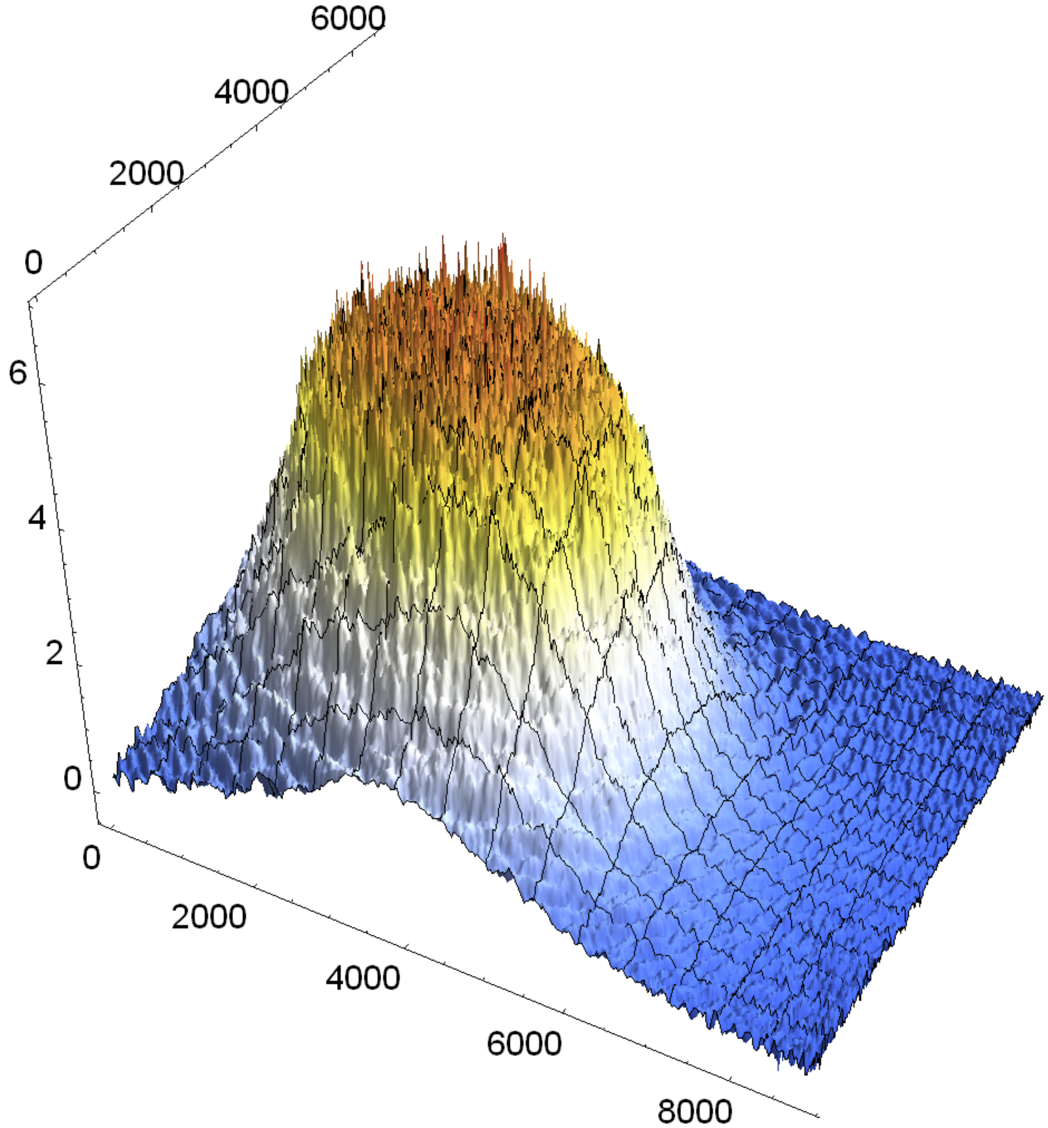

Figure 3.25: An absorption image of the magneto-optical trap.

Data analysis

The data analysis was done in *Mathematica* [71]. We determine three characteristics of the traps: the trap size, the numbers of atoms trapped, and the peak density of the trap.

The intensities are measured with a CCD camera. Consider figure 3.26. Each pixel counts the number of photons per frame, *i.e.* measures a power at the location of that pixel. It is helpful to think of each pixel as an infinitesimal area element, A_{ij}, which (if A_{ij} is small enough) can map out the intensity profile illuminating the CCD chip.

To this end, we take three pictures. Picture 1 is a CCD image of the resonant probe beam in the presence of the trapped atoms; call this image *Absorption*. Picture 2 is a CCD image of the probe beam absent any atoms; call this image *Probe*. Finally, we take a third image of the background scattered light; call this image *Background*. This is accomplished by shuttering the probe beam, while keeping all other lasers unblocked.

From, equation (3.8), the optical density measured at the ith, jth pixel is then determined by

$$\mathrm{OD} = \ln(Probe - Background) - \ln(Absorption - Background), \tag{3.9}$$

Now, we will consider the CCD data. Ultimately, the data from the CCD is saved as a tab delimited text file arrayed with 1028×256 numbers. A photon count in the ith and jth array element corresponds to the number of photon counts made by a pixel in the ith row and j column. Consider figure 3.26. Thus the CCD chip gives us a spatial distribution of intensities. Therefore, computing equation (3.9) at each pixel yields

$$\mathrm{OD}_{ij} = \ln(Probe_{ij} - Background_{ij}) - \ln(Absorption_{ij} - Background_{ij}), \tag{3.10}$$

which we can then use to map out spatial distribution of optical densities, and ultimately learn many characteristics about our traps. Next, we can convert equation (3.10) to column densities using the resonant scattering cross-section.

$$\sigma_0 = (BR)\frac{3\lambda^2}{2\pi}, \tag{3.11}$$

where σ_0 is the resonant scattering cross-section [41, 70]. In addition, $BR = \Gamma_{4\to 3}/(\sum \Gamma_i)$ is the branching ratio, $\Gamma_{4\to 3}$ is the decay rate from $|F' = 4\rangle$ to $|F = 3\rangle$ and the factor $\sum \Gamma_i$ is the sum of all the possible decays[4].

$$\tilde{n}_{ij} = \frac{1}{\sigma_0}\mathrm{OD}_{ij} \tag{3.12}$$

---

[4] For the case that the probe laser is resonant with the $|F = 3\rangle \to |F' = 4\rangle$ transition in ^{85}Rb

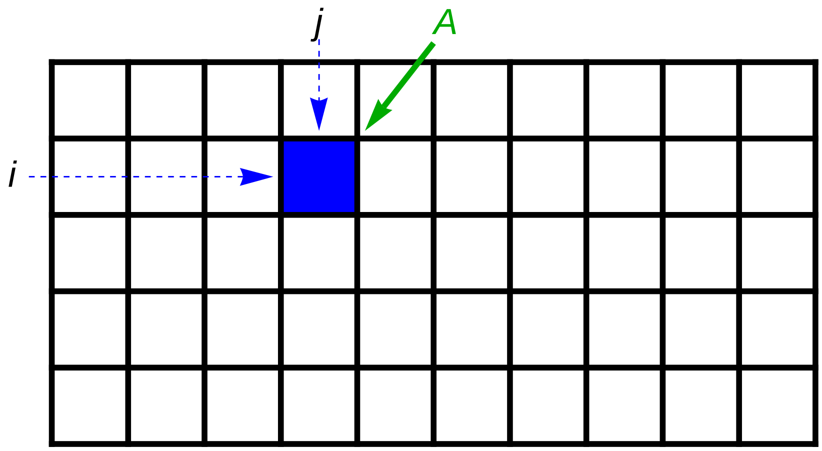

Figure 3.26: An example of a CCD chip. Each white square represents a pixel. The blue square is a pixel under consideration, located in the ith row and jth column. It has an area A_{ij}.

Recognize that a consideration of the entire matrix $\tilde{n}_{ij}$ should match the form of our model found in equation (3.7). Thus, we use *Mathematica* to fit equation (3.7) to the data contained in the matrix described by equation (3.12). For clarity, we write down the exact form that we are fitting to the data.

$$\mathrm{OD}(x,y) = \mathrm{OD}_{\mathrm{peak}} \exp\left(-\frac{(x-x_0)^2}{2\chi^2} - \frac{(y-y_0)^2}{2\psi^2}\right) \tag{3.13}$$

Using OD_{peak}, x_0, y_0, χ, and ψ as fitting parameters, we will have an analytical column density definition for the optical density that can be used to determine various trap characteristics.

3.6.4 Trap size, and trap numbers

After making the fit described in equation (3.13), we need only read off the vales of χ and ψ to get the trap size. The matrix expressed in equation (3.12) can be used to directly measure the trap numbers. Alternatively, we could use the fitted model. In fact, we have *Mathematica* perform both methods. To be clear, I will call the first method a "direct measurement", and the second method a "measurement from a model". Consider the first method.

Direct measurement

The column density is defined in equation (3.12). The column density is the number of atoms per unit area. Therefore, the total trap numbers can be determined by integrating over the entire area of the trap. With a CCD image, this is performed by summing over all the pixels.

First, consider a specific pixel, like in figure 3.26. If the area of the pixel, A_{ij}, is sufficiently small[5] then we can approximate the pixel to be an infinitesimal measurement of the column density. Namely, we can write the column density

$$\tilde{n}_{ij} = \frac{N_{ij}}{A_{ij}}, \tag{3.14}$$

---

[5] $A \ll \chi\psi$

where N_{ij} is the number of atoms measured by the pixel located in the row i and column j, A_{ij} is the area of the pixel located in the row i and column j (for our CCD cameras, $A_{ij} = A = \text{const.}$).

$$\mathrm{OD}_{ij} = \frac{N_{ij}}{A}\sigma_0. \tag{3.15}$$

Therefore, we determine the total number of atoms by summing over i and j.

$$N_{\text{tot}} = \sum_i \sum_j N_{ij} = \frac{A}{\sigma_0} \sum_i \sum_j \mathrm{OD}_{ij} \tag{3.16}$$

Measurement from model

Since we have the fitted function in equation (3.13), we can just as easily get trap numbers by analytically integrating this function.

$$\begin{aligned} N &= \int \tilde{n}(x,y)\,\mathrm{d}A = \frac{1}{\sigma_0}\int \mathrm{OD}(x,y)\,\mathrm{d}A \\ &= \frac{1}{\sigma_0}\int_{-\infty}^{+\infty}\int_{-\infty}^{+\infty} \mathrm{OD}_{\text{peak}} \exp\left(-\frac{(x-x_0)^2}{2\chi^2} - \frac{(y-y_0)^2}{2\psi^2}\right)\mathrm{d}x\,\mathrm{d}y \end{aligned}$$

Therefore, for a trap described by our model, the total number of atoms can be computed from the model with

$$N = \frac{2\pi\chi\psi}{\sigma_0}\mathrm{OD}_{\text{peak}}. \tag{3.17}$$

The factors χ, ψ, and $\mathrm{OD}_{\mathrm{peak}}$ are all fit parameters that are determined by the *Mathematica* code. We find that there is (typically) a factor of 2 discrepancy between the determination of N from the CCD pixels, and from the model. This occurs when the MOT density profile is non-Gaussian (which occurs at high densities with the so-called "flat-top MOT"). The measurement of N from summing CCD pixels is the most accurate method.

3.6.5 Densities

The fitted equation in equation (3.13) follows directly to the column density.

$$\begin{aligned}\tilde{n}(x,y) &= \frac{1}{\sigma_0}\mathrm{OD}(x,y) \\ &= \frac{1}{\sigma_0}\mathrm{OD}_{\mathrm{peak}}\exp\left(-\frac{(x-x_0)^2}{2\chi^2}-\frac{(y-y_0)^2}{2\psi^2}\right) \\ &= \tilde{n}_{\mathrm{peak}}\exp\left(-\frac{(x-x_0)^2}{2\chi^2}-\frac{(y-y_0)^2}{2\psi^2}\right),\end{aligned} \tag{3.18}$$

where $\tilde{n}_{\mathrm{peak}} = \mathrm{OD}_{\mathrm{peak}}/\sigma$ is the peak column density of the trap. Finally, to get the peak density of our trap, we use equation (3.18).

$$\tilde{n}_{\mathrm{peak}} = \sqrt{2\pi}\psi n_{\mathrm{peak}} = \frac{\mathrm{OD}_{\mathrm{peak}}}{\sigma_0}$$

Therefore,

$$n_{\mathrm{peak}} = \frac{1}{\sqrt{2\pi}\psi\sigma_0}\mathrm{OD}_{\mathrm{peak}} \tag{3.19}$$

3.6.6 Probe transmission

The experimental set-up for this procedure consists of a weak probe laser focused at the center of the trap. Focusing the laser allows us to only sample the peak density. Start with equation (3.3), and incorporate equation (3.6). The size of the probe is small compared to that of the MOT (probe is $\sim 10\%$ the size of the MOT). The total power of the transmitted probe is measured by a photodiode. In addition, the frequency is scanning over a transition. This will be referenced to the cycling transition, $|F=3\rangle \rightarrow |F'=4\rangle$, by the quantity,

$$\Delta = \omega - \omega_{\text{cycle}}, \tag{3.20}$$

where Δ is the detuning, ω is the frequency of the incident photon, and ω_{cycle} is the frequency of the cycling transition. Now, consider equation (3.3). Is the intensity independent of the coordinate z? Well, let's consider our set-up. A weak laser beam with a waist of $w_1 = 340\ \mu\text{m}$ is tuned to the above mentioned cycling transition passes through a lens of focal point, $f = 0.3$ m. The focus of the laser pierces the center of trap. For a laser of wavelength $\lambda = 780$ nm, this corresponds to a Rayleigh range of about $z_R = 30$ cm. The trap has a $1/e^2$ radius of about 1 mm. Therefore, for all practical purposes, the laser remains well collimated. The input and output intensity profiles are of the form of a collimated Gaussian distribution.

$$\begin{aligned} I_0(x,y) &= I_0 e^{-2(x^2+y^2)/w_0^2} \\ I_{\mathrm{out}}(x,y) &= I_{\mathrm{out}} e^{-2(x^2+y^2)/w_0^2} \end{aligned} \tag{3.21}$$

So, the explicit z-dependence of the laser drops out, and the Gaussian factor is the same for both the input and output beams (since the beam is collimated over the region of the trap). Beer's law reduces to:

$$\begin{aligned} \ln\left(\frac{I_{\mathrm{out}}(x,y)}{I_0(x,y)}\right) = \ln\left(\frac{I_{\mathrm{out}}}{I_0}\right) &= -\mathrm{OD}(x,y;\Delta) \\ &\equiv -\sigma(\Delta)\sqrt{2\pi}\psi n_{\mathrm{peak}} \exp\left(-\frac{(x-x_0)^2}{2\chi^2} - \frac{(y-y_0)^2}{2\psi^2}\right), \end{aligned} \tag{3.22}$$

where Δ is defined in equation (3.20), $I_{\mathrm{out}}(x,y)$ is the transmitted intensity of the probe beam at a particular detuning, $I_0(x,y)$ is the incident intensity of the probe beam at a particular detuning, and $\sigma(\Delta)$ is the photon scattering cross-section for a given detuning from the cycling resonance. Before we delve into the scattering cross-section, let us look at the density term. Assuming the laser passes through the center of the trap, consider the density that the center of the laser beam sees and the density that the wings of the laser see. From Table 3.3, we see that the density is uniform across the probe laser beam. Then, the density right-hand side

Table 3.3: A comparison of the density distribution across the probe laser when the $w_0 = 10\%$ of the trap size. For all practical purposes, the density is uniform for all regions of the probe laser. In addition, we are probing the peak density of the trap.

Center Position of Probe	$\boldsymbol{x^2 + y^2 = w_0^2}$ **Position of Probe**
$\tilde{n} = \sqrt{(2\pi)} n_{\text{peak}}$	$\tilde{n} = (0.98)\sqrt{(2\pi)} n_{\text{peak}} \approx \tilde{n}(x = 0, y = 0)$

of equation (3.22) reduces to the following.

$$\ln\left(\frac{I_{\text{out}}}{I_0}\right) = -\text{OD}(\Delta) = -\sigma(\Delta)\sqrt{2\pi}\psi n_{\text{peak}} \tag{3.23}$$

The scattering cross-section off-resonance is given as [41, 72]:

$$\sigma(\omega) = \sum_i \frac{\sigma_{0,i}}{1 + 4((\omega - \omega_{0,i})/\Gamma_i)^2 + (I_0/I_{\text{sat},i})}, \tag{3.24}$$

where $\sigma_{0,i}$ is the resonant scattering cross-section for the ith transition, Γ is the natural line width of the ith transition, I_0 is the intensity of incident probe laser, and $I_{\text{sat},i}$ is the saturation intensity of the ith transition. We will choose our laser intensity to be much less than the saturation intensity, $(I_0/I_{\text{sat},i} \ll 1)$.

$$\begin{aligned} \sigma(\omega) &= \sum_i \frac{\sigma_{0,i}}{1 + 4((\omega - \omega_{0,i})/\Gamma_i)^2} \\ &= \sum_i \sigma_{0,i} \frac{(\Gamma_i/2)^2}{(\Gamma/2)^2 + (\omega - \omega_i)^2}, \end{aligned} \tag{3.25}$$

It is often helpful to write this in terms of a detuning, Δ. As was mentioned before (and from hence forth), Δ will always be the detuning with respect to the primary cycling transition. To this end, I will add and subtract ω_{cycle}'s where ever appropriate.

$$\sigma(\omega) = \sum_i \sigma_{0,i} \frac{(\Gamma_i/2)^2}{(\Gamma/2)^2 + (\omega - \omega_{\text{cycle}} + \omega_{\text{cycle}} - \omega_i)^2}, \tag{3.26}$$

We recognize that $\omega - \omega_{\text{cycle}} \equiv \Delta$ and that $\omega_{\text{cycle}} - \omega_i \equiv \Delta_i$ is the detuning of the transition from the main cycling transition. Then, the photon scattering cross-section can be written in terms of the detuning, Δ.

$$\sigma(\omega) = \sum_i \sigma_{0,i} \frac{(\Gamma_i/2)^2}{(\Gamma/2)^2 + (\Delta + \Delta_i)^2}, \tag{3.27}$$

In Rubidium 85, there are three possible transitions from the upper hyperfine ground state, $|F = 3\rangle \rightarrow |F' = 2, 3, 4\rangle$.

3.7 Instrument and computer interface

Successful atomic experiments require a choreographed ballet performed by a number instruments and devices. This dance is synchronized by two primary controllers: a computer and a digital pulse generator. What follows is description of all the instruments involved the MOT and EIT, a description of our digital signal generator, and a description of the computer interface.

3.7.1 Computer control

We use an HPE-360z computer to control and analyze our experiment. Two software programs are used to interface with our instruments: CamWare and LabVIEW. CamWare is a program designed by pco.imaging to interface with their charge coupled device (CCD) camera, pco.pixelfly. The software interfaces through USB connections. From CamWare, the user can control all the camera settings (exposure time, triggering, etc.). The CCD camera accepts TTL triggers. In general, we set the camera setting using CamWare, then trigger the camera to record an image from an external source (such as LabVIEW or the digital signal generator). The CCD camera can store up to 100 images within its own memory. This allows us to execute an experimental sequence, store all data on the CCD camera, then transfer all images through the USB interface after the experiment is complete.

Loaded onto the HP computer is the software called LabVIEW, for which we use to communicate with most instruments. LabVIEW is created by the company National Instruments. The software is a graphical programming language that allows the user to acquire and analyze measurements, control instruments, send/receive analogue and digital signals, etc. In our lab, we use LabVIEW to communicate through a GPIB interface, and two SCB-68A I/O modules.

The GPIB interface is used for two instruments: Tektronix TDS 3054 Oscilloscope and a Sorensen HPD 1520 power supply. For a typical EIT experiment, the photodiode measurement of a probe transmission through the atomic medium is recorded by the oscilloscope. We use LabVIEW to transfer the data from the oscilloscope to the computer, where it is saved as a text file. The Sorensen serves as our MOT current supply. From LabVIEW we control the current output for the anti-Helmholtz coils. GPIB communication is slow ($\sim$ 100 ms), but this is the only mode of communication between the computer and power supply. In this experiment, we require faster control of the current. A home-built circuit was implemented that accepts a TTL pulse.

The SCB-68A I/O module is a board produced by National Instruments that has analog inputs and outputs, as well as digital inputs and outputs. We use analog inputs to monitor the fluorescence recorded by a photodiode. We use analog outputs to control RF frequency modulation on the acousto-optical drivers and for set-point adjustments on the diode laser servo-sidelock circuits.

This computer runs Windows 8 as its operating system, and suffers from the usual interruptions that we have all come to love about Microsoft. For this reason, the best we can do is $\sim$ 10 ms timing precision. This is not adequate to control the EIT experiment. Therefore, we implemented a digital signal generator to control the EIT timing sequence, while the computer handles the slower processes (such as reading and analyzing data).

3.7.2 Digital signal generator

To control the EIT timing sequence, we use an HP 8175A digital signal generator (DSG). The DSG serves as a master clock for the computer, shutters the lasers on and off via their AOMs, and controls the fast switch for the MOT current. The user interface is through a monitor and key-pad fixed to the front panel of the DSG. There is an option to communicate via HPIB (the predecessor to GIPB), but front panel operation is sufficient for our applications. There are twenty-one possible output channels for which digital signals can be sent. A program can be entered as "data" by navigating to the appropriate screen, and entering a series of 1's and 0's a sequence. Entering a "1" ("0") indicates that the DSG is to send 5 V (0 V) through the appropriate channel for appropriate time interval. The time interval may range from 20 ns to 9.99 s. For EIT spectra experiments, we find that 100μs is sufficient.

A typical EIT run involves sustaining a steady-state MOT, turning OFF the MOT, then switching-ON the two EIT laser fields. The DSG controls all these operations. A DSG signal is used as the TTL trigger for the MOT coil switch circuit, and another signal is used to trigger the CCD camera. We shutter the probe, control, and repumping laser using their corresponding AOMs. The RF drivers for the AOMs accept anolog inputs that range from 0-1 V (0 V being off, and 1 V being full RF power). Since the signal originating from the DSG is digital (not analog) we use home-built voltage follower circuits to convert the digital signals. Finally, we use the DSG as a master clock for the HPE-350v computer. The SCP-68A I/O module has a counter on-board. We send a series of TTL pulses from the DSG to the counter synchronize the computer generated RF frequency modulation with the EIT sequence. The RF frequency modulation is the method by which we ramp the probe laser (or control laser) frequency to generate the spectra reported in this dissertation.

Chapter 4

Electromagnetically induced transparency with Gaussian and Laguerre-Gaussian mode lasers

4.1 Introduction

Electromagnetically induced transparency (EIT) is an optical technique used to manipulate quantum states of atoms and photons [1]. A control laser modifies the absorption profile of a probe laser, causing coherent destructive interference of excitation pathways of the atom. The result is an increased transmission of the probe laser tuned to an atomic resonance where absorption is otherwise expected. Applications of EIT range from coherent storage of light in the atomic medium for quantum information storage [2,3], nonlinear optics [4], and lasing without population inversion [5].

Initial spectroscopic studies of EIT were performed in an atomic gas at room temperature [6]. Large laser powers can overcome the Doppler broadening, but cause homogeneous line broadening, though specific Doppler-free techniques produce EIT signals in a room temperature gas with moderate laser powers [7–10]. Alternatively, experiments that produce ultracold samples of atomic gases result in Doppler-broadening smaller than the natural linewidth of the atomic transition. The reduced transverse motion of cold atoms also suppresses the decoherence due to diffusion. Ultracold gases also offer high densities, typically in the range from $10^9 - 10^{12}$ cm^{-3}. For these reasons, EIT has been extensively studied in this environment [11–15].

One consequence of EIT is the slowing of light in an atomic sample. The destructive interference of excitation pathways in EIT leads to a sub-natural linewidth transmission feature. There is no theoretical minimum to the linewidth, which is only limited by experimental constraints, such as background magnetic fields, laser linewidth, atomic collisions, and other homogeneous broadening [1]. Slow light results from enhancement of the slope of the dispersion in the frequency range near the EIT resonance. Lowering of the intensity of the control field leads to narrowing of the EIT linewidth and results in the decreasing of probe group velocity. Speeds many orders of magnitude less than c have been achieved in an ultracold gas [16] and in room temperature gases [17,18]. A slowed probe pulse propagating through the medium can be coherently stored in and retrieved from the atoms by adiabatically switching the control laser off and on [2,3].

Incorporation of a laser propagating in a Laguerre-Gaussian (LG$_p^\ell$) mode to EIT is of considerable interest. The azimuthal winding phase ($e^{i\ell\phi}$) leads to quantized orbital angular momentum (OAM) of $\ell\hbar$ per photon. A probe laser carrying OAM generates a manifold of information degrees of freedom, allowing multi-dimensional quantum computing and encryption [22]. Storage of LG_p^ℓ mode probe pulses in gases has been demonstrated in both room temperature gases [23–26], and in ultracold gases [27–30]. The OAM forces the intensity to go to zero at the center, and the additional p radial nodes give rise to "doughnut" shaped beams, or even concentric ring intensity patterns and a spatially varying Rabi frequency.

A control laser with a large Rabi frequency (as compared to the decoherence rates) increases the signal contrast of the EIT feature, while a small Rabi frequency results in a narrower EIT resonance. Placing a control laser in an LG_p^ℓ mode, and aligning the probe laser to the central node causes most of the probed atoms to experience a low control field, resulting in a narrowing of the EIT resonance. Then, the control laser power can be increased, improving the signal. Previously, subnatural linewidths were observed in the EIT transmission spectra using an LG_0^1 control beam in room temperature gases [19, 20]. Remarkably, the LG_0^1 control laser reduced the EIT linewidth by a factor of 2 as compared to a similar experiment with the control in a Gaussian mode. The transmission results were reported in arbitrary units, so a comparison of the contrast for the two modes could not be made. It was proposed in ref. [20] that the OAM of the control beam could decrease the decoherences due to transit effects of the room temperature gas. However, they show that increasing OAM does not increase the narrowing and argue that the reduction in EIT linewidth is due entirely to the spatial dependence of the control Rabi frequency.

We measure EIT transmission spectra using an LG_0^1 laser mode in ultracold atoms prepared in a magneto-optical trap (MOT). We find narrowing of the EIT resonance, and in the ultracold system transit decoherences are negligible. We measure EIT linewidths with the control beam in the LG_0^1 mode and the probe in the fundamental Gaussian mode for four different EIT configurations of the D2 line for both ^{85}Rb and ^{87}Rb. We compare this data with EIT spectra where both the probe and the control lasers are in the fundamental Gaussian mode. A theoretical model is used to analyze each configuration. We use a density matrix formalism for a six level system presented in chapter 2. The six levels are composed of the two ground-state hyperfine levels and the four excited-state hyperfine levels of the D2 transition in ^{85}Rb and ^{87}Rb. In our model, we do not include the magnetic sub-levels of each of the hyperfine levels. We model the fields as plane-waves when the control is in the fundamental mode, and include the spatially varying Rabi frequency when the control is in the LG_0^1 mode [19, 21]. A transmission spectrum is generated from the steady-state solutions of the density matrix equations. We find good agreement between the model and the experiment. For both theory and experiment, we observe narrower EIT resonance features with the control laser in the LG_0^1 mode than with the control laser in the Gaussian mode.

4.2 Experimental Design

The experimental set-up for our MOT is shown in Fig. 4.1 and is similar to that found in [73]. The trapping laser is a low-powered external-cavity diode laser locked $\simeq 15$ MHz to the red of the $|F = 3\rangle \rightarrow |F' = 4\rangle$ ($|F = 2\rangle \rightarrow |F' = 3\rangle$) atomic transition in ^{85}Rb (^{87}Rb) as shown in Fig. 4.2. It is amplified by a tapered amplifier in the master-oscillator power-amplifier configuration and spatially filtered using a polarization maintaining single-mode fiber. The output of the fiber has a power of 175 mW, and is telescoped to a $1/e^2$ beam diameter of 2.5 cm. It is further split into six beams, three of the beams are directed toward the cell along three orthogonal axes, and the other three beams counter-propagate along these axes with opposite circular polarizations. The repumping laser is locked on resonance with the $|F = 2\rangle \rightarrow |F' = 3\rangle$ ($|F = 1\rangle \rightarrow |F' = 2\rangle$) atomic transition in ^{85}Rb (^{87}Rb) as shown in Fig. 4.2. The laser has a power of 10 mW, is telescoped to a $1/e^2$ diameter of 2.5 cm, and is directed through a polarizing beam-splitter (PBS) to co-propagate with the trapping laser. The MOT routinely traps 10^8 atoms at a temperature of 50 μK. The density distribution of the atoms is Gaussian with a peak density of $(1 - 5) \times 10^{10}$ cm^{-3} and $1/e^2$ radius of $\simeq 2$ mm. Three sets of Helmholtz coils eliminate the effects of background magnetic fields.

The probe laser is also an external cavity diode laser. The frequency of the probe is scanned $150 - 500$ MHz across the resonances indicated in Fig. 4.2 by

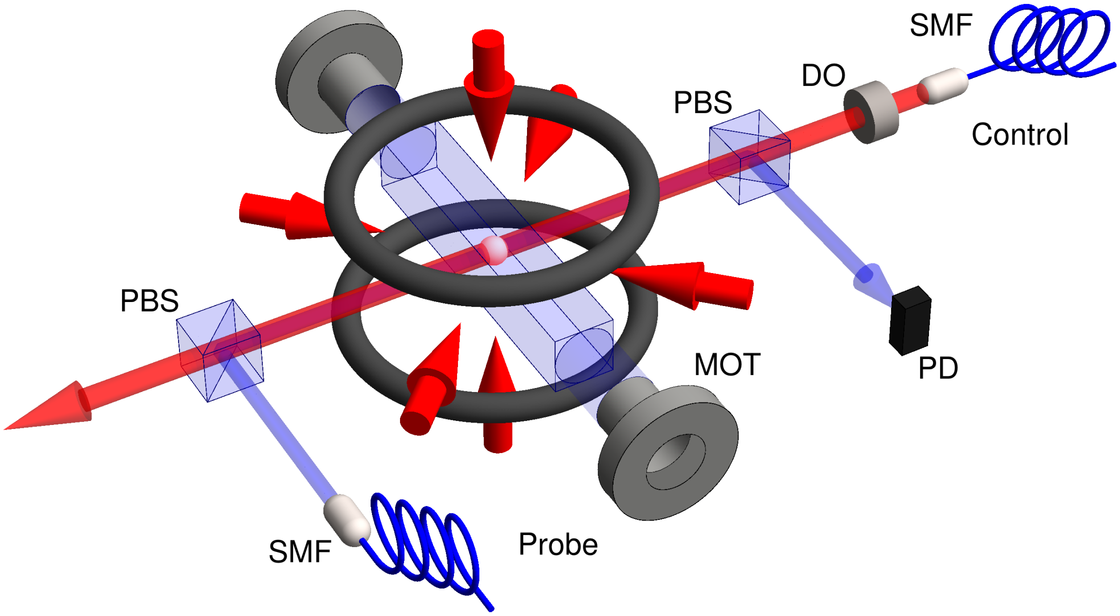

Figure 4.1: Schematic of the ultracold EIT experimental apparatus. The magneto-optical trap (MOT) consists of a pair of anti-Helmholtz coils, six orthogonal and counter-propagating trapping lasers, and a repumping laser (co-propagating with the trapping laser). The control laser is indicated by the transparent red beam. The probe laser is indicated by the transparent blue beam. The control and the probe have orthogonal linear polarizations, and are combined/separated using polarizing beam-splitters (PBS), and are counter-propagating. The probe is imaged on a photodiode (PD).

ramping the voltage across a piezoelectric transducer attached to the grating that serves as the output coupler on the external cavity [55]. The probe laser is shuttered using an acoustic optical modulator (AOM), and is spatially filtered using a polarization maintaining fiber optic cable. The power after the fiber is approximately 10 μW and is linearly polarized. The beam is overlapped with the control laser with a PBS and directed through the center of the MOT (Fig. 4.1) with a $1/e^2$ radius of 430 μm. After passing through the ultracold atomic sample, the probe is separated from the counter-propagating control laser with another PBS and is focused onto a Thorlabs DET200 photodiode (PD) that records the EIT transmission spectrum.

The control laser is locked near the transition indicated in each of the four configurations shown in Fig. 4.2. We use a dichroic atomic vapor laser lock (DAVLL) [74], resulting in a frequency stability of $\simeq$ 1.5 MHz. The laser is shuttered using an AOM, and spatially filtered using a polarization maintaining fiber optic cable. The output of the fiber is $\simeq$ 10 mW. To select an appropriate Rabi frequency, we attenuate the power using a set of neutral density filters. The polarization of the control laser is orthogonal to the probe, and the beam is directed counter-propagating to the probe using a PBS (Fig. 4.1). At the MOT, the control laser has a $1/e^2$ radius of 1.1 mm when in the Gaussian mode and 270 μm when in the LG_0^1 mode. The LG_0^1 mode beam waist is smaller than the Gaussian mode waist to increase the peak intensity of the control beam. This is necessary

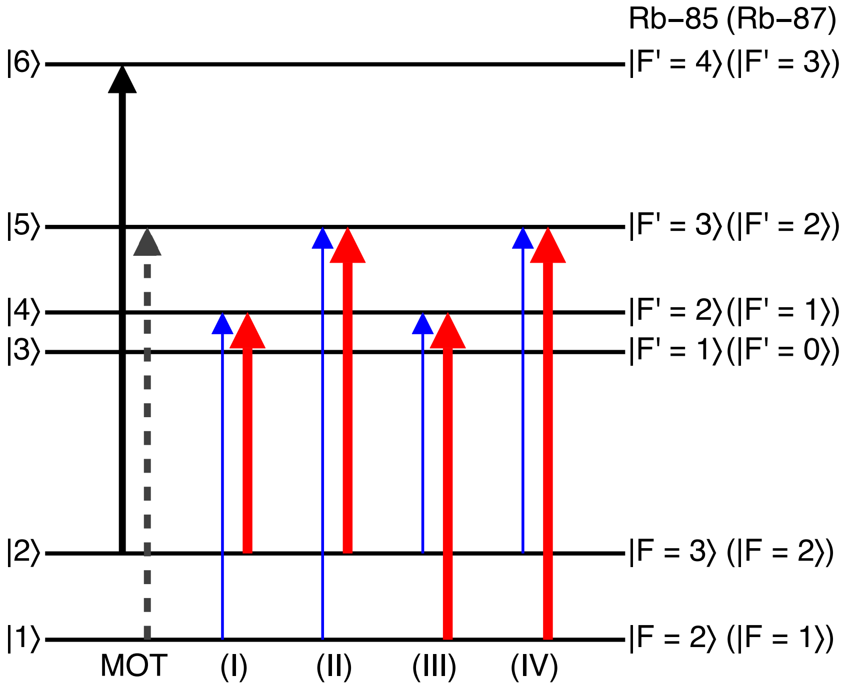

Figure 4.2: The six hyperfine states for the D2 transition in ^{85}Rb (^{87}Rb). The solid black arrow corresponds to the trapping laser, and the gray dashed arrow corresponds to the repumping laser in our magneto-optical trap (MOT). Four EIT configurations on the D2 transition are indicated with Roman numerals. The thin blue arrows represent the probe laser, while the thick red arrows represent the control laser.

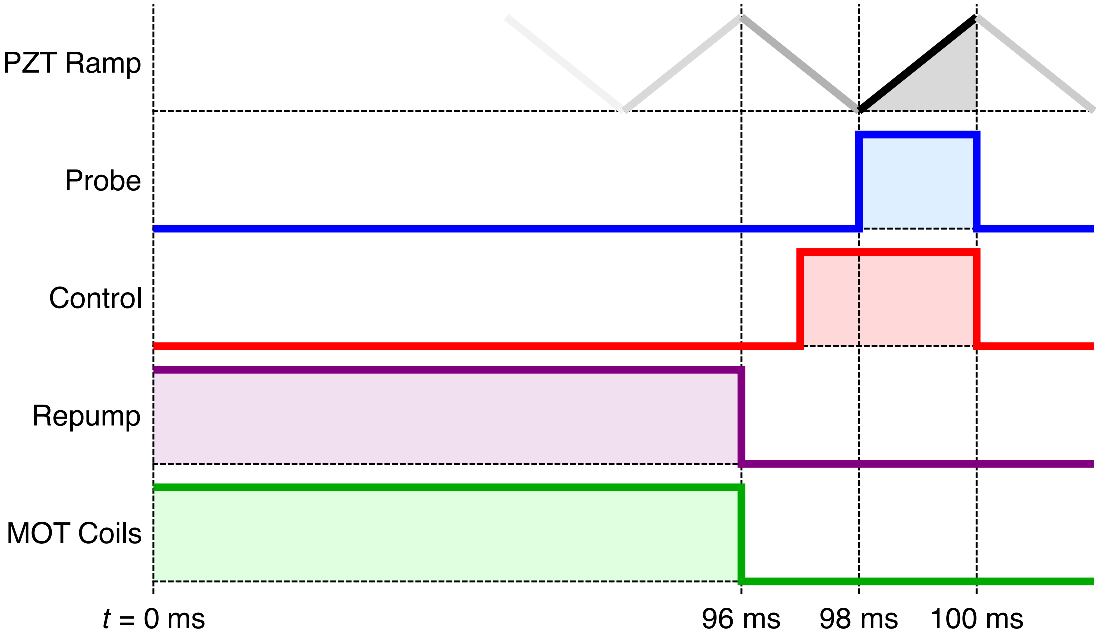

Figure 4.3: The timing sequence used to measure the transmitted probe profile using a CCD camera.

to counteract the loss of laser power after converting the Gaussian mode to the LG_0^1 mode[1]. Since the control laser is a diode laser, the generation of LG_p^ℓ modes must occur external to the cavity. We shape the control laser into an LG_0^1 mode using diffractive optics [62].

The EIT sequence is controlled by a Hewlett-Packard 8175A Digital Signal Generator. Digital pulses shutter the AOMs on the probe, control, and the repump lasers, and control the current flowing through the MOT coils, which can be turned off in 10 μs. Initially, the MOT is held in a steady state for 96 ms, and the probe and the control lasers are off. Next, the magnetic field is switched

---

[1] This is also necessary to fight the strong decohernece rate introduced into our system by producing the probe and control lasers with independent ECDLs. This is elaborated upon in the results section

off and we optically pump the atoms for 1 ms. The optical pumping procedure depends on the EIT configuration. For configurations (I) and (II), the repump laser is switched off while the trapping laser optically pumps all the atoms into the lower hyperfine ground-state. For configurations (III) and (IV), the repump laser stays on to optically pump any atoms from the lower hyperfine ground state to the upper hyperfine ground state. After optical pumping, the control and probe lasers perform the EIT spectroscopy. The control laser pulse is 3 ms and precedes the probe laser pulse by 1 ms to prepare the atoms for EIT. The probe laser is on for 2 ms, during which it scans between $150 - 500$ MHz, depending on the EIT configuration studied. A photodiode detects the probe transmission and the signal is read on a TDS-3054 oscilloscope. The entire procedure takes 0.1 s, and we cycle continuously so the MOT is approximately in a steady state. Each measurement is a single cycle. We do not average multiple cycles because the frequency stabilization of the control laser is noisy. Averaging multiple cycles artificially removes a large fraction of the EIT signal.

4.3 Results

Spectra for all four EIT configurations are measured for ^{87}Rb, and configurations (I) and (II) are measured for ^{85}Rb. Figure 4.4 (a) shows a measurement of the EIT spectra of ^{85}Rb when the control is in the LG_0^1 mode, and Fig. 4.4 (b) shows the same measurement with the control in the Gaussian mode. A best fit from the model is also shown in Figs. 4.4 (a) and (b). The control laser is locked near the $|F = 3\rangle \rightarrow |F' = 2\rangle$ hyperfine transition, while the probe scans over the $|F = 2\rangle \rightarrow |F' = 1, 2, 3\rangle$ dipole allowed transitions. The EIT feature occurs in the $|F = 2\rangle \rightarrow |F' = 2\rangle$ transmission peak, which corresponds to configuration (I) in Fig. 4.2. We find excellent agreement between the model and data. We determine the EIT characteristics from the model. In Fig. 4.4 (a), the control laser is in the LG_0^1 mode with $\Omega_{0c,32} = 16$ MHz, and the laser frequency is 1.4 MHz above the $|F = 3\rangle \rightarrow |F' = 2\rangle$ transition. The FWHM of the EIT feature is 0.67Γ, where $\Gamma = 2\pi \times 6.07$ MHz. In Fig. 4.4 (b), the control laser is in the Gaussian mode with $\Omega_{0c,32} = 9.5$ MHz, and the laser frequency is 1.8 MHz below the $|F = 3\rangle \rightarrow |F' = 2\rangle$ transition. The FWHM of the EIT feature is 0.73Γ. The different values for the control laser frequency detuning are due to a drift in the lock of the control laser.

Figure 4.5 (a) shows a measurement of the EIT spectra of ^{87}Rb when the control is in the LG_0^1 mode, and Fig. 4.5 (b) shows the same measurement with the control in the Gaussian mode. A best corresponding fit from the model is also shown in Figs. 4.5 (a) and (b). The control laser is locked near the $|F = 2\rangle \rightarrow |F' = 1\rangle$ hyperfine transition, while the probe scans over the $|F = 1\rangle \rightarrow |F' = 0, 1, 2\rangle$ dipole allowed transitions. The EIT feature occurs in the $|F = 1\rangle \rightarrow |F' = 1\rangle$ transmission peak, which corresponds to configuration (I) in Fig. 4.2. We again determine the EIT characteristics from the fit. In Fig. 4.5 (a), the control laser is in the LG_0^1 mode with $\Omega_{0c,21} = 20$ MHz, and the laser frequency is 0.1 MHz below

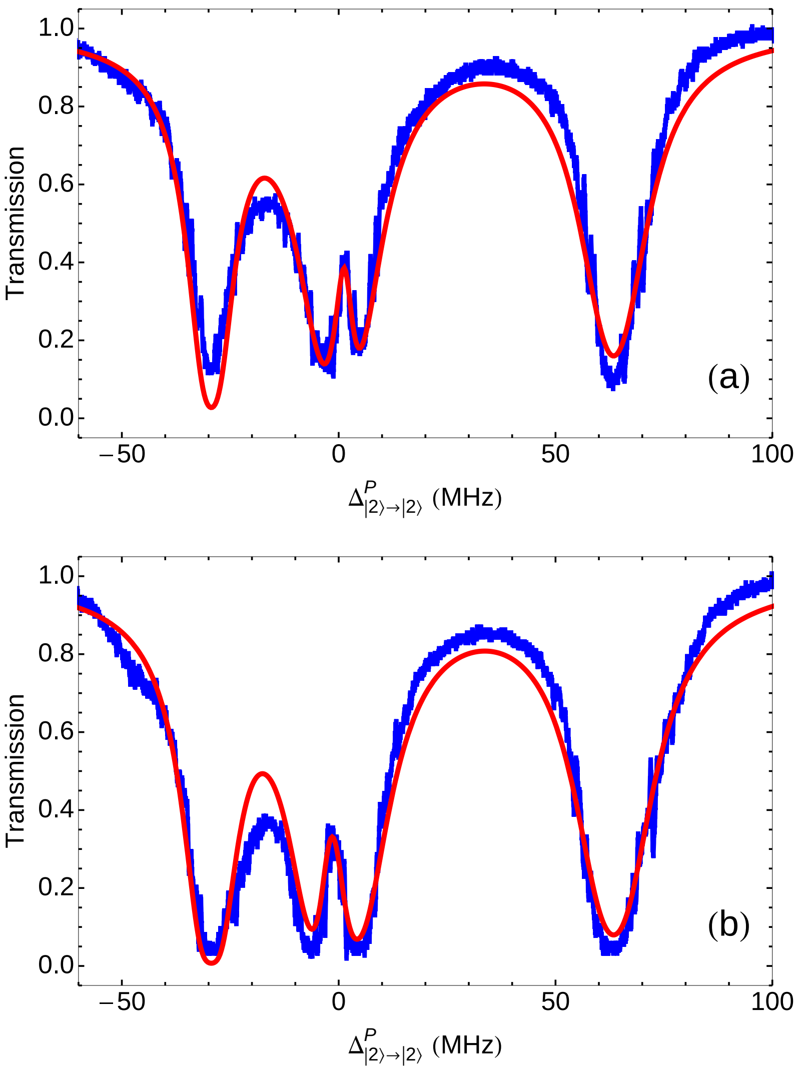

Figure 4.4: The transmission spectrum for a probe laser scanning over the transitions $|F = 2\rangle \to |F' = 1, 2, 3\rangle$ in ^{85}Rb. The blue curve is the observed signal, and the red curve is the model. (a) The control laser is in the LG_0^1 mode 1.4 MHz above the $|F = 3\rangle \to |F' = 2\rangle$ transition with $\Omega_{0c,32} = 16$ MHz. (b) The control laser is in the Gaussian mode 1.8 MHz below the $|F = 3\rangle \to |F' = 2\rangle$ transition with $\Omega_{0c,32} = 9.5$ MHz. Both data sets represent Configuration-(I).

the $|F=2\rangle \rightarrow |F'=1\rangle$ transition. The FWHM of the EIT feature is 0.8Γ. In Fig. 4.5 (b), the control laser is in the Gaussian mode with $\Omega_{0c,21} = 9.5$ MHz, and the laser frequency is 0.7 MHz above the $|F=2\rangle \rightarrow |F'=1\rangle$ transition. The FWHM of the EIT feature is 0.46Γ. Again, there is excellent agreement between experiment and theory.

We make similar measurements on the other configurations in Fig. 4.2. The results for ^{85}Rb are found in table 4.1, and the results for ^{87}Rb are in table 4.2. For ^{85}Rb, the observed EIT linewidths are approximately the same, but $\Omega_{0c,kl}$ for the control laser for the LG_0^1 system is 70% larger. The larger intensity is necessary to achieve sufficient signal. Increasing the intensity of the Gaussian control laser for direct comparison would lead to an additional feature in the transmission profile due to effects coming from the degenerate Zeeman sublevels not included in our model [75]. For ^{87}Rb, the EIT linewidths we observe are a factor of two larger than those with a Gaussian control beam, but the corresponding values of $\Omega_{0c,kl}$ are 2.5 to 5 times larger. We also used our model to investigate the predicted linewidths of the EIT for the opposite control mode with same $\Omega_{0c,kl}$ (shown in the final column of Tables 4.1 and 4.2). The measured linewidths of a configuration with a given $\Omega_{0c,kl}$ in the LG_0^1 mode are narrower than the predicted linewidths of the identical configuration with the control in the Gaussian mode. Similarly, the predicted linewidths of a configuration with a given $\Omega_{0c,kl}$ of the control in the LG_0^1 mode are narrower than the measured linewidths of the identical configuration with the

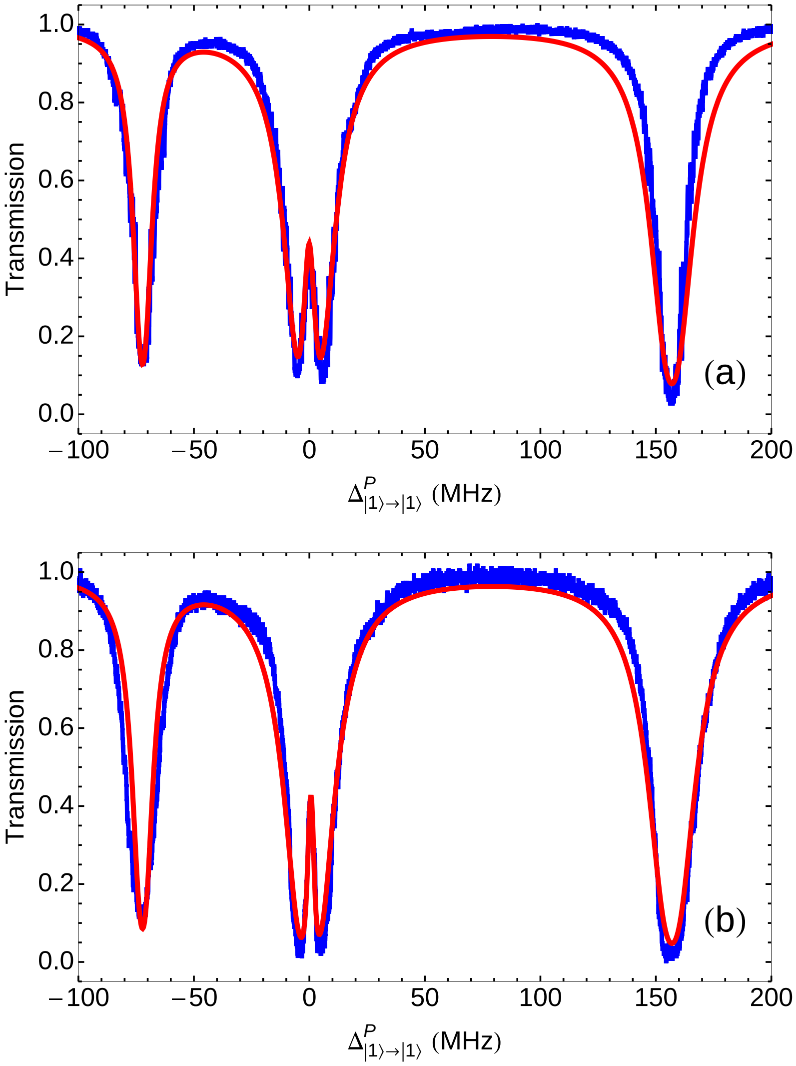

Figure 4.5: The transmission spectrum for a probe laser scanning over the transitions $|F = 1\rangle \rightarrow |F' = 0, 1, 2\rangle$ in ^{87}Rb. The blue curve is the observed signal, and the red curve is the model. (a) The control laser is in the LG_0^1 mode 0.1 MHz below the $|F = 2\rangle \rightarrow |F' = 1\rangle$ transition with $\Omega_{0c,21} = 20$ MHz. (b) The control laser is in the Gaussian mode 0.7 MHz above the $|F = 2\rangle \rightarrow |F' = 1\rangle$ transition with $\Omega_{0c,21} = 6.7$ MHz. Both data sets represent Configuration-(I).

Mode	Config.	$\Omega_{0c,kl}$ (MHz)	FWHM	Predicted FWHM (for opposite mode)
LG_0^1	(I)	16	0.67Γ	1.46Γ
	(II)	19	0.78Γ	1.87Γ
Gaussian	(I)	9.5	0.73Γ	0.37Γ
	(II)	11	0.85Γ	0.41Γ

Table 4.1: The mode, configuration, $\Omega_{0c,kl}$, and linewidth for EIT experiments in ^{85}Rb. The final column gives the theoretically predicted FWHM of the EIT signal if the control laser is in the opposite mode given in the first column, but same $\Omega_{0c,kl}$. Each configuration is described in Fig. 4.2.

control in the Gaussian mode.

We could not make a direct comparison between the control laser in the Gaussian and the LG_0^1 laser modes while keeping $\Omega_{0c,kl}$ fixed. This is due to the large decoherence rate in our system. The primary source of decoherence in this experiment is from the two, independent lasers that generate the probe and control fields. The two ECDLs operate separate from one another. The value of $\Omega_{0c,kl}$ had to be larger for the LG_0^1 mode to combat the dominant decoherence rate in regions of low control intensity.

Given these results and the quality of the fit of the model (Figs. 4.4 and 4.5), both for LG_0^1 and Gaussian control lasers, we conclude that the linewidth is narrower with the LG_0^1 control beam for equal $\Omega_{0c,kl}$ in an ultracold gas. Because the atoms travel ~ 10 μm during the experiment, the effect is independent of the transit time of the atoms. This is consistent with what has previously been observed in gases at room temperature where it was shown to be independent of the OAM of the control beam [19, 20].

Mode	Config.	$\Omega_{0c,kl}$ (MHz)	FWHM	Predicted FWHM (for opposite mode)
LG_0^1	(I)	20	0.8Γ	1.94Γ
	(II)	25	0.95Γ	2.64Γ
	(III)	33	1.5Γ	4.26Γ
	(IV)	33	1.2Γ	3.52Γ
Gaussian	(I)	7.3	0.46Γ	0.25Γ
	(II)	5.0	0.44Γ	0.22Γ
	(III)	6.9	0.61Γ	0.29Γ
	(IV)	8.2	0.75Γ	0.36Γ

Table 4.2: The mode, configuration, $\Omega_{0c,kl}$, and linewidth for EIT experiments in ^{87}Rb. The final column gives the theoretically predicted FWHM of the EIT signal if the control laser is in the opposite mode given in the first column, but same $\Omega_{0c,kl}$. Each configuration is described in Fig. 4.2.

4.4 Conclusion

We observe EIT transmission spectra using a control beam in an LG_0^1 laser mode in ultracold atoms prepared in a magneto-optical trap. We measure EIT linewidths with the control beam in the LG_0^1 mode, and compare to the spectra generated when the control beam is in the Gaussian mode. In both mode types, we observe sub-natural linewidths with similar signal contrast. Our theoretical model for this system shows good agreement with the experiment. We conclude that EIT in an ultracold gas results in a narrower resonance feature for the same value of $\Omega_{0c,kl}$ when a control beam is in an LG_0^1 mode as compared to the control beam in a Gaussian mode. Decoherences due to transit effects are negligible. Therefore, we conclude that the narrowing of the EIT resonance feature is due to the spatial variation of the Rabi frequency of a control laser in the LG_0^1 mode. Our physical interpretation is that the regions of high control intensity increases the EIT transmission, but also broadens the width of the resonance. Whereas the darker intensity regions of the LG_0^1 mode narrows the resonance feature. A detailed explanation of the effect on EIT by the spatial variation of the control laser intensity is performed in the next chapter. There, we will change the size of the LG_0^1 control laser with respect to the probe laser, thereby altering which regions of the LG_0^1 laser mode overlap with the probe laser. We need to increase the coherence to increase the sensitivity of our system for this measurement. The dominant source of decoherence is rooted in the independent laser operation of our probe and control. To combat this, we will move to a single laser source for the probe and control.

Chapter 5

Optimization of electromagnetically induced transparency using a Laguerre-Gaussian mode

5.1 Introduction

Chapter 4 examined EIT with the control laser in the fundamental mode and compared this to EIT with the control laser in the LG_0^1 mode. In this chapter, we consider EIT with the control laser in the LG_0^1 mode only. We choose several LG_0^1 mode sizes with respect to the probe laser. We measure the effect that "mode overlap" plays in the line-shape of the EIT spectrum.

Regions of high control laser intensity result in wide EIT features, while regions of low control laser intensity result in narrow EIT features. Previously, sub-natural linewidths were observed in the EIT transmission spectra using an LG_0^1 control beam in room temperature gases [19, 20, 53]. Additionally, the influence of the laser beam radial intensity distribution on Zeeman EIT was studied [76]. Zeeman EIT properties were studied using a control laser with Π-shaped (flat top) intensity profile, comparing to EIT with a control laser in the Gaussian mode. To the best of our knowledge, there is not a study addressing the influence of various LG_0^1 control beam sizes on EIT. The LG_0^1 laser mode is characterized with a donut intensity pattern (as described in chapters 2 and 4). For small LG_0^1 modes compared to that of the probe ($w_c \approx 0.1 w_p$), the high intensity region of the control laser is localized to a small region of the probe laser. The region in space where the atoms interact with the laser fields to yield high probe transmission is similarly small. Absorption will occur over a large fraction of the probe laser, and a faint EIT signal will be detected. Alternatively, a probe aligned to the central node of a large LG_0^1 mode ($w_c \approx 5 w_p$) will experience low control intensity throughout the entire interaction region of the probe. This too will result in a faint EIT signal. There is a competition between absorption from regions of low control Rabi frequency, and transparency from regions of high control Rabi frequency, resulting in widely varying EIT resonance characteristics.

In this chapter, we adapt our model to predict optimal conditions for EIT with a probe in the Gaussian mode and the control in an LG_0^1 mode. Adjusting the LG_0^1 size with respect to the probe beam has a predicted and observed effect on the EIT resonance shape, width, and contrast. We find that conditions for EIT are optimized when the probe and the control have the same waist. Additionally, we observed "waveguide"-like behavior similar. As is well known, the large Rabi frequency regions of the LG_0^1 drastically alters the susceptibility of the medium. The real part of the linear susceptibility describes the refractive index. The LG_0^1 mode control laser writes onto the medium a spatial variation of the index of

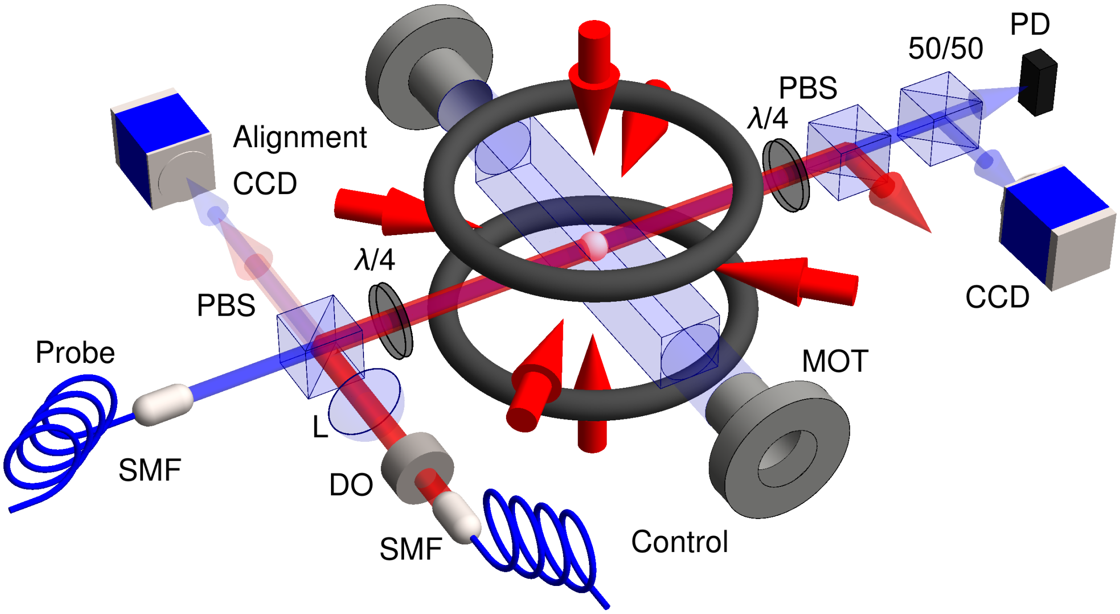

Figure 5.1: Schematic of the ultracold experimental apparatus used to study the effect of control LG_0^1 mode size on EIT spectra. The magneto-optical trap (MOT) consists of a pair of anti-Helmholtz coils, six orthogonal and counter-propagating trapping lasers, and a repumping laser (co-propagating with the trapping laser). The control laser is indicated by the transparent red beam. The probe laser is indicated by the transparent blue beam. The control and probe initially have orthogonal linear polarization, and are combined using a polarizing beam-splitter (PBS) cube. A quarter-wave plate ($\lambda/4$) converts the control to σ^- polarization and the probe to σ^+ polarization. After passing through the atomic medium, a second $\lambda/4$ wave plate returns the probe and control to orthogonal linear polarization, where the two beams can be separated with another PBS cube. A 50/50 cube splits the probe to be recorded on a photodiode (PD), and a charge-coupled device (CCD) camera.

refraction. We observe a lensing effect by the LG_0^1 mode similar to that studied by [77].

5.2 Experimental design

The ultracold EIT apparatus is shown in figure 5.1 and is similar to that found in [53, 73] as well as chapter 4. The MOT design and characteristics are described in chapter 4, section 4.2. We trap and perform EIT on ^{87}Rb because the level structure is simpler than that of ^{85}Rb.

The primary source of decoherence in the system used in chapter 4 was introduced by the two independent laser sources used for the probe and the control lasers. This can be addressed by phase locking the two lasers [78], or by using a single laser source to generate the probe and control laser fields. Phase locking requires additional circuitry and feedback. Therefore, we decided to use a single frequency source. An early generation of this experiment used a 1.5 GHz AOM from Brimrose Corporation on loan to us by Alberto Marion's Quantum Optics laboratory. However, due to the inflexibility of our driving source and the time constraints of the loan, we abandoned this configuration for one that utilizes our more versatile tools.

We use a single laser source to generate the probe and control lasers, where both fields have the same frequency. Therefore, we can only excite one hyperfine transition in ^{87}Rb. We create a Λ-configuration using the magnetic sublevels of the

$|5^2S_{1/2}, F = 1\rangle$ hyperfine ground state and the $|5^2P_{3/2}, F' = 0\rangle$ hyperfine excited state. The probe couples the $|F = 1, m_F = +1\rangle \rightarrow |F' = 0, m_{F'} = 0\rangle$ magnetic sublevels using σ^- polarization. The control couples the $|F = 1, m_F = -1\rangle \rightarrow |F' = 0, m_{F'} = 0\rangle$ magnetic sublevels using σ^+ polarization. Figure 5.2 shows a level diagram of the transition used in this experiment. Other Λ-configurations can be created on other D2 (or D1) transitions using the same polarizations. However, the transition chosen for this work involves the fewest number of magnetic sublevels, thus minimizing the channels that the environment can couple to the system.

Figure 5.3 shows the set-up for our single laser used to drive the probe and control coupling. The laser used to generate the probe and control fields is an external cavity diode laser. It is separated into two beams using a polarizing beams splitter (PBS) cube. The power of each beam can be adjusted using a half-wave plate placed before the PBS cube. For typical experiments, the control power is 0.1-1 mW and the probe power is < 10 μW. Each beam makes a double-pass through a NEOS N23080 acoustic optical modulator (AOM). The RF frequency coupled into either AOM can be modulated to scan the frequency of the respective laser, generating a desired EIT spectrum. We align the AOM in a double-pass configuration for two primary reasons. The first is to eliminate the unwanted change in diffraction angle as we modulate the RF frequency. We also double-pass the

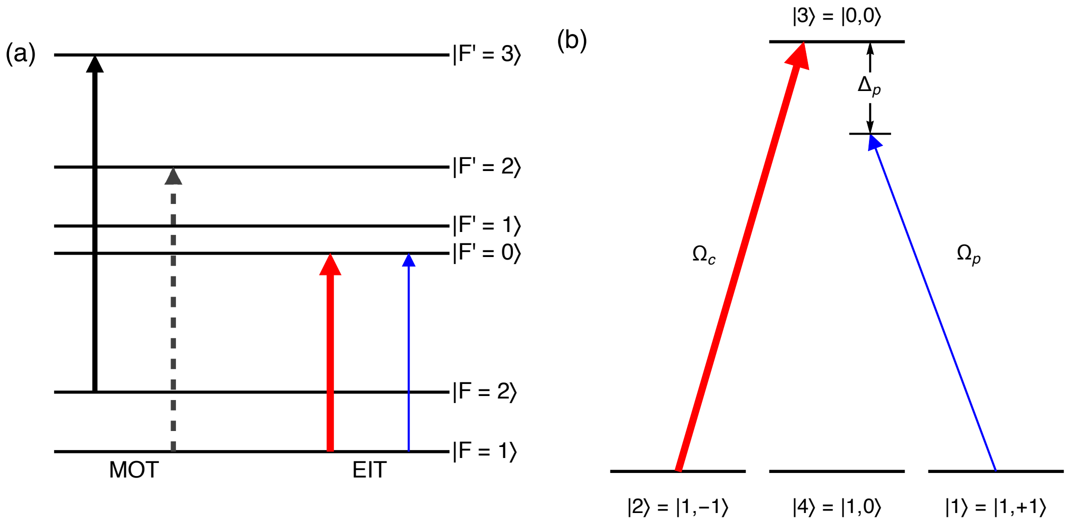

Figure 5.2: Level diagrams for ^{87}Rb. Figure (a) shows the hyperfine levels on the D2 transition. The MOT trapping transition is shown with the solid black arrow, the MOT re-pumping transition is shown with the gray dashed arrow, the probe transition is shown with the thin blue arrow, and the control laser is shown with the thick red arrow. Figure (b) shows the levels involved in EIT. The probe (thin blue arrow) couples the $|F = 1, m_F = +1\rangle \rightarrow |F' = 0, m_{F'} = 0\rangle$ magnetic sublevels using σ^- polarization. The control (thick red arrow) couples the $|F = 1, m_F = -1\rangle \rightarrow |F' = 0, m_{F'} = 0\rangle$ magnetic sublevels using σ^+ polarization. The state, $|4\rangle$, is included because the atom can decay to this state.

AOMs to double the range in which we can scan the lasers[1]. The AOM serves as a shutter to generate the probe and control pulses used in the EIT experiment. The output of the double-pass is then coupled into a single-mode, polarization maintaining fiber. The output of the fiber optic cable is directed to the magneto-optical trap (MOT) as described by figure 5.1. The control laser and the probe laser are overlapped with orthogonal polarization using a PBS cube. After passing through the PBS cube, the lasers are transformed into σ^+ and σ^- polarization using a quarter-wave plate ($\lambda/4$). The two beams pass through the atomic ensemble, then the beams are restored to orthogonal polarization with another $\lambda/4$ plate, and separated using another PBS cube. A 50/50 beam splitter directs half of the probe laser to a photodiode, and the other half of the probe laser to a CCD camera.

The control beam and the probe beam are nearly co-propagating, crossing at an angle of $\approx 0.2^\circ$. This is to prevent any light from the control beam from bleeding into the two detectors. We use high-quality PBS cubes polarizers. However, the control laser intensity is several orders of magnitude higher than that of the probe. The tiny fraction of laser light leaking through the PBS cube can rival the signal of the probe itself.

Figure 5.4 shows a CCD image of the transverse intensity profile of the Gaussian mode probe, and each of the five LG_0^1 mode sizes used in this study. To vary the size of the LG_0^1 mode control laser, we insert a series of lenses into the position

---

[1] The NEOS AOM drivers can modulate the RF frequency by 10 MHz. Double-passing the AOMs gives us a 20 MHz modulation range.

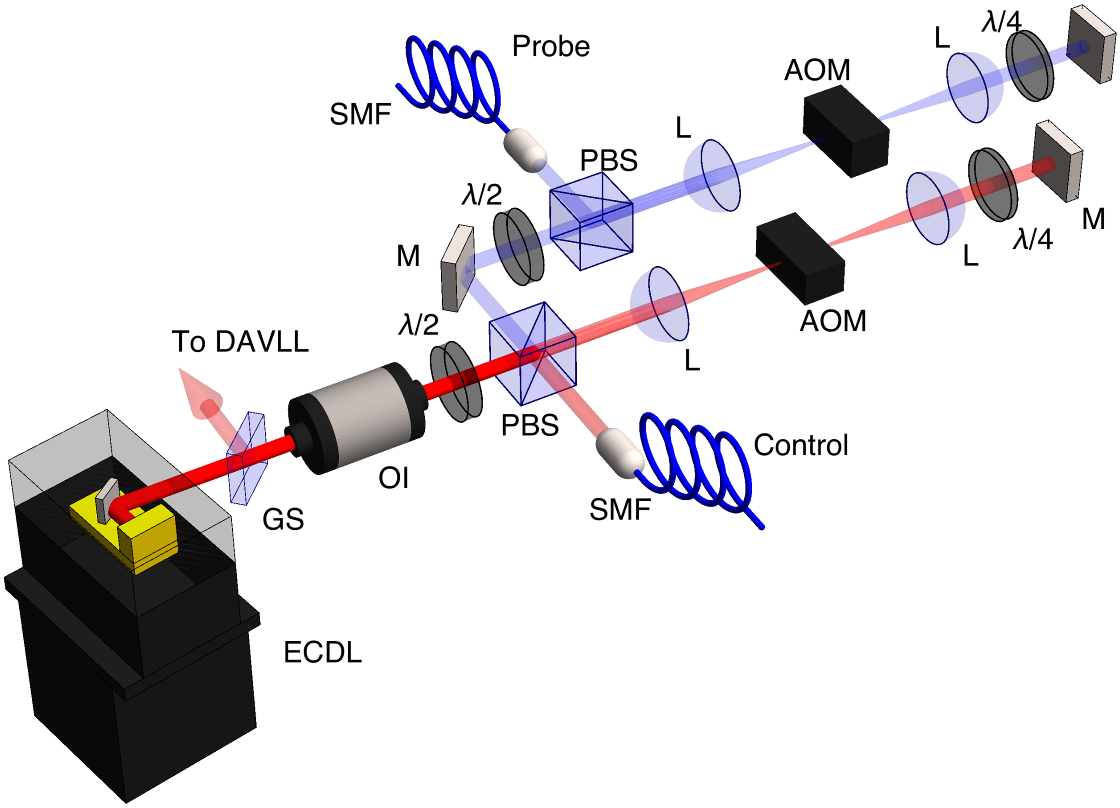

Figure 5.3: The single laser set-up to generate the probe and control fields for this EIT study. The external cavity diode laser is split into two beams using a PBS cube. Each beam makes a “double pass” through an 80 MHz AOM. Each beam is, therefore, shifted by 160 MHz. The AOMs act as shutters to control the probe and control pulses used in the EIT experiment. The output from each double pass set-up is coupled into a single mode, polarizations maintaining fiber, and sent to the experiment.

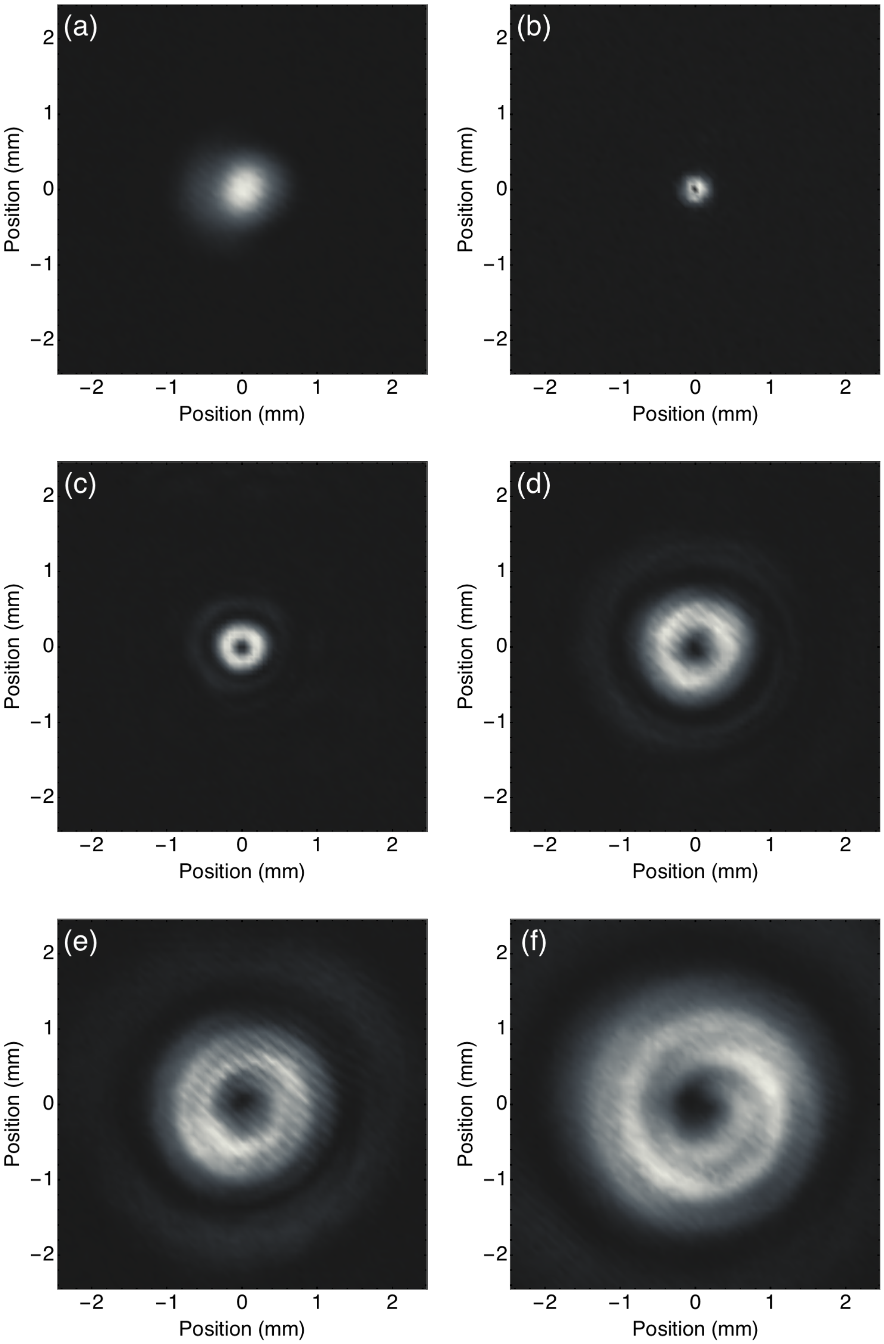

Figure 5.4: (a) CCD images of the probe Gaussian profile, (b) - (f) and images of the five LG_0^1 modes used to optimize the EIT spectrum. The waist of the LG_0^1 mode is controlled using a set of lenses, as prescribed by table 5.1.

labeled L in figure 5.1. Changing the focal point of the lens has the effect of changing the waist of the LG_0^1 mode at the MOT. Table 5.1 details five lens selections resulting in five LG_0^1 size (compared to the probe size). For each LG_0^1 mode size, an EIT spectrum is recorded on the photodiode and on the CCD.

When adjusting the size of the LG_0^1 mode control laser, the position of the laser changes with respect to the probe and the MOT. We monitor the position of the control and probe laser using a CCD camera. The camera is placed behind PBS cube used to combine the control and the probe lasers (see figure 5.1). After each sizing of the LG_0^1 mode control beam, we adjust the alignment of the probe to overlap with the probe symmetrically. To ensure that this occurs at the MOT, we position the CCD at the same distance from the PBS cube as the MOT is from that same location. The accuracy of this positioning is ≈ 0.5 cm. The two beams cross at an angle of $0.2°$. Therefore, the pointing-accuracy using this method is ≈ 20 μm.

The EIT sequence is controlled by a Hewlett-Packard 8175A Digital Signal Generator. Digital pulses shutter the AOMs on the probe, control, and the repump lasers, and control the current flowing through the MOT coils. Initially, the MOT is held in a steady state for 96 ms, and the probe and the control lasers are off. Next, the magnetic field is switched off and we optically pump the atoms for 1 ms. The repump laser is switched off while the trapping laser optically pumps all the atoms into the lower hyperfine ground-state. After optical pumping, the control and probe lasers perform the EIT spectroscopy. The control laser and the probe laser pulse-ON for 5 ms. During this time, the probe is scanned using the AOM. The AOM frequency is modulated using an analogue voltage sent to the NEOS analog driver system model N21080-1SAS. With a nominal operating RF frequency of 80 MHz, applying a voltage modulation from [-5 V,+5 V] corresponds to RF frequency modulation from [75 MHz, 85 MHz] (10 MHz modulation range). Since we are double passing the AOMs, we have 20 MHz available for the probe scan. A photodiode and a CCD camera detects the probe transmission. The entire procedure takes 0.1 s. There are two independent sequences for the photodiode and for the CCD camera. Figure 5.5 (a) shows the timing sequence for the photodiode sequence, while figure 5.5 (b) shows the timing sequence for the CCD sequence.

The measurements of the EIT spectrum with a photodiode are made in a similar fashion as in chapter 4. However, instead of ramping the voltage across the piezoelectric transducer attached to the grating on the external cavity of the of the probe laser, we ramp the RF driver for the AOM shuttering the probe beam. A triangle wave is sent to the AOM driver with an amplitude of 5 V and an offset of 0 V, resulting in a 20 MHz sweep across the $|^2S_{1/2}, F = 1\rangle \rightarrow |^2P_{3/2}, F' = 0\rangle$ transition in ^{87}Rb. The cycling rate of the ramp sweep is controlled by the digital pulse generator, and is typically cycling at 10 sweeps per probe pulse ($T_{\text{sweep}} = 200\ \mu$s). It was necessary to sweep this fast (as compared to the 2 ms sweep time in the previous chapter) because the frequency of the probe laser is near resonance throughout

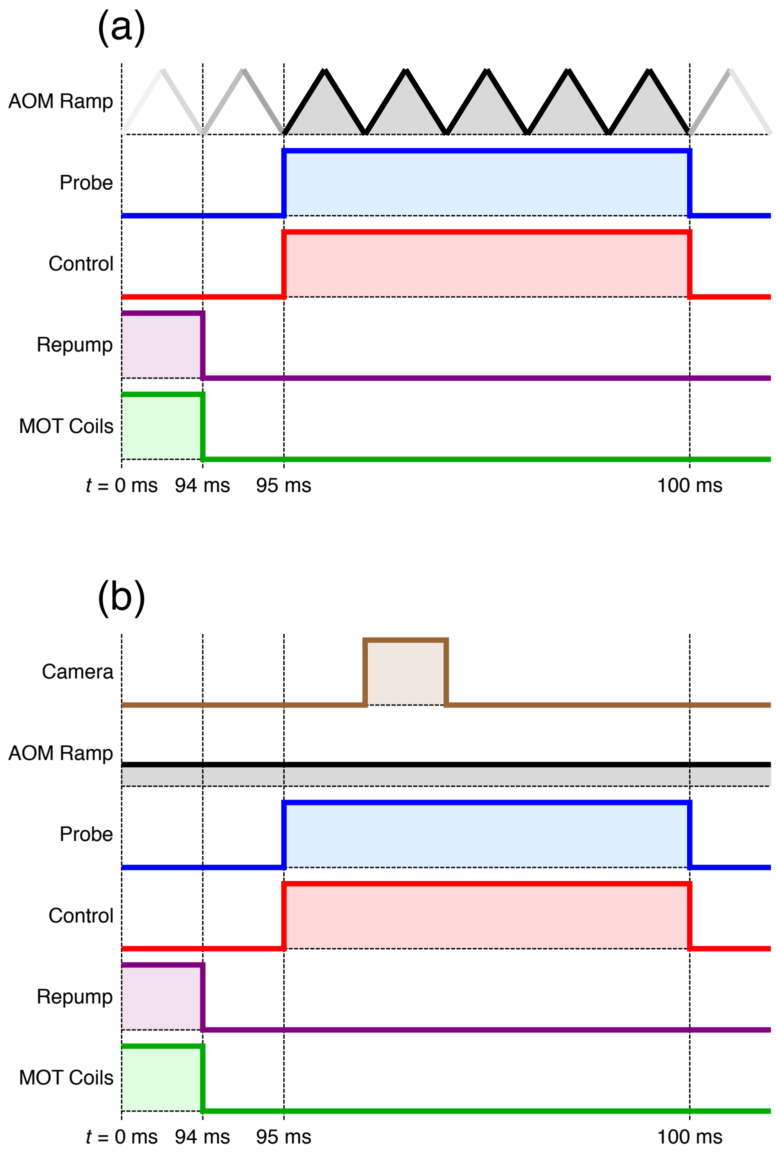

Figure 5.5: The timing sequence used for (a) measurements of EIT with the photodiode, and (b) measurements of EIT with the CCD camera.

the entire sweep. The increased photon scattering leads to an appreciable decrease in optical density over the entire duration of the probe pulse. We find that the 200 μs probe sweep period is sufficiently fast to ignore the dynamics of the system. The photodiode signal is read on a TDS-3054 oscilloscope.

A measurement of the EIT spectrum using a CCD camera is restricted by the frame rate of the camera. The CCD camera has a frame rate of about 30 Hz. We cannot measure the EIT resonance using the timing sequence found in figure 5.5 (a), where the AOM RF frequency is swept at a rate of 5 kHz. Therefore, we modify the photodiode sequence such that the AOM ramp signal is held at a fixed value. To perform a measurement of the EIT spectrum, we begin with the AOM ramp set at -2 V ($\Delta_p = -4$ MHz). After one cycle of the sequence described by figure 5.5 (b), we incrementally step the AOM ram voltage by units of 0.02 V ($\Delta_p = 0.04$ MHz). The AOM is stepped in this fashion until the signal reaches +2 V, requiring 100 steps to complete a scan. For each frequency step, we measure the CCD transmission as prescribed in subsection 3.6.2. Image$_1$ is an image of the transmitted probe after passing through the atomic ensemble under conditions of EIT. Image$_2$ is an image of the probe *incident* on the atomic ensemble. This image is taken by turning of our trap (removing the atoms from the beam path). All other conditions (appropriate laser ON states) are the same for Image$_1$ and Image$_2$. Even though we take great care in eliminating background light from entering the detector, scattered light ultimately finds its way into the CCD camera. This is

Table 5.1: Lens configurations to adjust the size of the LG_0^1 laser mode.

Laser	**Lens Focal Length (mm)**	$\boldsymbol{w}$ **μm**	$\boldsymbol{w/w_p}$
Probe	No Lens	573.1	1.00
LG_0^1 Control	250	138.8	0.25
	300	262.8	0.48
	430	563.7	1.02
	750	838.8	1.52
	No Lens	1,277.3	2.22

eliminated by taking an Image_3. For this image, we turn OFF the probe laser, but leave all other lasers ON. A transmission measurement is then accomplished by the following relation:

$$\text{Transmission} = \frac{\text{Image}_1 - \text{Image}_3}{\text{Image}_2 - \text{Image}_3}. \tag{5.1}$$

A spectrum is generated by taking all three images for each frequency step.

5.3 Results

Figure 5.6 shows the measured EIT spectra for each of the five sizes of LG_0^1 modes created for this experiment. The results are measured with the photodiode. Column (a) displays the radial cross-section of the LG_0^1 (colored curve) with the radial cross-section of the probe laser (black dashed curve). The gray filling is used to compare the regions of mode overlap for the probe and the control. The corresponding spectra is shown in column (b). A best-fit model is generated for each measured spectra, and is shown in column (c). The overlap of the LG_0^1 intensity profile with that of the profile of probe drastically alters the EIT resonance.

To characterize the optimization of EIT, we use two parameters: the height of the resonance (contrast), and the full width at half-max (FWHM) of the resonance. Using the measured spectra in figure 5.6, we determine the resonance height and width empirically. Figure 5.7 (a) plots the EIT contrast versus the LG_0^1 mode waist. We observe that the contrast is maximized when the two beams are mode-matched. That is, when the waist of the probe and control lasers are the same ($w_c \approx w_p$). Our interpretation of this result requires an analysis of the manipulation of the dispersion caused by the spatial variation of the LG_0^1 mode control laser. The inhomogeneous linear dispersion resulting from the spatial variation in intensity caused by the LG_0^1 mode leads to a "lensing effect". The LG_0^1 mode control laser manipulates the index of refraction such that the probe beam is optically guided by the control laser through the atomic medium [52]. When the waists of the two beams are approximately equal, then the probe is collimated well.

Figure 5.7 (b) shows the FWHM of the EIT resonance contrast for increasing waist of the LG_0^1 mode. When keeping the control power fixed while adjusting the size of the control beam, the FWHM maximizes for control waist $w_c \approx 0.5w_p$. The FWHM decreases for control waists larger than half the probe size ($w_c > 0.5w_p$). Our physical interpretation of this result relies on the relationship that the FWHM increases with increasing control laser intensity. The region of high control inten-

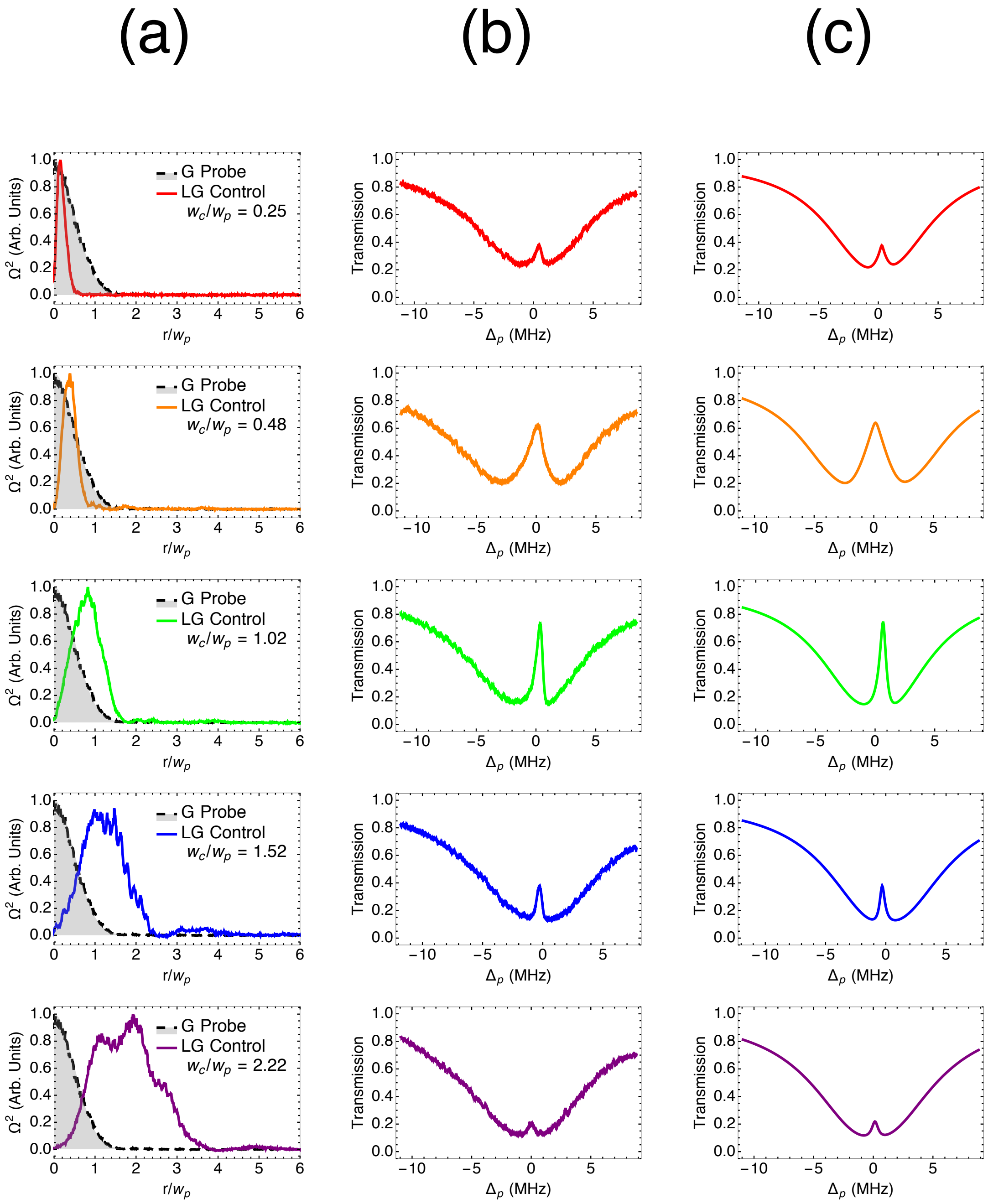

Figure 5.6: The resulting spectrum for several sizes of LG_0^1 mode control sizes. The column (a) reports the radial intensity cross-section of five different LG_0^1 mode sizes and the G probe. The column (b) is the resulting EIT spectrum recorded by the photodiode. The column (c) is a best-fit model for the measured spectra in column (b). A qualitative analysis concludes that $w_c \approx w_c$ yields the "best" EIT feature, verified by figure 5.7.

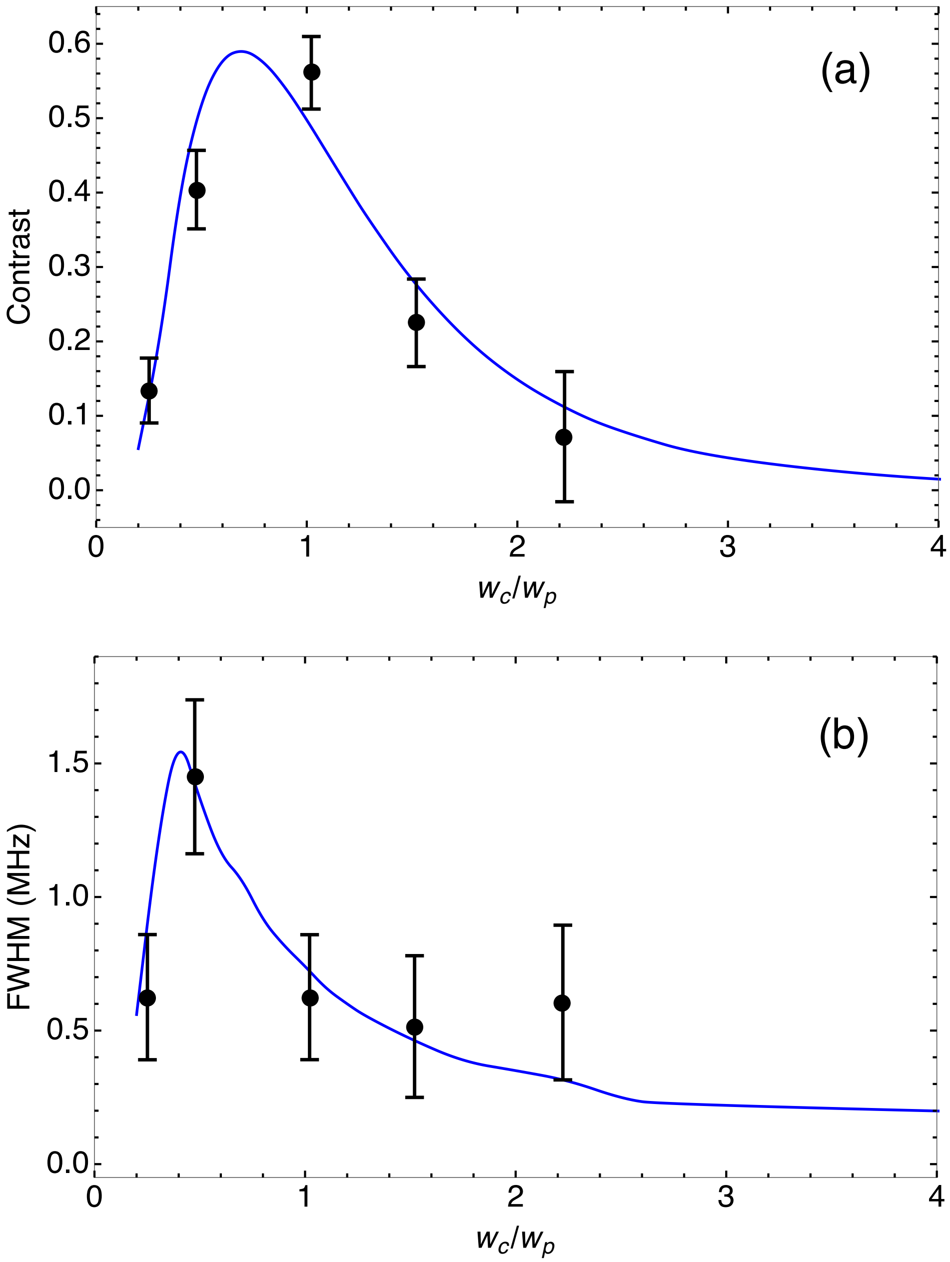

Figure 5.7: Measured (a) contrast and (b) FWHM of the EIT spectra resulting from a control laser in the LG_0^1 mode. The contrast is optimized with $w_c = w_p$, and the FWHM is maximized at $w_c \approx 0.5 w_p$.

sity is overlapped with the probe when $w_c < 0.5w_p$. The result is broadening of the EIT feature (large FWHM). Increasing the size of the LG_0^1 mode control laser has two effects: (1) decreases the peak intensity of the laser and (2) increases the overlap of the darker central region of the LG_0^1 mode with the probe laser. Overall, this decreases the "average" control Rabi frequency experienced by the probe laser, leading to narrower EIT features.

To help understand the role that the LG_0^1 waist size has in the optimization process, we imaged the probe beam during a frequency scan spanning the range -4 MHz $\leq \Delta_p \leq +4$ MHz in steps of 40 kHz. Figure 5.8 (a) shows an image of the Gaussian probe laser. Mapped onto the image, is the cross-section slice we take to produce panels (b)-(f). Figures 5.8 (b)-(f) show the transmission spectrum recorded by the CCD (as generated by equation 5.1). The two axes subtending the horizontal plane of the figure describe the probe detuning (Δ_p) and the position along the cross-section of the probe laser defined in figure 5.8 (a) (r_p/w_p). The axis labeled r_p/w_p describes the probe transmission spectrum for a CCD pixel located along the axis described by the white line in figure 5.8 (a). Fixing a value on the axis labeled r_p/w_p will produce an EIT spectrum for that particular CCD pixel. The vertical axis is the transmission of the probe, which is determined using equation (5.1).

Figures 5.8 (b)-(f) illustrate the process responsible for the optimization of the EIT spectrum. The LG_0^1 control laser modifies the linear susceptibility of the

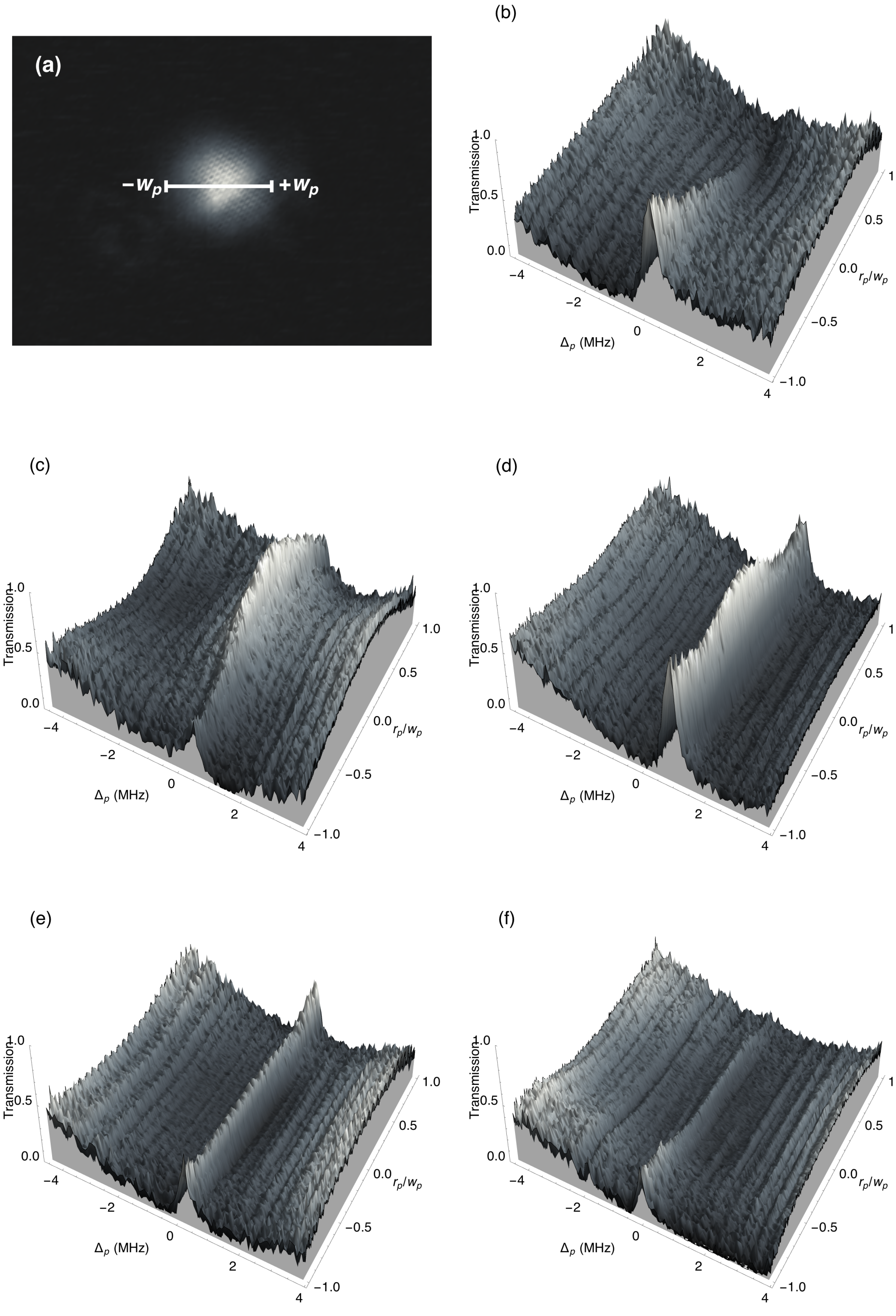

Figure 5.8: (a) An image of the probe. The white line indicates the cross-section slice used to produce the rest of the figures. The rest of the figures are EIT resonances for several transverse locations on the probe with LG_0^1 mode control laser waists (b) $w_c = 0.25w_p$, (c) $w_c = 0.48w_p$, (d) $w_c = 1.02w_p$, (e) $w_c = 1.52w_p$, and (f) $w_c = 2.22w_p$.

atomic medium. Similar experiments have shown that this configuration acts a waveguide, focusing a weak probe aligned to the center of the LG_0^1 mode [77]. The high transmission spatial regions near the EIT resonance in figures 5.8 (b)-(f) are evidence of this effect. As the control laser waist is increased moving from panel (a) to (c), so too does the fraction of the probe laser that lies within the central (dark) region of the LG_0^1. The waveguide is optimized in panel (d), where the waists are mode matched ($w_c \approx w_p$).

Our physical interpretation of the optimization relationships involves the modification of the index of refraction, as well as the effect that high and low control intensities have on the FWHM. The index of refraction has a steep modification moving along the control radial axis from the center to the peak intensity ($r = w_c/\sqrt{2}$). For the configuration $w_c < w_p$, the modification of the index of refraction occurs interior to w_p. Therefore, a small fraction of the probe is optically guided. For the configuration $w_c \approx w_p$, the modification of the index of refraction occurs across the entire region of the probe, optically guiding most of the probe. For the configuration $w_c > w_p$, the modification of the index of refraction occurs (mostly) exterior to the probe. Additionally, the dark central node of the control overlaps with the probe. For our experiment, the combination of weak control pumping and decoherences lead to higher absorption and a weak EIT signal.

5.4 Conclusion

We studied the effect on the EIT resonance properties from a control laser propagating in the LG_0^1 mode. Using the contrast and FWHM of the EIT resonance, we determined an optimum size of the LG_0^1 mode control with respect to the size of the Gaussian mode. The control laser power was held constant for these measurements. Therefore, increasing the control mode size results in a decrease in peak intensity. Using our model, we predicted that the contrast is maximized with a control waist of $w_c \approx w_p$, then asymptotically approaches zero for increasing control waist. We also predicted that the FWHM of the resonance will be maximized with a control waist of $w_c \approx 0.5w_p$, then asymptotically approaches zero for increasing control waist. The goal is to have large contrast with minimum FWHM. We conclude that matching the two laser modes optimizes these conditions. Our physical interpretation of this conclusion is that the contrast is optimized due to the steep change in index of refraction when the waists of the control and the probe are approximately equal. The behavior of the FWHM results from the control intensity overlap with the probe. At $w_c \approx 0.5w_p$, most of the LG_0^1 mode power is located within the waist of the probe, broadening the EIT feature. Increasing the size of the control reduces the control intensity overlapped with the probe, thus narrowing the EIT feature.

Chapter 6

Mapping the Laguerre-Gaussian image from the control laser to the probe laser

6.1 Introduction

The past two chapters focussed heavily on EIT spectroscopic properties. In chapter 5, we observed an optically written waveguide in an ultracold gas assisted by the spatial manipulation of the linear susceptibility using an LG_0^1 control laser. In this chapter, we measure the transverse spatial transmission of a probe.

Printing information onto a probe laser has applications in quantum computing, encoding of information, and telecommunications [31–33]. Use of the OAM states of the LG_0^1 laser mode for quantum information is gaining in popularity. A probe laser carrying OAM generates a manifold of information degrees of freedom, allowing multi-dimensional quantum computing and encryption [22]. Storage of LG_p^ℓ mode probe pulses in gases has been demonstrated in both room temperature gases [23–26], and in ultracold gases [27–30].

Transferring OAM states from the control laser in an LG_0^1 mode to the probe laser (originally in a Gaussian mode) was recently demonstrated using EIT assisted storage of a probe pulse in a solid state medium [31]. The experiment stored the probe pulse using a Gaussian control, then read the pulse using an LG_0^1 mode. Conservation of OAM resulted in the transfer of the OAM to the probe laser. Conservation of OAM in four-wave mixing processes was extensively studied, resulting in the production of quantum states of light carrying OAM [32]. Efficient transferring of the image of an LG_0^1 laser mode was transferred to a probe laser in a room temperature gas using an EIT apparatus [33]. Surprisingly, the free space propagation of the transmitted probe maintained a donut shape over long distances $\approx$ 2m.

This work explores the transferring of information from the control laser to the probe laser via EIT. We map the LG_0^1 spatial intensity structure from the control to the probe. However, we *do not* transfer OAM from the control to the probe. The intensity distribution of the LG_0^1 mode spatially manipulates the linear susceptibility of the atomic medium. We observed a transferred intensity pattern onto the probe laser, maintaining its shape for a propagation distance of ≈ 1 m.

6.2 Experiment

Figure 6.1 is a representation of the apparatus used to carry out this experiment. We perform EIT in an ultracold sample of ^{85}Rb atoms prepared in the MOT described in chapter 3. The probe laser and the control laser are two independent external cavity diode lasers (ECDL). Each laser is frequency stabilized using a

DAVLL set-up.

The control laser is locked to the $|^2S_{1/2}, F = 1\rangle \rightarrow |^2P_{3/2}, F' = 2\rangle$ transition in ^{85}Rb. The laser is shuttered using an acoustic optical modulator (AOM), and is spatially filtered using polarization maintaining single mode fiber (SMF) optics. The power transmitted through the fiber is approximately 10 mW. We shape the control laser into an LG_0^1 mode using diffractive optics [62] (see section 3.4). At the MOT, the control laser has a $1/e^2$ radius of 270 μm.

The probe laser is locked to the $|^2S_{1/2}, F = 2\rangle \rightarrow |^2P_{3/2}, F' = 2\rangle$ transition in ^{85}Rb. The laser is shuttered using an AOM, and is spatially filtered using a SMF. The power transmitted through the fiber is approximately 10 μW and is vertically polarized by reflecting off the face of a polarizing beam splitter (PBS) cube. A Mach-Zehnder interferometer is constructed to measure the azimuthal phase structure of the probe after propagating through the atomic ensemble under EIT conditions. The probe is split into two separated paths using a 50/50 beam splitter cube. One of the paths the freely propagates around the ensemble of atoms, recombined with the other arm using another 50/50 beam splitter. A beam block (BB) can be inserted/removed from the beam path on this arm. We insert the BB to measure the intensity profile of the transmitted probe, where as we remove the BB to measure the azimuthal phase structure of the transmitted probe. The other path is directed toward the MOT and overlapped with the LG_0^1 mode control laser in a counter-propagating configuration. At the MOT, the probe laser has a

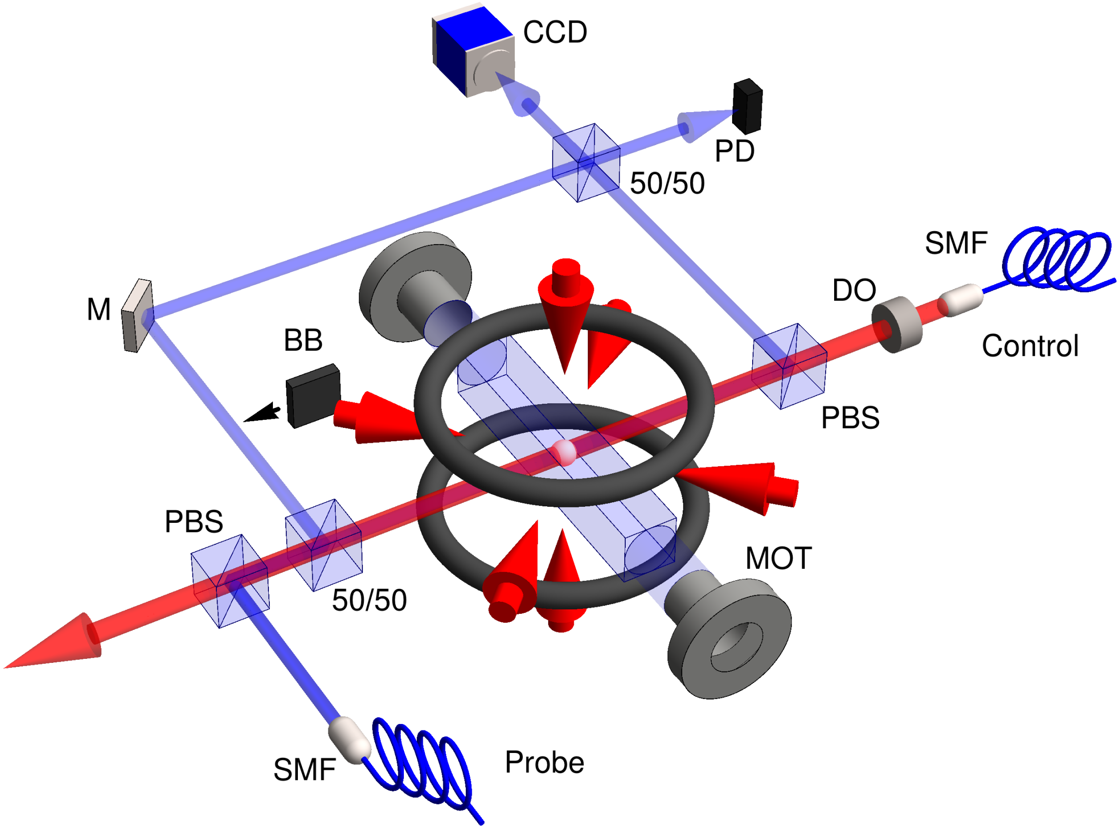

Figure 6.1: The apparatus used to transfer an image to the probe through electromagnetically induced transparency (EIT). An ensemble of ultracold ^{85}Rb atoms are prepared using a magneto-optical trap (MOT). The probe and the control laser is spatially filtered using a polarization maintaining single mode fiber (SMF).

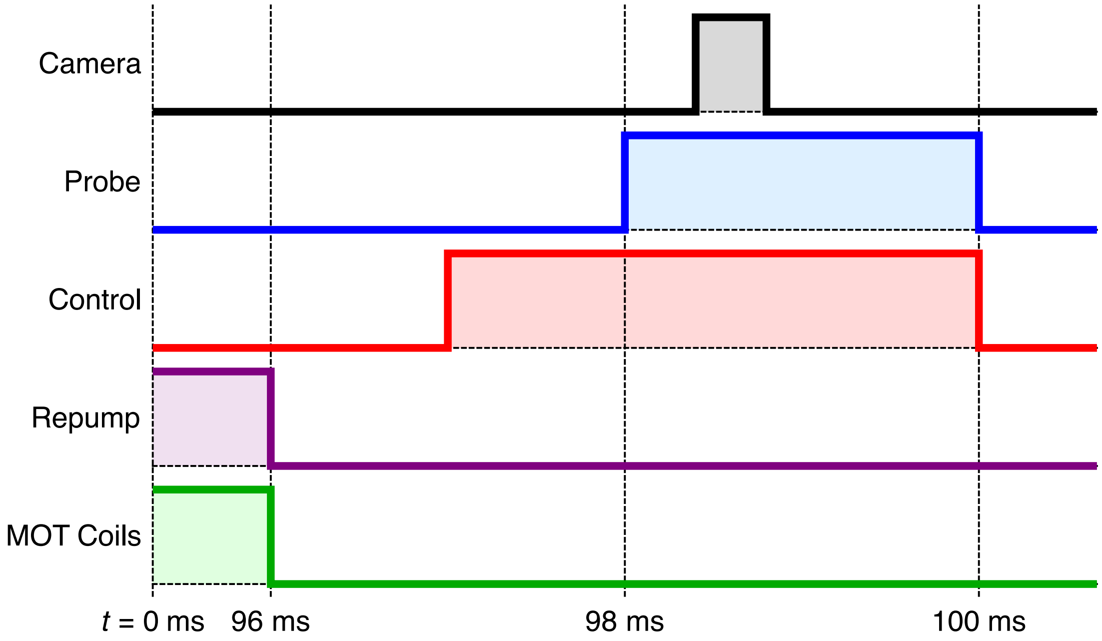

Figure 6.2: The timing sequence used to measure the transmitted probe profile using a CCD camera.

$1/e^2$ radius of 430 μm. As the probe propagates through the atomic ensemble, the profile is modified due to the EIT conditions established by the control laser. The transmitted probe is separated from the control laser using another PBS cube, and it is recombined with the free propagating arm of the interferometer. A charge-coupled device (CCD) camera is positioned at the output of the interferometer to measure the transmitted probe signal. A photodiode is positioned at the other output of the interferometer to monitor and empirically adjust the probe and control lock set-points such that the system is tuned to an EIT resonance.

The EIT imaging sequence (see figure 6.2) is controlled by a Hewlett-Packard 8175A Digital Signal Generator. Digital pulses control the switch on the current, and shutter the AOMs on the probe, control, and the repumping lasers. The MOT is initially held in steady state for 96 ms, and the control and probe lasers are off. The magnetic field is then switched-off. Simultaneously, we switch off the repumping laser so that the trapping laser optically pumps the atoms to the $|^2S_{1/2}, F = 2\rangle$ state. After optically pumping for 1 ms, the control laser is switched on for 3 ms to prepare the atoms for EIT. A 2 ms probe pulse proceeds the control laser 1 ms after the control laser is switched on. The CCD camera is triggered 0.5 ms after the probe pulse enters the atomic medium. The read-out of the CCD camera is recorded by our HPE computer through a USB interface. We cycle continuously for data averaging, and to keep the MOT in an approximate steady state.

6.3 Model & Results

Figure 6.3 shows three images of the probe: (a) the Gaussian input mode of the probe laser, (b) the transmitted probe profile after passing through an ultracold ^{85}Rb ensemble under EIT conditions, and (c) the interference of the transmitted probe with an approximation to a plane-wave. For a system undergoing decoherences, probe transmission increases with increasing control intensity. The LG_0^1 mode control laser has higher intensity in the ring. The probe transmission is higher in the region of the high intensity ring of the LG_0^1 mode.

The azimuthal phase of the LG_0^1 is not expected to be transferred to the trans-

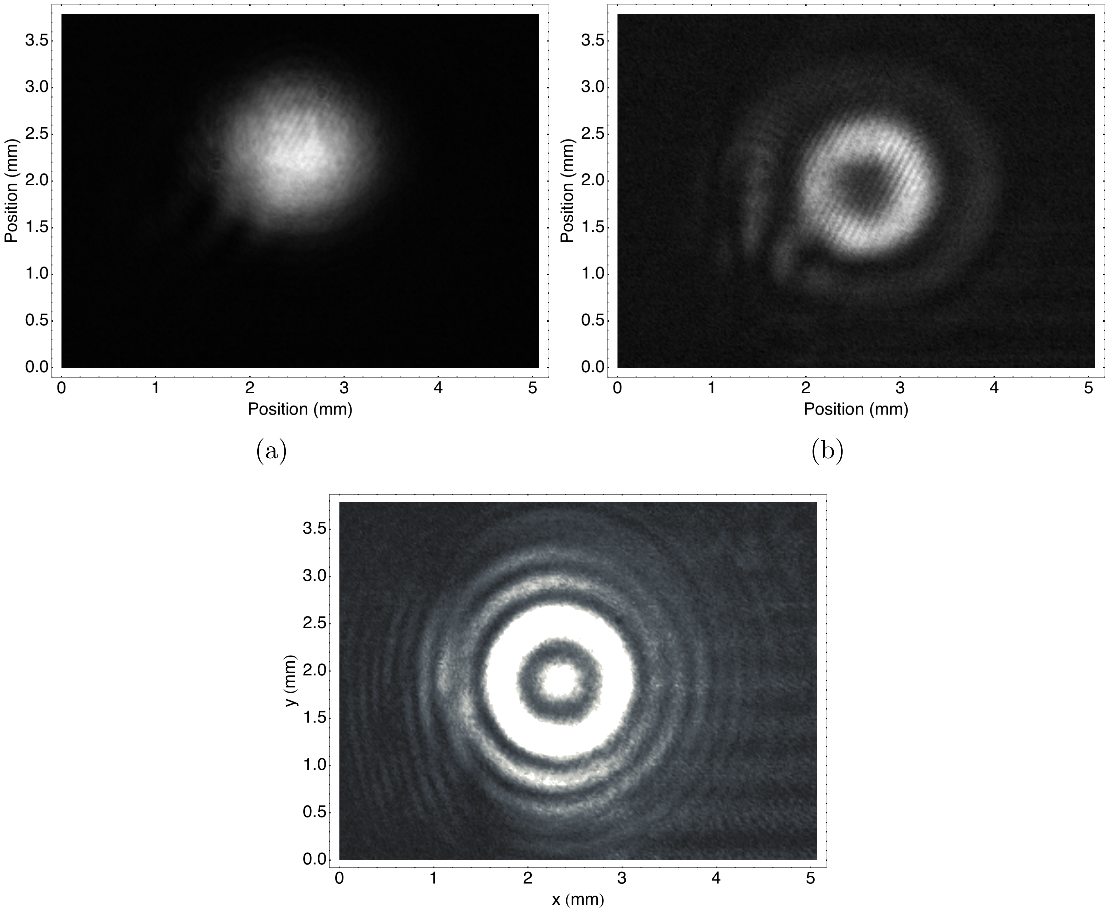

(a)

(b)

(c)

Figure 6.3: (a) An image of the probe incident on the ultracold ensemble of atoms. The probe is initially in the Gaussian mode. (b) An image of the transmission of a probe under conditions of EIT. The control laser is in the LG_0^1 mode, and its image is mapped onto the probe laser. (c) An image of the output of our EIT interferometer (as shown in figure 6.1). Based upon the concentric rings (no spiral pattern), we conclude that the control OAM is not transferred to the probe.

mitted probe. Even though the transmission of the probe in (b) has a dark central node, the intensity is not zero because we do not complete absorption where the control laser intensity goes to zero. Some probe light is transmitted because we do not have high optical density (OD ≈ 5). Figure 6.3 (c) is an image of the interference between the transmitted probe and a plane wave (as described by figure 6.1). The interference pattern is characteristic for that of a laser with a uniform azimuthal phase ($\ell = 0$). The bright fringe at the center results from constructive interference of the transmitted probe with the second arm of the interferometer. From the interference pattern, we conclude that the OAM from the control laser is not transferred to the probe laser.

Detection of the probe with a CCD camera provides spatial resolution of the transmission. To model this type of detection, we do not integrate over the position.

$$T(\Delta, r) = \frac{I_{0,p}(r) e^{-\mathrm{OD}(r)}}{I_{0,p}(r)} = \exp\left(-\mathrm{Im}\left[\chi(r)\right] k_p z\right). \tag{6.1}$$

For reference, we apply equation 6.1 to the data. Figure 6.4 is a plot of the model, predicting the observations of the experiment well.

Our physical interpretation of this result is that regions of high control laser intensity induces large EIT transmission. The LG_0^1 mode control laser forces high transmission in the region where the bright ring overlaps with the probe laser. Alternatively, the central dark region of the LG_0^1 cannot overcome the large de-

Figure 6.4: The model given by equation 6.1. The parameters used in the model are similar to the parameters used in figure 2.20. The control Rabi frequency is $\Omega_{0c,12} = 20$ MHz. The linewidth of the control laser is assumed to be $\gamma_c = 1$ MHz, the linewidth of the probe laser is set $\gamma_p = 0.1$ MHz, the number density is set to $N = 5 \times 10^{10}$ cm^{-3}, and the detuning of the control laser and the probe laser are set to $\Delta_c = \Delta_p = 0$. Due to the spatial dependence of a LG_0^1 mode laser, the model predicts that the transmission of the probe matches the intensity profile of the LG_0^1 laser.

coherences in the system. The overlap of the dark control region with the probe results in absorption from the atomic medium. The result is a ring shaped transmission of the probe that matches the intensity profile of the control laser.

6.4 Conclusions

We demonstrate the printing of the intensity profile of the LG_0^1 mode control laser onto the probe laser. A probe laser stabilized to the $|^2S_{1/2}, F = 2\rangle \rightarrow |^2P_{3/2}, F' = 2\rangle$ state transmitted through an ultracold ensemble of ^{85}Rb. The LG_0^1 mode control laser was stabilized to the $|^2S_{1/2}, F = 3\rangle \rightarrow |^2P_{3/2}, F' = 2\rangle$ transition in ^{85}Rb, and is aligned to the probe such that it is counter-propagating. The high intensity region of the control laser resulted in high transmission of the probe. As a result, the donut shape of the control laser is transferred to the probe laser. We do not transfer OAM from the control to the probe. This is explained through conservation of momentum arguments.

Chapter 7

Conclusions and outlook

Light is a superb transporter of information for quantum computing due to its speed and multi-dimensional parameters for the encoding of information. Electromagnetically Induced Transparency (EIT) is an optical technique used to manipulate quantum states of atoms and photons [1]. A control laser field modifies the absorption profile of a probe laser, causing coherent destructive interference of excitation pathways of the atom. There have been many advances toward the creation of a quantum memory, where light carrying the quantum information can be stored in an atomic ensemble and read at a later time. While many demonstrations of the storage of LG_p^ℓ mode information have been made, there has yet been a demonstration of the transfer of the azimuthal phase information to the stored light in a vapor cell.

We measured the effects that an LG_0^1 laser mode has on EIT. We observed that a configuration that employs a control laser in the LG_0^1 mode results in an EIT resonance with a narrower feature than a configuration with the control laser in the Gaussian mode. We developed a theoretical mode that includes the spatial distribution of the LG_0^1 control laser, as well as the spatial distribution of the Gaussian probe. We find good agreement between the model and the theory, concluding that the narrowing of the resonance is a result of the spatial structure of the control laser.

We expanded upon this result by varying the size of the LG_0^1 mode control laser with respect to the Gaussian probe laser size. As a result to varying the LG_0^1 mode waist, the location of high intensity anti-nodes varied as well. We observed that the contrast of the EIT signal was maximized when the two laser modes where approximately mode matched, then asymptotically approached zero for control waists larger than the probe. Additionally, we observed that the FWHM of the EIT signal maximized around $w_c \approx 0.5 w_p$, then asymptotically approached zero for increasing control waists.

Finally, we observed the transfer of the two-dimensional image of the transverse LG_0^1 mode control laser to the initially Gaussian mode probe laser. This is the result of the spatial manipulation of the linear susceptibility of the atomic medium due to EIT. The high intensity donut ring of the LG_0^1 mode control laser results in larger transmission of the probe laser. Whereas, the low intensity center of the LG_0^1 mode control laser results in high absorption of the probe laser. As a result, the ring intensity pattern was transferred to the probe. The probe propagated with this image for a distance of approximately 1 m, and it did not suffer from diffraction over this distance.

In the near future, our group has the opportunity to explore the effect of higher order LG_p^ℓ laser modes on EIT. The diffractive optics employed in this group can convert higher-order LG_p^ℓ modes with much higher mode purities than standard techniques (such has spiral wave plates and holograph plates). Extrapolating from the results in this work, we anticipate seeing narrower features than reported with the LG_0^1 mode. We have some preliminary results that look very encouraging (see appendix A). In particular, we have observed EIT resonances with a FWHM of $\Gamma/50$.

A not-so-near future project involves the transferring of OAM to a probe assisted by EIT. A theoretical analysis predicts that OAM can be transferred to probe light stored in a sample of ultracold atoms [79–81]. A demonstration of transferred OAM to probe light stored in a solid crystal was recently performed [31]. In principle, the a group velocity of the probe pulse propagating through the atomic medium is slowed due to the manipulation of the linear susceptibility by the control laser. Reducing the intensity of the control laser narrows the EIT resonance. The slope of the EIT resonance is inversely related to the group velocity of the probe pulse. Narrowing the EIT resonance leads to a decrease in the group velocity. A probe pulse can be coherently stored in the atomic medium by adiabatically turning-OFF the control laser. Retrieval of the probe pulse from the atomic medium is simply the time reversal of the storage process. Adiabatically turning the control laser ON reads the pulse from the atomic medium. Photon OAM can be transferred to the probe by storing the probe pulse with a Gaussian mode control laser, then retrieving the pulse with an LG_p^ℓ mode control laser.

Our current apparatus is not set-up to perform this experiment, and upgrades must be made. One limiting factor is the optical density of our magneto-optical trap. The major contributing factor to efficient optical quantum memory is the optical density [82]. We are currently operating within the optical density range of 5 to 15, and we would like to increase this by an order of magnitude.

Bibliography

[1] Fleischhauer, M., Imamoglu, A., and Marangos, J. P. Electromagnetically induced transparency: Optics in coherent media. Rev. Mod. Phys. **77**, 633–673, Jul (2005).

[2] Liu, C., Dutton, Z., Behroozi, C. H., and Hau, L. V. Observation of coherent optical information storage in an atomic medium using halted light pulses. Nature **409**(6819), 490–493, January (2001).

[3] Phillips, D. F., Fleischhauer, A., Mair, A., Walsworth, R. L., and Lukin, M. D. Storage of light in atomic vapor. Phys. Rev. Lett. **86**, 783–786, Jan (2001).

[4] Harris, S. E., Field, J. E., and Imamoğlu, A. Nonlinear optical processes using electromagnetically induced transparency. Phys. Rev. Lett. **64**, 1107–1110, Mar (1990).

[5] Agarwal, G. S. Inhibition of spontaneous emission noise in lasers without inversion. Phys. Rev. Lett. **67**, 980–982, Aug (1991).

[6] Boller, K.-J., Imamolu, A., and Harris, S. E. Observation of electromagnetically induced transparency. Phys. Rev. Lett. **66**, 2593–2596, May (1991).

[7] Gea-Banacloche, J., Li, Y.-q., Jin, S.-z., and Xiao, M. Electromagnetically induced transparency in ladder-type inhomogeneously broadened media: Theory and experiment. Phys. Rev. A **51**, 576–584, Jan (1995).

[8] Olson, A. J. and Mayer, S. K. Electromagnetically induced transparency in rubidium. American Journal of Physics **77**, 116–121 (2009).

[9] Mitra, S., Hossain, M., Ray, B., Ghosh, P., Cartaleva, S., and Slavov, D. On line shape of electromagnetically induced transparency in a multilevel system. Optics Communications **283**(7), 1500 – 1509 (2010).

[10] Chanu, S. R., Singh, A. K., Brun, B., Pandey, K., and Natarajan, V. Subnatural linewidth in a strongly-driven degenerate two-level system. Optics Communications **284**(20), 4957 – 4960 (2011).

[11] Hopkins, S., Usadi, E., Chen, H., and Durrant, A. Electromagnetically induced transparency of laser-cooled rubidium atoms in three-level -type systems. Optics Communications **138**(1–3), 185 – 192 (1997).

[12] Yan, M., Rickey, E. G., and Zhu, Y. Electromagnetically induced transparency in cold rubidium atoms. J. Opt. Soc. Am. B **18**(8), 1057–1062, Aug (2001).

[13] Wang, J., Zhu, Y., Jiang, K. J., and Zhan, M. S. Bichromatic electromagnetically induced transparency in cold rubidium atoms. Phys. Rev. A **68**, 063810, Dec (2003).

[14] Kowalski, K., Long, V. C., Viet, H. N., Gateva, S., Głódź, M., and Szonert, J. Simultaneous coupling of three *hfs* components in a cascade scheme of EIT in cold ^{85}Rb atoms. Journal of Non-Crystalline Solids **355**(24–27), 1295 – 1301 (2009).

[15] Tiwari, V. B., Singh, S., Rawat, H. S., Singh, M. P., and Mehendale, S. C. Electromagnetically induced transparency in cold ^{85}Rb atoms trapped in the ground hyperfine $F = 2$ state. Journal of Physics B: Atomic, Molecular and Optical Physics **43**(9), 095503 (2010).

[16] Hau, L. V., Harris, S. E., Dutton, Z., and Behroozi, C. H. Light speed reduction to 17 metres per second in an ultracold atomic gas. Nature **397**(6720), 594–598, February (1999).

[17] Budker, D., Kimball, D. F., Rochester, S. M., and Yashchuk, V. V. Nonlinear magneto-optics and reduced group velocity of light in atomic vapor with slow ground state relaxation. Phys. Rev. Lett. **83**, 1767–1770, Aug (1999).

[18] Kash, M. M., Sautenkov, V. A., Zibrov, A. S., Hollberg, L., Welch, G. R., Lukin, M. D., Rostovtsev, Y., Fry, E. S., and Scully, M. O. Ultraslow group velocity and enhanced nonlinear optical effects in a coherently driven hot atomic gas. Phys. Rev. Lett. **82**, 5229–5232, Jun (1999).

[19] Anupriya, J., Ram, N., and Pattabiraman, M. Hanle electromagnetically induced transparency and absorption resonances with a Laguerre Gaussian beam. Phys. Rev. A **81**, 043804, Apr (2010).

[20] Chanu, S. R. and Natarajan, V. Narrowing of resonances in electromagnetically induced transparency and absorption using a Laguerre-Gaussian control beam. Optics Communications **295**, 150 – 154 (2013).

[21] Kapoor, R. and Agarwal, G. S. Theory of electromagnetically induced waveguides. Phys. Rev. A **61**, 053818, Apr (2000).

[22] Molina-Terriza, G., Torres, J. P., and Torner, L. Twisted photons. Nature Physics **3**, 305 (2007).

[23] Pugatch, R., Shuker, M., Firstenberg, O., Ron, A., and Davidson, N. Topological stability of stored optical vortices. Phys. Rev. Lett. **98**, 203601, May (2007).

[24] Vudyasetu, P. K., Camacho, R. M., and Howell, J. C. Storage and retrieval of multimode transverse images in hot atomic rubidium vapor. Phys. Rev. Lett. **100**, 123903, Mar (2008).

[25] Wang, T., Zhao, L., Jiang, L., and Yelin, S. F. Diffusion-induced decoherence of stored optical vortices. Phys. Rev. A **77**, 043815, Apr (2008).

[26] Firstenberg, O., London, P., Yankelev, D., Pugatch, R., Shuker, M., and Davidson, N. Self-similar modes of coherent diffusion. Phys. Rev. Lett. **105**, 183602, Oct (2010).

[27] Inoue, R., Kanai, N., Yonehara, T., Miyamoto, Y., Koashi, M., and Kozuma, M. Entanglement of orbital angular momentum states between an ensemble of cold atoms and a photon. Phys. Rev. A **74**, 053809, Nov (2006).

[28] Moretti, D., Felinto, D., and Tabosa, J. W. R. Collapses and revivals of stored orbital angular momentum of light in a cold-atom ensemble. Phys. Rev. A **79**, 023825, Feb (2009).

[29] Veissier, L., Nicolas, A., Giner, L., Maxein, D., Sheremet, A. S., Giacobino, E., and Laurat, J. Reversible optical memory for twisted photons. Opt. Lett. **38**(5), 712–714, Mar (2013).

[30] Nicolas, A., Veissier, L., Giner, L., Giacobino, E., Maxein, D., and Laurat, J. A quantum memory for orbital angular momentum photonic qubits. Nature Photonics **8**(3), 234–238, March (2014).

[31] Zhai, Z., Li, Z., Xu, J., and Zhang, G. Transfer and computation of optical topological charges via light pulse buffer memory in an electromagnetically-induced-transparency solid. Phys. Rev. A **88**, 035807, Sep (2013).

[32] Marino, A. M., Boyer, V., Pooser, R. C., Lett, P. D., Lemons, K., and Jones, K. M. Delocalized correlations in twin light beams with orbital angular momentum. Phys. Rev. Lett. **101**, 093602, Aug (2008).

[33] Cao, M., Zhang, L., Yu, Y., Ye, F., Wei, D., Guo, W., Zhang, S., Gao, H., and Li, F. Transfer and conversion of images based on eit in atom vapor. Opt. Lett. **39**(9), 2723–2726, May (2014).

[34] Meschede, D. Optics, Light and Lasers. WILEY-VCH, second edition, (2007).

[35] J. Schwinger, L. L. Derad Jr., K. A. M. and Tsai, W. Classical Electrodynamics. Westview Press, (1998).

[36] Walborn, S. P., Pádua, S., and Monken, C. H. Conservation and entanglement of hermite-gaussian modes in parametric down-conversion. Phys. Rev. A **71**(5), 053812 (2005).

[37] Yao, A. M. and Padgett, M. J. Orbital angular momentum: origins, behavior and applications. Adv. Opt. Photon. **3**(2), 161–204, Jun (2011).

[38] Allen, L., Beijersbergen, M. W., Spreeuw, R. J. C., and Woerdman, J. P. Orbital angular momentum of light and the transformation of Laguerre-Gaussian laser modes. Phys. Rev. A **45**, 8185–8189, Jun (1992).

[39] Abramochkin, E. and Volostnikov, V. Beam transformations and nontransformed beams. Optics Communications **83**(1-2), 123 – 135 (1991).

[40] Grynberg, G., Aspect, A., and Fabre, C. Introduction to Quantum Optics. Cambridge University Press, (2010).

[41] Steck, D. A. Rubidium 85 D line data. Available online at http://steck.us/alkalidata.

[42] Steck, D. A. Rubidium 87 D line data. Available online at http://steck.us/alkalidata.

[43] Steck, D. A. Quantum and Atom Optics. 0.9.11 edition, , July (2014). Available online at http://atomoptics.uoregon.edu/ dsteck/teaching/quantum-optics/.

[44] Weissbluth, M. Atoms and Molecules. Academic Press, (1978).

[45] Dalibard, J. and Cohen-Tannoudji, C. Laser cooling below the doppler limit by polarization gradients: simple theoretical models. J. Opt. Soc. Am. B **6**(11), 2023–2045, Nov (1989).

[46] Steane, A. M. and Foot, C. J. Laser cooling below the doppler limit in a magneto-optical trap. EPL **14**(3), 231 (1991).

[47] Raab, E. L., Prentiss, M., Cable, A., Chu, S., and Pritchard, D. E. Trapping of neutral sodium atoms with radiation pressure. Phys. Rev. Lett. **59**(23), 2631–2634, Dec (1987).

[48] Lindblad, G. On the generators of quantum dynamical semigroups. Communications in Mathematical Physics **48**(2), 119–130 (1976).

[49] Tanasittikosol, M., Pritchard, J. D., Maxwell, D., Gauguet, A., Weatherill, K. J., Potvliege, R. M., and Adams, C. S. Microwave dressing of Rydberg dark states. Journal of Physics B **44**(18), 184020 (2011).

[50] Milonni, P. W. Fast Light, Slow Light and Left-Handed Light. Institute of Physics Publishing, (2005).

[51] Bhattacharyya, D., Ray, B., and Ghosh, P. N. Theoretical study of electromagnetically induced transparency in a five-level atom and application to doppler-broadened and doppler-free rb atoms. Journal of Physics B: Atomic, Molecular and Optical Physics **40**(20), 4061 (2007).

[52] Vudyasetu, P. K., Starling, D. J., and Howell, J. C. All optical waveguiding in a coherent atomic rubidium vapor. Phys. Rev. Lett. **102**, 123602, Mar (2009).

[53] Akin, T., Krzyzewski, S., Marino, A., and Abraham, E. Electromagnetically induced transparency with Laguerre-Gaussian modes in ultracold rubidium. Optics Communications **339**(0), 209 – 215 (2015).

[54] O'Hanlon, J. F. A User's Guide to Vacuum Technology. John Wiley & Sons, (1989).

[55] Wieman, C. E. and Hollberg, L. Using diode lasers for atomic physics. Review of Scientific Instruments **62**(1), 1–20 (1991).

[56] Overstreet, K. R., Franklin, J., and Shaffer, J. P. Zeeman effect spectroscopically locked cs diode laser system for atomic physics. Review of Scientific Instruments **75**(11), 4749–4753 (2004).

[57] Krzyzewski, S. P. Feshbach Optimized Photoassociation in Rubidium. PhD thesis, University of Oklahoma, (2015).

[58] Corwin, K. L., Lu, Z.-T., Hand, C. F., Epstein, R. J., and Wieman, C. E. Frequency-stabilized diode laser with the zeeman shift in an atomic vapor. Appl. Opt. **37**(15), 3295–3298 (1998).

[59] Harris, M. L., Cornish, S. L., Tripathi, A., and Hughes, I. G. Optimization of sub-doppler davll on the rubidium d2 line. Journal of Physics B: Atomic, Molecular and Optical Physics **41**(8), 085401 (7pp) (2008).

[60] Kennedy, S. A. Laser Cooling and Trapping using Laguerre-Gaussian Laser Beams. PhD thesis, Unversity of Oklahoma, (2003).

[61] Khonina, S., Kotlyar, V., Skidanov, R., Soifer, V., Laakkonen, P., and Turunen, J. Gauss–laguerre modes with different indices in prescribed diffraction orders of a diffractive phase element. Optics Communications **175**(4–6), 301 – 308 (2000).

[62] Kennedy, S. A., Szabo, M. J., Teslow, H., Porterfield, J. Z., and Abraham, E. R. I. Creation of Laguerre-Gaussian laser modes using diffractive optics. Phys. Rev. A **66**, 043801, Oct (2002).

[63] Streed, E. W., Norton, B. G., Jechow, A., Weinhold, T. J., and Kielpinski, D. Imaging of trapped ions with a microfabricated optic for quantum information processing. Phys. Rev. Lett. **106**, 010502, Jan (2011).

[64] Kim, T., Maunz, P., and Kim, J. Efficient collection of single photons emitted from a trapped ion into a single-mode fiber for scalable quantum-information processing. Phys. Rev. A **84**, 063423, Dec (2011).

[65] Brady, G., Ellis, A., Moehring, D., Stick, D., Highstrete, C., Fortier, K., Blain, M., Haltli, R., Cruz-Cabrera, A., B riggs, R., Wendt, J., Carter, T., Samora, S., and Kemme, S. Integration of fluorescence collection optics with a microfabricated surface electrode ion trap. Applied Physics B **103**(4), 801–808 (2011).

[66] Ivanov, V. V., Isaacs, J. A., Saffman, M., Kemme, S., Ellis, A., Brady, G., Wendt, J., Biedermann, G. W., and Samora, S. Atom trapping in a bottle beam created by a diffractive optical element. arXiv:1305.5309 [physics.atom-ph] (2013).

[67] Beijersbergen, M. W., Coerwinkel, R. P. C., Kristensen, M., and Woerdman, J. P. Helical-wavefront laser beams produced with a spiral phaseplate. Optics Communications **112**(5-6), 321 – 327 (1994).

[68] Clifford, M., Arlt, J., Courtial, J., and Dholakia, K. High-order Laguerre-Gaussian laser modes for studies of cold atoms. Optics Communications **156**(4Äì6), 300 – 306 (1998).

[69] Arlt, J., Dholakia, K., Allen, L., and Padgett, M. J. The production of multiringed Laguerre-Gaussian modes by computer-generated holograms. Journal of Modern Optics **45**(6), 1231–1237 (1998).

[70] Lewandowski, H. J. Coherences and correlations in and ultracold Bose gas. PhD thesis, University of Colorado, (2002).

[71] Research, W. Mathematica Edition: Version 8.0.1.0. Wolfram Research, Inc., Champaign, Illinois, (2008).

[72] Ritchie, N. W. M. A study of collisional trap loss in ultra-cold trapped ^{6}Li and ^{7}Li. PhD thesis, Rice University, (1994).

[73] Kennedy, S. A., Biedermann, G. W., Farrar, J. T., Akin, T. G., Krzyzewski, S. P., and Abraham, E. R. I. Confinement of ultracold atoms in a Laguerre-Gaussian laser beam created with diffractive optics. Optics Communications **321**, 110 – 115 (2014).

[74] Millett-Sikking, A., Hughes, I. G., Tierney, P., and Cornish, S. L. DAVLL lineshapes in atomic rubidium. Journal of Physics B: Atomic, Molecular and Optical Physics **40**(1), 187 (2007).

[75] Chen, Y.-C., Lin, C.-W., and Yu, I. A. Roles of degenerate Zeeman levels in electromagnetically induced transparency. Phys. Rev. A **61**, 053805, Apr (2000).

[76] Ćuk, S. M., Krmpot, A. J., Radonjić, M., Nikolić, S. N., and Jelenković, B. M. Influence of a laser beam radial intensity distribution on zeeman electromagnetically induced transparency line-shapes in the vacuum rb cell. Journal of Physics B **46**(17), 175501 (2013).

[77] Truscott, A. G., Friese, M. E. J., Heckenberg, N. R., and Rubinsztein-Dunlop, H. Optically written waveguide in an atomic vapor. Phys. Rev. Lett. **82**, 1438–1441, Feb (1999).

[78] Marino, A. M. and Stroud, C. R. Phase-locked laser system for use in atomic coherence experiments. Review of Scientific Instruments **79**(1), – (2008).

[79] Ruseckas, J., Mekys, A., and Juzelinas, G. Manipulation of slow light with orbital angular momentum in cold atomic gases. Optics and Spectroscopy **108**(3), 438–445 (2010).

[80] Ruseckas, J., Mekys, A., and Juzelinas, G. Optical vortices of slow light using a tripod scheme. Journal of Optics **13**(6), 064013 (2011).

[81] Ruseckas, J., Kudriašov, V. c. v., Yu, I. A., and Juzeliūnas, G. Transfer of orbital angular momentum of light using two-component slow light. Phys. Rev. A **87**, 053840, May (2013).

[82] Lvovsky, A. I., Sanders, B. C., and Tittel, W. Optical quantum memory. Nat Photon **3**(12), 706–714, 12 (2009).

[83] Marzlin, K.-P., Zhang, W., and Wright, E. M. Vortex coupler for atomic bose-einstein condensates. Phys. Rev. Lett. **79**(24), 4728–4731, Dec (1997).

[84] Wright, K. C., Leslie, L. S., and Bigelow, N. P. Optical control of the internal and external angular momentum of a bose-einstein condensate. Phys. Rev. A **77**(4), 041601, Apr (2008).

[85] Kuga, T., Torii, Y., Shiokawa, N., Hirano, T., Shimizu, Y., and Sasada, H. Novel optical trap of atoms with a doughnut beam. Phys. Rev. Lett. **78**, 4713–4716, Jun (1997).

[86] Davidson, N., Jin Lee, H., Adams, C. S., Kasevich, M., and Chu, S. Long atomic coherence times in an optical dipole trap. Phys. Rev. Lett. **74**, 1311–1314, Feb (1995).

[87] Chaloupka, J. L., Fisher, Y., Kessler, T. J., and Meyerhofer, D. D. Single-beam, ponderomotive-optical trap for free electrons and neutral atoms. Opt. Lett. **22**(13), 1021–1023, Jul (1997).

[88] Ozeri, R., Khaykovich, L., and Davidson, N. Long spin relaxation times in a single-beam blue-detuned optical trap. Phys. Rev. A **59**, R1750–R1753, Mar (1999).

[89] Ozeri, R., Khaykovich, L., and Davidson, N. Erratum: Long spin relaxation times in a single-beam blue-detuned optical trap [phys. rev. a **59** , r1750 (1999)]. Phys. Rev. A **65**, 069903, Jun (2002).

[90] Ozeri, R., Khaykovich, L., Friedman, N., and Davidson, N. Large-volume single-beam dark optical trap for atoms using binary phase elements. J. Opt. Soc. Am. B **17**(7), 1113–1116, Jul (2000).

[91] Kulin, S., Aubin, S., Christe, S., Peker, B., Rolston, S. L., and Orozco, L. A. A single hollow-beam optical trap for cold atoms. Journal of Optics B: Quantum and Semiclassical Optics **3**(6), 353 (2001).

[92] Isenhower, L., Williams, W., Dally, A., and Saffman, M. Atom trapping in an interferometrically generated bottle beam trap. Opt. Lett. **34**(8), 1159–1161, Apr (2009).

[93] Olson, S. E., Terraciano, M. L., Bashkansky, M., and Fatemi, F. K. Cold-atom confinement in an all-optical dark ring trap. Phys. Rev. A **76**, 061404, Dec (2007).

[94] Xu, P., He, X., Wang, J., and Zhan, M. Trapping a single atom in a blue detuned optical bottle beam trap. Opt. Lett. **35**(13), 2164–2166, Jul (2010).

[95] Li, G., Zhang, S., Isenhower, L., Maller, K., and Saffman, M. Crossed vortex bottle beam trap for single-atom qubits. Opt. Lett. **37**(5), 851–853, Mar (2012).

[96] Tempere, J., Devreese, J. T., and Abraham, E. R. I. Vortices in Bose-Einstein condensates confined in a multiply connected Laguerre-Gaussian optical trap. Phys. Rev. A **64**, 023603, Jul (2001).

[97] Thanvanthri, S., Kapale, K. T., and Dowling, J. P. Ultra-stable matteräìwave gyroscopy with counter-rotating vortex superpositions in boseäìeinstein condensates. Journal of Modern Optics **59**(13), 1180–1185 (2012).

[98] Ryu, C., Andersen, M. F., Cladé, P., Natarajan, V., Helmerson, K., and Phillips, W. D. Observation of persistent flow of a bose-einstein condensate in a toroidal trap. Phys. Rev. Lett. **99**, 260401, Dec (2007).

[99] Wright, E. M., Arlt, J., and Dholakia, K. Toroidal optical dipole traps for atomic Bose-Einstein condensates using Laguerre-Gaussian beams. Phys. Rev. A **63**(1), 013608, Dec (2000).

[100] Akin, T., Kennedy, S., Dribus, B., Marzuola, J. L., Johnson, L., Alexander, J., and Abraham, E. Boseäìeinstein condensation transition studies for atoms confined in laguerreäìgaussian laser modes. Optics Communications **285**(1), 84 – 89 (2012).

[101] MacAdam, K. B., Steinbach, A., and Wieman, C. A narrow-band tunable diode laser system with grating feedback, and a saturated absorption spectrometer for cs and rb. American Journal of Physics **60**(12), 1098–1111 (1992).

[102] Grimm, R., Weidemüller, M., and Ovchinnikov, Y. B. Optical dipole traps for neutral atoms. volume 42 of Advances In Atomic, Molecular, and Optical Physics, 95 – 170. Academic Press (2000).

[103] Akin, T. G. and Abraham, E. R. I. *Mathematica*™ calculation, (2013).

[104] Franke-Arnold, S., Leach, J., Padgett, M. J., Lembessis, V. E., Ellinas, D., Wright, A. J., Girkin, J. M., Ohberg, P., and Arnold, A. S. Optical ferris wheel for ultracold atoms. Opt. Express **15**(14), 8619–8625, Jul (2007).

Appendix A

Electromagnetically induced transparency using higher-order Laguerre-Gaussian modes

A.1 Introduction

Thus far, we have explored electromagnetically induced (EIT) using LG_0^1 laser modes. It is natural, then, to explore some properties of EIT using control lasers with more complex modes. In this chapter, we will consider the effect on line shape, width, and contrast for EIT configurations using two higher-order modes: the LG_0^5 mode and the LG_1^2 mode.

The experimental apparatus for this study is identical to that shown in figure 5.1. The only alteration is that we use a different set of diffractive optics. This is done by swapping the glass slides (shown in figure 3.12) with plates designed to convert the laser from the LG_0^5 and LG_1^2 modes. The AOM frequency of the *control laser* is modulated using an analogue voltage sent to the NEOS analog driver system model N21080-1SAS. With a nominal operating RF frequency of 80 MHz, applying a voltage modulation from [-5 V,+5 V] corresponds to RF frequency modulation from [75 MHz, 85 MHz] (10 MHz modulation range). Since we are double

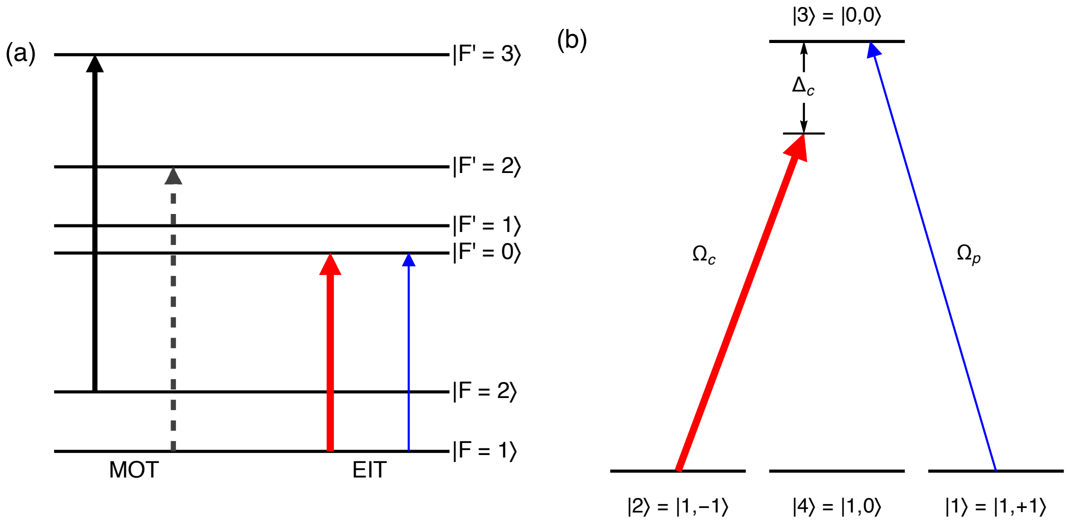

Figure A.1: Level diagrams for ^{87}Rb. Figure (a) shows the hyperfine levels on the D2 transition. The MOT trapping transition is shown with the solid black arrow, the MOT re-pumping transition is shown with the gray dashed arrow, the probe transition is shown with the thin blue arrow, and the control laser is shown with the thick red arrow. Figure (b) shows the levels involved in EIT. The probe (thin blue arrow) couples the $|F = 1, m_F = -1\rangle \rightarrow |F' = 0, m_{F'} = 0\rangle$ magnetic sublevels using σ^+ polarization. The control (thick red arrow) couples the $|F = 1, m_F = +1\rangle \rightarrow |F' = 0, m_{F'} = 0\rangle$ magnetic sublevels using σ^- polarization. The state, $|4\rangle$, is included because the atom can decay to this state.

passing the AOMs, we have 20 MHz available for the probe scan. We choose to keep the probe laser stabilized on resonance while we modulate the control laser frequency for this experiment in order to simplify the transmission profiles. This appendix will present spectra recorded by the photodiode for a control laser of each of the two laser modes, as well as CCD images of the probe showing spatial resolution of the EIT spectrum.

As an interesting note, the narrowest resonance feature ($\approx \Gamma/50$) was measured using the LG$_1^2$ laser mode. The following sections highlight selected spectra recorded by the photodiode, as well as a spatial analysis of the EIT spectrum as recorded by the CCD camera.

A.2 EIT with a LG_0^5 Control

Figure A.2 shows the spectrum recorded by a photodiode when the control laser is in the LG_0^5 mode. Figure A.3 shows the spectrum recorded by the CCD camera. Similar to chapter 5, the two axes subtending the horizontal plane correspond to the control detuning (Δ_c) and the position along a cross-section that spans the probe from $-w_p$ to w_p. We observe similar waveguide behavior of the atomic medium, as was observed in chapter 5.

A.3 EIT with a LG_1^2 Control

Figure A.4 shows the spectrum recorded by a photodiode when the control laser was in the LG_1^2 mode. It should be noted that the FWHM of the EIT resonance feature is one-fiftieth the natural linewidth (0.02Γ). Figure A.5 shows the spectrum recorded by the CCD camera. Similar to chapter 5, the two axes subtending the horizontal plane correspond to the control detuning (Δ_c) and the position along a cross-section that spans the probe from $-w_p$ to w_p. We observe similar waveguide behavior of the atomic medium, as was observed in chapter 5.

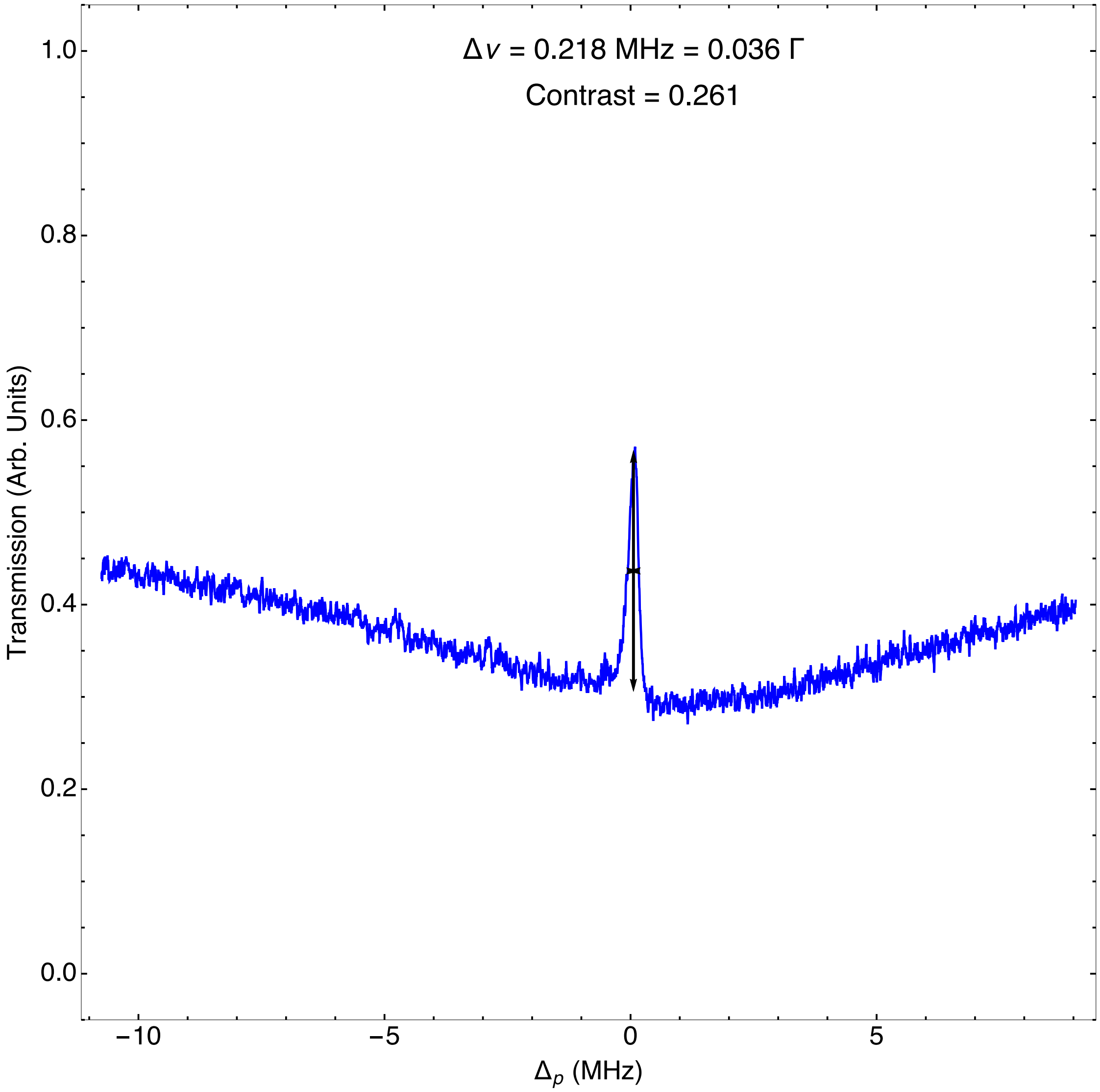

Figure A.2: EIT spectrum recorded on a photodiode. The probe laser is in the Gaussian mode, and the control laser is in the LG_0^5 mode.

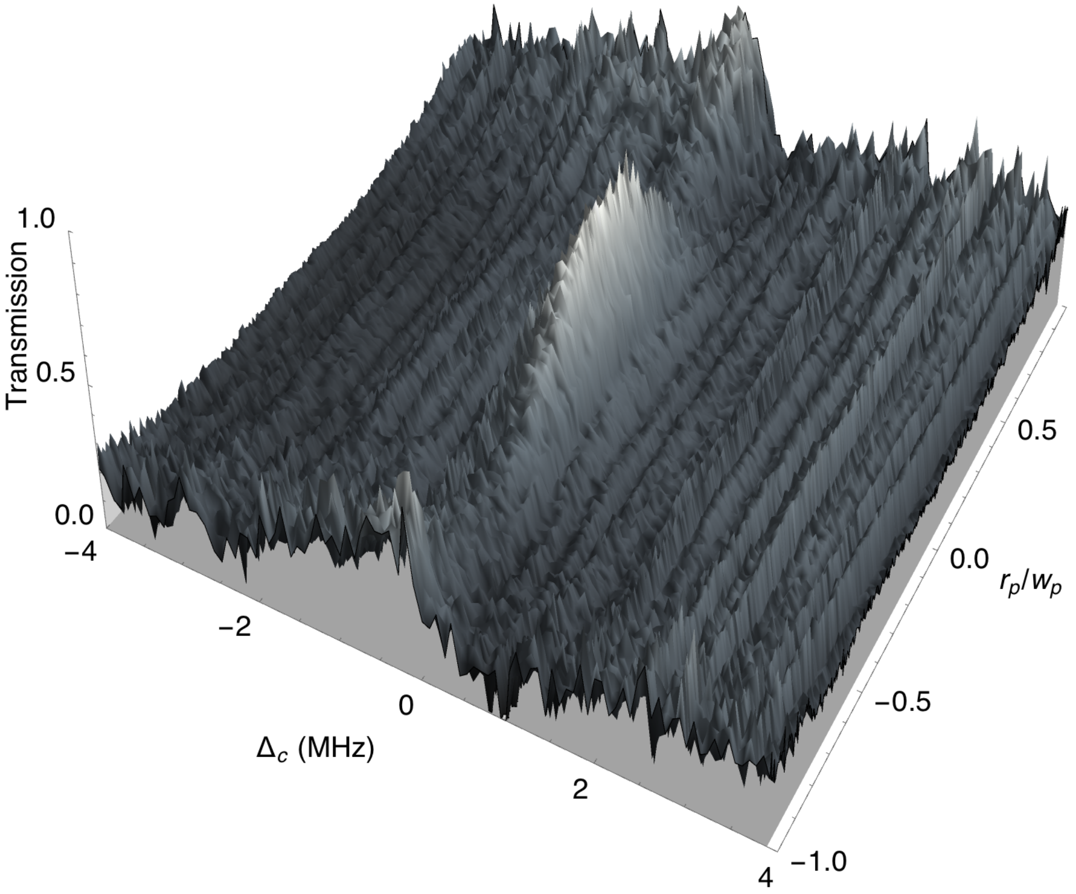

Figure A.3: A spatial resolution of the EIT spectrum recorded by the CCD camera. The two axes subtending the horizontal plane are the control detuning (Δ_c), and the probe transverse position (r_p/w_p). We observe a waveguide effect caused by a manipulation of the linear susceptibility by the LG_0^5 laser.

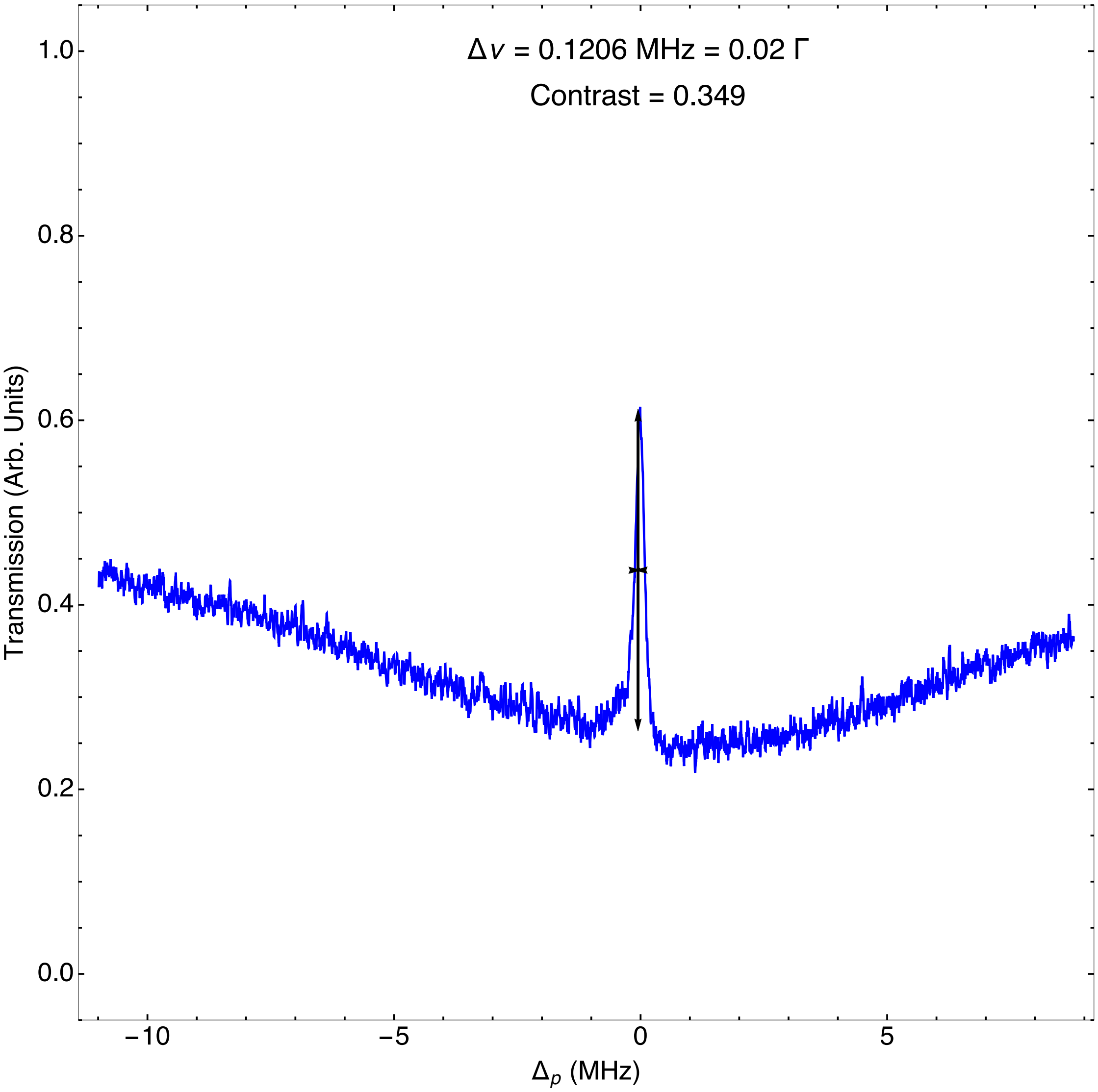

Figure A.4: EIT spectrum recorded on a photodiode. The probe laser is in the Gaussian mode, and the control laser is in the LG_1^2 mode. This is the narrowest resonance feature recorded in our lab.

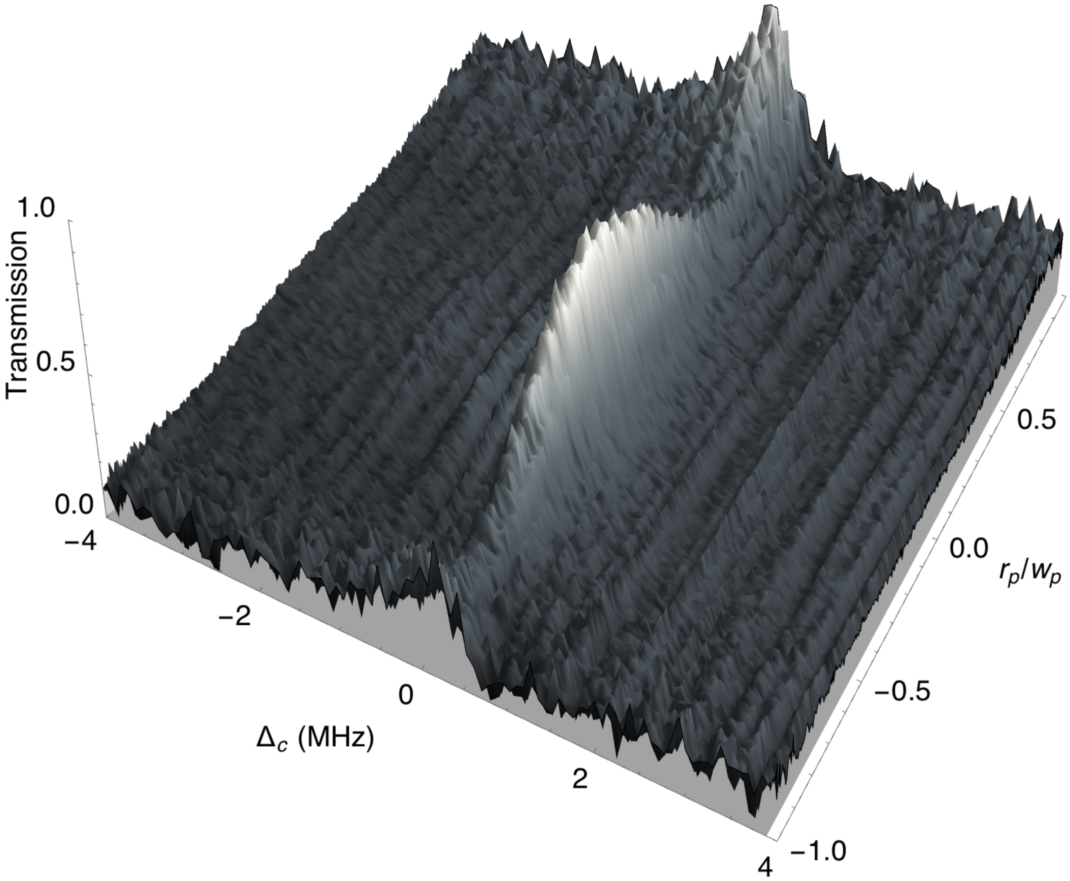

Figure A.5: A spatial resolution of the EIT spectrum recorded by the CCD camera. The two axes subtending the horizontal plane are the control detuning (Δ_c), and the probe transverse position (r_p/w_p). We observe a waveguide effect caused by a manipulation of the linear susceptibility by the LG_0^5 laser.

Appendix B

Optical confinement of Rb using Laguerre-Gaussian beams

B.1 Introduction

A laser propagating in the Laguerre-Gaussian (LG_p^ℓ) transverse mode is a versatile tool in atomic, molecular, and optical (AMO) physics. The $e^{\imath\ell\phi}$ azimuthal winding phase gives rise to an intrinsic quantized orbital angular momentum of $\ell\hbar$ per photon [38]. The additional quantum number may allow multi-dimensional quantum computing and encryption [22]. Experiments have been proposed [83] and demonstrated [84] that orbital angular momentum can be coupled from the optical field to the atomic internal states, revealed as a vortex state in a Bose-Einstein condensed (BEC) gas. The $p+1$ radial intensity nodes create cylindrically symmetric geometries, generating a manifold of multiply connected traps.

Blue-detuned dipole traps attract atoms to regions of low intensity, where the atoms scatter fewer photons and experience smaller ac Stark shifts. Cold atoms trapped in this configuration may be used in an atomic clock, and other precision measurements. Dark optical traps have confined large numbers of atoms using an LG_0^3 beam [85], an arrangement of blue detuned lasers [86], and in other complex laser modes [87–92]. A dark toroidal geometry trap was created using a superposition of LG_p^ℓ beams [93]. A blue-detuned dipole trap generated from a spatial light modulator [94] and two crossed LG_p^ℓ laser modes generated from a spatial phase plate [95] trapped single atoms with long coherence times. For the LG_0^ℓ mode laser, the azimuthal winding phase ensures that the intensity necessarily goes to zero at the center of the laser beam, confining the atoms in the central region of the laser beam.

Alternatively, red-detuned dipole traps confine atoms in the high intensity region of the trapping laser. Degenerate gases excited into vortex states confined in toroidal geometry traps exhibit unique matter wave interference patterns [96]. Multiply connected traps locally pin vortices in BECs, making them ideal for ring shaped BEC rotational gyroscopes [97]. While it is possible to create a multiply connected trap using a magnetic trap whose center is plugged by a blue detuned fundamental mode laser [98], these traps are species and state selective. Optical traps circumvent this problem. For a red-detuned LG_0^1 mode laser, the atoms are confined in a toroidal geometry. A theoretical analysis has concluded that a BEC whose initial conditions are similar to those found in standard traps can be loaded into an LG_p^ℓ mode [99], and a theoretical calculation of the transition of a thermal gas to a BEC within the LG_p^ℓ laser mode itself has been done [100].

Diffractive optics can transform, external to the laser cavity, the Gaussian output of a laser into LG_p^ℓ modes. A diffractive optic is a transparent optic where lithography techniques are used to etch microscopic structures on the surface.

These structures are designed such that the laser wavefront evolves into the desired form via Huygens' principle. Two optics are necessary to control both the intensity and phase. Diffractive optics can create high-order LG_p^ℓ modes [61], with demonstrated mode purities much higher than those formed with other methods [62]. The compact diffractive optics have proven advantageous in quantum information processing, where the large numerical aperture of these optics gather the largest fraction of the fluorescence emitted by an ion trapped on a chip [63–65]. Recently, diffractive optic elements have been used to create blue detuned bottle beam traps [66].

We report 2D confinement of ultracold ^{87}Rb atoms loaded from a magneto-optical trap (MOT) in both blue-detuned and red-detuned LG_0^1 (doughnut mode) laser beams. The atoms are confined to the central node of the LG_0^1 mode in the blue-detuned case, and the atoms are confined in the toroidal anti-node of the LG_0^1 for the red-detuned case. We align our LG_0^1 mode vertically (along the direction of gravity), maintaining cylindrical symmetry. Study of the atomic density distribution reveals asymmetries in the LG_0^1 mode. This provides an *in situ* measurement of the LG_p^ℓ mode purity and the possibility of more exotic confinement potentials.

B.2 Experiment

Figure B.1 shows a schematic of the experiment. The trapping laser consists of a low-power external-cavity diode laser [101] amplified by an SDL tapered ampli-

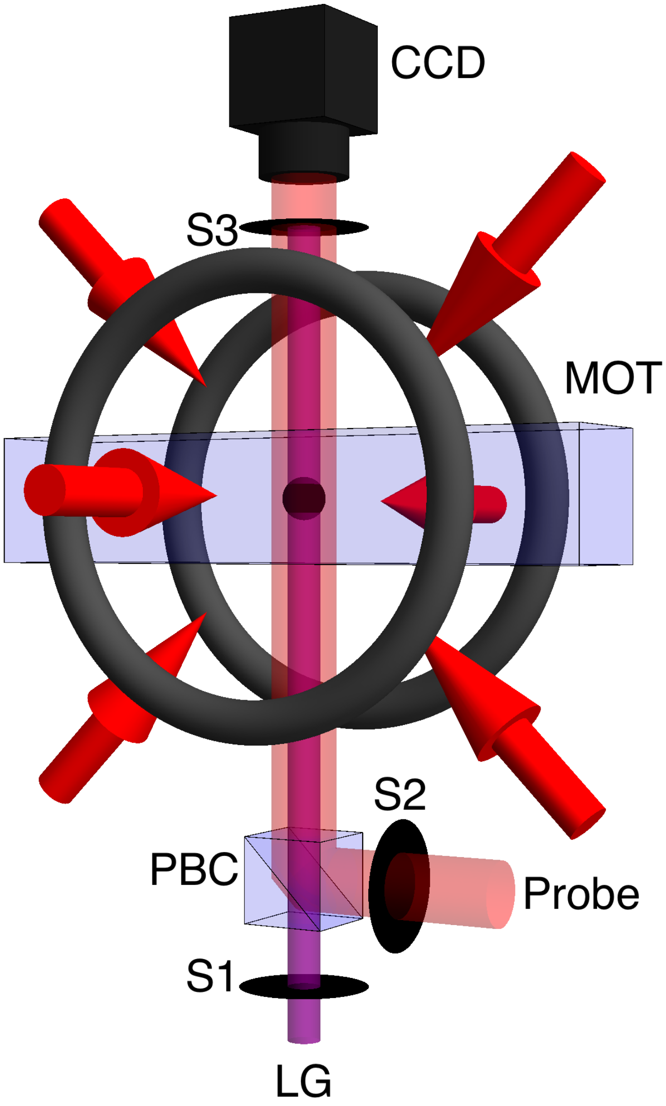

Figure B.1: This figure is a conceptional diagram of our experimental setup. Two of the MOT beams are directed at 45° relative to the cell. The third beam goes through the face of the cell along the axis of the magnetic field coils. The collinear probe and LG_0^1 laser beams are directed vertically through the center of the MOT and are then sent into a CCD camera.

fier in the Master Oscillator Power Amplifier (MOPA) configuration locked at a frequency to the red of the $|^2S_{1/2}, F = 2\rangle \rightarrow |^2P_{3/2}, F' = 3\rangle$ cycling transition in ^{87}Rb using a Dichroic-Atomic-Vapor Laser Lock (DAVLL) [74]. A series of three cylindrical lenses shape and expand the elliptical 300 mW output of this laser to a symmetrical Gaussian profile with an $1/e^2$ beam radius of 12.5 mm. The beam is sent through two polarizing beam splitter cubes (PBC) to create three beams that are directed through the cell along orthogonal axes and then retro-reflected. Three $\lambda/2$ retarding optics adjust the fraction transmitted and reflected by the PBCs, and thus the relative intensity of the three beams. Two of the beams are directed at 45° angles relative to the cell, while the third beam is directed along the axis of the anti-Helmholtz coils through the side of the cell.

A 10 mW external cavity diode laser repumps the atoms that fall into the $|F = 1\rangle$ hyperfine level back into the cycling transition. After reshaping the output with an anamorphic prism pair and expanding the beam to an $1/e^2$ beam radius of 12.5 mm, we inject the repump laser through the back of one of the PBCs so that it is collinear with the trapping beam. This laser is tuned to the $|^2S_{1/2}, F = 1\rangle \rightarrow |^2P_{3/2}, F' = 2\rangle$ transition. Originally, this laser was locked on resonance using saturated absorption spectroscopy. However, we find it easier to use the saturated absorption spectrometer [101] to find the right transition, and lock the laser with a DAVLL. We then optimize the frequency of the repump laser by simply maximizing the number of trapped atoms in the MOT.

The vapor-cell MOT is created from a Rb vapor in a 1.4 x 1.4 x 11 in rectangular glass cell that offers large optical access. This cell is pumped with a Varian Turbo-V 250 ℓ/s vacuum pump roughed by a Varian DS 102 mechanical pump. Typical vacuum pressure is 10^{-8} to 10^{-7} Torr. At the center of the trap a magnetic field gradient of 20 G/cm is created by supplying 13 A through two 20-turn, 11 cm diameter coils placed 8 cm apart in an anti-Helmholtz configuration. The MOT regularly produces $\sim 10^8$ atoms with temperatures between 0.1-20 mK depending on the degree to which background magnetic fields are canceled.

To optically confine the cold atom sample, we overlap a laser in the LG_p^ℓ mode with the MOT. The LG_p^ℓ modes have a radial electric field whose magnitude is proportional to the product of a Gaussian and an associated Laguerre polynomial $L_p^\ell(x)$, which gives the characteristic $p+1$ radial intensity nodes when $\ell > 0$. For a planar wave front propagating along the z-axis, the magnitude of the electric field at $z = 0$ is given by:

$$u_p^\ell(r) = \sqrt{\frac{2P}{\pi w^2}}(-1)^p e^{-\imath\ell\phi} e^{-r^2/w^2} \left(\frac{\sqrt{2}r}{w}\right)^{|\ell|} L_p^\ell\left(2r^2/w^2\right), \tag{B.1}$$

where P is the laser power and w is the beam waist. The $e^{-\imath\ell\phi}$ term in Equation (B.1) implies that there is a quantized azimuthal phase change of $2\pi\ell$ in the electric field. This results in an intensity node at the center of the beam and an angular momentum of $\ell\hbar$ per photon. A Gaussian beam occurs when $\ell = p = 0$, whereas a donut beam occurs when $\ell > 0$ and $p = 0$. As ℓ increases, so does the orbital angular momentum, and thus so does the effective size of the central node. This can be seen from Equation (B.1), where the intensity has a functional form of $r^{2\ell}$ near $r = 0$.

Cold atoms can be confined to either the nodes or the antinodes of these beams by means of the optical dipole force potential, which in the approximation of a two-level system and in the limit of the detuning being large compared to the natural linewidth, has the form:

$$U(r) = \frac{\hbar\Gamma^2}{4\Delta}\frac{I(r)}{I_{\text{sat}}}, \tag{B.2}$$

where $I(r)$ is the intensity distribution of the laser, I_{sat} is the saturation intensity, Δ is the detuning (the difference between the laser frequency and the transition frequency between the two states), and Γ is the linewidth of the excited atomic state. If the LG_p^ℓ laser is tuned above resonance (blue detuned, $\Delta > 0$), then the atoms will be repelled from regions of high intensity and confined to the nodes of the LG_p^ℓ laser mode, whereas if the laser is tuned below resonance (red detuned, $\Delta < 0$) then the atoms will be attracted to the anti-nodes.

The LG_0^1 laser beam is created using diffractive optics developed in collaboration with the research department of Diffractive Optics Corporation. These optics are advantageous in that they offer an external cavity method of creating very pure, higher-order LG_p^ℓ laser modes. Creating high-order LG_p^ℓ beams with computer generated holograms has a maximum mode purity of 80% intensity in the p mode of interest [69]. Our diffractive optics have demonstrated LG_p^ℓ beam creation with $> 92\%$ of the output beam intensity in the desired mode [62]. We use two optics to generate the desired LG_p^ℓ beam, one to control the intensity, and the other to control the phase.

We spatially filter the 300 mW output of a second MOPA to obtain a more pure Gaussian beam. (Previously, for the highest mode purity we used a single mode optical fiber to filter the beam.) The resulting 100 mW output of the spatial filter is telescoped to a $1/e^2$ beam radius of 0.5 mm and sent through the two LG_0^1 optics. We routinely get $\simeq 30$ mW of power in a pure LG_0^1 laser mode. The beam is then expanded by approximately a factor of four to increase the trapping volume. This results in a radial trap frequency of 30 Hz, at a detuning of 2 GHz. The beam is directed vertically through the center of the MOT.

A weak probe laser is resonant with the $|^2S_{1/2}, F = 1\rangle \to |^2P_{3/2}F' = 2\rangle$ transition, and propagates co-linearly with the LG_0^1 beam. The probe beam is shuttered using a NEOS N23080 Acoustic Optical Modulator, and is used to image the cloud of atoms onto a Pulnix TM-300NIR CCD camera. Because the intensity of the LG_0^1 beam saturates our camera, a Uniblitz LS6T2 shutter is placed in the LG_0^1 beam path and a second shutter placed in front of the camera, so the LG_0^1 beam never enters the camera. First, the LG_0^1 shutter is closed. After 0.1 ms, the camera shutter is opened, and the probe is flashed 1.9 ms later. The shutter in front of the camera does not always fully open for shorter delays.

B.3 Results

The cold atoms absorb the resonant light from the weak probe beam, and there is a reduction in intensity following Beer's law: $\ln(I_0/I_{\text{out}}) = \sigma_0 n$. Here, I_0 is the incident probe intensity, I_{out} is the probe intensity after passing through the atomic ensemble, σ_0 is the resonant photon scattering cross-section, and n is the integrated column density. In order to extract the atomic column density, we take a series of three CCD images. The probe beam is first imaged in the presence of the trapped atoms, measuring I_{out}. Then, I_0 is measured by imaging the probe absent any confined atoms. After blocking the probe laser, we expose the CCD chip and subtract this information (I_{bg}) from the previous two images. The column density at each CCD pixel is determined by:

$$n = \frac{1}{\sigma_0} \ln\left(\frac{I_0 - I_{\text{bg}}}{I_{\text{out}} - I_{\text{bg}}}\right). \tag{B.3}$$

The array of CCD pixels map out the column density in a plane transverse to the direction of the probe beam propagation.

We confine 10^7 ^{87}Rb atoms in the central node of an LG_0^1 laser beam detuned 2 GHz to the blue of the $|^2S_{1/2}, F = 1\rangle \rightarrow |^2P_{3/2}\rangle$ resonance frequency. We first superimpose the LG_0^1 beam over the MOT. The repump laser is blocked, and the

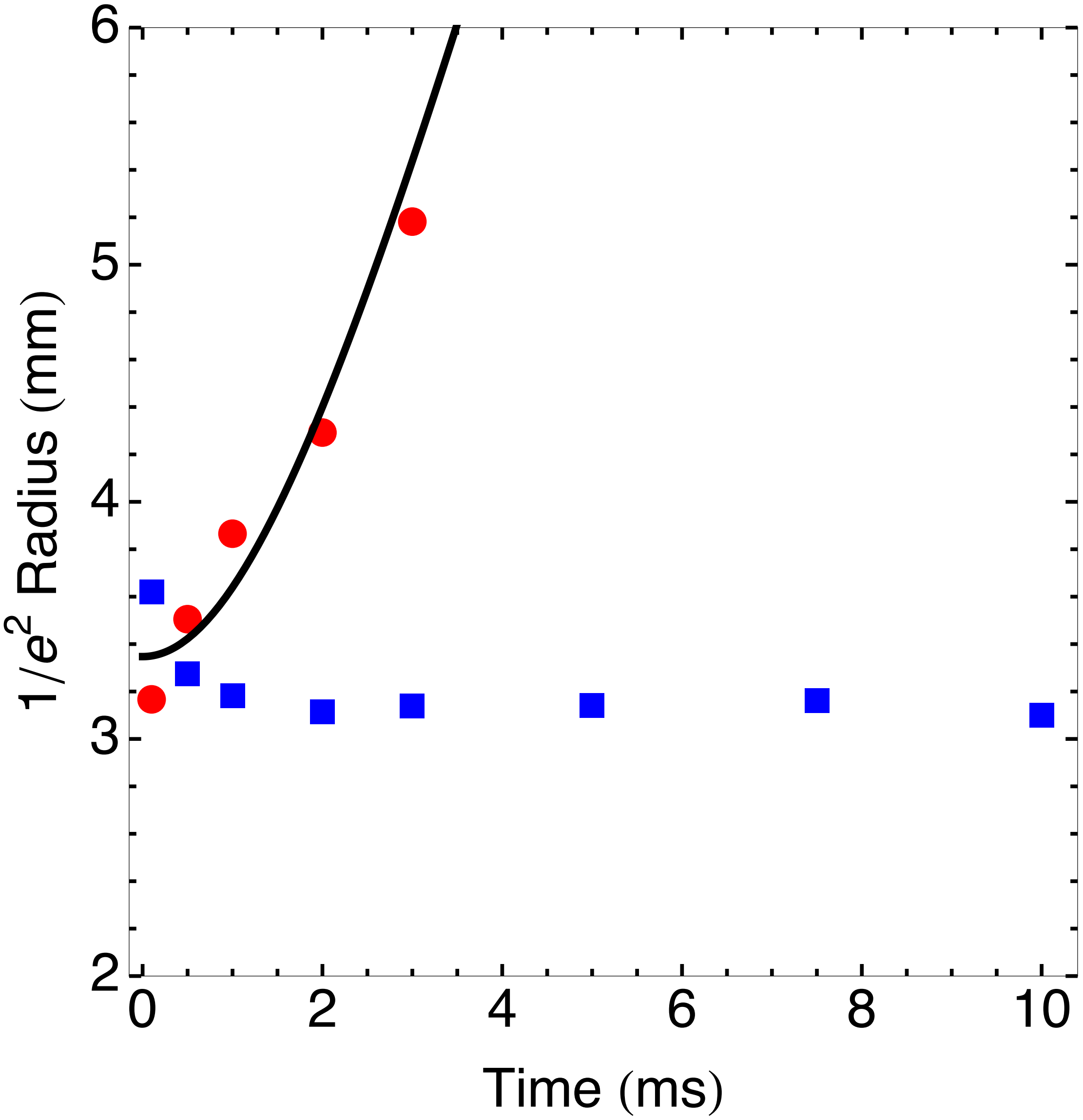

Figure B.2: (Color online) The size of the atom cloud as a function of expansion time. The red circles represent the size of the atom cloud when there was no LG_0^1 beam present. The blue squares represent the size of the cloud with an LG_0^1 laser beam present detuned to the blue of the atomic resonance. With the LG_0^1 laser present, the size of the cloud remains approximately the same. This implies that the atoms are indeed confined to the center node of the LG_0^1 laser mode. Without the LG_0^1 laser beam present, in 4 ms the full cloud cannot be imaged nor a full $1/e^2$ radius be determined. The line is a fit to the expanding atoms with a fitted temperature of 20 mK.

atoms are optically pumped into the $|F = 1\rangle$ hyperfine level where they no longer interact with the MOT beams. The atoms are confined in 2D due to the repulsive force from the toroidal LG_0^1 beam surrounding the atoms. To detect the atoms we block the LG_0^1 beam and probe the remaining atoms with the absorption imaging procedure described above. We vary the delay between blocking the repump and probing the atoms. If the atoms are confined to the central node of the LG_0^1 beam, then the size of the atom cloud will not change with longer delays. If there is no confinement, then the atom cloud will expand at a rate related to its temperature.

The image from the CCD camera is fit to a Gaussian profile from which we can obtain the $1/e^2$ radius of the atom cloud. We find the density distribution is modelled accurately by a Gaussian. Figure B.2 shows the size of the atom cloud as a function of the delay between when the repump is blocked and the atoms are observed. The size of the atom cloud with and without the LG_0^1 beam are shown as blue squares and red circles respectively. When the LG_0^1 beam is superimposed over the MOT, the size of the atom cloud does not vary significantly as the delay time increased, indicating that the atoms are indeed confined to the central node of the LG_0^1 beam. When the LG_0^1 beam is not superimposed over the MOT, the atom cloud increases at a rate consistent with a temperature of 20 mK. The discrepancy in the cloud sizes between the two data sets at $t = 0$ is consistent with run-to-run variations. It is also possible that the repulsive interactions of the of the blue-detuned LG_0^1 mode with the atoms at the edge of the MOT distorts the initial distribution, making it larger than the MOT without the LG_0^1 beam. The initial decrease in the optically confined cloud size is due to the loss of those atoms from the MOT not confined by the LG_0^1 mode.

Figure B.3 (a) shows an absorption image of 10^4 ultracold atoms trapped in a toroidal potential formed by a 30 mW LG_0^1 beam tuned 2 GHz to the red of the $|^2S_{1/2}, F = 2\rangle \rightarrow |^2P_{3/2}\rangle$ transition. To perform this experiment we superimpose the LG_0^1 beam over the MOT, and image the atoms as described above. In this case, we do not turn off the MOT, so there are still atoms confined within the MOT that are not trapped in the LG_0^1 beam. We have subtracted these atoms from the absorption image to obtain Figure B.3 (a).

The density distribution contained within the LG_0^1 is consistent with a Gaussian that is offset and rotated around the axis of symmetry. However, there is an azimuthal asymmetry in the density distribution, from variations in the intensity of the LG_0^1 laser beam due to misalignment of the diffractive optics [62]. This asymmetry in the intensity distribution manifests itself in the trap potential which causes a larger trap depth and more atoms in regions of higher intensity, shown in Figures B.3-B.5.

To model the system we assume the atoms obey Maxwell-Boltzmann statistics and the atomic density distribution is given by [102]:

$$n(r, \phi) = n_0 e^{-U(r,\phi)/k_B T}, \tag{B.4}$$

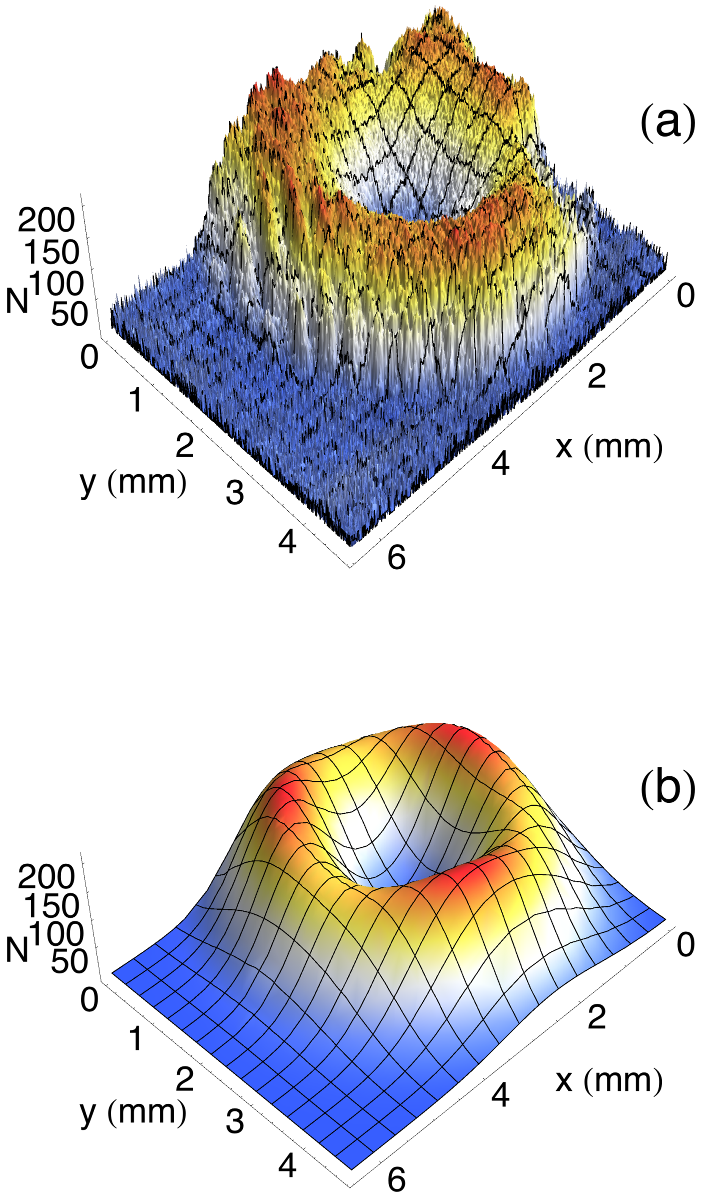

Figure B.3: (Color online) (a) 3D CCD image of the number of atoms in the high-intensity region of our red-detuned LG_0^1 laser mode. In this image the Gaussian shaped profile of the atoms still confined in the MOT, but not confined in the high-intensity area has been removed. (b) Fit of Equation (B.7) to the atom distribution in (a).

where n_0 is the peak density, k_B is the Maxwell-Boltzmann constant, T is the temperature, and $U(r,\phi)$ is the confining potential. The confining potential is given by Equation (B.2), where $I(r) = |u_0^1(r)|^2$ for a pure LG_0^1 mode. Since the intensity of this mode is azimuthally symmetric, it does not fit our data. Tracing a path azimuthally around the absorption image, we note an oscillatory behavior in the atomic density distribution with a frequency of 3 Hz. We add a term to the model for the potential that oscillates with the same frequency. Our phenomenological model of the potential becomes:

$$U_{\mathrm{LG}}(r,\phi) = -a\frac{2r^2}{w^2}e^{-r^2/w^2}\left(1 + b\sin(3\phi + \phi_0)\right), \tag{B.5}$$

where b and ϕ_0 are fitting parameters that give the fractional size and location of the azimuthal asymmetries in the intensity profile. The parameter $a = \hbar\Gamma^2 I_0/4I_{\mathrm{sat}}\Delta k_B T$ is also a fitting parameter, where $I_0 = P/\pi w^2$ is the peak intensity of the trapping laser, and P is the power of the trapping laser. To simplify our model, we approximate the potential as a simple harmonic oscillator. Expanding the potential to the second order about the equilibrium position $r = w/\sqrt{2}$, the potential becomes:

$$U_{\mathrm{sho}}(r,\phi) = \left(\frac{4a}{ew^2}\left(r - \frac{w}{\sqrt{2}}\right)^2 - \frac{a}{e}\right)(1 + b\sin(3\phi + \phi_0)) + \frac{a}{e}(1 + b), \tag{B.6}$$

where the last term defines the zero of the potential to be at the minimum. Combining Equation (B.6) with Equation (B.4) gives the density distribution function:

$$n(r,\phi) = n_0 \exp\left\{-\left(\frac{4a}{ew^2}\left(r-\frac{w}{\sqrt{2}}\right)^2 - \frac{a}{e}\right)(1+b\sin(3\phi+\phi_0)) - \frac{a}{e}(1+b)\right\}. \tag{B.7}$$

Equation (B.7) is fit to the data in Figure B.3 (a), using *Mathematica*™, where a, b, w, and ϕ_0 are fitting parameters. Figure B.3 (b) shows our best fit of our model for the density distribution. From the fit, we determine that the laser intensity varies by 13%. From our known laser power and the fitting results, we can also conclude that the temperature of the two-dimensionally confined atoms is 13 μK. This temperature is much less than the temperature of the MOT due to the shallow trap depth of the toroidal confining potential. Only the coldest fraction of the atoms from the MOT are confined. The measured temperature in the dipole trap is consistent with the theoretical trap depth of 10 μK calculated using the known power, detuning, and beam size.

Figure B.4 (a) is a 2D CCD image of the data shown in Figure B.3 (a). Each cross section for Figures B.4 (b)-(d) is indicated in the CCD image, Figure B.4 (a). Figures B.4 (b)-(d) show 1D cross sections of this data for fixed azimuthal angle ϕ. The blue points in each of the figures represent the absorption data along the cross section. The red dashed, dot-dashed, and solid lines are the theoretical fits from the model in Equation (B.7). Figure B.4 (d) shows the largest azimuthal density

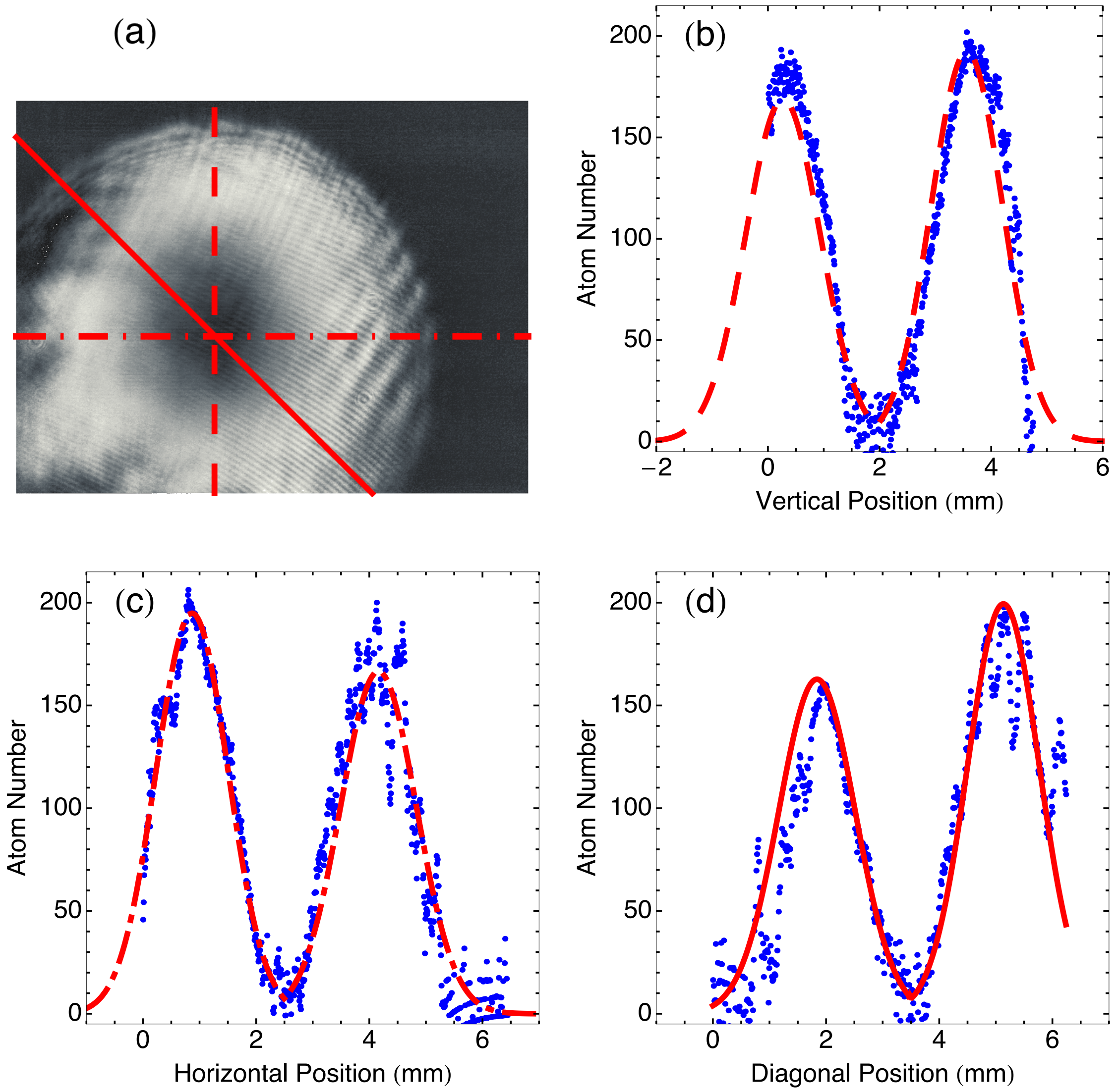

Figure B.4: (Color online) (a) A 2D CCD image of the data shown in B.3 (a). Each cross sections in (b)-(d) is indicated in the CCD image (a). The dashed red curve shows the vertical cross section, the dot-dashed red curve shows the horizontal cross section, and the solid red curve shows the diagonal cross section. The blue points are the data. For each cross section, ϕ is fixed and r is varied. (d) Shows the largest azimuthal density difference.

difference.

Sixty cross sections of the data in Figure B.3 (a), in which the radial coordinate r is fixed but $0 \leq \phi \leq 2\pi$, were taken in 40 μm steps. Figure B.5 (a) is the same as Figure B.4 (a), where the cross section at the radial antinode is indicated. Figure B.5 (b) shows an average of seven cross-sections centered at the peak density. The blue points represent the absorption data along the cross section. The red line is the theoretical fit from the model in Equation (B.7). The $\sin 3\phi$ variation in density is clear in the data, and consistent with effects qualitatively observed in the intensity distribution of the LG_0^1 laser beam [62]. For cross sections interior and exterior to the peak density, the $\sin 3\phi$ azimuthal trend is difficult to resolve due to the noise in the data including large variations due to interference in the probe laser from multiple reflections[1].

B.4 Conclusion

We successfully demonstrated 2D confinement of atoms from a MOT for both a blue-detuned LG_0^1 laser mode in which the atoms were confined in the center node of the laser beam and for a red detuned LG_0^1 laser mode in which the atoms were confined in the high-intensity ring. Asymmetries in the azimuthal intensity profile of the trapping laser appear as density inhomogeneities. From our model of the density distribution, we determined that the confining potential fluctuates by

---

[1] A *Mathematica*™ notebook containing the data and all 60 cross-sections can be found online at [103].

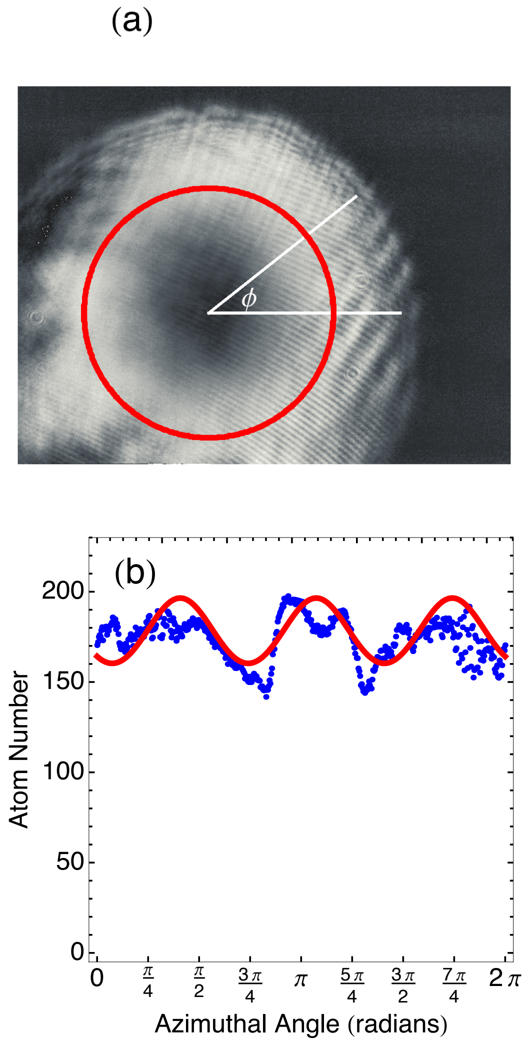

Figure B.5: (Color online) (a) A 2D CCD image of the data shown in B.3 (a). The cross section is indicated in the CCD image by the solid red curve. (b) The blue points are the average of seven cross section separated by 40 μm, centered on the peak density. For each cross section, r is fixed and $0 \leq \phi \leq 2\pi$. The red curve is a fit of the data using Equation B.7, showing the $\sin 3\phi$ variations in the density.

13% along the azimuthal direction. We did not make any attempt to optimize azimuthal symmetry in this study. From previous work [62], these variations can be eliminated with better alignment through the diffractive optics. However, this work also indicates that a systematic study of the purposeful misalignment of the diffractive optics in warranted to create new confinement potentials such as ferris wheel traps [104].

High purity (symmetric) LG_p^ℓ modes are important for degenerate gas applications, gyroscopes, and vortex matter-wave creation, stability, and interferometry. We have shown that analysis of the atomic distribution is a method to analyze the symmetry of the LG_p^ℓ transverse mode *in situ* for systems where regular analysis of the full, high-intensity trapping beam is not feasible. Also, purposeful creation of periodic, azimuthal intensity variations in the LG_p^ℓ modes may provide multiple traps for the toroidal geometries, increasing the range of experiments accessible to LG_p^ℓ beams made by diffractive optics.